NEW ASPECTS OF PARTICLE ACCELERATION IN COLLAPSING MAGNETIC TRAPS

Solmaz Eradat Oskoui

A Thesis Submitted for the Degree of PhD
at the
University of St Andrews

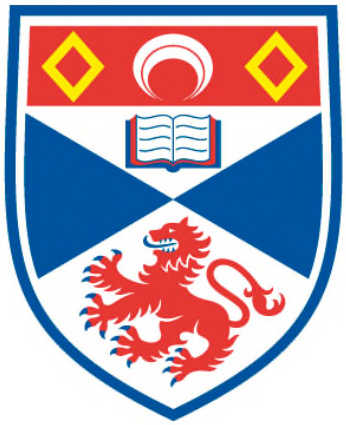

2014

New Aspects of Particle Acceleration in Collapsing Magnetic Traps

Solmaz Eradat Oskoui

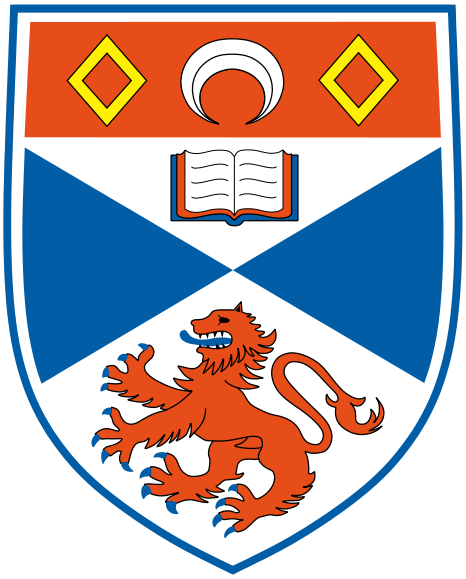

Thesis submitted for the degree of Doctor of Philosophy

of the University of St Andrews

20/01/2014

Abstract

Collapsing magnetic traps (CMTs) have been suggested as one of the mechanisms that could contribute to particle energisation in solar flares. The basic idea behind CMTs is that charged particles will be trapped on the magnetic field lines below the reconnection region of a flare. This thesis discusses a number of important new aspects in particle energisation processes in CMTs, based on the model by Giuliani et al. (2005).

In particular, we extend previous studies of particle acceleration in this CMT model to the relativistic regime and compare our results obtained using relativistic guiding centre theory with results obtained using the non-relativistic guiding centre theory. The similarities and differences found are discussed.

We then present a detailed study of the question, what leads to the trapping or escape of particle orbits from CMTs. The answer to this question is investigated by using results from the non-relativistic orbit calculations with guiding centre theory and a number of simple models for particle energy gain in CMTs. We find that there is a critical pitch angle dividing trapped particle orbits from the escaping particle orbits and that this critical pitch angle does not coincide with the initial loss cone angle.

Furthermore, we also present a calculation of the time evolution of an anisotropic pressure tensor and of the plasma density under the assumptions that they evolve in line with our kinematic MHD CMT model and that the pressure tensor satisfies the double-adiabatic Chew-Goldburger-Low (CGL) theory.

Finally, we make a first step to introduce Coulomb scattering by a Maxwellian background plasma into our guiding centre equations by changing them into a set of stochastic differential equations. We study the influence of a static background plasma onto selected particle orbits by pitch angle scattering and energy losses, and look at its effect on the particle energy and the trapping conditions.

Declarations

I, Solmaz Eradat Oskoui, hereby certify that this thesis, which is approximately 34000 words in length, has been written by me, that it is the record of work carried out by me and that it has not been submitted in any previous application for a higher degree.

I was admitted as a research student in April 2010 and as a candidate for the degree of Doctor of Philosophy in April 2008; the higher study for which this is a record was carried out in the University of St Andrews between April 2010 and 2014 January.

Date: _____ Signature of Candidate: _____.

I hereby certify that the candidate has fulfilled the conditions of the Resolution and Regulations appropriate for the degree of Doctor of Philosophy in the University of St Andrews and that the candidate is qualified to submit this thesis in application for that degree.

Date: _____ Signature of Supervisor: _____.

In submitting this thesis to the University of St Andrews we understand that we are giving permission for it to be made available for use in accordance with the regulations of the University Library for the time being in force, subject to any copyright vested in the work not being affected thereby. We also understand that the title and the abstract will be published, and that a copy of the work may be made and supplied to any bona fide library or research worker, that my thesis will be electronically accessible for personal or research use unless exempt by award of an embargo as requested below, and that the library has the right to migrate my thesis into new electronic forms as required to ensure continued access to the thesis. We have obtained any third-party copyright permissions that may be required in order to allow such access and migration, or have requested the appropriate embargo below.

The following is an agreed request by candidate and supervisor regarding the electronic publication of this thesis:

Embargo on both all of printed copy and electronic copy for the same fixed period of 2 years on the following ground(s):

- publication would preclude future publication.

Date: _____ Signature of Candidate: _____ Signature of Supervisor: _____.

Acknowledgements

I have been most fortunate and lucky to have had the opportunity to be part of the Solar and Magnetospheric Theory Group at the University of St. Andrews and had the support and belief of my supervisor Professor Thomas Neuikich. I cannot thank him enough for all that he has done for me. There are so many people who have helped make this time in my life memorable and I thank you from the bottom of my heart. Particularly, Keith for helping me with all the coding and programming questions when I started. My officemates and friends Julie, Sarah, Greg and Gordon (adopted from the office next door!) thank you for all the chats and laughs. It would have not been the same without you all. Ruth for always reminding me to "just keep swimming" and for all the much needed tea breaks during the write up time. Dee and Lyndsey for the nights out and in, particularity, DC and GA nights and our spin classes. My long time friends John and Shona for their loyalty and support over the years. Clare, for the great weekend in Ireland when I needed it the most. My school friend Sarah for all our Pizza Hut catch ups. Fiona and Niki for all your advice and support. Most importantly, my mum, dad and my sister Layla for their continual support, love and faith in me. I don't now what I would have done without you.

When I begin my PhD, my expectation was one where the course of this time would be pretty smooth with maybe only a few pumps here and there. It turns out it looks a bit like one of the many stochastic graph in chapter 6! You don't know when the next bump or jump is coming but it's learning how to deal with the unexpected that teaches you a lot about yourself and what you are able to do. I only hope to draw from what I have learn over this period in the future. I dedicate this thesis to my mum, sister and dad, for always believing in me. This is the best I have done so for and its for you.

Publications

Loss cone evolution and particle escape in collapsing magnetic trap models (Eradat Oskoui et al., 2014, Published in Astronomy & Astrophysics) .

Contents

Chapter 1

The Sun: A Brief Overview

The Sun is the closest Star to us and hence it can be studied observationally in great detail. Due to the energy generated in the Sun's core, the temperature of both the interior and the atmosphere in general are so high that all matter is ionised. Such ionised gas is often called plasma, i.e. a collection of free charged particles (electrons, protons and ions). The Sun is therefore an ideal "laboratory" for studying naturally occurring plasma processes. In the following we will first give a brief overview of the general structure of the Sun (interior and atmosphere) and then discuss solar flares and in particular particle acceleration, which is the topic of this thesis.

1.1 Stratified Structure of the Sun

The Sun is held together by its own gravitational force which always points towards its centre (Priest, 1982). The interior is made up of three major zones: the *core*, *radiative zone* and the *convection zone* moving outwards from the centre of the Sun. The atmosphere of the Sun is made of the *photosphere*, *chromosphere*, *transition region* and the *corona* moving outwards in the direction of interstellar medium. In the next two sections we will give a brief overview of these regions.

1.1.1 The Interior

The *core* is the innermost part of the Sun. It is about $0.25R_\odot$ [1] in radius and it is the hottest (1.5×10^7K) and the densest (1.6×10^5) kg m^{-3} region of all the Sun's structures. Inside the core energy is generated by nuclear fusion processes. The *radiative zone* is the region in between $\approx 0.25R_\odot$ to $0.7R_\odot$ where the generated energy is transferred upwards through about 70% of the Sun's radius. Its density and temperature drop from 2.0×10^4 kg m^{-3} to 10 kg m^{-3} and 8×10^6K to 5×10^5K from the bottom to the top of the radiative zone. The *convection zone* is the outermost zone where convection transfers the energy to the solar surface (Dwivedi, 2003). It extends from about $0.7R_\odot$ right up to the visible surface on the Sun (about 2.0×10^5 km in

[1] One solar radius, $R_\odot = 6.955 \times 10^8$m $= 6.955 \times 10^5$km

depth) where the temperature and density drop from 10 kg m^{-3} to 4×10^{-4}kg m^{-3} and 5×10^5K to 6.6×10^3K from the bottom of the convective zone to the top of the solar surface.

1.1.2 The Atmosphere

The photosphere is the lowest part of the solar atmosphere and can be identified with the Sun's visible surface (Golub and Pasachoff, 1997). It is the densest (10^{23} m^{-3}) region in the solar atmosphere, with a temperature of $\approx$ 5800K. It is a very thin region (about 550 km thick) from which most of the Sun's visible light escapes (Priest, 1982). Just above the photosphere lies the *chromosphere*. One would expect the temperature of the solar atmosphere above the photosphere to decrease with increasing height. However, over a range of $\approx$ 5000 km (i.e. less than a thousandth of $R_\odot$) the temperature of the solar atmosphere rises from 4300K at its base in the chromosphere to near coronal temperatures of almost 1MK (Gibson, 1977). The region in between the chromosphere and the *corona* in which this sharp temperature change occurs is known as the *transition region*. Over the height of about 2000 km to about 7000 km above the photosphere the temperature in this region increases by $\approx$ 1MK (Golub and Pasachoff, 1997).

Figure 1.1: Event viewed in 304 Angstrom wavelength of extreme ultraviolet light on the 31 August 2012 by the AIA instrument on SDO. A filament breaks off from an active flaring region. Credit: NASA's Solar Dynamics Observatory.

The solar *corona* is the high temperature ($>$ 1MK), low density part (about 10^{15} m^{-3}) of the Sun's atmosphere, where the primary emission falls in the Ultra-violet (UV) and X-ray region of the electromagnetic spectrum. Observations made over a range of wavelengths show that the corona is highly dynamic and spatially structured (inhomogeneous) where an example for such a dynamic process can be seen in Fig. 1.1, showing a filament eruption (Golub and Pasachoff,

1997). The reason for the inhomogeneity in the structure of the corona is the Sun's magnetic field. Generally the magnetic field in the corona consists of two distinct topological types: open and closed field lines (Sturrock et al., 1986). A *coronal hole* for instance, can be seen as an open magnetic field line phenomenon which appears darker and plasma continually flows outwards along these open field lines to give rise to what is called the *solar wind*, and *coronal loops* which may be seen as closed magnetic field lines (Priest, 1982).

One feature of the Sun's magnetic field is its cyclic behaviour (Sturrock et al., 1986). Traditionally the solar cycle is measured by counting the number of sunspots; cooler regions of stronger magnetic field which appear darker than the surrounding solar surface. One solar cycle "on average" lasts 11 years. At the end of an 11 year cycle the polarity on the Sun reverses and it takes one more cycle (in total 22 years) for the polarity to be restored. Maximum number of sunspots represent solar maximum, where solar activity on the Sun increases and minimum number of sunspots represent solar minimum, where solar activity on the Sun decreases. Therefore, the magnetic fields of the Sun, "of which a sunspot is the most intense example" (Priest, 1982) influences the phase and evolution of features like flares in the solar atmosphere which we will look at next.

1.2 Solar Flares

A flare is a localised, sudden transient brightening in the solar atmosphere. Seen as the most powerful event observed on the Sun (Fletcher et al., 2011), flares are often observed across a broad range of wavelengths, from gamma rays at the short wavelength end with high energy (above 100keV to some hundred of MeV) to radio waves at the long wavelength end with low energy (about 10^{-10}eV). It is generally considered to be a slow accumulation of magnetic energy and its subsequent fast conversion into *bulk flow*, *thermal (heating)*, *non-thermal (acceleration)* and *radiation energy* in the solar atmosphere. The durations of flares range from seconds to hours where energies in excess of 10^{25}J can be released. With the release of this energy charged particles like electrons, protons and heavy nuclei are heated and accelerated in the solar atmosphere. In general, we expect high energy radiation to be generated when non-thermal (energetic) electrons interact with low energy (thermal) protons. This process is called bremsstrahlung (braking radiation). In a flare, this process is assumed to happen when non-thermal high energy electrons generated by the energy release in a flare, interact with the dense plasma of the lower solar atmosphere, e.g. the chromosphere. This results in the emission of radiation over a broad range of wavelengths.

X-ray observations are a key diagnostic tool used in flare observations. X-ray observations from flares can be observed both in thermal (Soft X-rays (SXRs)) and non-thermal (Hard X-rays (HXRs)) energy ranges. SXRs in solar flares have a range of energies from about $0.1 - 10$keV and HXRs

from about 10keV − 1MeV. Assuming that electron bremsstrahlung is the correct mechanism by which high-energy radiation is generated during a flare, HXR emission provide information on the spectral, spatial and temporal variation of the high energy electrons in the flare. HXR emission is mainly observed from the lower part of the solar atmosphere (chromosphere), but recent results from RHESSI show that coronal HXR emission from solar flares is much more common than previously thought. Coronal HXR sources are of particular interest as they occur closest to where electron acceleration is believed to happen. Furthermore, because of the low plasma density in the corona compared to the chromosphere, it is currently an open question how the HXR emission (and in some cases γ emissions) in coronal/loop-top sources is generated (e.g. see review by Krucker et al., 2008). Solar flares most often occur in regions of strong magnetic field called active regions, which are associated with sunspots. Therefore, the frequency with which flares occur is also correlated to the solar cycle.

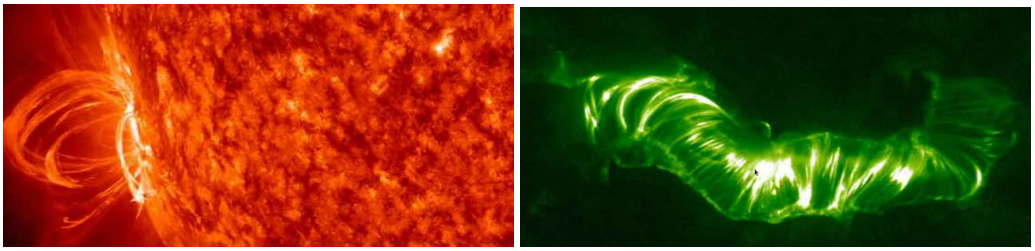

Figure 1.2: *Left*: Solar flare of 21 March 2011, observed in EUV by SDO. Credit: NASA's Solar Dynamics Observatory. *Right*: A flare arcade characteristic of the gradual phase in the flare evolution observed with TRACE in UV on the 14th of July 2000. (Adapted from the TRACE website.)

The evolution of a flare can be divided into two main stages/phases: *impulsive phase* and *gradual phase*. There may be a third stage where some initial sign of activity know as *pre-flare phase* is also observed before the impulsive phase. A brief description of each phase is given below.

In the pre-flare phase, brightenings in UV to SXR wavelengths have been reported. These brightenings can start a few minutes before the onset of the impulsive phase and correspond to plasma temperatures of roughly $1 - 3$MK (e.g. see observational review by Fletcher et al., 2011).

The impulsive phase is believed to happen when the primary energy release occurs in the evolution of a flare. This phase in the flare activity lasts from seconds to tens of minutes where the temperature can reach $10 - 20$MK. Observations of HXR and γ rays emissions during the impulsive phase are interpreted as evidence for the acceleration of electrons and proton/ions during this phase respectively, with radiation being caused by bremsstrahlung as mentioned above.

The gradual phase in the flare evolution is characterised by a slow decay in SXR and microwave emission. It is during this phase that one observes a series of post flare loops as seen in the right

hand image in Fig. 1.2. The flare loops are filled with hot dense plasma due to *chromospheric evaporation* where plasma from the chromospheric region is forced to expand into the corona as it is rapidly heated by particle energy deposition during the impulsive phase of the flare. These hot loops subsequently cool down during this phase of the flare evolution. This phase may last for several hours, however this very much depends on the characteristic of the flare itself (Fletcher et al., 2011).

As mentioned before flare emission can be observed across all of the electromagnetic spectrum. In particular, HXR, EUV and white-light ($H\alpha$) emissions are mainly observed from the lower regions of the solar atmosphere as seen on the left hand figure in 1.2. These emissions are thought to be associated with the foot points of magnetic field lines which have undergone magnetic reconnection. However, as mentioned before coronal sources in HXRs are also detected (Krucker et al., 2008).

1.3 Acceleration Mechanisms in Solar Flares: Overview

The production of a significant number of high energy particles within a short period of time is a main feature of a solar flare. Currently the release of magnetic energy from stressed coronal magnetic fields is believed to be the primary source of energy in solar flares (see e.g. review papers by Miller et al. (1997); Aschwanden (2002); Neukirch (2005); Krucker et al. (2008); Fletcher et al. (2011)). This energy is converted into bulk flow energy, thermal and non-thermal particle energy and radiation energy. How this energy is divided up and why a large fraction of this energy goes into non-thermal energy is still an important question in solar physics (see Miller et al. (1997); Emslie et al. (2004), 2005; Sui et al. (2005) and Krucker et al. (2008) for discussions). As discussed above, with the detection of various types of emissions particularly SXR, HXR and γ rays, there is clear evidence of heating and particle acceleration occurring during a flare. HXRs are evidence of electron acceleration whereas γ ray emissions are considered evidence of ion/proton acceleration. In this section we will give a brief outline of some of the different acceleration mechanisms which could be responsible for generating high-energy particles in solar flares. Fig.1.3 attempts to give a schematic overview of the possible location of several acceleration mechanisms which could be at work during a flare (Neukirch et al., 2007). Some of the proposed acceleration mechanisms (see reviews by Miller et al. (1997); Aschwanden (2002); Neukirch (2005); Krucker et al. (2008); Zharkova et al. (2011); Cargill et al. (2012) are: (1) direct current electric field acceleration in the magnetic reconnection regions; (2) stochastic acceleration due to 2^{nd} order Fermi acceleration by turbulence or resonant wave-particle interactions; (3) shock acceleration where the reconnection

outflow encounters strong magnetic field regions beneath the reconnection site; (4) relaxing magnetic field lines moving downwards could also accelerate particles. The main topic of this thesis is the investigation of point (4) in the list above. This particle acceleration mechanism is called Collapsing Magnetic Traps (CMTs).

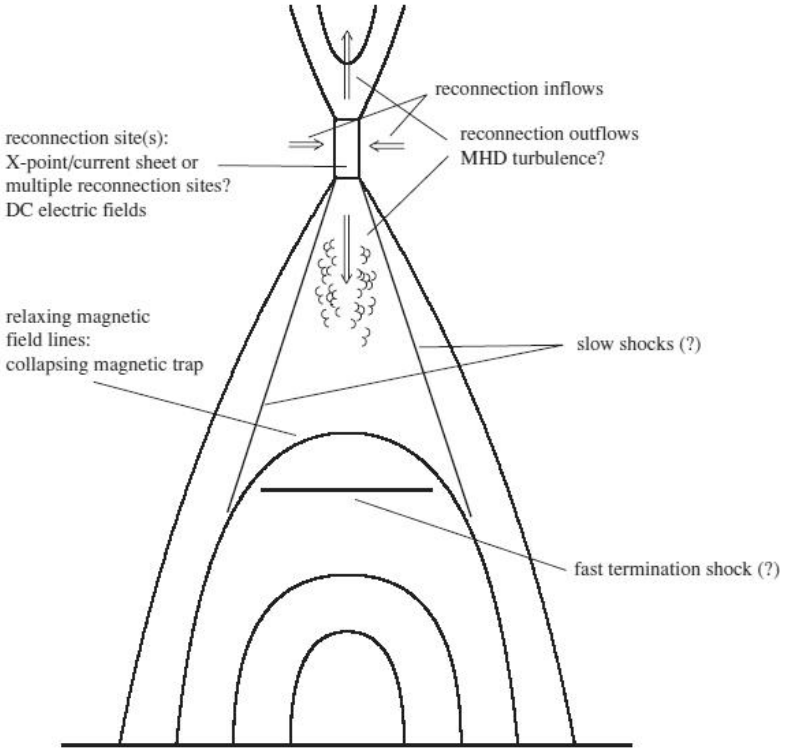

Figure 1.3: Sketch of the general magnetohydrodynamic (MHD) flare scenario.(Neukirch et al., 2007)

The electron flux required in large flares would imply that the part of the corona in which the flare occurs would have to be completely devoided of electrons in a very short amount of time (seconds). There is also the associated problem of large and complex magnetic fields being generated due to particle beams travelling down to the chromosphere, as well as the closure of the large scale return current systems due to charge balance. These problems have so far not been solved in any satisfactory manner.

Next we will give a brief outline of some of the different acceleration mechanisms that have been suggested for particle energisation in solar flares.

1.3.1 DC Electric Field Acceleration

In general, charged particles will be accelerated by electric fields. Therefore, it is logical to look at plasma processes which are associated with electric fields capable of explaining the observed particle energies. A process which has been discussed for decades as being key to particle acceleration in flares is magnetic reconnection (e.g. see reviews by Zharkova et al., 2011; Cargill et al., 2012). It is widely accepted that magnetic reconnection plays a crucial role in solar flares. Furthermore, magnetic reconnection is naturally associated with large-scale electric fields parallel to the magnetic field (see e.g. Schindler, 2006). Theoretical and observational estimates show that typical electric field strengths in a flare can be of the order of $10^2 - 10^3 V/m$. These values are much larger than the so-called Dreicer field E_D. This Dreicer field (see e.g. Aschwanden, 2004b) indicates the electric field strength needed for the accelerated particles to overcome the deceleration by Coulomb collisions with the thermal background plasma. The Dreicer field E_D is given by (e.g. Aschwanden, 2002),

$$E_D = \frac{q_i \ln \Lambda}{4\pi\epsilon_0 {\lambda_D}^2} \approx 6.10^{-3} \left[\frac{\rho}{10^{15} m^{-3}}\right] \left[\frac{T}{10^6 K}\right]^{-1} \frac{V}{m} \tag{1.1}$$

where q_i is the charge of a particle, $\epsilon_0 = 8.8542 \times 10^{-12} F m^{-1}$ is permittivity of free space, $\ln \Lambda$ is the Coulomb Logarithm and for typical coronal values is of the order 20. $\lambda_D = \sqrt{[\epsilon_0 k_B T]/[\rho_i {q_i}^2]}$ is the Debye length, where $k_B = 1.3807 \times 10^{-23} J K^{-1}$ is the Boltzmann constant, T is the temperature in Kelvin and ρ is the plasma density. The DC electric field models are generally divided into the *(weak) sub-Dreicer model* and the *(strong) super-Dreicer model*. This division is reached by the comparison of $E_{\parallel}$ to the Dreicer field E_D.

When the parallel electric fields associated with magnetic reconnection exceed the Dreicer field, we speak of a super-Dreicer acceleration mechanism. The simplest models for solar flares usually only involve a single reconnection site (e.g. current sheet or X-point). Given the large electric fields associated with magnetic reconnection, reaching the particle energies required to explain the intense flare emissions is not a problem. However, due the small size of the non-ideal region where $E_{\parallel} \neq 0$, it is very difficult to generate the required particle fluxes (see e.g. Wood and Neukirch, 2005). More recent models suggest that multiple reconnection sites could be present in flares and this may help to alleviate the problem with generating the necessary particle fluxes (see Cargill et al., 2012, for review). There have also been suggestions of flare particle acceleration by sub-Dreicer electric fields (see e.g. Neukirch et al., 2007, for discussion). Such fields would need to be maintained over large distances and it is unclear how this could be achieved.

1.3.2 Stochastic Acceleration

Stochastic acceleration mechanisms are processes by which particles can either gain or loose energy over short time scales but on average gain energy over longer time scales. Many such mechanisms have been suggested for solar flares (see e.g. Miller et al., 1997) and no complete overview will be attempted here.

One class of stochastic acceleration is based on the interaction of particles with small-amplitude waves ("wave turbulence"), where particle energisation occurs due to resonance between the particle motion and the waves (e.g. between the gyro-frequency and the wave frequency). Some issues associated with such acceleration mechanisms are as follows: 1) the frequency/time scales of the particle motion and the wave have to match. This is, for example not to easy to achieve for electrons and magnetohydrodynamic (MHD) waves, hence other wave modes are needed to make wave-particle resonance mechanisms work for electrons. 2) as particles are accelerated, they move out of the resonance with the waves that have accelerated them and to have a continually working mechanism, a broad spectrum of waves is needed.

Another class of acceleration mechanisms is based on strong turbulence, in which the perturbation amplitudes are non-linear. While it has been suggested that such mechanisms could operate in flares (see e.g. Miller et al., 1997), work has been somewhat limited, particularly due to our lack of understanding of plasma turbulence. Details of the acceleration mechanism usually depend strongly on the assumptions made for the plasma turbulence.

1.3.3 Shock Acceleration

It is well known from other areas of astrophysics that shocks can be very efficient particle accelerators (e.g. shock formation during a supernova). Hence, particle acceleration by shocks has been suggested for solar flares as well. In particular, for flares, over the last few years the possibilities of a fast shock being formed where the reconnection outflow encounters the strong magnetic field region beneath the reconnection site (see Fig. 1.3) has been discussed (see e.g. Mann et al., 2009; Warmuth et al., 2009).

Two main mechanisms are usually associated with particle acceleration by shocks. The first one is called *drift acceleration* and is very similar to DC-electric field acceleration. In this process, particles moving along the shock front, gain energy from the shock electric field (see e.g. Miller et al., 1997). Particles can also gain energy if the magnetic field increases in the downstream direction due to the approximate conservation of the magnetic moment. The second mechanism is called *diffusive shock* acceleration. In this process the particles are scattered back to the shock

numerous times by interacting with moving scattering centres (waves/turbulence). This allows the particles to gain more energy than in a single shock crossing (see e.g Fermi, 1949). For shock acceleration to be effective in generating the energies observed in flares (typically $20 - 100$keV, see e.g. Neukirch et al., 2007), the injected particles need to have relatively high energies compared to the typical thermal energies in the corona. This is often considered to be a problem for shock acceleration in solar flares.

1.4 Collapsing Magnetic Trap Models: Overview

It has been suggested (see e.g. Somov and Kosugi, 1997) that as reconnecting magnetic field lines in solar flares relax/collapse to lower altitudes, they could capture pre-accelerated particles escaping from the reconnection current sheet and accelerate them further in a so-called collapsing magnetic trap (CMT). Newly reconnected field lines are frozen into the reconnection outflow, and are carried downwards. As the field lines collapse, the magnetic field strength increases with time. When the outflow is very fast and encounters the strong magnetic field below the flaring region a fast shock could form (see e.g. Somov and Kosugi (1997) for discussion of a CMT model with shocks). However, we will not investigate this possibility in this thesis.

Some evidence of stressed pre-flare magnetic field relaxation into a lower energy state, supposedly by shrinkage of magnetic field lines due to reconnection at higher altitudes has been found in observations. Forbes and Acton (1996) for example found loop shrinkage of about 20% and 32% over 2 hours and 8 hours respectively in two separate events using observations from the Yohkoh satellite. Reeves et al. (2008), using data from Hinode, found in two events, plasma loops that change from a cusp-like shape to a more rounded configuration. In both cases, loop shrinkage of about $17\% - 27\%$ was measured. These observational results are of the later phases of the flare evolution and evidence of faster loop evolution at earlier stages has yet to be reported, but, theoretically is expected. Observations of coronal loop shrinkage showing a correspondence with field line shrinkage in the core of a flare during the impulsive phase (i.e. "implosion") was reported by Simões et al. (2013). More examples on implosion can be found in Liu et al. (2009) and Liu et al. (2012).

There are two major effects contributing to the particle acceleration in this model, namely, *first order Fermi* and *betatron acceleration*. Generally in a CMT, first order Fermi acceleration happens when there is an increase in parallel energy of the trapped particles due to longitudinal/bounce invariance. Defined as $J = \oint p_{\|} ds$, this invariant is associated with the bouncing motion between mirror points, which are located either between the legs of the relaxing loops or at the fast-mode loop-top shock (see Fig. 1.3). A decrease in the length of the field lines in a CMT leads to a de-

crease in the distance between the mirror points. The decrease in spatial length of the collapsing magnetic field lines must on average be accompanied by the same increase in the parallel momentum $p_{\parallel}$ of the trapped particles for J to remain conserved. Betatron acceleration is the increase in perpendicular energy of the trapped particle due to the adiabatic invariance of magnetic moment. Defined as $\mu = \frac{mv_{\perp}^2}{2B}$, it is associated with the gyro-motion of the particle around magnetic field lines. As the magnetic field lines are transported out of the reconnection region the magnetic field strength increases with time. The same increase in the magnetic field magnitude B must be accompanied by the same increase in the perpendicular energy of the trapped particle for μ to remain conserved. Hence, the conservation of the particle's magnetic moment and the bounce invariant (see e.g Grady et al., 2012) give rise to the possibility of increase in the particle's kinetic energy by betatron acceleration and by first order Fermi acceleration (see e.g. Somov and Kosugi, 1997; Bogachev and Somov, 2005). A more detailed discussion of these two mechanisms will be given in Chapter 2.

Particle acceleration processes in CMTs have been investigated by Somov & co-workers using simple CMT models. For example, Bogachev and Somov (2001, 2005, 2007, 2009) investigated acceleration efficiencies between betatron and Fermi effects, evolution of energy distribution and the effect of coulomb collisions in CMTs respectively. In particular, Bogachev and Somov (2005) and (2007) found that thermal sources are formed in the trap when betatron acceleration dominates and non-thermal sources when electrons are accelerated by the Fermi mechanism. Due to the simple geometry of their CMT model they were able to separate the two acceleration mechanisms. The physics behind this model can be found in Somov (2004) which we will discuss in Chapter 4 alongside another simple model by Aschwanden (2004a). This decoupling of the mechanisms is not seen in more detailed models which we will discuss next.

Karlicky & co-workers looked into acceleration processes in CMTs with the viewpoint of finding an explanation for the formation of HXR and radio loop-top sources. Karlický and Kosugi (2004) used a very simple test-particle numerical model, which includes Coulomb collisions and pitch angle scattering. They investigated particle acceleration and heating processes by betatron type acceleration in CMTs and found the high energy electrons accumulated in the central part of the CMT. In the latter parts of the collapse all these high energy particles escape from the trap. Karlický (2005) and (2006) investigated the downward motion of X-ray loop-top sources and modelled the X-ray emission of the April 6, 2001 flare respectively. Subsequently, Karlický and Bárta (2006) used a 2D MHD simulation to model a CMT. They found particles are accelerated by the simultaneous operation of betatron and Fermi acceleration in CMT.

Minoshima et al. (2010) used a 2D relativistic drift kinetic approach where pitch angle scattering and Coulomb energy losses was neglected. Betatron acceleration was found to enhance the velocity distribution in the perpendicular direction, resulting in the generation of HXR emissions

at the loop-top where almost all the electrons were trapped at the loop-top. Minoshima et al. (2011) for the same model included energy dependent pitch angle scattering. They found intermediate energy particles at higher altitudes, consistent with above the loop-top HXR sources and lower and higher energy electrons at lower altitudes, consistent with microwave emissions. For this energy dependent distribution, they found more particles enter the loss cone and are lost from the trap.

Winter et al. (2011) investigated a case for long lived HXR loop-top sources that initially begin at the loop apex, move down the loop legs and then move up to the loop apex for a static magnetic field (see Reeves et al., 2012, for further investigation using this model). Recently, Simões and Kontar (2013) looked at four flares and found 2-8 times more electrons trapped at the loop tops. An explanation for these results is believed to be due to magnetic trapping and pitch angle scattering caused by turbulence causing the particles to remain at the loop top and not to enter the loss cone.

Giuliani et al. (2005) set up the frame work for an analytical non-relativistic CMT model in 2D and 2.5D, with a vanishing velocity field (bulk flow) in the invariant direction, i.e. $v_z = 0$. The basic magnetic field is created by two point sources and the evolution of the electromagnetic field is described through the ideal kinematic MHD equations. The evolution of the model is given in terms of the time dependent Eulerian to Lagrangian coordinate transformations. For a given set of initial conditions the flow field $\mathbf{v}$, the magnetic field $\mathbf{B}$, and the electric field $\mathbf{E}$ can be determined from the given transformation. Since the gyro-radius and gyro-period of the electrons are much smaller compared to typical time and length scales of the collapsing trap, the trajectories of the particles were determined using the non-relativistic guiding centre theory (Northrop, 1963).

Giuliani et al. (2005) found that trapped particles were accelerated due to the curvature terms in the parallel equations of motion, a result confirmed by Karlický and Bárta (2006). Subsequently, Grady and Neukirch (2009) investigated the effect of a shear flow in the invariant direction for a 2.5D and fully 3D non-relativistic model. They found similar energy gains by a factor of 5 or 6, which was consistent with the energy increase found by Giuliani et al. (2005) without a shear flow.

More recently, Grady et al. (2012) further investigate the energisation processes in a symmetric and an asymmetric [2] trap model. They found for a symmetric trap, most of the particle orbits remain trapped during the collapse time. They also found that, not surprisingly, different initial positions (x, y), initial energies E and initial pitch angles θ have an effect on the position of the mirror points, the energy gain of the particle orbits and on whether they remain trapped or escape. In particular, they found that the particle orbits that gain most energy during the trap collapse

[2] For an asymmetric trap model, they found smaller energy gains and and a large number of particles escape from the trap.

have initial pitch angles θ close to 90° and initial positions in a weak magnetic field region in the middle of the trap. These particle orbits having the largest energy gain remained trapped during the collapse and due to their pitch angle staying close to 90° have mirror points very close to the centre of the trap. Grady et al. (2012) argue that these particle orbits are energised mainly by the betatron mechanism. Other particle orbits with initial pitch angles closer to 0° (or 180°) seem to be energised by the Fermi mechanism at the beginning, but as already pointed out by Giuliani et al. (2005) and corroborated by Grady et al. (2012), these particle orbits gain energy when passing through the centre of the trap where the field line curvature has its maximum. At later stages these particle orbits also seem to be undergoing mainly betatron acceleration.

For this thesis, we will utilise and build upon the findings from Giuliani et al. (2005) and Grady et al. (2012). After an overview of guiding centre theory and the CMT model of Giuliani et al. (2005) in Chapter 2, we begin our investigation in Chapter 3 were we will compare non-relativistic particle orbits with relativistic particle orbits. In Chapter 4 we investigate the trapping and escape conditions for CMT models through comparing the evolution of the loss cone angle and particle pitch angle in our model. In Chapter 5 the pressure and density evolution in our model using the double-adiabatic approximation is investigated and in Chapter 6 we take the initial steps into introducing Coulomb collisions into the CMT model. The discussion and conclusions in Chapter 7 conclude the main body of this thesis.

Chapter 2

Overview of Particle Orbit Theory and the Giuliani et al. (2005) CMT Model

In this thesis we describe the evolution of charged particles in a given electric field, **E**, and a given magnetic field, **B**, by calculating their orbits/trajectories and neglecting the back reaction of the particle motion on the fields. This is known as *Test Particle Orbit Theory*. Consider a charged particle q_i, with mass m_i at a position $\mathbf{r}_i(t)$ moving in given **E** and **B** field. We use both the non-relativistic equation of motion (in SI units) which is given by,

$$m_i \frac{d}{dt}(\dot{\mathbf{r}}_i) = q_i \left[\mathbf{E}(\mathbf{r},t) + \dot{\mathbf{r}}_i \times \mathbf{B}(\mathbf{r},t)\right], \tag{2.1}$$

and the relativistic equation of motion which is,

$$m_i \frac{d}{dt}(\dot{\mathbf{r}}_i \gamma) = q_i[\mathbf{E}(\mathbf{r},t) + \dot{\mathbf{r}}_i \times \mathbf{B}(\mathbf{r},t)]. \tag{2.2}$$

Here, $c = 2.9979 \times 10^8\ ms^{-1}$ is the speed of light in vacuum and $\gamma = 1/\sqrt{1 - v^2/c^2}$ is the Lorentz factor. The quantities with the dots, i.e. $\dot{\mathbf{r}}$, $\ddot{\mathbf{r}}$ and so on represent the first derivative, second derivative and so on with respect to time.

In principle, the motion of a charged particle in our CMT model is determined by integrating the full particle orbit equations of motion as stated above. Integrating the full particle orbit equations would mean taking many time steps in order to resolve the gyro-motion and hence for the particle to move a considerable distance along the field lines. However, we can make use of the vast separation of length and time scales between the gyrational motion of the particle orbits and the MHD length-scales (L) for our models. Denoting the Larmor or gyro-radius of a particle by r_L, T as the characteristic time scale and the Larmor or gyro-frequency as Ω, the conditions $r_L \ll L$ and $\frac{2\pi}{T} \ll \Omega$ are always very well satisfied (see detailed discussion later in this chapter). This means that we can use the so called guiding centre equations of motion, which average over the gyro-motion and hence eliminate the need for very small time steps (see Fig. 2.1). The guiding centre equations are split into one equation describing the time evolution of the parallel velocity, $v_\parallel(t)$, of the guiding centre and the other equation describing the time evolution of the guiding centre position , $\mathbf{R}(t)$, perpendicular to the magnetic field direction. We start by looking at the

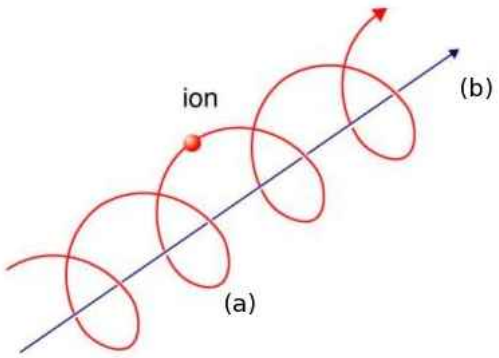

Figure 2.1: **(a)** shows the exact motion of the particle and **(b)** shows the guiding centre trajectory. Image adapted from the IPO blog http://www.iopblog.org/2010-schools-lecture-part-6/new-picture-10/

non-relativistic and relativistic equations for the parallel velocity, which are given by Northrop (1963) as,

Non-Relativistic

$$\left(\frac{m}{q}\right)\frac{dv_\parallel}{dt} = \cancelto{0}{E_\parallel} - \frac{\mu}{q}\frac{\partial B}{\partial s} + (\frac{m}{q})\mathbf{u}_E \cdot (\frac{\partial \mathbf{b}}{\partial t} + v_\parallel \frac{\partial \mathbf{b}}{\partial s} + \mathbf{u}_E \cdot \nabla \mathbf{b}), \tag{2.3}$$

Relativistic

$$m\frac{d(\gamma v_\parallel)}{dt} = \frac{dp_\parallel}{dt} = q\cancelto{0}{E_\parallel} - \frac{\mu_r}{\gamma}\frac{\partial}{\partial s}\left[B\left(1 - \frac{{E_\perp}^2}{c^2B^2}\right)^{1/2}\right] + m\gamma\mathbf{u}_E \cdot (\frac{\partial \mathbf{b}}{\partial t} + \frac{v_\parallel}{\gamma}\frac{\partial \mathbf{b}}{\partial s} + \mathbf{u}_E \cdot \nabla \mathbf{b}), \tag{2.4}$$

where

- m, q and c are the particle rest mass, charge and speed of light.
- $\mathbf{b} = \frac{\mathbf{B}}{B}$ is the unit vector along the magnetic field $\mathbf{B}$.
- s is the coordinate along the magnetic field lines.
- $v_\parallel = \mathbf{b} \cdot \dot{\mathbf{R}}$ is the particle velocity parallel to $\mathbf{B}$.
- $v_\perp$ is the particle velocity perpendicular to $\mathbf{B}$ (also know as the gyro-velocity).
- The electric field $\mathbf{E} = (0, 0, E_\perp)$ is given by ideal Ohm's law, where $E_\parallel = 0$.
- $\mathbf{u}_E = \frac{\mathbf{E}\times\mathbf{b}}{B}$ is the $\mathbf{E} \times \mathbf{B}$ drift velocity perpendicular to both $\mathbf{E}$ and $\mathbf{B}$.

- $\mu = \frac{W_\perp}{B} = \frac{m{v_\perp}^2}{2B}$ is the non-relativistic magnetic moment (see detailed discussion later).
- $\mu_r = \frac{m(\gamma v_\perp)^2}{2B}$ is the relativistic magnetic moment (see detailed discussion later).

The blue term in the above equations represent the magnetic mirror force. The green term is due to the curvature of the field lines.

The part of the guiding centre equations describing the perpendicular motion of the guiding centre to the magnetic field is:

Non-Relativistic

$$\begin{aligned}\dot{\mathbf{R}}_\perp &= \frac{\mathbf{b}}{B}\times\left[-\mathbf{E}+\frac{\mu}{q}\nabla B+\frac{m}{q}\left(v_\parallel\frac{\partial\mathbf{b}}{\partial t}+{v_\parallel}^2\frac{\partial\mathbf{b}}{\partial s}\right.\right.\\ &+ \left.\left. v_\parallel\mathbf{u}_E\cdot\nabla\mathbf{b}+\frac{\partial\mathbf{u}_E}{\partial t}+v_\parallel\frac{\partial\mathbf{u}_E}{\partial s}+\mathbf{u}_E\cdot\nabla\mathbf{u}_E\right)\right],\end{aligned} \tag{2.5}$$

Relativistic

$$\begin{aligned}\dot{\mathbf{R}}_\perp &= \frac{\mathbf{b}}{B(1-{E_\perp}^2/c^2B^2)}\times\left\{-\left(1-\frac{{E_\perp}^2}{c^2B^2}\right)\mathbf{E}\right.\\ &+ \frac{\mu_r}{\gamma q}\nabla\left[B\left(1-\frac{{E_\perp}^2}{c^2B^2}\right)^{1/2}\right]+\frac{m\gamma}{q}\left(v_\parallel\frac{d\mathbf{b}}{dt}+\frac{d\mathbf{u}_E}{dt}\right)\\ &+ \left.\frac{v_\parallel E_\parallel}{c^2}\mathbf{u_E}+\frac{\mu_r}{\gamma q}\frac{\mathbf{u}_E}{c^2}\frac{\partial}{\partial t}\left[B\left(1-\frac{{E_\perp}^2}{c^2B^2}\right)^{1/2}\right]\right\},\end{aligned} \tag{2.6}$$

where $E_\perp \ll cB$ or $\frac{E_\perp}{B} \ll c$ has been assumed in the relativistic equations. The terms in red in both equations represent the $\mathbf{E}\times\mathbf{B}$ drift velocity and give the largest contribution to the perpendicular velocity component. For ideal MHD, the $\mathbf{E}\times\mathbf{B}$ drift is usually identical to the perpendicular component of the MHD flow velocity. Since this drift is independent of charge and mass of the particle, it is the same for both electrons and ions.

The blue term is the gradient B drift (grad-B) which is in the direction of $\mathbf{B}\times\nabla\mathbf{B}$. Generally, it arises due to the transverse spatial gradient of the magnitude of $\mathbf{B}$. For a particle moving into a strong field region, the gyro-radius decreases since $r_L \propto \frac{1}{B}$ or as it moves into a weak field region, the gyro-radius increases. Hence, such a gradient causes the circular motion of the charged particle to be smaller in radius in regions of larger B than in regions of smaller B. The difference in gyro-radii is what causes the drift. Contrary to the $\mathbf{E}\times\mathbf{B}$ drift, the grad-B drift does depend on the charge, causing oppositely charged particles to drift in opposite directions perpendicular to both $\mathbf{B}$ and $\nabla\mathbf{B}$.

The terms in black results from the spatial and time derivatives of the magnetic and electric fields and include, e.g., what is usually called the curvature drift.

As mentioned before, some important assumptions need to be made in order for guiding centre theory to be valid. These are: (i) $\frac{2\pi}{T} \ll \Omega$, where $\Omega = \frac{q_i B}{m_i}$ is the gyro-frequency and T is the characteristic time, (ii) $r_L \ll L$, where r_L is the gyro-radius and L is the characteristic length-scale.

To give a more detailed calculation, we now compare typical gyro-radii with typical length-scales for the MHD models we will use later. The non-relativistic electron gyro-radius is $r_e = 2.38{T_e}^{1/2}B^{-1}cm$ and the proton/ion gyro-radius is $r_i = 1.02 \times 10^2 \mu^{1/2} Z^{-1} {T_i}^{1/2} B^{-1} cm$, where the electron temperature, T_e and the ion temperature, T_i is expressed in eV units. The ion mass (m_i) expressed in units of the proton mass $\mu = m_i/m_p = 1$, the charge state $z = 1$ and B is the magnetic strength in Gaussian cgs units. For a magnetic field strength of 10G and a typical solar coronal temperature of $10^2 eV$, the approximate values for the gyro-radii are, $r_e \approx 2.38cm$ and $r_i \approx 1.02 \times 10^2 cm$. For the relativistic case, the electron gyro-radius is

$$\begin{aligned} r_e &= \frac{mc^2}{eB}(\gamma^2 - 1)^{1/2} \qquad (cgs) \\ &= 1.70 \times 10^3 (\gamma^2 - 1)^{1/2} B^{-1} cm, \end{aligned} \tag{2.7}$$

where, $e = 4.8032 \times 10^{-10}$ (statcoul), $m_e = 9.1094 \times 10^{-28}$ (g), $c = 2.9979 \times 10^{10}$ (cm/s) and magnetic field strength is B measured in Gauss. The relativistic proton gyro-radius is

$$\begin{aligned} r_p &= \frac{mc^2}{eB}(\gamma^2 - 1)^{1/2} \qquad (cgs) \\ &= 3.13 \times 10^6 (\gamma^2 - 1)^{1/2} B^{-1}, cm \end{aligned} \tag{2.8}$$

where $m_p = 1.6726 \times 10^{-24}$ (g). All of the equations above for the gryo-radii (non-relativistic and relativistic) are taken exactly from NRL Book (2007). The typical gryo-radii are clearly much smaller than our MHD length-scales which are of the order 10^7m.

Therefore, Guiding Centre Theory and the concept of adiabatic invariants (see later) is a good approximation for the purpose of the studies in this thesis.

2.1 Adiabatic Invariants

As already mentioned in Section 1.4 the acceleration processes operating in CMTs can be understood at a basic level by using the two main adiabatic invariants. The first invariant, the magnetic

moment μ, is associated with the gyro/circulatory motion of a particle around a magnetic field line. The second invariant, the longitudinal/bounce invariant J, is associated with the mirroring of a particle back and forth along the field line.

2.1.1 The Invariance of μ

The proof of μ being an adiabatic invariant can be found in many text books on plasma physics. Following for example, Boyd and Sanderson (2003) we consider a static axially symmetric magnetic field which is increasing slowly in the direction of z as seen in Fig. 2.2. Using the solenoidal constraint for **B** in cylindrical polar coordinates gives,

$$\begin{aligned} \nabla.\mathbf{B} = \frac{1}{r}\frac{\partial}{\partial r}(rB_r) &+ \frac{\partial B_z}{\partial z} = 0 \\ \frac{1}{r}\frac{\partial}{\partial r}(rB_r) &= -\frac{\partial B_z}{\partial z} \\ rB_r &= -\int r\frac{\partial B_z}{\partial z}dr. \end{aligned} \tag{2.9}$$

Since $|B_r| \ll B_z$ and the magnetic field is approximately constant over one Larmor orbit, the above equation becomes

$$B_r(r_L) \simeq -\frac{r_L}{2}\frac{\partial B_z}{\partial z} \simeq -\frac{r_L}{2}\frac{\partial B}{\partial z}.$$

The same approximation for the z component of Eqn. 2.1 gives

$$\begin{aligned} m\frac{dv_\parallel}{dt} &= |q||v_\perp|B_r(r_L) \\ &= -\frac{W_\perp}{B}\frac{\partial B}{\partial z} \\ &= -\mu\frac{\partial B}{\partial z}, \end{aligned} \tag{2.10}$$

where q is the charge of the particle, $\mu = \frac{W_\perp}{B}$, with $W_\perp = \frac{mv_\perp{}^2}{2}$ the perpendicular particle energy and B is the magnetic field strength. Multiplying Eqn. 2.10 with the parallel velocity of the particle $v_\parallel \equiv \frac{dz}{dt}$ and using the chain rule gives

$$\frac{d}{dt}(\frac{1}{2}mv_\parallel{}^2) = -\mu v_\parallel\frac{\partial B}{\partial z} = -\mu\frac{\partial B}{\partial t}. \tag{2.11}$$

Since

$$\frac{d}{dt}(\frac{1}{2}mv_\perp{}^2) \equiv \frac{d}{dt}(\mu B), \tag{2.12}$$

adding equations 2.11 and 2.12 and using energy conservation gives $B\frac{d\mu}{dt} = 0$. Since the magnetic

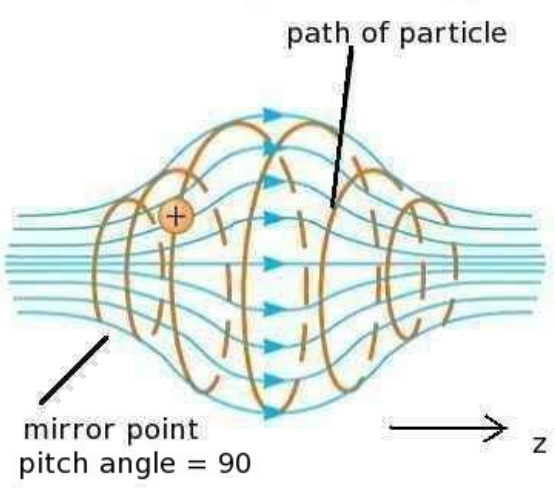

Figure 2.2: Particle moving in an inhomogeneous magnetic field towards increasing **B** and oscillating between the two end points. Adapted from http://www.kshitij-school.com/Study-Material/Class-12/Physics/Magnetic-fields/Motion-of-a-charged-particle-in-a-uniform-magnetic-field.aspx

.

field strength $B \neq 0$,

$$\frac{d\mu}{dt} = 0, \tag{2.13}$$

which implies that the magnetic moment is constant for all times to the order of approximation used above. An important point needs to be made here. Above we have been looking at a time-independent magnetic field and thus the total energy will remain constant. For the case of a CMT the magnetic field is time-dependent, meaning the energy is no longer conserved, however, the physical principles will remain the same. In the next section the most important consequence from the invariance of μ for the purpose of this thesis, namely, its effect on particle trapping and escape will be discussed.

2.1.2 Magnetic Mirrors

Let us now assume that a particle, for which μ is conserved, is moving towards a region of increasing magnetic field strength, as shown in Fig. 2.2. As the magnetic field strength B increases, the perpendicular energy $W_\perp$ must also increase due to the conservation of μ. The increase in the particle's perpendicular velocity $v_\perp$ is known as *betatron acceleration*. From the conservation of energy this means that $W_\parallel$ must decrease. Hence for some value of B the parallel velocity can become zero ($W_\parallel = 0$) and the particle pitch angle $\theta = 90°$. At this point the particle cannot penetrate further into the magnetic field and is reflected back towards weaker fields, with decreasing pitch angle. The point at which the particle is reflected is called the mirror point. A field

configuration as seen in Fig. 2.2 with two mirror points is known as a *magnetic bottle* or *adiabatic mirror trap* (see e.g. Boyd and Sanderson, 2003).

Of course, whether particles mirror or not depends on the details of the magnetic field configuration and the specifics of the particle orbit. To investigate this in more detail, one can look at the velocity vector **v** geometrically. As seen in Fig. 2.3 we have

- $v_{\parallel} = v\cos(\theta) \qquad v_{\perp} = v\sin(\theta)$,
- $\mu = \frac{mv^2\sin^2(\theta)}{2B}$,
- $\mu \equiv \frac{W}{B_m}$ $(W_{\parallel} = 0)$ at the mirror point.
- $\sin^2(\theta)/B = 1/B_m = constant$ which gives

$$\sin(\theta) = (\frac{B}{B_m})^{1/2}.$$

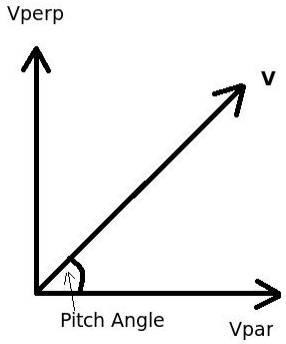

Figure 2.3: The $v_{\parallel}$ and $v_{\perp}$ components of the velocity vector **v**.

Here, θ is the particle pitch angle, B_m is the mirror point magnetic field, where the expression on the right hand side $(\frac{B}{B_m})^{1/2}$ represents the magnetic field ratio for which mirroring will occur. Whether a particle remains trapped in a magnetic bottle depends on if this ratio is $\leq$ or $>$ $(\frac{B}{B_{max}})^{1/2}$. Here, B_{max} represents the maximum field strength in the magnetic bottle.

If $(B_m \leq B_{max})$ then $\sin(\theta) > (\frac{B}{B_{max}})^{1/2}$, and the particle is reflected. If $(B_m > B_{max})$ then $\sin(\theta) \leq (\frac{B}{B_{max}})^{1/2}$, and the particle escapes. The ratio $(\frac{B}{B_{max}})^{1/2}$ represents $\sin(\alpha)$, where α is the loss cone angle which can be expressed as,

$$\alpha = \arcsin(\frac{1}{R})^{1/2}. \tag{2.14}$$

Here, $R = \frac{B_{max}}{B}$ is called the mirror ratio. For an increasing magnetic field strength the mirror ratio R decreases, causing the loss cone angle α to increase. For a decreasing magnetic field the mirror ratio begins to increase, causing α to decrease. In a CMT like in a magnetic bottle particles will be reflected back and forth when $\theta > \arcsin(\frac{1}{R})^{1/2} = \alpha$ and are lost when $\theta \leq \arcsin(\frac{1}{R})^{1/2} = \alpha$. We will investigate the trapping and escape conditions for our CMT model in Chapter 4.

2.1.3 The Longitudinal Adiabatic Invariant

The second adiabatic invariant important in the study of collapsing magnetic traps is the *longitudinal invariant*, *J*, defined by

$$J = \oint p_{\parallel} ds \tag{2.15}$$

where $p_{\parallel}$ is the parallel momentum of the particle, ds is the line element of the guiding centre path and the integral is taken over one complete bounce of the guiding centre. The proof of this quantity being invariant is given in Boyd and Sanderson (2003). This invariant arises due to the charged particle being reflected back and forth between mirror points and it proves useful in situations in which the mirror points are no longer static. Let the position of the mirror points be denoted by s_1 and s_2 at one time and by ${s_1}'$ and ${s_2}'$ at some other time. The invariance of J means that, denoting $s_1 - s_2 = s_0$ and ${s_1}' - {s_2}' = {s_0}'$ that

$${v_{\parallel}}' {s_0}' = v_{\parallel} s_0.$$

This implies that

$${v_{\parallel}}' \simeq v_{\parallel} \frac{s_0}{{s_0}'}.$$

If the ratio $\frac{s_0}{{s_0}'} > 1$, then the parallel velocity of the particle will increase. This is the basis behind *first order Fermi acceleration*.

Betatron and Fermi acceleration mechanisms associated with the invariance of magnetic moment μ and bounce invariant J, respectively, are important in the study of CMTs.

2.2 Theoretical Setup for the CMT Model

We start by outlining the approach to the CMT modelling used in Giuliani et al. (2005). Their CMT model uses: (1) A kinematic description of the magnetic field obeying ideal Ohm's Law, assuming that the CMT is outside the non-ideal reconnection region (i.e. $E_{\parallel} = 0$). (2) A time dependent transformation from Eulerian to Lagrangian coordinates which gives the time evolution of: the *flow field*, **v**(**x**,t), the *magnetic field*, **B**(**x**,t) and the *electric field*, **E**(**x**,t). The ideal kinematic MHD equations,

$$\mathbf{E} + \mathbf{v} \times \mathbf{B} = \mathbf{0} \qquad \text{(Ideal Ohm's Law)}, \tag{2.16}$$

$$\frac{\partial \mathbf{B}}{\partial t} = -\nabla \times \mathbf{E} \qquad \text{(Faraday's Law)}, \tag{2.17}$$

$$\nabla \cdot \mathbf{B} = 0 \qquad \text{(solenoidal Constraint)}, \tag{2.18}$$

describe the evolution of electric and magnetic fields for a given flow field $\mathbf{v}(\mathbf{x}, t)$. These equations provide the general framework for our analytical CMT model. We in addition assume that the magnetic field is translationally invariant in the z-direction and that the flow velocity has vanishing v_z. A Cartesian coordinate system $\mathbf{x} = (x, y, z)$ is set up as: x-axis is parallel to the photosphere, y-axis is perpendicular to the photosphere, representing the height above the solar surface, and the z-axis is perpendicular to both the x-axis and y-axis, representing the invariant direction.

Under the assumptions of translational invariance one can use a flux function $A(x, y, t)$ (equal to the z-component of the vector potential $\mathbf{A}$ where $\mathbf{B} = \nabla \times \mathbf{A}$) to write the magnetic field in the form

$$\mathbf{B} = \nabla A \times \mathbf{e}_z + B_z \mathbf{e}_z, \tag{2.19}$$

which automatically satisfies Eqn. 2.18. The other two equations, namely, the ideal Ohm's law and Faraday's Law can be written as

$$\frac{dA}{dt} = \frac{\partial A}{\partial t} + \mathbf{v}.\nabla A = 0, \tag{2.20}$$

$$\frac{\partial B_z}{\partial t} + \nabla.(B_z \mathbf{v}) = 0, \tag{2.21}$$

with the electric field given by

$$\mathbf{E} = -\frac{\partial \mathbf{A}}{\partial t} = -\frac{\partial A}{\partial t}\mathbf{e}_z. \tag{2.22}$$

In principle equations 2.20 and 2.21 have to be solved for a given flow field $\mathbf{v}(\mathbf{x}, t)$. In the theory of Giuliani et al. (2005), instead of defining the flow field directly, it is given implicitly by choosing a time-dependent transformation between Lagrangian and Eulerian coordinates. The coordinate transformation will be denoted by $x_0(x, y, t)$, $y_0(x, y, t)$, where x_0 and y_0 are the positions of fluid elements at a time $t = t_0$. The advantage is that one can then immediately solve Eqn. 2.20 using a flux function $A(x, y, t) = A_0(x_0, y_0)$ as an initial condition or, as was the choice of Giuliani et al. (2005), final condition.

In Giuliani et al. (2005) and this thesis the flux function A_0 is given by

$$A_0 = c_1 \arctan\left(\frac{y_0 + d/L}{x_0 + w}\right) - c_1 \arctan\left(\frac{y_0 + d/L}{x_0 - w}\right). \tag{2.23}$$

where usually we have chosen $L = 10$Mm as the characteristic length of the loop, $d = L$, x_0 and y_0 give the two coordinates of the two monopoles places that $x_0 = -L/2$, $y_0 = -d$ and $x_0 = L/2$, $y_0 = -d$ respectively. This flux function represents a potential magnetic field loop at time t_0 (we assume that $t_0 \to \infty$) created by two line sources of strength $c_1 = 150$G (one of positive and one of negative polarity) located at the positions $(-w, -d)$ and $(w, -d)$ below the lower boundary. All lengths here are scaled to the fundamental length scale L. Following Giuliani et al. (2005), we choose $w = 0.5$ and $d = L$, creating a symmetric magnetic loop (Fig. 2.4) [1] .

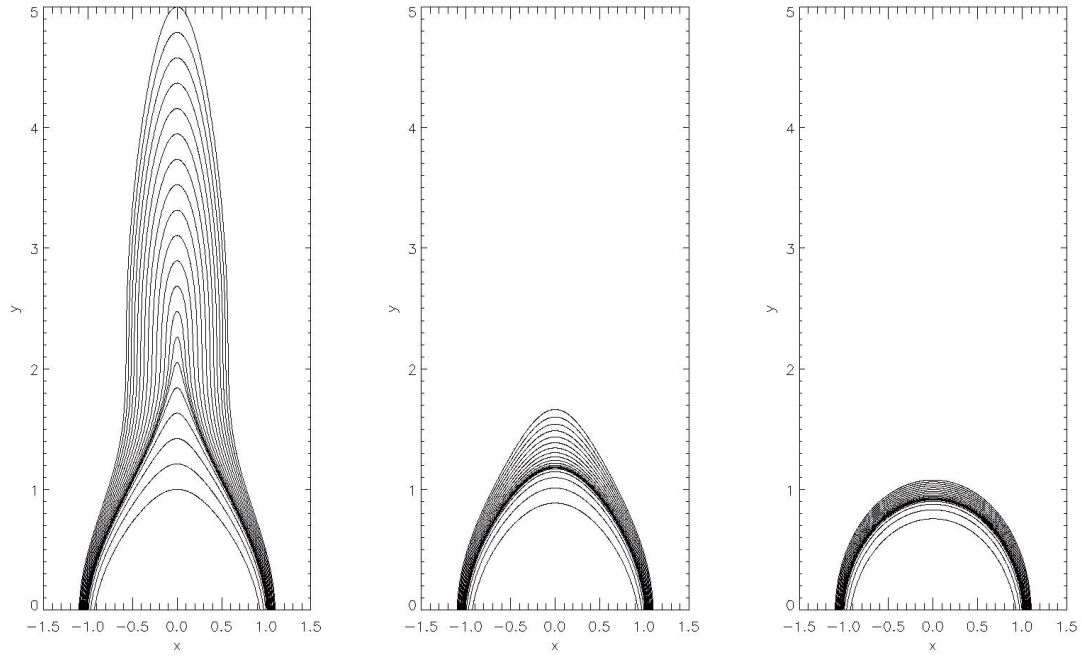

Figure 2.4: Magnetic field lines for the CMT model at the initial normalised time $t = 1.05$, final collapse time $t = 2.0$ and the asymptotic state $(t \to \infty)$ respectively.

The equation for the evolution of the transformation has the same form as the flux function $A(x, y, t)$ due to the flux being transported with the plasma flow (frozen-in condition). These time dependent transformations between Eulerian and Lagrangian coordinates are (Giuliani et al., 2005)

$$x_\infty = x, \tag{2.24}$$

$$y_\infty = (at)^b \ln\left[1 + \frac{y}{(at)^b}\right]\left\{\frac{1 + \tanh\left[(y - L_v/L)a_1\right]}{2}\right\} + \left\{\frac{1 - \tanh\left[(y - L_v/L)a_1\right]}{2}\right\} y. \tag{2.25}$$

[1] A point to note here is that for a loop like magnetic field model in the asymptotic limit, Eqn. 2.23 is chosen. If a different magnetic field structure is required then a different flux function can be chosen.

L_v is the characteristic height above which the magnetic field is stretched by the transformation. Below this height the magnetic field is largely unchanged. The parameter a_1 determines the scale over which this transition from unstretched to stretched field takes place, whereas a and b are parameters which are related to the timescale of the evolution of the CMT. We use the same values for the parameters as Giuliani et al. (2005), i.e. $a = 0.4$, $b = 1.0$, $L_v/L = 1.0$ and $a_1 = 0.9$. The transformations x_∞ and y_∞ represent the final coordinate values for the fluid element as $t \to \infty$. Using the final coordinates gives the added advantage of being able to use the transformations for both stretching and collapsing of the field lines (Giuliani et al., 2005). The behaviour of y_∞ as a

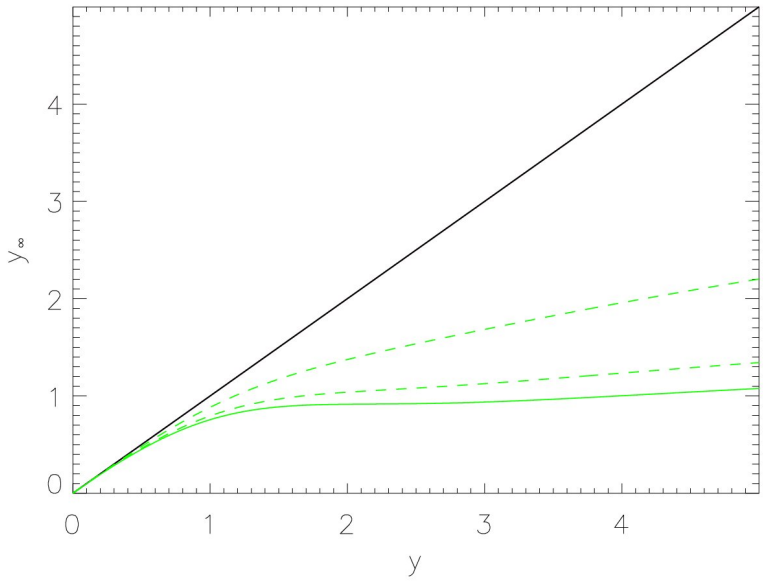

Figure 2.5: Graph of the transformation 2.25 at an initial time $t = 1.05$ (green) and for larger times $t \to \infty$ (black) are shown. Length scales are normalised with respect to $L = 10Mm$. The graph has an initial sharp transition at $y = 1$ where the function seems to be growing and has an almost plateau behaviour on the right. The transformation approaches the straight line in black $y_\infty = y$ as $t \to \infty$. (See analytical calculation below).

function on y is given illustrated in Fig. 2.5. For large t

$$\frac{y}{(at)^b} \ll 1 \Rightarrow y \ll (at)^b \Rightarrow y^{1/b} \ll at \Rightarrow t \gg \frac{y^{1/b}}{a}. \tag{2.26}$$

When t satisfies this condition then the argument of the $\ln$ in transformation 2.25 can be expressed as a Taylor series. This gives

$$y_\infty = (at)^b \left[\frac{y}{(at)^b} - \frac{y^2}{2(at)^{2b}} + \frac{y^3}{3(at)^{3b}} + \dots \right] \left\{ \frac{1 + \tanh[(y - L_v/L)a_1]}{2} \right\} + \left\{ \frac{1 - \tanh[(y - L_v/L)a_1]}{2} \right\} y.$$

As $t \to \infty$ it follows,

$$y_\infty \sim y \left\{ \frac{1 + \tanh[(y - L_v/L)a_1]}{2} \right\} + \left\{ \frac{1 - \tanh[(y - L_v/L)a_1]}{2} \right\} y = y. \tag{2.27}$$

As can be seen in Fig. 2.5, as $t \to \infty$ the green line representing the evolution of y_∞ approached the straight line in black. One can see from the figure that this transformation is a one-to-one transformation between $y \in [0, \infty)$ and $y_\infty \in [0, \infty)$, which insures that there is one and only one unique solution for any time and prevents any singularities occurring in the model.

2.2.1 Velocity, Electric and Magnetic Fields

In general going from Lagrangian coordinates

$$\mathbf{x}_0 = x_0(x, y, t)\mathbf{e}_x + y_0(x, y, t)\mathbf{e}_y \tag{2.28}$$

to Eulerian coordinates,

$$\mathbf{x} = x\mathbf{e}_x + y\mathbf{e}_y, \tag{2.29}$$

since $x_0(x, y, t)$ and $y_0(x, y, t)$ are constants, the total time derivative of Eqn. 2.28 is

$$0 = \frac{dx_0}{dt} = \frac{\partial x_0}{\partial x}\frac{dx}{dt} + \frac{\partial x_0}{\partial y}\frac{dy}{dt} + \frac{\partial x_0}{\partial t}$$
$$0 = \frac{dy_0}{dt} = \frac{\partial y_0}{\partial x}\frac{dx}{dt} + \frac{\partial y_0}{\partial y}\frac{dy}{dt} + \frac{\partial y_0}{\partial t}.$$

Since $v_x = \frac{dx}{dt}$ and $v_y = \frac{dy}{dt}$, from the transformations 2.24 and 2.25 the two equations above become

$$\cancel{\frac{\partial x_0}{\partial t}}^{0} + \cancel{\frac{\partial x_0}{\partial x}}^{1} v_x + \cancel{\frac{\partial x_0}{\partial y}}^{0} v_y = 0 \qquad \Rightarrow \quad v_x = 0$$
$$\frac{\partial y_0}{\partial t} + \cancel{\frac{\partial y_0}{\partial x}}^{0} v_x + \frac{\partial y_0}{\partial y} v_y = 0 \qquad \Rightarrow \quad v_y = -\frac{\frac{\partial y_0}{\partial t}}{\frac{\partial y_0}{\partial y}}$$

In our model the magnetic field and the electric field is given by

$$\mathbf{B} = \frac{\partial A}{\partial y}\mathbf{e}_x - \frac{\partial A}{\partial x}\mathbf{e}_y,$$
$$\mathbf{E} = -\frac{\partial A}{\partial t}\mathbf{e}_z$$

where we have assumed $B_z = 0$ and velocity field $v_z = 0$. In particular, if we enforce that the field lines of the collapsing trap relax to a loop like structure described by the flux function

$$A(x, y, t) = A_0(x_\infty(x, y, t), y_\infty(x, y, t)),$$

the x and y components of the magnetic field and the z component of the electric field at time t are given by

$$B_x = \frac{\partial A}{\partial y} = \frac{\partial A_0}{\partial x_\infty}\frac{\partial x_\infty}{\partial y} + \frac{\partial A_0}{\partial y_\infty}\frac{\partial y_\infty}{\partial y}, \tag{2.30}$$

$$B_y = -\frac{\partial A}{\partial x} = -\left(\frac{\partial A_0}{\partial x_\infty}\frac{\partial x_\infty}{\partial x} + \frac{\partial A_0}{\partial y_\infty}\frac{\partial y_\infty}{\partial x}\right). \tag{2.31}$$

$$E_z = -\frac{\partial A}{\partial t} = -\left(\frac{\partial A_0}{\partial x_\infty}\frac{\partial x_\infty}{\partial t} + \frac{\partial A_0}{\partial y_\infty}\frac{\partial y_\infty}{\partial t}\right) \tag{2.32}$$

The evolution of B_z is given by the z-components of the induction equation whereby

$$\begin{aligned}
\frac{\partial \mathbf{B}}{\partial t} &= \nabla \times (\mathbf{v} \times \mathbf{B}), \\
\frac{\partial B_z}{\partial t} &= -\mathbf{v} \cdot \nabla B_z - B_z \nabla \cdot \mathbf{v} = -\nabla \cdot (B_z \mathbf{v}), \\
\frac{\partial B_z}{\partial t} &+ \nabla \cdot (B_z \mathbf{v}) = 0.
\end{aligned} \tag{2.33}$$

The evolution of B_z has the same form as the continuity equation

$$\frac{\partial \rho}{\partial t} + \nabla \cdot (\rho \mathbf{v}) = 0. \tag{2.34}$$

Hence, when comparing Eqns. 2.33 and 2.34 if we find an expression for the evolution of B_z the same expression for the evolution of ρ can be used. Eqn. 2.33 is solved using the Jacobian determinant J_c of the time-dependent transformation

$$\mathbf{x} = \mathbf{x}(\mathbf{x}_0, t) = (x(x_\infty, y_\infty, t), y(x_\infty, y_\infty, t), t).$$

J_c satisfies the equation

$$\frac{1}{J_c}\frac{DJ_c}{Dt} = \nabla.\mathbf{v},$$

with the initial condition $J_c = 1$ at $t = t_0$. Expanding Eqn. 2.33 gives

$$\underbrace{\frac{\partial B_z}{\partial t} + \mathbf{v}.(\nabla B_z)}_{\frac{DB_z}{Dt}} + \underbrace{B_z(\nabla.\mathbf{v})}_{B_z(\frac{1}{J_c}\frac{DJ_c}{Dt})} = 0,$$

where $\frac{D}{Dt} = \frac{\partial}{\partial t} + (\mathbf{v}.\nabla)$ is the convective derivative. This gives,

$$\frac{1}{B_z}\frac{DB_z}{Dt} = -\frac{1}{J_c}\frac{DJ_c}{Dt}. \tag{2.35}$$

Integrating both sides of Eqn. 2.35 with respect to time results in

$$\ln(B_z) = -\ln(J_c) + \ln(I),$$

$$B_z J_c = I, \tag{2.36}$$

where I represents the constant of integration. Eqn. 2.36 can be seen as representing the invariance of magnetic flux through an infinitesimal area, where B_z is the magnetic field strength in the invariant direction, J_c is a measure of the area and I is the flux. A similar equation will be used in Chapter 5 where the behaviour of the pressure and density in the CMT model is investigated. Once the spatial and temporal derivatives of the electric and magnetic fields are found they are used in the guiding centre equations of motion (see Eqns. 2.3- 2.6) to calculate the particle trajectories in the CMT model.

Chapter 3

Examination of Particle Energisation and Motion in a Relativistic CMT

The main aim of this chapter is to examine the relativistic particle orbits in the fully analytical 2.5D CMT model developed by Giuliani et al. (2005) and Grady et al. (2012). These papers only consider particle trajectories/orbits in the non-relativistic regime but find that particles in the initial energy range they investigated are accelerated to mildly relativistic energies. Here we go a step further and replace the non-relativistic guiding centre equations with their relativistic counterparts taken from Northrop (1963). Using the guiding centre approximation which was discussed in detail in Section 2.2, in Section 3.1 the results obtained from the relativistic calculations will be compared with results obtained from the non-relativistic particle orbit calculations which are presented fully in Grady (2012)[1]. In Section 3.2 the effects of different initial conditions, i.e., initial pitch angle, initial injection position and initial energy using the relativistic code will be discussed and compared with the non-relativistic results. The chapter ends with discussions and conclusions.

3.1 Particle orbits and energy evolution for different initial energies

As a starting point for investigating the differences between relativistic and non-relativistic guiding centre orbits, modifications were made to the non-relativistic code through introducing relativistic guiding centre equations. For the relevant files in the numerical code which were written for the purpose of this study see Appendix A.1. For a typical test particle the particle orbit and energy graphs using the relativistic approximation are compared with results obtained from the non-relativistic approximation. The normalised relativistic drift equations of motion in the code are

$$\begin{aligned}\dot{\mathbf{R}}_{\perp} = \mathbf{u}_E \quad &+ \quad \frac{1}{\Omega_0 t_0}\left\{\frac{\mathbf{b}}{B}\times\left[\frac{\mu_r \nabla B}{\gamma} + \gamma(v_{\parallel}\frac{d\mathbf{b}}{dt} + \frac{d\mathbf{u}_E}{dt}) + \frac{{v_0}^2}{c^2\gamma}\mu_r \mathbf{u}_E \frac{\partial B}{\partial t}\right]\right\} \\ &+ \quad \frac{{v_0}^2}{c^2} v_{\parallel} E_{\parallel}\frac{\mathbf{b}}{B}\times\mathbf{u}_E \end{aligned} \tag{3.1}$$

[1]For the entirety of this thesis we only use a 2.5D model, however a generalisation into a 3D model was initially presented in an appendix in Giuliani et al. (2005) and investigated in Grady (2012).

and

$$\frac{dv_\parallel}{dt} = \mathbf{u}_E \cdot \frac{d\mathbf{b}}{dt} + \Omega_0 t_0 \frac{E_\parallel}{\gamma} - \frac{\mu_r}{\gamma^2}\frac{\partial B}{\partial s} - \Omega_0 t_0 \frac{{v_0}^2}{c^2}\frac{v_\parallel}{\gamma}\left(\dot{\mathbf{R}}_\perp + \mathbf{b}v_\parallel\right)\cdot\mathbf{E} - \frac{{v_0}^2}{c^2}\frac{\mu_r}{\gamma^2}\frac{\partial B}{\partial t}v_\parallel. \tag{3.2}$$

For the full derivation for the normalised equations see Appendix A.2. Equation 3.2 is obtained from applying the product rule to the left hand side of Eqn. 2.4 and using the energy equation (Northrop, 1963)

$$\frac{d}{dt}(m_0 c^2 \gamma) = q(\dot{\mathbf{R}}_\perp + \mathbf{b}v_\parallel)\cdot\mathbf{E} + \frac{\mu_r}{\gamma}\frac{\partial B}{\partial t}, \tag{3.3}$$

where $\Omega_0 = \frac{qB_0}{m_0}$ is the gyro-frequency of the charged particle m_0 is the rest mass of the charged particle, v_0 is the normalisation velocity and t_0 is the normalisation time. In Eqn. 3.1 the terms $\frac{1}{\Omega_0 t_0}$ and $\frac{v_0^2}{c^2}$ give very small contributions. Therefore, the main contributing term is the $\mathbf{E}\times\mathbf{B}$ drift or denoted as $\mathbf{u}_E$ in the equations.

The non-relativistic kinetic energy of the particle averaged over a gyro-period, E_K, is given by

$$E_k = \frac{m{v_\parallel}^2}{2} + \mu B + \frac{m{u_E}^2}{2}, \tag{3.4}$$

where $\frac{m{v_\parallel}^2}{2}$ is the parallel energy of the particle, μB is the rotational energy about the guiding centre (i.e. the perpendicular energy) and $\frac{m{u_E}^2}{2}$ is the energy associated with the perpendicular drift of the particle which give a negligible contribution. In the relativistic regime however, the total energy of the particle cannot be separated into different components and is expressed as

$$E_k = E_{rest}(\gamma - 1), \tag{3.5}$$

where $E_{rest} = mc^2 \approx 511keV$ is the rest mass energy of an electron and the Lorentz factor is $\gamma = 1/\sqrt{1 - v^2/c^2}$. The absolute particle velocity is given by $v = \sqrt{v_\parallel^2 + v_\perp^2 + u_E^2}$. Recalling that ${v_\perp}^2 = \frac{2\mu_r B}{m\gamma^2}$, the Lorentz factor can be expressed as

$$\gamma = \sqrt{\frac{1 + \frac{2\mu_r B}{c^2}}{1 - \frac{v_\parallel^2 + u_E^2}{c^2}}}. \tag{3.6}$$

The evolution of the energy expressions 3.4 and 3.5 and the particle trajectories will be investigated in detail in this section. We investigate four cases and will look at differences in particle orbit and energy evolution for a specific test particle using the non-relativistic and relativistic particle orbit

codes.

3.1.1 Case 1

We start by looking at a test particle with the initial conditions as seen in Table 3.1. The test

Range of initial conditions for Case1	
$\theta_{step} = 1$	$y_{step} = 1$
$\theta_{min} = 160°$	$y_{min} = 4.2L$
$\theta_{max} = 160°$	$y_{max} = 4.2L$
$x_{step} = 1$	$E_{step} = 1$
$x_{min} = 0L$	$E_{min} = 5.5keV$
$x_{max} = 0L$	$E_{max} = 5.5keV$

Table 3.1: Initial injection position, pitch angle and energy set up for the simulation.

particle starts at an initial pitch angle $\theta_{init} = 160°$ and initial kinetic energy $E_{init} = 5.5keV$. The particle injection position is $(x, y, z) = (0, 4.2L, 1.25 \times 10^{-6}L)$. Fig. 3.1 gives the trajectory of the test particle and the evolution of the kinetic energy calculated with the relativistic and non-relativistic equations. The panel on the left shows the particle trajectories for the relativistic and non-relativistic case. The relativistic orbit in turquoise is overplotted on the non-relativistic graph in black. The second panel on the right shows the energy evolution for the particle. The black line represents the total energy evolution for the non-relativistic orbit and the turquoise graph represents the energy evolution for the relativistic orbit. Looking at the energy graphs a step like pattern is seen which is a consequence of the exchange of parallel and perpendicular kinetic energy. Giuliani et al. (2005) speculated the mirror term was responsible for the continuous exchange between the parallel and perpendicular energies causing an oscillatory behaviour in the total non-relativistic energy. Since the initial kinetic energy, $E_{init} = 5.5keV$, is not highly relativistic there are no visible discrepancies seen in the orbit plots in Fig. 3.1. This can be explained by looking at the right hand graph in Fig. 3.1 where the total E_k for the non-relativistic case is given by Eqn. 3.4, $E_k = \frac{mv_{\parallel}{}^2}{2} + \mu B + \frac{mu_E{}^2}{2}$ and for the relativistic case by Eqn. 3.5, $E_k = mc^2(\gamma - 1)$. Table 3.2 gives the starting energy and the final energy for the particle,

Table 3.2: Minimum and maximum particle energies

	Relativistic	Non-Relativistic	Energy difference
$E_{min}(eV)$	5500	5500	0
$E_{max}(eV)$	14609.776	15017.167	407.391

obtained from the relativistic and non-relativistic codes. For this case the discrepancy between the final energies obtained from the non-relativistic and relativistic code is $407.391eV$. We can see from Fig. 3.1 the discrepancy between the two energy graphs is relatively small. Rearranging the

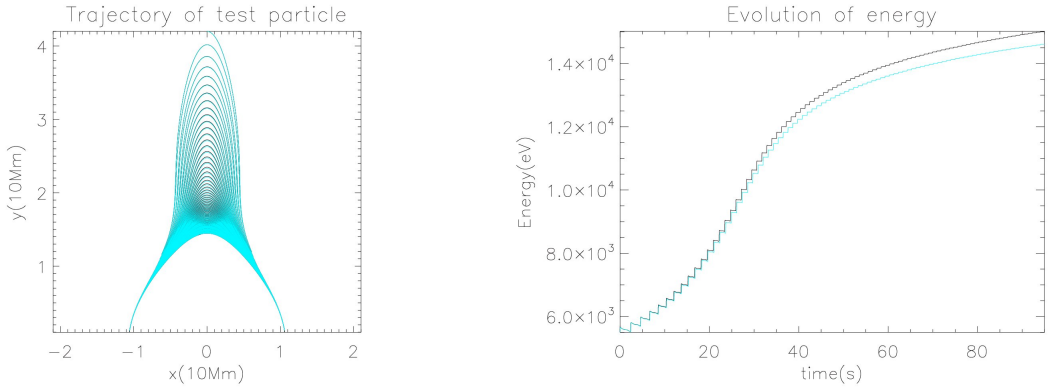

Figure 3.1: *Left*: The graph of test particle trajectory in the x-y plane for a non relativistic particle and a relativistic particle. *Right*: The graph for the energy evolution for $E_{init} = 5.5keV$ where the black line represents the non-relativistic result and the turquoise graph the relativistic result. Length scales are normalised to $L = 10Mm$ and the simulation runs for a finite time of 95 seconds.

relativistic energy equation 3.5 for γ gives

$$\gamma = \frac{E_k}{E_{rest}} + 1, \tag{3.7}$$

where the rest mass of an electron is $E_{rest} \approx 511keV$. Rearranging γ for v gives,

$$v = \sqrt{(1 - \frac{1}{\gamma^2})}c. \tag{3.8}$$

The initial starting energy given by the non-relativistic and relativistic code is $5.5keV$. Table

Table 3.3: γ & v for the relativistic case.

Relativistic	γ	v
$E_{min}(eV)$	1.0107	0.145c,
$E_{max}(eV)$	1.0286	0.234c.

3.3 shows the results for γ and v for the initial starting energy and final particle energy from the relativistic code. For $E_{k(min)} = 5.5keV$ using Eqns. 3.7 and 3.8,

$$\begin{aligned} \gamma &= \frac{5500}{511000} + 1 \approx 1.0107 \\ v &= \sqrt{1 - \frac{1}{\gamma^2}}c \approx 0.145c \end{aligned}$$

For $E_{k(max)} = 14609.775eV$, $\gamma = \frac{14609.776}{511000} + 1 \approx 1.0286$ and $v = \sqrt{1 - \frac{1}{\gamma^2}}c \approx 0.234c$. Also to reach the same energy using the relativistic code takes longer, since γ increases as the velocity of the particle v approaches $0.234c$. As a result of this relativistic effect the energies calculated using

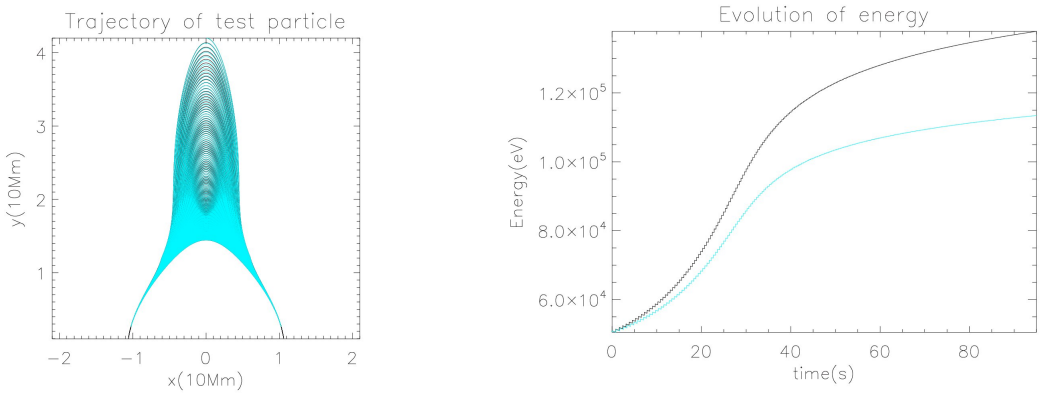

Figure 3.2: *Left*: The graph of test particle trajectory in the x-y plane for a non relativistic particle and a relativistic particle. *Right*: The graphs for the energy evolution for $E_{init} = 50.5keV$ where the black line represents the non-relativistic result and the turquoise graph the relativistic result. Length scales are normalised to $L = 10Mm$ and the simulation runs for a finite time of 95 seconds.

the relativistic code will be smaller compared to the non-relativistic case at the same time. This discrepancy is shown more clearly in the highly relativistic cases which will be discussed next in sections 3.1.2, 3.1.3 and 3.1.4.

3.1.2 Case 2

For this test particle case, the initial conditions for pitch angle and position are the same as for case 1, however, the initial particle energy is now $E_{init} = 50.5keV$. Like in the previous case, Fig.3.2 gives the trajectories and the energy evolution of the particles. The panel on the left shows the particle trajectories, where the relativistic turquoise result is overplotted on to the non-relativistic result in black. Small changes in the particle orbits become more prominent as the starting energy is increased. The discrepancy can be seen close to the foot points, where the relativistic orbit has higher mirror points than the non-relativistic orbit. Looking at the right panel the discrepancy between the energy graphs can also been seen. Table 3.4 gives E_{min} and E_{max} for the particle

Table 3.4: Minimum and maximum particle energies

	Relativistic	Non-Relativistic	Energy difference
$E_{min}(eV)$	50500	50500	0
$E_{max}(eV)$	113441.02	137902.88	24461.863

obtained from the relativistic and non-relativistic particle orbit code. The initial starting energy given by the non-relativistic and relativistic code is $50.5keV$. Table 3.5 shows the results for γ and v for the energies E_{min} and E_{max} for $t = 0s$ and $t = 95s$ respectively. Initially for $E_{init} = 50.5keV$, $\gamma = 1.098$ and $v = 0.414c$ at $t = 0s$. For the final time of $t = 95s$ at $E_{max} =$

$113441.02keV$, $\gamma = 1.22$ and $v = 0.574c$. For this case the discrepancy between the final energy for the relativistic orbit and the non-relativistic orbit is approximately $24461.863eV$, a significant difference from the result seen in case 3.1.1 which was $407.391eV$. With increasing starting energy E_{init}, the relativistic effects are enhanced due to the particle travelling at $v = 0.414c$. Since γ increases as the velocity of the particle approaches $0.574c$, to reach the same velocity using the relativistic code takes even longer, hence the energies calculated using the relativistic code will be even smaller compared to the non-relativistic case.

Table 3.5: γ & v for the relativistic case.

Relativistic	γ	v
$E_{min}(eV)$	1.098	0.414c
$E_{max}(eV)$	1.22	0.574c

3.1.3 Case 3

For this test particle case, the initial conditions for initial pitch angle and position are the same as before, however, the initial particle energy is now $E_{init} = 100keV$. Like in the previous two cases,

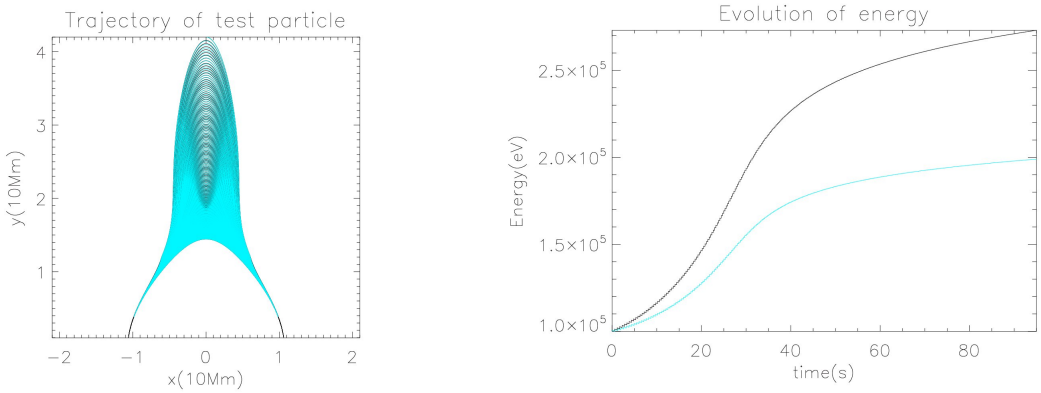

Figure 3.3: *Left*: The graph of test particle trajectory in the x-y plane for a non relativistic particle and a relativistic particle. *Right*: The graphs for the energy evolution for $E_{init} = 100keV$ where the black line represents the non-relativistic result and the turquoise graph the relativistic result. Length scales are normalised to $L = 10Mm$ and the simulation runs for a finite time of 95 seconds.

Fig. 3.3 gives the trajectories and the energy evolution of the particles. Changes in the particle orbits become more prominent as the starting energy is increased significantly. The discrepancy can be seen again clearly at the foot points where the relativistic orbit has higher mirror points than the non-relativistic orbit. The discrepancy between the energy graphs, seen clearly in Fig. 3.3 is much more prominent than the previous two cases since the initial energy $E_{init} = 100keV$ is already mildly-relativistic. Table 3.6 gives E_{min} and E_{max} for the particle for the relativistic

Table 3.6: Minimum and maximum particle energies

	Relativistic	Non-Relativistic	Energy difference
$E_{min}(eV)$	100000	100000	0
$E_{max}(eV)$	198979.76	273068.12	74088.351

Table 3.7: γ & v for the relativistic case.

Relativistic	γ	v
$E_{min}(eV)$	1.1957	0.548c
$E_{max}(eV)$	1.389	0.694c

and non-relativistic cases, where Table 3.7 shows the results for γ and v for the energies E_{min} and E_{max} for $t = 0s$ and $t = 95s$ respectively. Initially for $E_{min} = 100keV$, $\gamma = 1.1957$ and $v = 0.548c$ at $t = 0s$. For the final time of $t = 95s$, $E_{max} = 198979.76keV$ gives $\gamma = 1.389$ and $v = 0.694c$. For this case the discrepancy between the final energy for the relativistic orbit and the non-relativistic orbit is approximately $74088.351eV$, a significant increase to the differences seen in Case 1 which is $407.391eV$ and $24461.863eV$ in Case 2.

3.1.4 Case 4

For this final case, the initial conditions for pitch angle and position are the same as before, however, the initial particle energy is now $E_{init} = 200keV$. Fig.3.4 gives the trajectory and the energy evolution of the particles. Again changes in the particle orbits become more prominent as the starting energy is increased significantly compared to the previous cases. The discrepancy

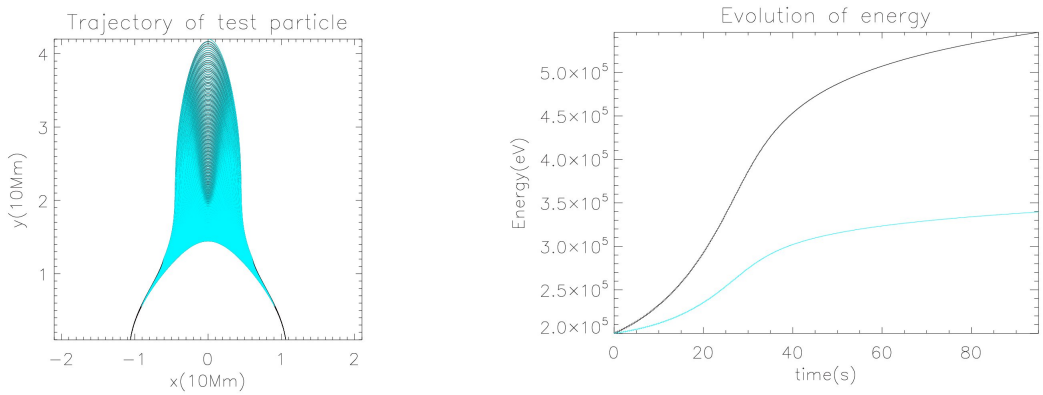

Figure 3.4: *Left*: The graph of test particle trajectory in the x-y plane for a non relativistic particle and a relativistic particle. *Right*: The graphs for the energy evolution for $E_{init} = 200keV$ where the black line represents the non-relativistic result and the turquoise graph the relativistic result. Length scales are normalised to $L = 10Mm$ and the simulation runs for a finite time of 95 seconds.

again is seen clearly at the foot points where the relativistic orbit has much higher mirror points than the previous cases.The initial kinetic energy E_{init} is now mildly relativistic and the discrepancy between the energy graphs can be seen clearly in the figure. Table 3.8 gives E_{min} and E_{max}

Table 3.8: Minimum and maximum particle energies

	Relativistic	Non-Relativistic	Energy difference
$E_{min}(eV)$	200000	200000	0
$E_{max}(eV)$	339488.68	546157.38	206668.71

Table 3.9: γ & v for the relativistic case.

Relativistic	γ	v
$E_{min}(eV)$	1.391	0.695c
$E_{max}(eV)$	1.664	0.799c

for the particle obtained from the relativistic and non-relativistic particle orbit codes, and Table 3.9 shows the results for γ and v for the energies E_{min} and E_{max} for $t = 0s$ and $t = 95s$, respectively. Initially for $E_{init} = 200keV$, $\gamma = 1.391$ and $v = 0.695c$ at $t = 0s$. For the final time of $t = 95s$ at $E_{max} = 339.49439keV$, $\gamma = 1.664$ and $v = 0.799c$. For this case the discrepancy between the final energy for the relativistic orbit and the non-relativistic orbit is approximately $206.66871keV$. This is a significant difference in energy compared to the other cases seen previously.

A point to mention here that for an energy of $5keV$, $\gamma \approx 1.01$. The relativistic electron gyro-radius (see Eqn. 2.7) for a magnetic field strength of $B = 150$G, $r_e = 1.6$ cm. For an energy of $200keV$, $\gamma \approx 1.39$. The relativistic electron gyro-radius, $r_e = 10.94$ cm. Both these gryo-radii are much smaller than the typical length scales in our CMT model which is of the order 10^7m. So even for strongly relativistic energies the guiding centre approximation remains valid.

As the initial energy is systematically increased, two main differences between the relativistic and non-relativistic approximations are seen. First, the final particle energy calculated using the relativistic approximation is always smaller than the non-relativistic case. This is due to the Lorentz factor affecting the terms in the equation of motion by reducing the size of the contributing terms. Secondly, the mirror points for the particles using the relativistic approximation are much higher than the non-relativistic case. This may be due to terms in the parallel guiding centre equation becoming smaller as γ increases with increasing particle velocity. Higher mirror points in the relativistic case might lead to more particles being trapped in the model since the particles do not travel all the way down to the foot points.

3.2 Effects of particle initial conditions on energy gain

In this section we will look at the effects of different initial pitch angle θ_{init}, energy E_{init} and injection positions in the x and y directions. Like in the last section, the results obtained from the relativistic particle orbit code will be directly compared with the results from Grady (2012) and Grady et al. (2012) and will be presented as case studies.

3.2.1 Case 1

Grady et al. (2012) found that the initial injection positions, pitch angle θ_{init} and initial energy E_{init} can affect the particle trapping time, location of mirror points and therefore the energy gain of the particles. The list below shows the initial conditions for 13310 particle orbits using the relativistic guiding centre approximation. For this case, 11 values for the pitch angle, θ_{step}, injection position in the x direction, x_{step}, in the y direction, y_{step} and for energy, E_{step} are chosen.

- Injection position: 11 values of x between $-0.5L$ to $0.5L$ and 11 values of y between $1L$ to $5L$.
- Initial energy: 11 values of energy between $5keV$ to $6keV$.
- Initial pitch angle: 10 values of pitch angle θ between 10° to 170°.

Multiplying all theses values for position, energy and pitch angle gives 13310 particle orbits. Table

Range of initial conditions for Case 1	
$\theta_{step} = 10$ $\theta_{min} = 10^\circ$ $\theta_{max} = 170^\circ$	$y_{step} = 11$ $y_{min} = 1L$ $y_{max} = 5L$
$x_{step} = 11$ $x_{min} = -0.5L$ $x_{max} = 0.5L$	$E_{step} = 11$ $E_{min} = 5keV$ $E_{max} = 6keV$

Table 3.10: Initial injection position, pitch angle and energy set up for Case 1.

3.10 summarises range of initial conditions for pitch angle, position and energy. In Fig. 3.5 the final energy of the particles starting with different initial injection position, pitch angles and energies are shown. The horizontal axis shows the initial particle pitch angle and the vertical axis shows the initial energy of the particle orbit. Each box on the graph represents one specific particle orbit. Here 10×11 particle orbits are selected, i.e., 110 particles where the colours indicate their final energy once the magnetic trap has stopped for a finite time. The colour bar on the right indicates the final energy of the particle. It can be seen that the highest energy particles come

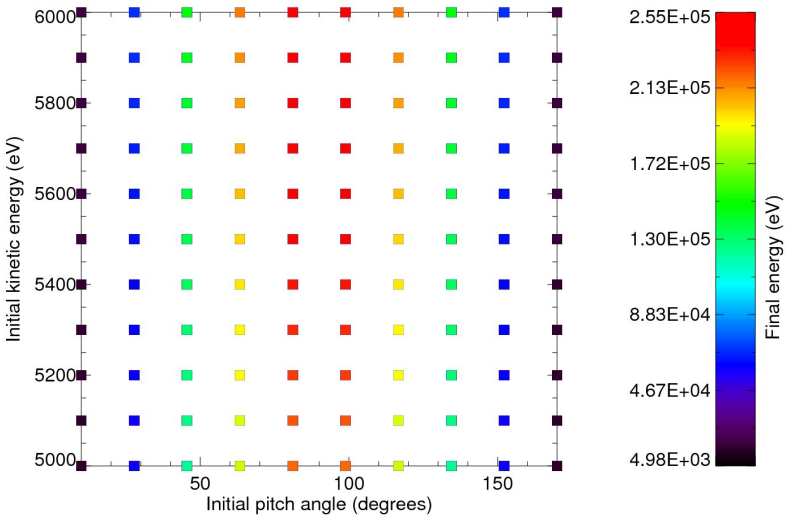

Figure 3.5: Final energy of the particles starting with different initial injection positions, initial pitch angles and initial energies is shown. It can be seen that the highest energy particles come from regions in the middle of the trap with initial pitch angles close to 90°.

from an initial injection position close to the middle of the trap and an initial pitch angle close to 90°. Comparing this result obtained of Grady (2012), the energy range in the non-relativistic case is approximately $4.98 - 317keV$. However, in the relativistic case it is $4.98 - 255keV$, which gives a difference in the final energy of $60keV$for the highest energy. The two plots in Fig. 3.6 show the final particle position of all the particles that remain trapped in the model with their corresponding final energies. The plot on the left is calculated using the non-relativistic case and the relativistic case on the right. Grady (2012) found particle orbits are kept close to the centre and are trapped at the loop top. The red region in the middle representing the highest energy particle orbits, which is more visible in the left plot (non-relativistic), implies there are less particle orbits with the highest energy gain when using the relativistic code than when using the non-relativistic code. The highest particle energy from the non-relativistic approximation (left-graph) is approximately $3.17 \times 10^5 eV$ whereas in the relativistic case its $2.55 \times 10^5 eV$.

The previous experiment was repeated for higher initial energies E_{init} set between $50 - 100keV$. The two top figures in Fig. 3.7 show the final particle position with the corresponding final energy. On the left the highest energy gain is about $5.32 \times 10^6 eV$ worked out with the non-relativistic particle orbit code. These particles with the highest energy have a Lorentz factor of $\gamma \approx 11.41$ and speeds of $v = 0.996$c. On the right the highest energy gain is about $1.99 \times 10^6 eV$ worked out with the relativistic particle orbit code. These particles have a Lorentz factor of $\gamma \approx 4.89$ and a speed of $v = 0.978$c.

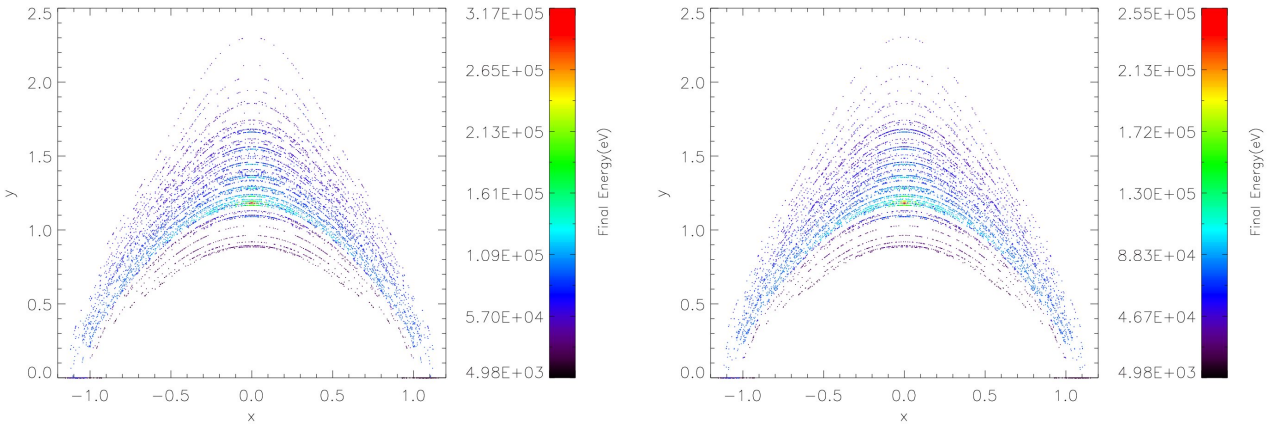

Figure 3.6: Graphs of final particle position with the corresponding final energy. *Left* non-relativistic and *Right* relativistic results. Both these graphs have an initial starting energy of $5keV$ to $6keV$.

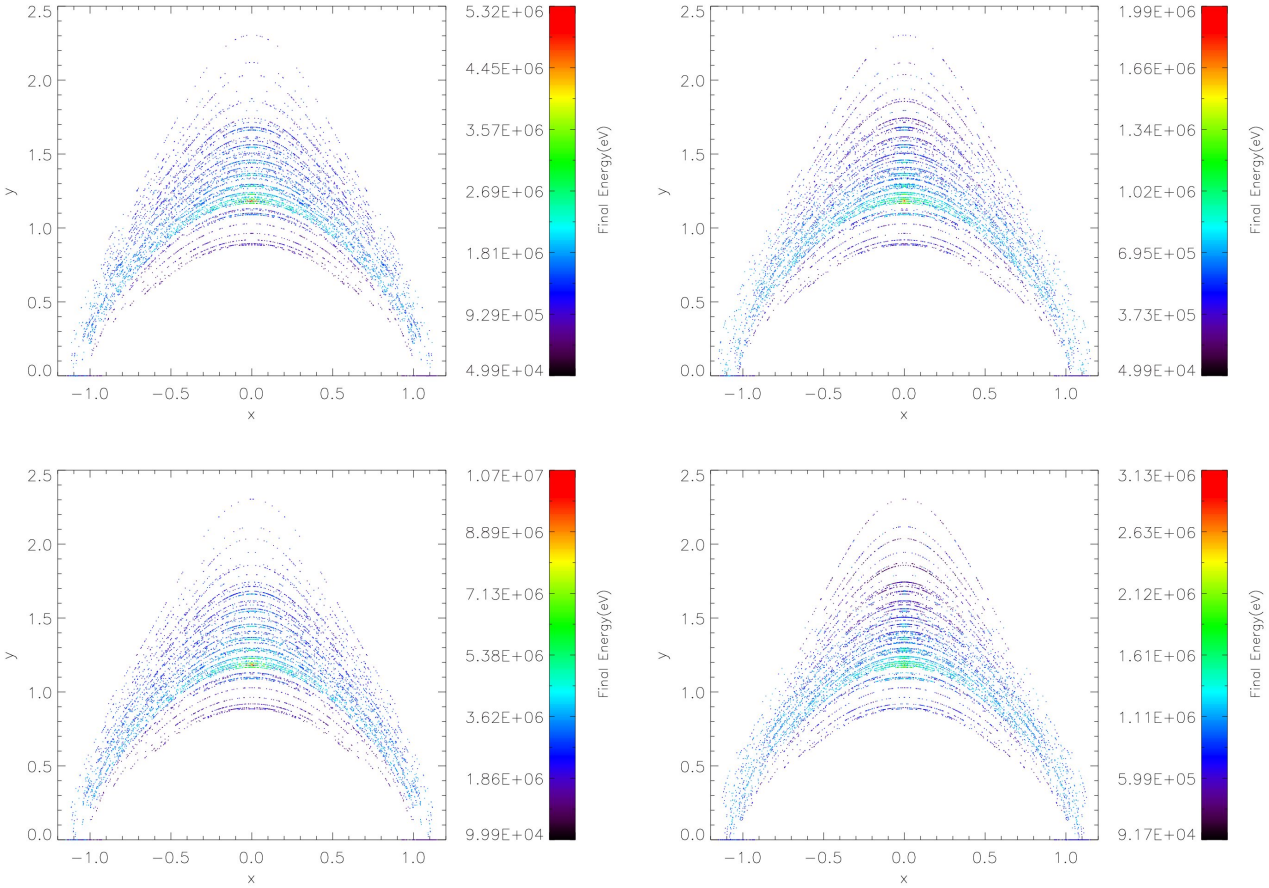

Figure 3.7: Graph of final particle position with the corresponding final energy. *Left* non-relativistic and *Right* relativistic results. Top two plots have initial starting energy $E_{init} = 50keV$ to $100KeV$ and bottom two plots have $E_{init} = 100keV$ to $200keV$.

We then increase the initial energy E_{init} to values between $100 - 200keV$. The bottom two plots in Fig 3.7 shows again the final particle position with the corresponding final energy. On the left the highest energy gain is about $1.07 \times 10^7 eV$, implying these particles have a Lorentz factor of $\gamma \approx 21.93$ and speeds of $v = 0.99$c. On the right the highest energy gain is about $3.13 \times 10^6 eV$, implying these particles have a Lorentz factor of $\gamma \approx 6.125$ and a speed of $v = 0.99$c. Not all of the particles will remain in the trap for the duration of $t = 95s$ as some will escape the trap depending on their initial pitch angles. The escaped particles are all represented by the points shown in Figures 3.6 and 3.7 along the x axis when $y = 0$.

From looking at the final energies of the particles for all three setups it is clear that the results obtained with the non-relativistic particle orbit code are not valid for this range of initial energies. Even starting with initial energy $E_{init} = 5 - 6keV$ (left figure in 3.6 where $E_{max} = 317keV$) the final velocity for the highest energy gain ($v \approx 0.78$c) is already mildly relativistic.

3.2.2 Case 2

The following case is for test particle orbits with a fixed initial energy of $E_{init} = 5.5keV$. This initial energy is similar to the initial energy used by Grady (2012) and Grady et al. (2012) in the investigation with a non-relativistic code. The list below is the initial conditions for 10000 particle orbits using the relativistic guiding centre code. Here, 100 values for the initial pitch angle, θ_{init}, 10 values for the injection position in the x direction and 10 values for the injection position in the y direction are chosen. Therefore

- Injection position: 10 values of x between $-0.5L$ to $0.5L$, 10 values of y between $1L$ to $5L$ and 1 value of $z = 1.25 \times 10^{-6}L$.
- Initial energy: 1 value of energy $5.5keV$.
- Initial pitch angle: 100 values of pitch angle θ between $10°$ to $170°$.

Range of initial conditions for Case 2	
$\theta_{step} = 100$ $\theta_{min} = 10°$ $\theta_{max} = 170°$	$y_{step} = 10$ $y_{min} = 1L$ $y_{max} = 5L$
$x_{step} = 10$ $x_{min} = -0.5L$ $x_{max} = 0.5L$	$E_{step} = 1$ $E_{min} = 5.5keV$ $E_{max} = 5.5keV$

Table 3.11: Initial injection position, pitch angle and energy set up for Case 2.

Table 3.11 gives the minimum and maximum values for the pitch angle, x position, y position and the energy. In Figs. 3.8 and 3.9 the ratio of the final particle energy to the initial particle energy against different starting initial pitch angles for different combinations of particle positions in x and y are shown. Each box represents a specific particle coordinate in the trap with the same starting energy $E_{init} = 5.5keV$ for different initial pitch angles. The red points indicate all the particles that have escaped from the trap. From the figure it can be seen that the highest energy ratio comes from a location in the middle of the trap at a height of $2.2Mm$, where this represents a coordinate $(0, 2.2L, 1.25 \times 10^{-6}L)$. Comparing this with the finding in Grady (2012) the location where the highest energy ratio occurs is the same as the non-relativistic guiding centre approximation. However, looking at the energy ratios for the relativistic and non-relativistic case at this coordinate, it can be seen that in Fig. 3.8 the ratio is between $40-45$ for the relativistic case and for the non-relativistic case seen in Fig. 3.9 this energy ratio is between $50-55$. Looking at location $(0, 4.2L, 1.25 \times 10^{-6})$ specifically, the secondary peaks seen for small and large angles are believed to be a result of first order Fermi acceleration. We make a point of exploring this location further in chapter 4 when we look at the trapping and escape conditions for our CMT model.

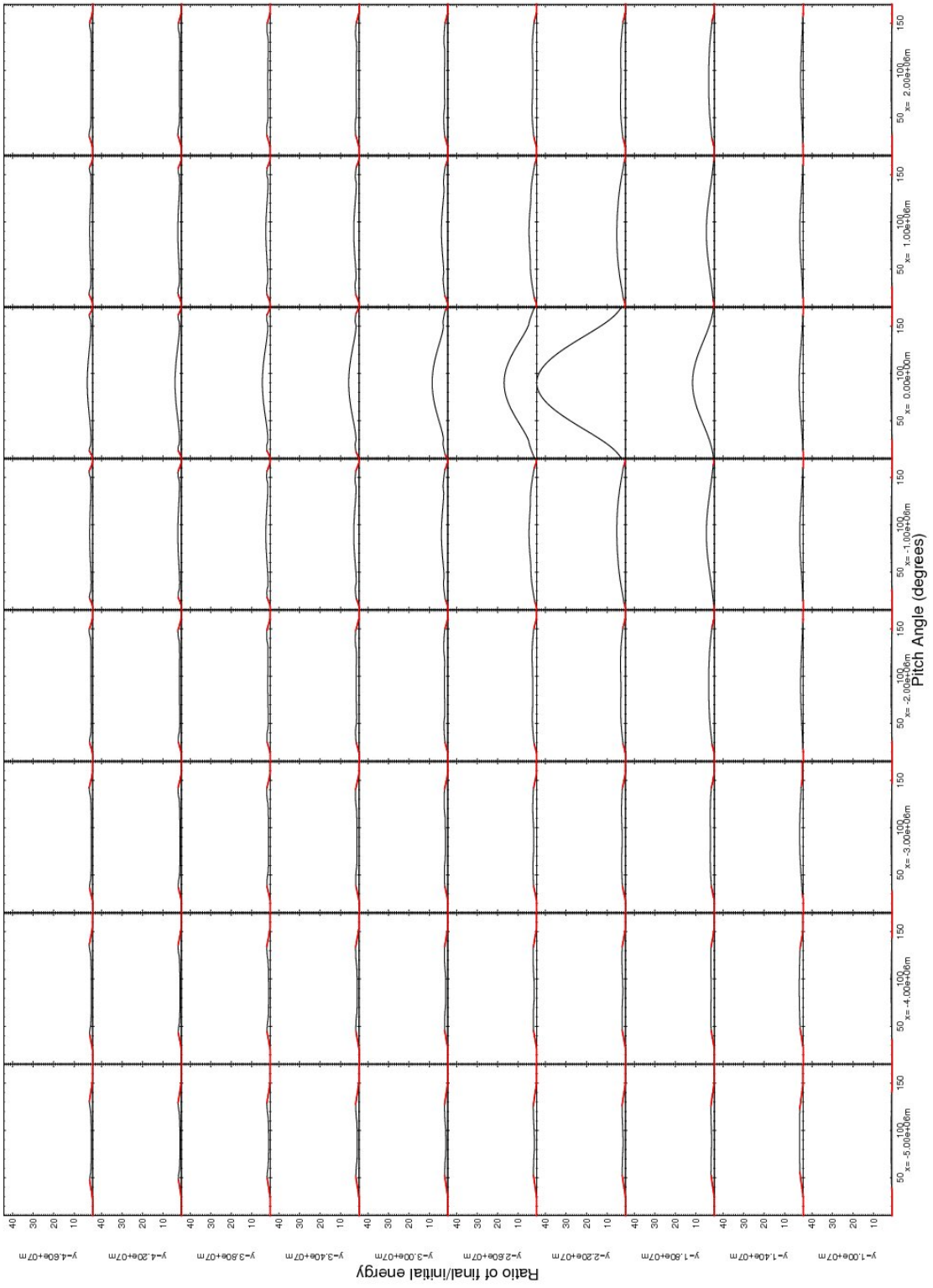

Figure 3.8: The ratio of final/initial energy against initial pitch angle using the relativistic guiding centre approximation. All particle orbits start with the same initial energy ($5.5keV$). Red points show which particle orbits escape.

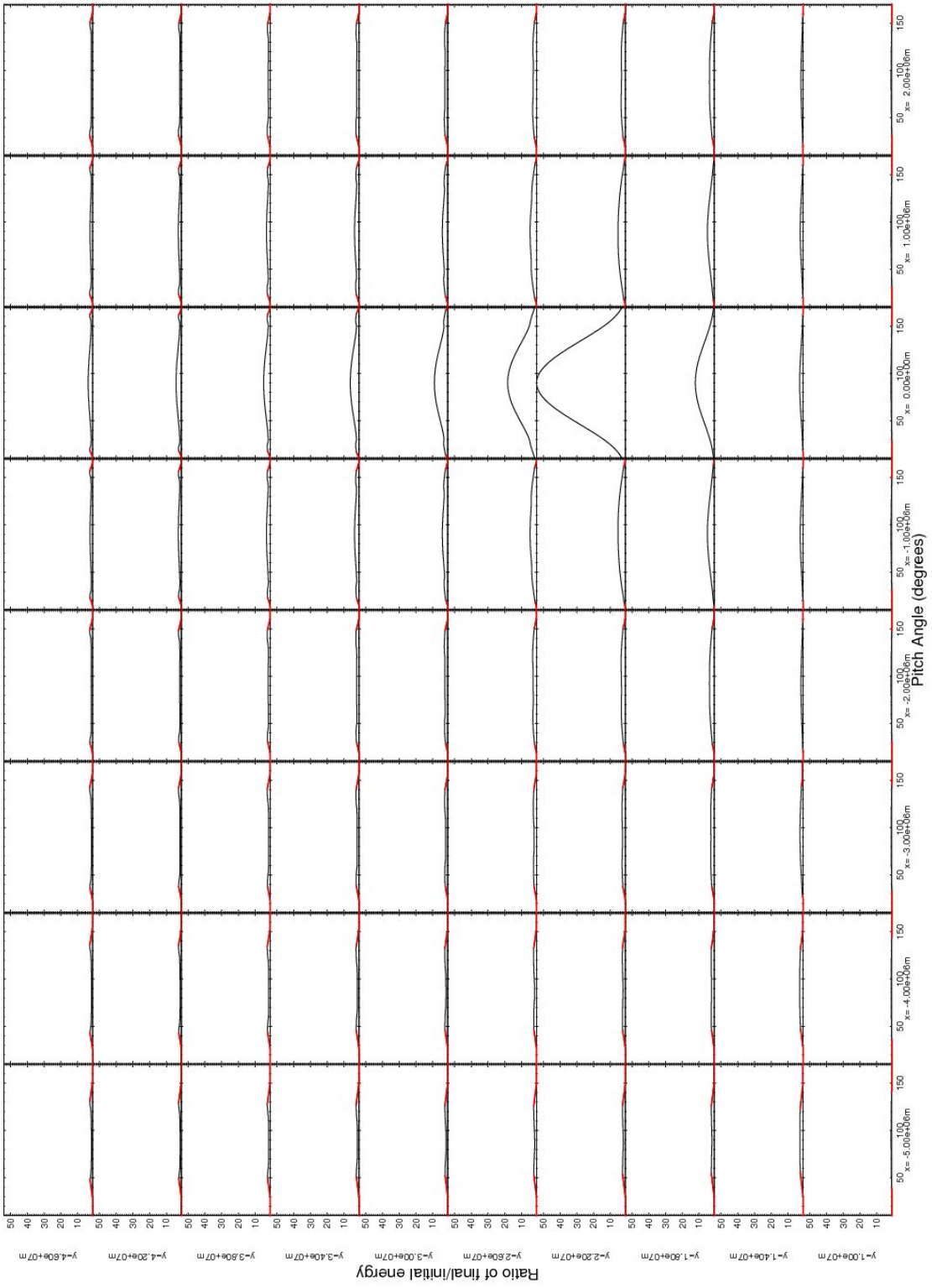

Figure 3.9: The ratio of final energy to initial energy against initial pitch angle using the non-relativistic guiding centre approximation. All particle orbits start with the same initial energy ($5.5keV$). Red points show which particle orbits escape. Grady et al. (2012) found the position in the trap is also key for maximum energy gain alongside particle orbits starting with pitch angles close to $90°$.

3.2.3 Case 3

The following case is for a test particle orbit with a fixed injection position of $x = 0.1L$, $y = 2.0L$ and $z = 1.25 \times 10^{-6}L$. Using the relativistic guiding centre code the effects of different initial pitch angle and initial energy on the energy gain of this specific test case is investigated. The list below shows the initial conditions for 10000 particle orbits. For this case, 10 values for the pitch angle θ_{init} and 10 values for energy E_{init} are chosen. The injection position here is kept constant at coordinates $(0.1L, 2.0L, 1.25 \times 10^{-6}L)$. Therefore,

- Injection position: 1 value of $x = 0.1L$, 1 value of $y = 2.0L$ and 1 value of $z = 1.25 \times 10^{-6}L$.
- Initial energy: 100 values of energy between $5keV$ to $6keV$.
- Initial pitch angle: 100 values of pitch angle θ between 10° to 170°.

Range of initial conditions for Case 3.	
$\theta_{step} = 100$ $\theta_{min} = 10^{\circ}$ $\theta_{max} = 170^{\circ}$	$y_{step} = 1$ $y_{min} = 2L$ $y_{max} = 2L$
$x_{step} = 1$ $x_{min} = 0.1L$ $x_{max} = 0.1L$	$E_{step} = 100$ $E_{min} = 5keV$ $E_{max} = 6keV$

Table 3.12: Initial injection position, pitch angle and energy set up for Case 3.

Table 3.12 gives the minimum and maximum values for the initial pitch angle, particle injection position and energy. Figure 3.10 shows the graph of initial pitch angle against initial energy for a particle starting for each orbit at $(x, y, z) = (0.1L, 2L, 1.25 \times 10^{-6})$, where the colour contours represent the final energy of the particle E_{final}. The colour bar on the right shows the range of final energy in (eV). It can be seen that the highest energy particles come from the pitch angles close to 90° and start with the highest energy, consistent with Grady et al. (2012). In the relativistic results the highest final energy for the particles is about $3.29keV$, however, in the non-relativistic case, the highest energy is found to be about $3.45keV$. The white crosses at the top and bottom of the graph show the particle orbits which escape from the magnetic trap. Figure 3.11 is for the same initial set up as in Fig 3.10, however this time the final energy to initial energy ratio is shown as a surface plot on the left and as a contour plot on the right. For the figure on the right the white squares at the top and bottom again show all the particle orbits which have escaped. The colour bar shows the range of ratios starting from $\approx 1 - 5.5$.

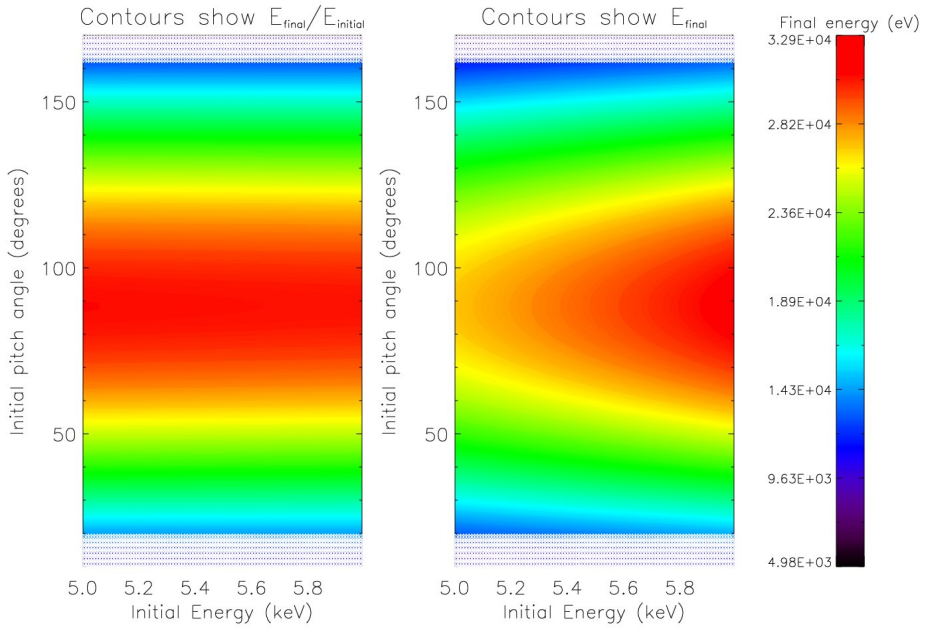

Figure 3.10: *Left*:The contours of final/initial energy ratio; *Right*: Contours of final energy E_{final} for test particle orbits starting with different $E_{init} = 5 - 6keV$, $\theta_{init} = 10 - 170°$ and starting position $(0.1L, 2.0L, 1.25 \times 10^{-6})$. The white squares at the top and bottom of the graph show the particle orbits that have escaped from the trap.

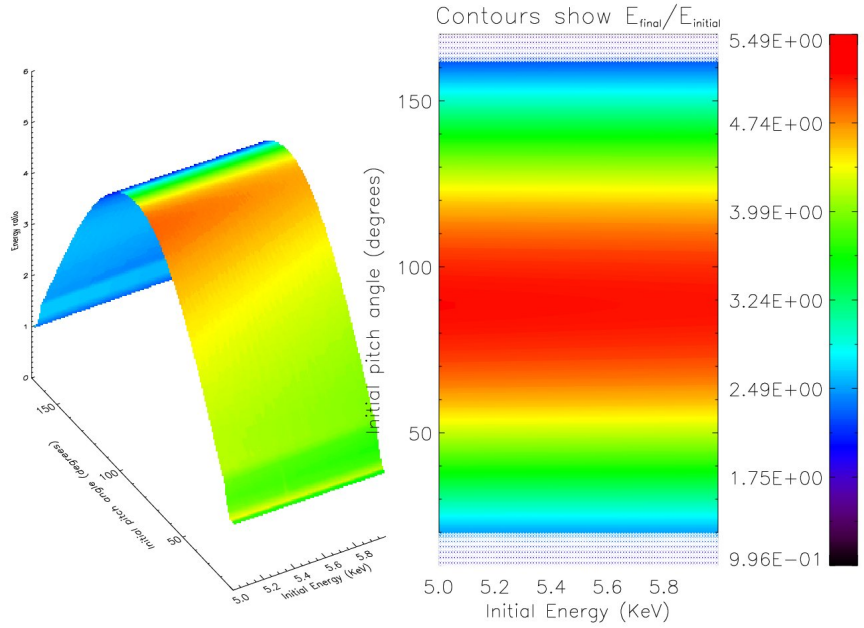

Figure 3.11: *Left*: The energy ratio from Fig. 3.10 as a surface plot. *Right*: The final/initial energy ratio $E_{final}/E_{initial}$ where the colour bar shows the range of ratios. White squares represent escaped particle orbits.

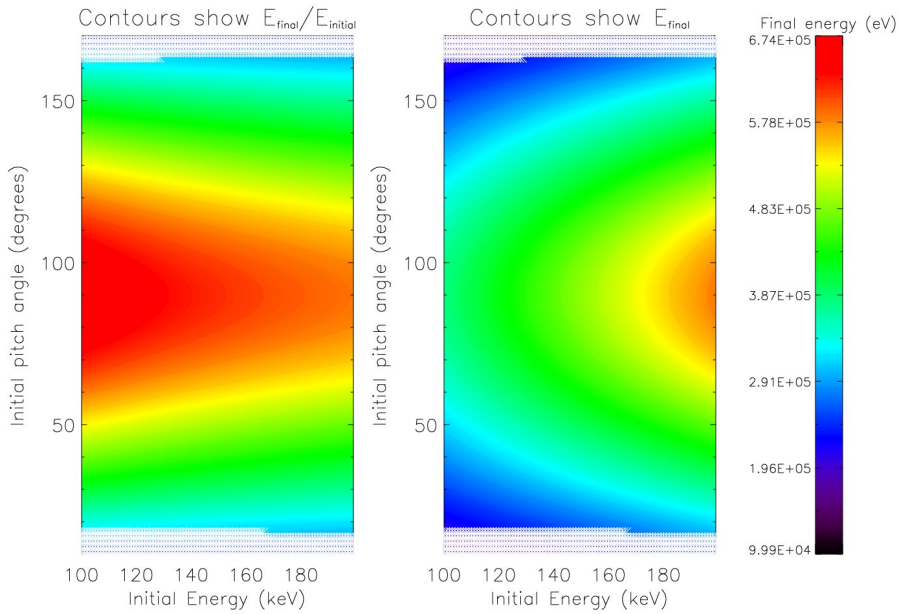

Figure 3.12: *Left*:The contours of final/initial energy and *Right*: Contours of final energy E_{final} for test particle orbits starting with different $E_{init} = 100-200keV$, $\theta_{init} = 10-170°$ and starting position $(0.1L, 2.0L, 1.25 \times 10^{-6})$. The white squares at the top and bottom of the graph show the particle orbits that have escaped from the trap.

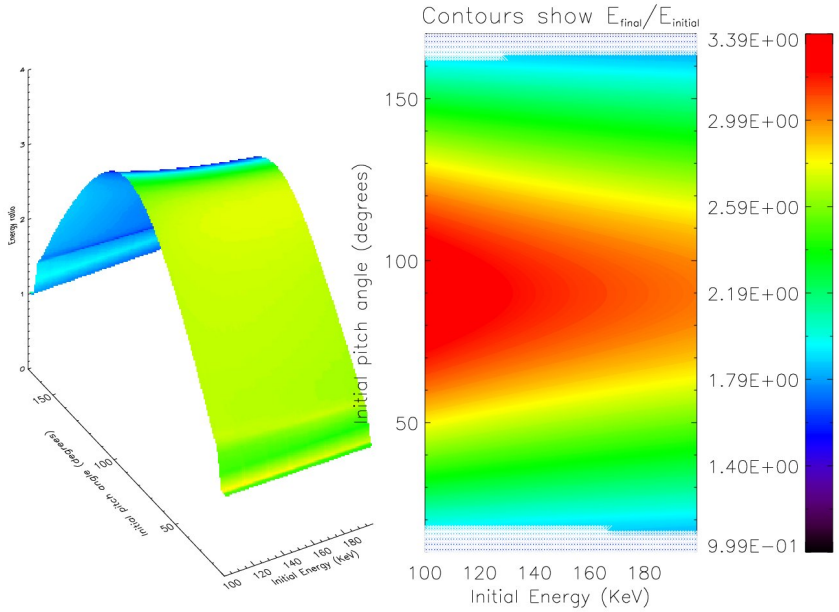

Figure 3.13: *Left*: The energy ratio from Fig. 3.12 as a surface plot. *Right*: The final/initial energy ratio $E_{final}/E_{initial}$ where the colour bar shows the range of ratios. White squares represent escaped particle orbits. The highest energy gain comes from particle with θ_{init} close to 90° and low starting energies as the red region seems to taper off with increasing E_{init}.

Now, starting with the same initial set up but a different initial energy range $E_{init} = 100 - 200keV$ Fig 3.12 and 3.13 are shown. As in the previous set up, Figure 3.12 shows the graph of initial pitch angle against initial energy for a particle starting for each orbit at $(0.1L, 2L, 1.25\times10^{-6})$, where the colour contours represent the final energy of the particle E_{final}. The colour bar on the right shows the range of final energy in (eV). It can be seen that the highest energy particles come from the pitch angles close to 90° and start with the highest energy. In this case the highest final energy for the particles is about $674keV$. The white crosses at the top and bottom of the graph again show the particle orbits lost from the trap.

Figure 3.13 is for the same initial conditions in Fig. 3.12, where the final energy to initial energy ratio is represented as a surface plot on the left and as a contour plot on the right. For the figure on the right the white squares at the top and bottom show all the particle orbits that have escaped. The colour bar shows the range of ratios starting from $\approx 1 - 3.4$. It is found that the energy ratio deceases as the initial energy becomes mildly relativistic. It also seems the highest ratio comes from particle starting close to 90°, with the lowest initial energy. This can be seen in the surface plot where the height of the peak seems to decrease with increasing initial energy. In the contour plot the red colour indicating the highest energy seems to taper off in the middle region with increasing initial energy, implying that particles starting with lower starting energies and close to 90° gain higher energies since relativistic effects are less dominant. Regarding the number of escaping particles, there are more particle orbits lost from the trap in the case of lower initial energy (Fig 3.10) than for higher initial energy (Fig 3.12). This could be connected to the previous remarks that more particles are trapped due to higher mirror points.

3.3 Discussions and Conclusions

We have presented a detailed comparison of the particle energisation process for the CMT model between the non-relativistic results found by Giuliani et al. (2005) and Grady et al. (2012) and our new findings based on relativistic guiding centre theory.

Comparing the results we find not surprisingly, the discrepancy in energies and particle orbits grows with increasing initial energies. The final energy of the particle using the non-relativistic guiding centre theory is generally higher than the final energy of the same particle orbit using the relativistic theory. The discrepancy between the energies and the final energy of the particles can be seen clearly for the case for a particle starting with $E_{init} = 200keV$ as seen in Fig. 3.4. Comparing the final energies of the same particle using the non-relativistic theory gives a final energy of almost $206keV$ higher than the relativistic theory. This can be explained by the reasoning that in the non-relativistic regime the Lorentz factor $\gamma = 1$, however, as the speed of the particle approaches the speed of light c, γ should become greater than 1. Basically, the non-relativistic equations cease to be accurate for higher energies. Since γ is present in both the perpendicular 3.1 and parallel 3.2 equations of motion it takes longer to reach the same energy using the relativistic code. For the case of $E_{init} = 200keV$ as discussed above, γ increases to 1.664 with increasing particle velocity. As a result of this relativistic effect the energies calculated using the relativistic code will be smaller compared to the non-relativistic case.

Looking at the particle trajectories it seems the mirror points for the particle using the relativistic approximation are higher than the mirror points using the non-relativistic approximation. This effect is due to the terms in the relativistic guiding centre equation for the parallel velocity becoming smaller as γ increases with increasing energy which could result in more particles being trapped in the relativistic model since they do not travel all the way down to the foot points. In section 3.2 we looked at the effect of different E_{init}, θ_{init} and injection position of the particle as was done in the non-relativistic approximation by Grady et al. (2012) and Grady (2012). The same qualitative behaviour is seen in the relativistic approximation in that, the highest energy particles come from a region in the middle of the trap, with pitch angles close to 90° and from a region of weak magnetic field.

From the results presented in Figs. 3.6 and 3.7, again the final energies in the non-relativistic approximation are higher than the energies found from the relativistic case. From looking at the final energies of the particles for all three set ups it is clear that the energies obtained with the non-relativistic particle orbit code are not valid for these range of initial conditions. Even starting with initial energy $E_{init} = 5 - 6keV$ (left figure in 3.6 where $E_{max} = 317keV$) the final velocity for the highest energy gain ($v \approx 0.78$c) is already mildly relativistic. Hence for the highest starting

energy case $E_{init} = 100$ to $200keV$ as see in Fig. 3.7, the final energy is almost $1.0 \times 10^4 keV$ using the non relativistic approximation and $3.13 \times 10^3 keV$ from the relativistic approximation which are both highly relativistic. The energies obtained from the non-relativistic approximation are determined only for comparison and are not valid energy values.

The final key finding from this comparison study is the change in the particle energy increase. In the non-relativistic approximation it was found by Grady et al. (2012) that the particle energies could increase by a factor of almost 50 and with the relativistic approximation this factor was found to be lower at almost 40 as seen in Fig. 3.8. The rest of the particles again like in the non-relativistic case experience a modest energy increase. Also in Fig. 3.13 we saw that for a relativistic approximation the higher the initial energy, the lower the final energy of the particles.

The work done by authors like Giuliani et al. (2005), Karlický and Bárta (2006), Minoshima et al. (2011) and Grady et al. (2012) have tried to further develop CMT models first proposed in the 90's e.g.(see e.g. Somov and Kosugi, 1997). Relativistic effects become an important factor in particle energisation for velocities mildly/close to the speed of light which are observationally evident. In this chapter we have incorporated this effect by introducing the relativistic guiding centre equations into the Giuliani et al. (2005) and Grady et al. (2012) model. The present form of the model is in line with findings from other models, where particle trapping at the loop top is seen and this could give an explanation into X-ray emissions observed at coronal/loop-top sources.

Chapter 4

Loss Cone Evolution and Particle Escape in CMTs

(Parts of this chapter have been submitted for publication in Astronomy & Astrophysics.)

The main aim of this chapter is to gain a better understanding of the conditions leading to either particle trapping or escape in a CMT and try to answer what determines whether particles remain trapped or escape during the evolution of a CMT. This may seem a trivial question to answer since all particles which move into the loss cone will escape from the trap. However, at second thought, things are not as simple as they seem for two reasons: (a) the loss cone itself changes in time due to the changing magnetic field strength and (b) the particle pitch angle also evolves due to betatron and Fermi acceleration. In order to set up our investigation of time evolution of particle orbit pitch angles and compare it with the loss cone angle evolution in our CMT model, we initially outline some of the basic theory, a summary of the key findings from Grady et al. (2012) which forms the basis for our detailed study and a numerical set up in order to look at the evolution of the magnetic field and loss cone angle in our model. We summarise the results of Grady et al. (2012) that are relevant for this chapter in section 4.1. The numerical results are presented in section 4.2. In section 4.3 and 4.4 we investigate how the loss cone angle and the particle pitch angle evolve in our CMT model for a collapse time and for a $t \rightarrow \infty$ respectively. In section 4.5 we then try to understand our results by comparing them with the predictions of a number of simple models published in the literature (Aschwanden, 2004a; Somov, 2004). As we will see, these two models make predictions about particle trapping and escape which are not consistent with our results. These inconsistencies can be explained by different assumptions made by the authors for their models. Hence, we construct a family of simplified models of our own which are in line with the properties of our particle orbit calculations and compare the results for particle trapping obtained from these models with the findings of the particle orbit calculations.

4.1 Loss Cone Angle: Overview

In section 2.1.2 we discussed the relationship between the particle pitch angle θ, mirror ratio $R(t)$ and the loss cone angle $\alpha(t)$. The particle pitch angle is defined as

$$\theta = \arccos\left(\frac{v_{\|}}{v}\right), \tag{4.1}$$

where $v_{\|}$ is the velocity of the particle along the field line and v the total velocity of the particle. We define the mirror ratio for our CMT model as

$$R(t) = \frac{B_{fp}}{B(t)}, \tag{4.2}$$

where $B(t)$ is the value of the magnetic field in the middle of the trap (i.e. $x = 0$) for a particular field line and B_{fp} is the foot point field strength for the same field line which represents the maximum magnetic field strength B_{max} as seen in Chapter 3. The mirror ratio $R(t)$ is related to the loss cone angle $\alpha(t)$ by

$$\alpha(t) = \arcsin\left(\frac{1}{\sqrt{R}}\right). \tag{4.3}$$

Therefore, as the magnetic field increases with strength, the mirror ratio will decrease and the loss cone will increase or vise versa. For ease of notation we have omitted the spatial dependence in the definitions of the loss cone angle and mirror ratio, but we point out here that not only will both the loss cone angle and the mirror ratio vary with time due to the time evolution of the magnetic field, but also from field line to field line, i.e. in space.

To apply these definitions to our CMT model we need to determine the magnetic field strength at the top of the field line and the corresponding foot point given by the model. The magnetic field in the CMT is given by

$$\mathbf{B} = \nabla A \times \mathbf{e}_z + B_z \mathbf{e}_z = \frac{\partial A}{\partial y}\mathbf{e}_x - \frac{\partial A}{\partial x}\mathbf{e}_y,$$

where we have chosen $B_z = 0$. In particular, if we enforce that the field lines of the collapsing trap relax to a loop like structure described by the flux function

$$A(x, y) = A_\infty(x_\infty(x, y, t), y_\infty(x, y, t), t_0),$$

the x and y components of the magnetic field at time t are given by

$$B_x = \frac{\partial A}{\partial y} = \frac{\partial A_\infty}{\partial x_\infty}\frac{\partial x_\infty}{\partial y} + \frac{\partial A_\infty}{\partial y_\infty}\frac{\partial y_\infty}{\partial y}, \tag{4.4}$$

$$B_y = -\frac{\partial A}{\partial x} = -\left(\frac{\partial A_\infty}{\partial x_\infty}\frac{\partial x_\infty}{\partial x} + \frac{\partial A_\infty}{\partial y_\infty}\frac{\partial y_\infty}{\partial x}\right). \tag{4.5}$$

So, we have six partial derivatives to calculate. Using the transformation in Eqn. (2.25), $\frac{\partial x_\infty}{\partial x} = 1$, $\frac{\partial x_\infty}{\partial y} = 0$ and $\frac{\partial y_\infty}{\partial x} = 0$. The remaining three derivatives are

$$\begin{aligned}\frac{\partial y_\infty}{\partial y} &= \left[\frac{1}{(1+y/(at)^b)}\right]\left\{\frac{1+\tanh[(y-L_v/L)a_1]}{2}\right\} \\ &+ \tfrac{1}{2}(at)^b \ln\left[1+y/(at)^b\right]\left\{1-\tanh^2\left[(y-L_v/L)a_1\right]\right\}a_1 \\ &+ \left\{\frac{1-\tanh[(y-L_v/L)a_1]}{2}\right\} \\ &+ \left\{-\tfrac{1}{2}+\frac{\tanh^2[(y-L_v/L)a_1]}{2}\right\}a_1 y,\end{aligned} \tag{4.6}$$

$$\frac{\partial A_\infty}{\partial x_\infty} = -\frac{c_1\left(y_\infty+\frac{d}{L}\right)}{\left(x_\infty+\frac{1}{2}\right)^2+\left(y_\infty+\frac{d}{L}\right)^2} + \frac{c_1\left(y_\infty+\frac{d}{L}\right)}{\left(x_\infty-\frac{1}{2}\right)^2+\left(y_\infty+\frac{d}{L}\right)^2}, \tag{4.7}$$

and

$$\frac{\partial A_\infty}{\partial y_\infty} = \frac{c_1}{\left(\left(x_\infty+\frac{1}{2}\right)+\frac{(y_\infty+\frac{d}{L})^2}{(x_\infty+\frac{1}{2})}\right)} - \frac{c_1}{\left(\left(x_\infty-\frac{1}{2}\right)+\frac{(y_\infty+\frac{d}{L})^2}{(x_\infty-\frac{1}{2})}\right)}. \tag{4.8}$$

It follows that the expressions for B_x and B_y become,

$$B_x = \frac{\partial A_\infty}{\partial y_\infty}\frac{\partial y_\infty}{\partial y}, \tag{4.9}$$

$$B_y = -\frac{\partial A_\infty}{\partial x_\infty}. \tag{4.10}$$

Using Eqns. 4.6 - 4.8, substituting the transformation 2.25 into the expressions for B_x and B_y, we find an expression for the magnetic field using $B = |B| = \sqrt{{B_x}^2 + {B_y}^2}$. One important point to be noted here is the time dependence for the magnetic field comes from $\frac{\partial y_\infty}{\partial y}$ in B_x. Also, the field line strength at the foot point (i.e, y = 0) remains constant over time, because the transformation given by 2.24 and 2.25 ensures that the B_y component of the magnetic field on the lower boundary does not change, although the B_x component could change in time. This change is so small that one can regard the absolute value of the magnetic field strength at the foot point as constant.

Before we begin our investigation into what determines whether particles remain trapped or escape during the evolution of a CMT model, we summarise some of the key findings of Grady et al. (2012). The results from their study are important in initiating our study in this chapter.

In Chapter 3 the graph of final position with corresponding particle energies from Grady et al. (2012) can be seen on the left in Fig. 3.6. They found this result by stepping through different positions (x, y), initial energies E and initial pitch angles θ. This consequently had an effect on the position of the mirror points, the energy gain of the particle orbits and on whether they remain trapped or escape. In particular they found that the particle orbits that gain most energy during the trap collapse have initial pitch angles θ close to $90°$ and initial positions in a weak magnetic field region in the middle of the trap. Those particle orbits having the largest energy gain remained trapped during the collapse and due to their pitch angle staying close to $90°$ have mirror points very close to the centre of the trap. Grady et al. (2012) argue that these particle orbits are energised mainly by the betatron mechanism. Other particle orbits with initial pitch angles closer to $0°$ (or $180°$) seem to be energised by the Fermi mechanism at the beginning, but as already pointed out by Giuliani et al. (2005) and corroborated by Grady et al. (2012), these particle orbits gain energy when passing through the centre of the trap. At later stages these particle orbits also seem to be undergoing mainly betatron acceleration.

We will make use of these results later in this chapter but going back to our motivation for this study, we want to investigate how the loss cone angle $\alpha(t)$ at the loop top evolves in relation to the particle pitch angle $\theta(t)$ at the same position. In order to gain insight into the behaviour of the particle loss cone angle along a magnetic field line, first, knowledge about the particle position along a field line is needed.

In this section we use this idea to build a grid along the field line and use these positions to look at the evolution of the magnetic field $B(t)$ and loss cone angle $\alpha(t)$. Consider the set up for the coordinate system as describe in Chapter 3 for the Giuliani et al. (2005) model where the x and z coordinate run parallel to the solar surface and y represents the height above the surface. Using the flux function where $A_0(x, y) = A_\infty(x_\infty, y_\infty, t_0)$ at a given time t_0 expressions for x_0 and y_0 along the field lines can be found. The flux function describing the magnetic field in our CMT model is given by Eqn. 2.23 as

$$A_0 = c_1 \arctan\left(\frac{y_0 + d/L}{x_0 + 1/2}\right) - c_1 \arctan\left(\frac{y_0 + d/L}{x_0 - 1/2}\right).$$

We begin by solving the above equation for x_0 and y_0 respectively (see Appendix B.1 for details). From Eqn. B.4 and Eqn. B.5 the equations for the field lines are

$$x_0 = \sqrt{-\cot\left(\frac{A_0}{c_1}\right)(y_0 + \frac{d}{L}) - (y_0 + \frac{d}{L})^2 + \frac{1}{4}}, \tag{4.11}$$

or

$$y_0 = -\frac{1}{2}\left\{\frac{2d}{L} + \cot\left(\frac{A_0}{c_1}\right)\right\} + \frac{1}{2}\sqrt{\cot^2\left(\frac{A_0}{c_1}\right) - 4{x_0}^2 + 1}. \tag{4.12}$$

Using the transformations

$$\begin{aligned} x_\infty &= x, \\ y_\infty &= (at)^b \ln\left[1 + \frac{y}{(at)^b}\right]\left\{\frac{1 + \tanh\left[(y - L_v/L)a_1\right]}{2}\right\} \\ &+ \left\{\frac{1 - \tanh\left[(y - L_v/L)a_1\right]}{2}\right\} y, \end{aligned} \tag{4.13}$$

the field lines and hence the positions in x and y are stretched in the y-direction. y_∞ is normalised with respect to L. Using the, *Newton Raphson Method*, we try to find the root of the non-linear equation $f(y) = y_\infty$. As a result of this routine different values of y at different points in time along the field lines are calculated. We can then use these values to track the evolution of $B(t)$ and $\alpha(t)$ along a specific field line.

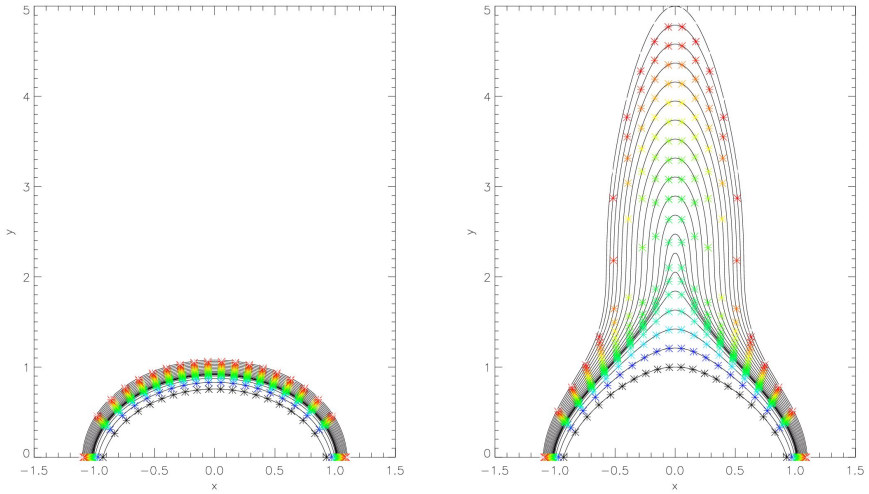

Figure 4.1: Illustrates the magnetic field lines (black) for a collapsing magnetic trap at the final time on the left and the start time on the right. The x-coordinates run horizontally and the y-coordinate is perpendicular to the solar surface. The multi-coloured crosses show the coordinate positions in x and y along the field lines.

In the Newton Raphson method the root of $f(y) - y_\infty = 0$ is found. In order to build our grid for each specific value of the flux function A, we carry out the following steps:

1. For $x_0 = 0$, choose a range of values in y with a set step size n_y,

$$\Delta y = \frac{y_{max} - y_{min}}{n_y - 1}$$

$$y = y_{min} + (iy - 1)\Delta y$$

2. Calculating y_∞ from Eqn. 2.25 and using this value of y_∞ to find the appropriate $A(x_0, y_\infty)$.

3. For $y = 0$, choose a range of values in x with a set step size n_x,

$$\Delta x = \frac{x_{max} - x_{min}}{n_x - 1}$$

$$x = x_{min} + (ix - 1)\Delta y \tag{4.14}$$

4. Substituting the different values of x into Eqn. B.5 for y, we find a range of values for y which lie on the field lines for $A =$ constant.

Figure 4.1 illustrates the contours for the magnetic field line after the trap has completely collapsed on the left and the contours for a starting time on the right hand side. For the figure on the left, we see that for different values of x and a specific value for the flux function A we find a corresponding value of y as discussed above. The contours for the magnetic field lines as seen in Fig. 4.1 are obtained via the transformation 2.25 by:

1. The values of x_∞ and y_∞ corresponding with a certain A_∞ are fed into the Newton Raphson method.

2. The Newton Raphson method calculates the y_{init} at $t = t_{init}$ for some $x \neq 0$ along $A =$ constant.

3. The coordinates (x_{init}, y_{init}) are then plotted along the field lines as seen on the right hand side of Fig 4.1.

Using a similar approach to finding a grid along the field lines as seen in Fig. 4.1, we can find the evolution of the magnetic field strength $B(t)$ and consequently the evolution of the loss cone angle $\alpha(t)$ at the apex of the field line ($x = 0$) by:

- Picking $y_{initial}$ at $t_{initial}$. Substituting into the equation for y_∞.
- Substituting $x_\infty = 0$ and y_∞ into A_∞ in the centre of the trap.
- Solving x_0 by using $A = A_\infty$ for $y = 0$ at the foot points.
- Calculating $B(0, y, t)$ for all time in the centre of the trap.

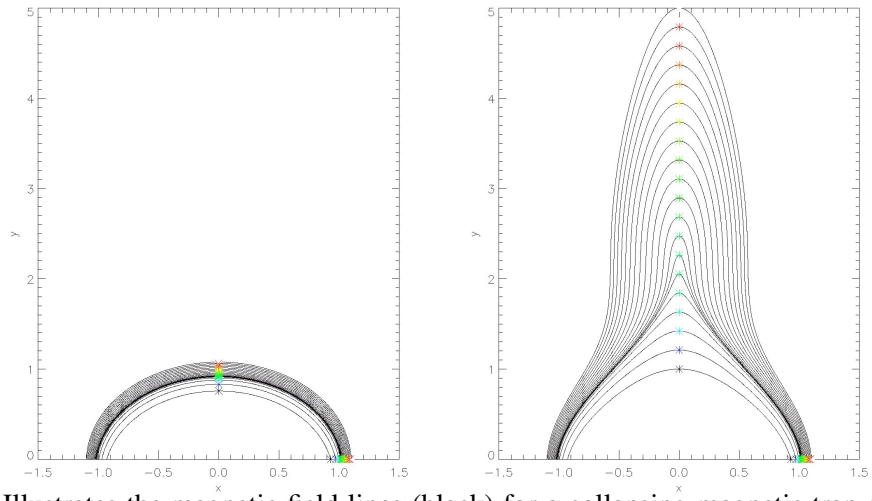

Figure 4.2: Illustrates the magnetic field lines (black) for a collapsing magnetic trap at the final time on the left and the start time on the right. The x-coordinates run horizontally and the y-coordinate runs vertical to the solar surface. The multi-coloured crosses show the coordinate positions in x and y along the field lines.

- Calculating $B(x_\infty, 0, t)$ for all time at the foot points of the trap.

In Fig. 4.2 each multi-coloured coordinate marks the loop top and the foot point of specific field lines. These initial coordinates of the loop top and the foot points are fed into the Newton Raphson method. Hence we:

- Feed the values of $x_\infty = 0$, y_∞ for a specific A_0 at the foot point and the mid-plane into the Newton Raphson method see Fig.(4.2).
- Calculate y_{int} for t_{int} to t_{final} at $x = 0$ along $A =$ constant.
- Calculate the corresponding values for the magnetic field $B(t)$.
- Find the loss cone angle by calculating $\alpha = \arcsin\left(\frac{1}{\sqrt{R}}\right)$.

In the next section we analyse the data produced from this numerical code. The findings will be important for our main goal of comparing loop top particle pitch angle evolution with loss cone angle in the CMT model.

4.2 Temporal and Spatial Evolution of the Loss Cone Angle α

In this section we look at the temporal and spatial evolution of the magnetic field strength B and the mirror ratio R at the top of the field lines in our model. From these quantities the behaviour of the loss cone angle α can be deduced. At the normalised starting time $t = 1.05$, position $x = 0$ and range of values for y starting from 1 to 5, the corresponding loss cone angles α, magnetic field strengths B_{field}, foot point magnetic field strengths B_{fp} and magnetic mirror ratio R are given in the Table 4.1. At the highest point in the trap considered here, which corresponds to $y \approx 5$, the loss cone angle α starts at 10.8°. The loss cone angle continues to gradually increase to $\alpha = 11.15^{\circ}$ for $y \approx 4$. Just below this point in the model the field lines are very stretched which is equivalent to the magnetic field being weaker. The B_{field} continues to decrease in value with decreasing height until $y \approx 2$. The decreasing B_{field} corresponds to an increase in magnetic mirror ratio R leading to a decrease in the loss cone angle α. For values of $y < 2$ the magnetic field begins to increase again causing a decrease in R, leading to an increase in $\alpha \approx 30^{\circ}$. The final values of all the positions discussed in Table 4.1 are given in Table 4.2 for a final time of $t_{final} = 2.0$. The y column represents the final height of each field line when the trap has completely stopped. The corresponding loss cone angles show a trend of increasing from 19.73° at the top to 37.4° since there no longer is a weak magnetic field region. The magnetic field is measured in Tesla, where the maximum magnetic field at $(x, y) = (0, 0)$ is 0.015 Tesla at the foot points. Looking at the values of B_{fp} it is seen that it remains constant for all time, a point that we mentioned at the beginning of this Chapter.

To see how $\alpha(t)$ evolves at the loop top in the trap for a finite time of $95s$, Fig. 4.3 shows the variation of α as a function of y. Starting from $t_{init} = 1.05$ (first figure top row) the loss cone α moves through the region of increasing B_{field} (initial increase) then moves into the region of decreasing B_{field} (initial decrease) and finally into a region of increasing B_{field} (second increase). This pattern is still evident in the second row and half way through the third row. At $t = 1.4775$ the tenth figure (second figure, third row) the loss cone starts to completely move out of the decreasing B_{field} region and move into an increasing B_{field} region. From this point onwards the loss cone steadily increases and reaches final value at $t_{final} = 2.00$. A point to note here is that each field line will have its own loss cone angle associated with it, hence if we picked a specific height at the loop top we would track the evolution of that specific loss cone angle.

Fig. 4.4 shows the evolution of α at $x = 0$ for a number of field lines from $t = 1.05 - 2.0$, corresponding to a finite time of 95 seconds. Starting from $t_{init} = 1.05$, as α moves out of the region of increasing B_{field} into a region of decreasing B_{field} it seems there is a decline in the growth rate for the loss cone angle α. These are shown in the plots by the points where they are overplotted on top of each other. At $t = 1.4775$ the tenth figure (second figure, third row)

Table 4.1: Values of y, α, time, magnetic field, B_{field} at the middle of the trap, magnetic field, B_{fp} at the foot points and mirror ratio, R for $x = 0$ at the initial time $t = 1.05$.

$y(L)$	α (°)	B_{field} (Tesla)	B_{fp} (Tesla)	R
1.0000002	29.9370515	0.0024085	0.0096708	4.0152717
1.2000000	23.5440511	0.0015043	0.0094276	6.2670965
1.3999997	17.7094941	0.0008575	0.0092672	10.8070583
1.5999992	12.5057103	0.0004303	0.0091762	21.3273106
1.7999976	8.0986821	0.0001813	0.0091327	50.3861046
1.9999903	4.8702100	0.0000657	0.0091156	138.7382050
2.1999836	3.7858708	0.0000397	0.0091085	229.3748474
2.3999889	4.8756825	0.0000657	0.0091010	138.4276886
2.6000066	6.4807736	0.0001158	0.0090874	78.4954453
2.8000016	7.9007225	0.0001713	0.0090656	52.9256287
2.9999995	9.0173274	0.0002220	0.0090353	40.7078552
3.1999996	9.8444425	0.0002630	0.0089976	34.2090378
3.4000010	10.4265914	0.0002933	0.0089539	30.5323257
3.5999982	10.8115726	0.0003134	0.0089056	28.4202728
3.8000004	11.0427445	0.0003248	0.0088542	27.2568245
3.9999971	11.1564742	0.0003295	0.0088008	26.7108059
4.2000074	11.1822417	0.0003289	0.0087463	26.5894051
4.4000001	11.1433409	0.0003246	0.0086917	26.7730064
4.6000032	11.0578812	0.0003177	0.0086373	27.1831799
4.8000054	10.9397784	0.0003091	0.0085836	27.7659283
4.9999962	10.7995435	0.0002995	0.0085309	28.4828663

corresponds to the loss cones moving through a region of increasing magnetic field B_{field}. It seems the loss cone angles begin to follow a linear growth rate from this point onwards and in the latter stages this linear rate decreases to a point where the changes between the final four figures is indistinguishable.

Finally Fig. 4.5 gives the plots for the variation of mirror ratio R as a function of y for different times. Starting from $t = 1.05$ and height $y = 5$ the mirror ratio, R begins to decrease gradually from approximately 28.5 to 26.6 for $y = 4.2$ as seen in Table 4.1. From this point the ratio begins to increase gradually corresponding to gradual decease in B_{field}. From about $y \approx 3$ the mirror ratio begins to increase rapidly reach $R \approx 300$ at $y \approx 2.2$. Finally it begins to decrease sharply and reaches $R = 4$ at $y = 1$. This pattern is clearly illustrated by the first plot in Fig. 4.5, where the distinctive peak corresponds to a large R implying a weak magnetic field region. The size of this peak decreases with time until it begins to decrease linearly from $t = 1.4775$ onwards since the magnetic field is no longer decreasing. The final values for the mirror ratio R at the finite time of $t_{final} = 2.0$ are seen in table 4.2. Therefore, Fig. 4.4 - 4.5 show the clear relationship between loss cone evolution $\alpha(t)$, mirror ratio $R(t)$ and magnetic field $B(t)$; when the magnetic

Table 4.2: Values of y, α, time, magnetic field, B_{field} at the middle of the trap, magnetic field, B_{fp} at the foot points and mirror ratio, R for $x = 0$ at the final time of $t = 2.0$.

$y(L)$	α ($^\circ$)	B_{field} (Tesla)	B_{fp} (Tesla)	R
0.8856972	37.4415266	0.0035744	0.0096708	2.7055912
1.0048827	33.8947216	0.0029319	0.0094276	3.2154927
1.0899003	31.5586847	0.0025384	0.0092672	3.6507297
1.1415356	30.2114305	0.0023234	0.0091762	3.9494071
1.1672972	29.5589969	0.0022226	0.0091327	4.1090689
1.1776700	29.3000136	0.0021831	0.0091156	4.1754456
1.1819861	29.1928682	0.0021669	0.0091085	4.2034283
1.1865929	29.0789056	0.0021497	0.0091010	4.2335339
1.1949950	28.8721608	0.0021187	0.0090874	4.2890687
1.2087098	28.5376854	0.0020691	0.0090656	4.3814998
1.2281016	28.0711262	0.0020007	0.0090353	4.5160270
1.2529582	27.4840891	0.0019164	0.0089976	4.6951804
1.2828406	26.7948589	0.0018196	0.0089539	4.9208155
1.3172717	26.0233755	0.0017142	0.0089056	5.1950517
1.3558331	25.1886836	0.0016038	0.0088542	5.5207181
1.3981992	24.3081765	0.0014913	0.0088008	5.9014063
1.4441558	23.3974191	0.0013792	0.0087463	6.3414106
1.4935760	22.4709330	0.0012697	0.0086917	6.8451858
1.5464320	21.5410506	0.0011644	0.0086373	7.4177284
1.6027452	20.6234307	0.0010649	0.0085836	8.0604830
1.6625705	19.7316209	0.0009724	0.0085309	8.7731800

field increases the mirror ratio decreases which causes the loss cone angle to increase or vise versa.

Intuition would lead us to believe that in a CMT for a large mirror ratio the loss cone angle will be small so the probability of particles being trapped is much larger. However, the magnetic field strength on average increases as the CMT collapses. This results in the mirror ratio decreasing and the loss cone angle increasing which consequently will lower the probability of the particles been trapped. In the section to follow we will look at a seemingly simple question; how does the particle pitch angle for specific test particle evolve in relation to the loss cone angle?

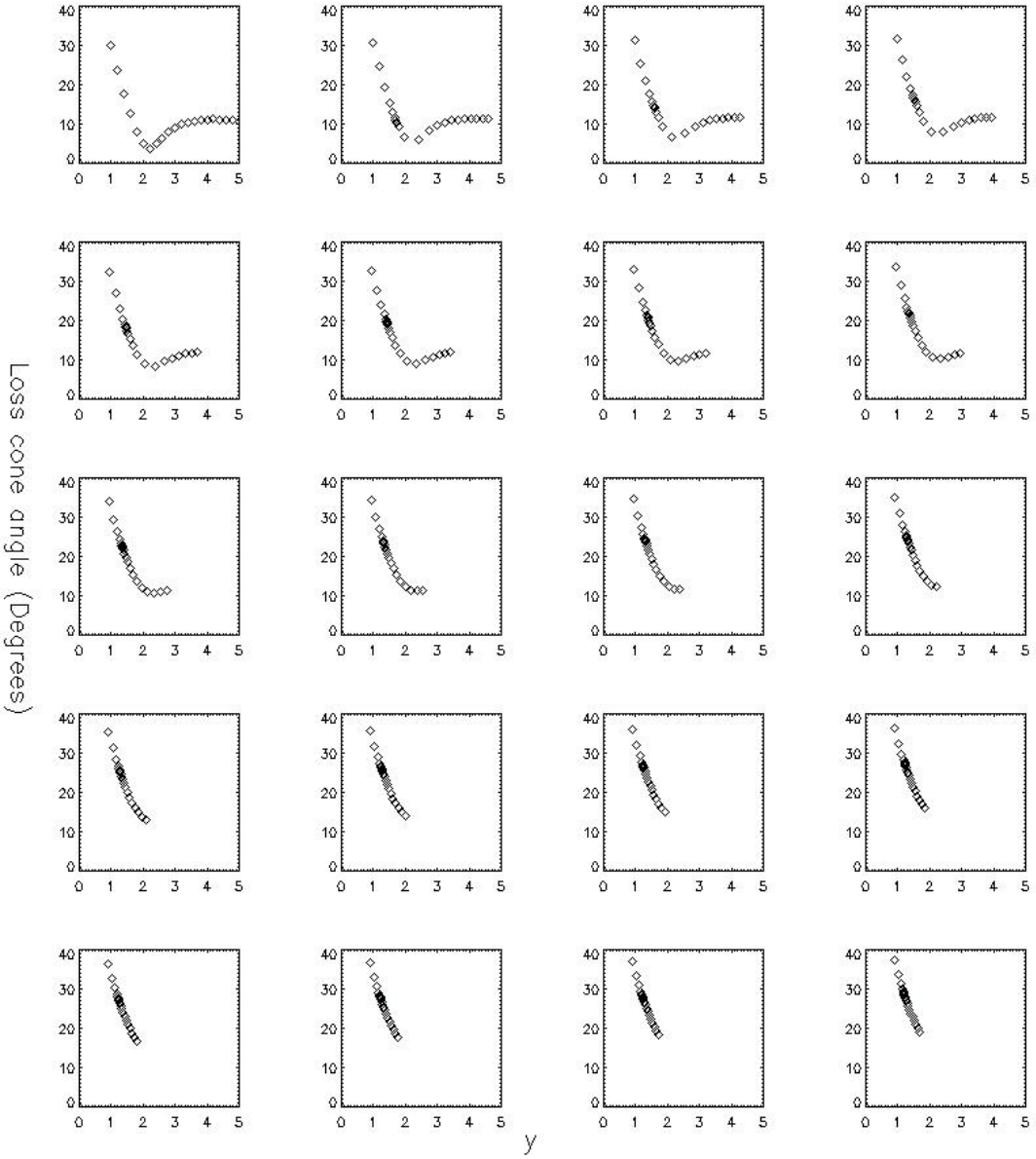

Figure 4.3: Illustrates the variation of the loss cone angle with changing height at the centre of the trap. The code runs from the normalised time of $t = 1.05$ to final time of $t_{final} = 2.0$ which corresponds to 95 seconds. Each frame is taken at 0.04275 (4.75 seconds).

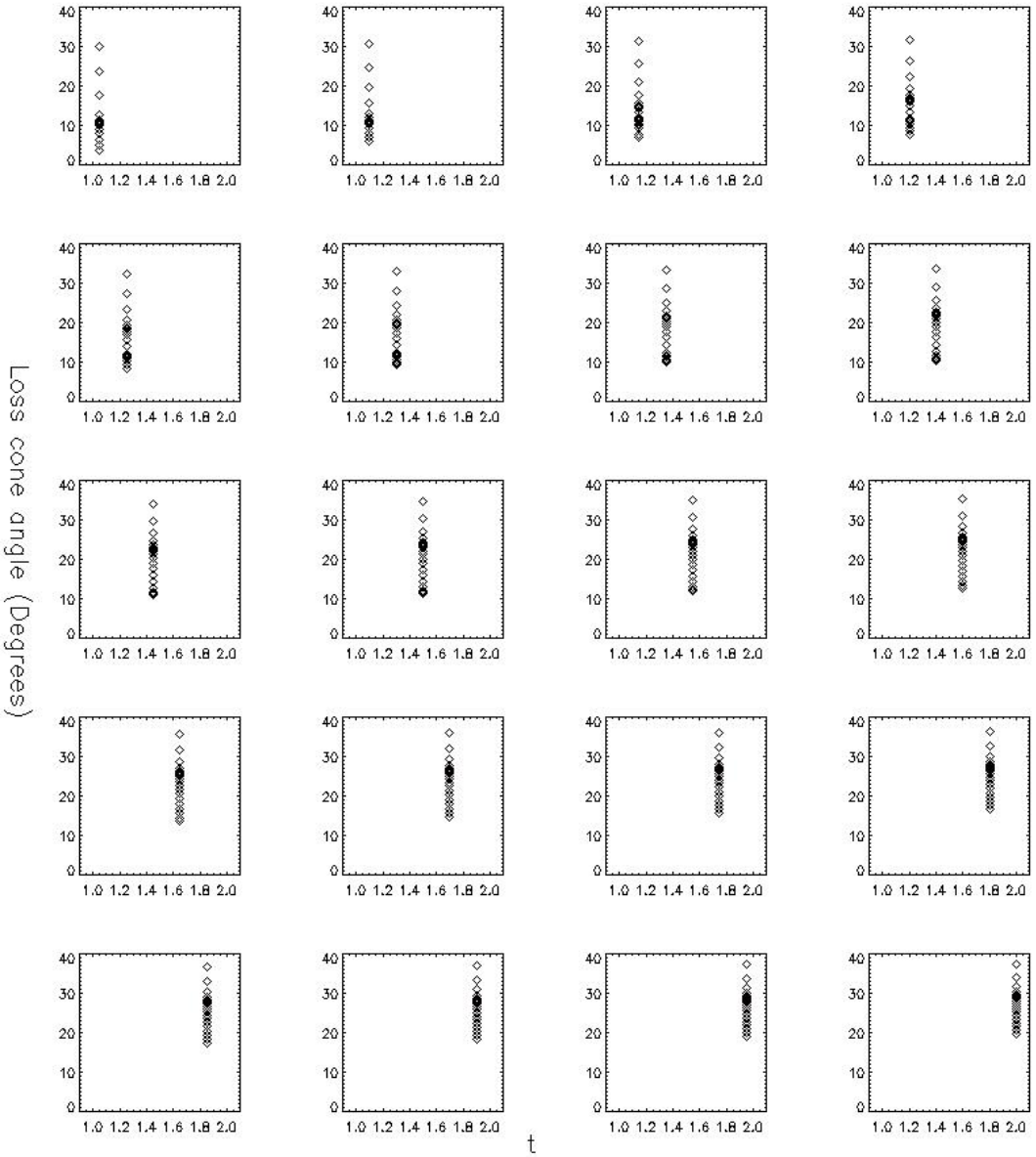

Figure 4.4: Illustrates the evolution of the loss cone at the centre of the trap where each frame is taken at 0.04275 (4.75 seconds).

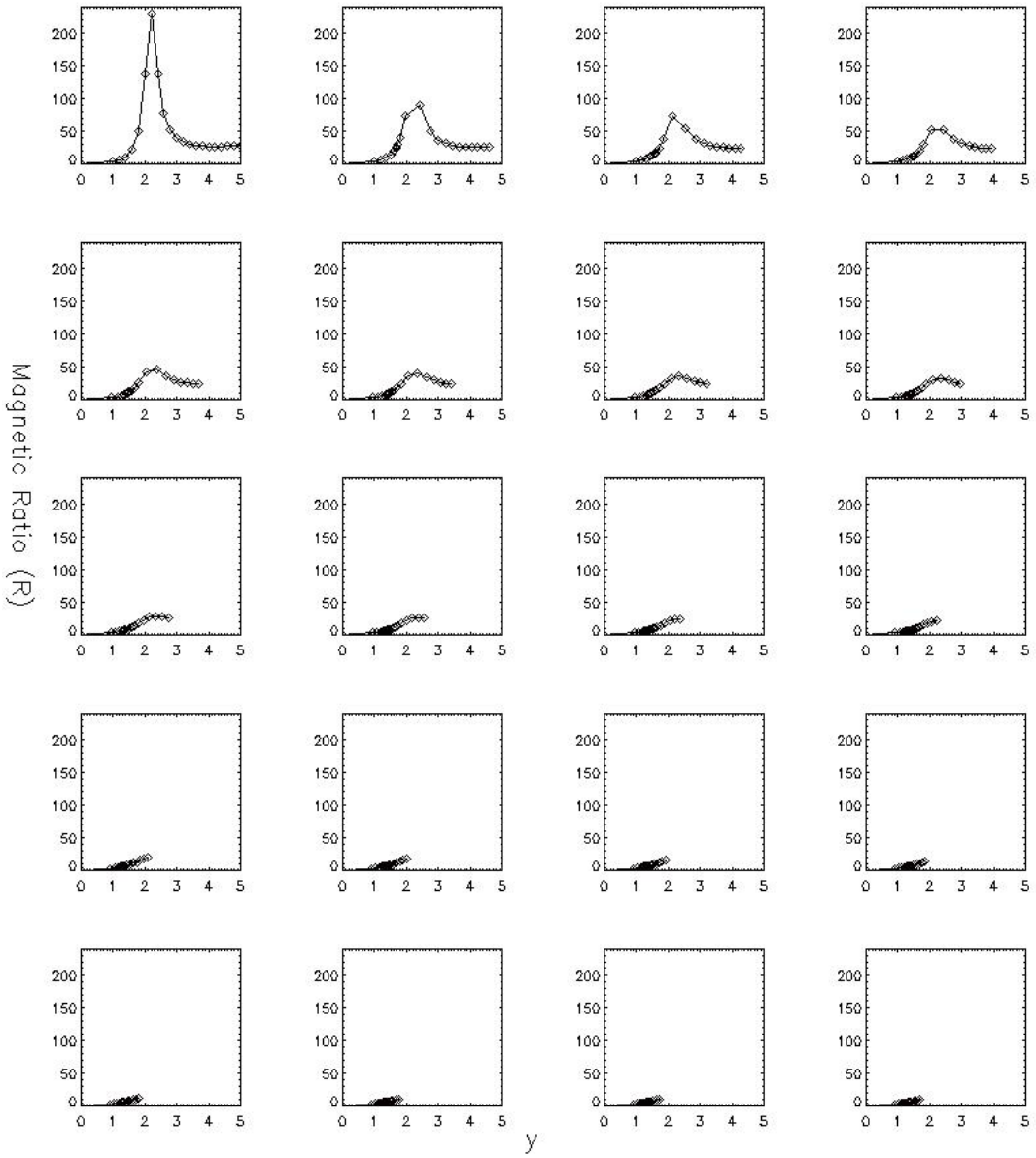

Figure 4.5: Illustrates the variation of the mirror ratio R at the centre of the trap where each frame is taken at 0.04275 (4.75 seconds).

4.3 Evolution of α and θ for Two Representative Particle Orbits

We start our investigation by looking in more detail at two particle orbits starting at the same initial position ($x = 0$, $y = 4.2$) and the same initial energy (5.5 keV), but with different initial pitch angles of $87.3°$ (orbit 1) and $160.4°$ (orbit 2). These initial conditions are representative of the typical behaviour of particle orbits with an initial pitch angle close to $90°$ (orbit 1), which has very little movement along the field lines, and orbits with a much larger component of the velocity vector parallel (or in this case anti-parallel) to the magnetic field at the initial time (orbit 2). The two sets of initial conditions chosen here are very similar (albeit not identical) to the two examples of orbits discussed in Grady et al. (2012) and thus the orbits (shown in Fig 4.6) are very similar to the orbits discussed in their paper. As one can clearly see in Fig. 4.6, orbit 1 (red) remains confined to the middle of the trap due to the fact that the initial pitch angle is close to $90°$, whereas orbit 2 (black) has mirror points very close to the bottom boundary, but does not escape during the time of the calculation. We also point out that after a brief initial period there is very little change in the position of the mirror points over time, which is consistent with previous findings (Grady et al., 2012).

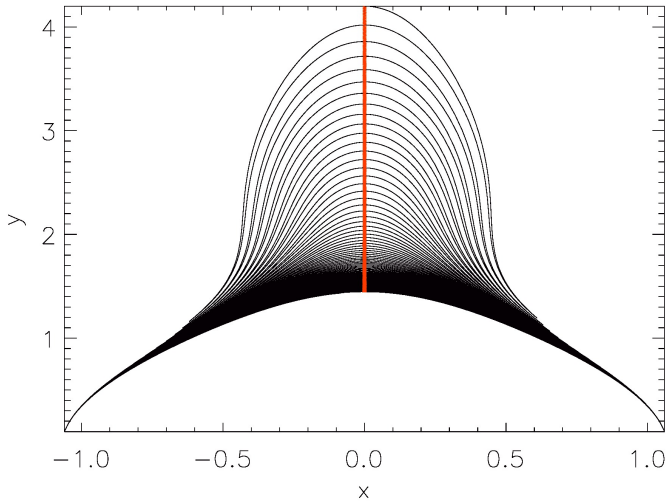

Figure 4.6: Two illustrative particle orbits starting at the same initial position $x = 0$, $y = 4.2$ and with the same initial energy (5.5 keV), but different initial pitch angle. Orbit 1 (red) has an initial pitch angle of $87.3°$ (i.e. close to $90°$) and hence stays close to the middle of the CMT at all times, whereas orbit 2 (black) has an initial pitch angle of $160.4°$ and has mirror points close to the lower boundary.

To analyse the situation further, the loss cone angle at the loop-top (discussed in the previous section) is compared with the time evolution of the pitch angles of the two particle orbits. The results are shown in Fig. 4.7. In the figures the time evolution of the loss cone angle α for the magnetic field line passing through the initial positions of the particle orbits at the initial time is shown in green (towards the bottom of the plots). We also show the angle $180° - \alpha$ (green line

towards the top of the plots), because particle orbits will escape from the trap if their pitch angle becomes either less than α or larger than $180^\circ - \alpha$. Since the CMT we consider here has a magnetic field which is symmetric with respect to $x = 0$, the graph of $180^\circ - \alpha$ here is nothing but a mirror image of the graph of $\alpha(t)$ when reflected at the line 90°. The blue line marks the point

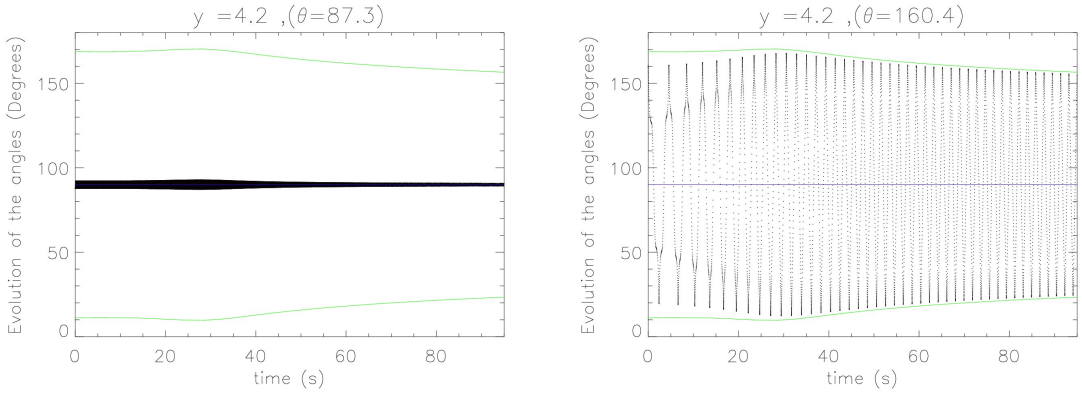

Figure 4.7: The evolution of the particle orbit pitch angle θ (black dotted line) is compared with the evolution of the loss cone angle α (green lines) for particle orbits 1 (initial pitch angle $\theta = 87.3^\circ$) and 2 (initial pitch angle $\theta = 160.4^\circ$). The blue line marks the 90° point. In both plots we show the loss cone angle $\alpha(t)$ as defined in Eqn. (4.3) and $180^\circ - \alpha(t)$. As expected, the pitch angle for orbit 1 oscillates around the 90° line with a slightly decreasing amplitude. Orbit 2 seems to approach the loss cone angle and then follow it without crossing into the loss cone within the time of the calculation.

where the pitch angle of the particle becomes 90°. This is the point where the parallel velocity changes its orientation and the particle begins to travel in the opposite direction. For orbit 1 (in red) the mirror points are close to the centre of the trap and for orbit 2 (in black) the particle travels almost all the way to the foot points before mirroring.

The initial value of the loss cone angle α for this particular magnetic field line is 11.8° and its value at the end of the calculation is 23.4°. As expected the loss cone angle generally increases with time, because the magnetic field strength at the apex of the magnetic field line at $x = 0$ increases with time. However, one can see from the plots that up to a time around 30 seconds the loss cone angle is decreasing. This is a particular feature of the CMT model of Giuliani et al. (2005), which in the initial stages of its time evolution has a region of very weak magnetic field through which the field lines have to move first, before the field strength starts to increase again, and this is the reason for the initial dip in the graph of the loss cone angle. The time evolution of the pitch angle of particle orbit 1 and 2 are shown by the black dotted lines in Fig. 4.6 with orbit 1 on the left and orbit 2 on the right. For particle 1 ($\theta = 87.3^\circ$) the pitch angle of the particle through the duration of the collapse stays close to 90°. The oscillatory behaviour of the particle pitch angle for this case is not as clearly visible as it is for particle 2. However, the amplitude of oscillation seems to be decreasing as time progresses. This can be understood by recalling that Grady et al. (2012) showed that particle orbits of this type do not experience any significant changes in their parallel

energy. They do however gain a considerable amount of perpendicular energy due to betatron acceleration. As the velocity of the particle v increases due to the increase in the perpendicular velocity and the parallel velocity of the particle $v_{\|}$ on average remains constant, from Eqn. 4.1 the pitch angle θ will tend closer to $90°$.

Orbit 2 ($\theta = 160.4°$) shows the more interesting behaviour of the two orbits. This is a particle where the starting pitch angle is closer to the loss cone angle ($180° - 11.8° = 168.2°$) and has a much larger initial $v_{\|}$ than particle 1. In the first 30 seconds or so the pitch angle of the maximum (minimum) values of θ increase (decrease) and approach the green loss cone curve. After this time the pitch angle maxima (minima) start decreasing (increasing) and seem to come closer and closer to the loss cone angle, but never cross into the loss cone for the time of the calculation. It looks like the pitch angle follows the shape of the decrease (increase) of the loss cone, a result which is different from claims made by Aschwanden (2004a) and Somov (2004) that particle orbits should generally move into the loss cone with increasing B. These models will be discussed later on in the chapter. For now, the general behaviour seen in orbit 1 can be explained by the increase of the magnetic field at the apex of the trap, corresponding to an average gain in perpendicular energy and increase in θ due to betatron acceleration, but for orbit 2 further analysis needs to be carried out to see which acceleration mechanism is responsible for the behaviour seen in figure 4.7.

Not all the particles starting at $(x, y) = (0, 4.2L)$ will be trapped. Hence, next we look at particle orbits which start with the same initial position and energy as particle 1 and 2, but with initial pitch angles $\theta = 5°$, $11°$, $12°$, $14°$, $15°$ and $19.6°$. These values cover a range of initial pitch angles which start inside the initial loss cone $11.8°$, just outside the initial loss cone and up to the initial pitch angle of $19.6°$, which is $180° - 160.4°$ as seen in Fig. 4.8. Like the labelling for Fig. 4.7 the green line represents the loss cone angle, the black line the pitch angle and the blue line the $90°$ mirror line.

The particle orbits with θ equal to $5°$ and $11°$ (top two in Fig. 4.8) do not reach the mirror point (the blue line in the figures), since their initial pitch angle is smaller that α, and escape the trap. We systematically increase the pitch angle to $12°$, $14°$, $15°$ and $19.6°$. The orbits for $\theta = 12°$ (second row, Fig. 4.8), $\theta = 14°$ (third row, Fig. 4.8) and $\theta = 15°$ (fourth row, Fig. 4.8) perform a number of bounces within the CMT (each bouncing for a bit longer than the one previously) before escaping after they cross into the loss cone angle (green line). For each plot on the left the corresponding plots on the right show blow-ups of the relevant parts of the graph where the pitch angle crosses into the loss cone angle. In the fifth row, the plot of $\theta = 19.6°$ shows the same behaviour already discussed in Fig. 4.6 for $\theta = 160.4°$ where the pitch angle seems to be edging closer to the loss cone angle but never crosses it.

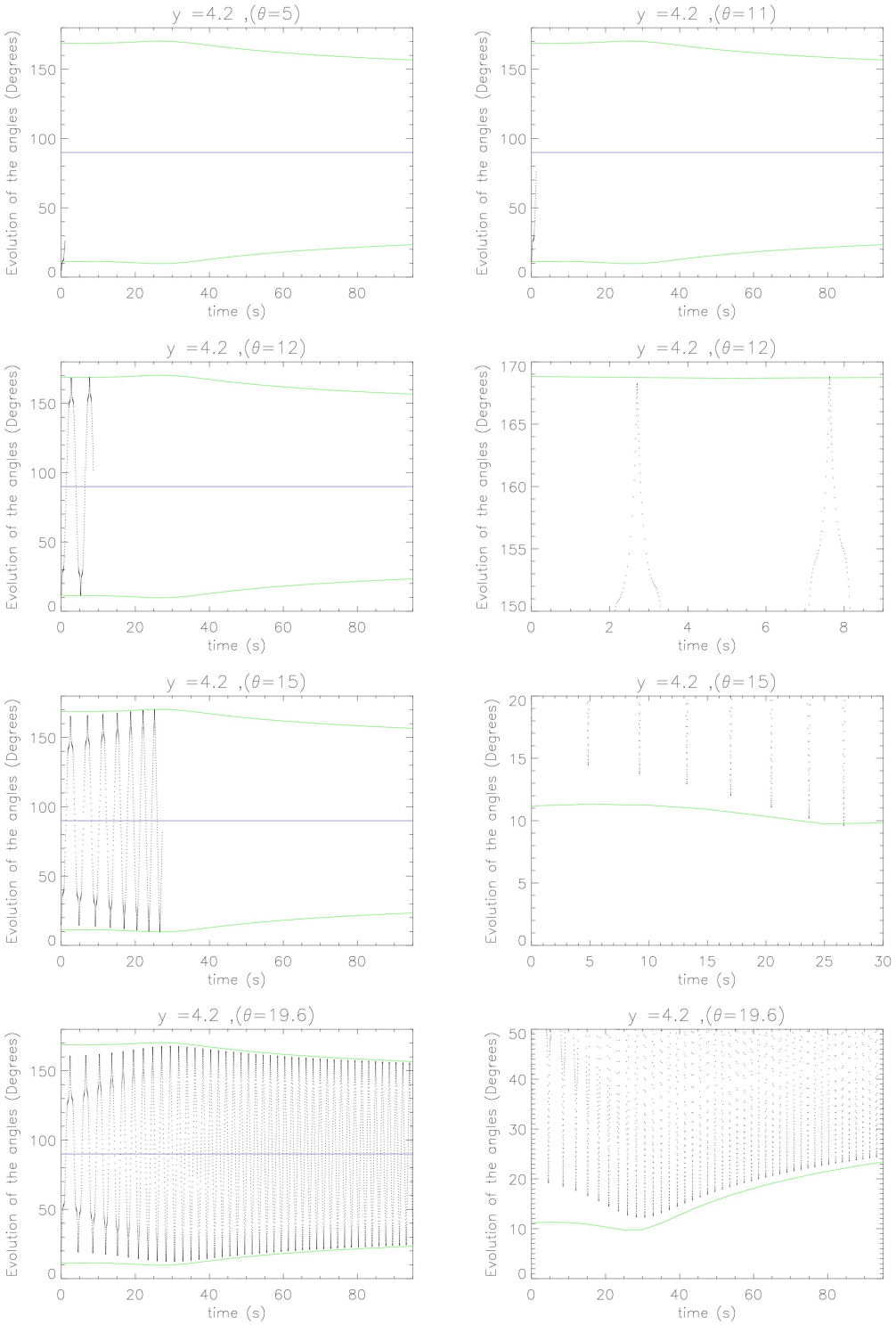

Figure 4.8: The time evolution of θ (black dotted line) for the particle orbits with initial pitch angles varying from 5° (top left) to 19.6°. The two panels in the top row show the pitch angle evolution for the two orbits with initial pitch angles of 5° and 11°. Since $\theta < \alpha$ in both cases they are immediately lost from the trap without mirroring. The other rows show the pitch angle evolution for particles with initial pitch angles of 12°, 14°, 15° and 19.6°, with the full time evolution shown on the left panels and blow-ups of the curves close to the loss cone angle in green shown on the right. All particle orbits except the last one escape in the time period shown.

In general for all the other angles greater that the loss cone angle $\alpha \approx 11.8°$, it can be seen in Fig. 4.8 that particles do get to the mirror points and are reflected back into the trap, so long as $\theta \not< \alpha$, the particle will remain trapped and is accelerated. Therefore, one could conclude that all particles which start at $(x = 0, y = 4.2)$ and have a pitch angle $\theta > 19.6°$ will be trapped for the finite time of the trap collapse. Would this conclusion be different if we were to look at the problem in the limit $t \to \infty$? This is the question we will investigate in the next section.

4.4 Evolution of θ and α as $t \to \infty$

What happens to the evolution of θ and α in the limit $t \to \infty$? Does a particle orbit starting with $\theta = 19.6°$ (or $160.4°$ anti-parallel) still remain trapped when $t \to \infty$? In this section we look at the asymptotic behaviour of the loss cone in the model and compare it the evolution of θ to see if the particles which remained trapped for the finite time (95 seconds) will still be trapped if the calculation is continued beyond this time. Using the definition of the magnetic field seen at the start of this chapter, the asymptotic loss cone α_∞ is analytically calculated for $t \to \infty$. We then compare the evolution of θ and α in the asymptotic limit numerically by increasing the stopping time for the collapse by almost a factor of 100.

4.4.1 Analytical Results

The aim is to analytically find the asymptotic loss cone angle α_∞ for a test case where $(x, y) = (0, 4.2L)$ for $t \to \infty$. Recalling that $\alpha = \sin^{-1}(\sqrt{1/R})$, where $R = B_{fp}/B_\infty$ we need to know what B_{fp} and B_∞ are at $t \to \infty$. The magnetic field is described by the flux function $A(x, y, t_0)$. Since A is constant along the magnetic field lines for all time i.e. $A(x, y) = A_\infty(x_\infty, y_\infty, t_0)$, from Eqn. 4.9 and 4.10 and the fact that $y_\infty = y$ at $t \to \infty$ gives $\frac{\partial y_\infty}{\partial y} = 1$ (see chapter 3), the x and y component of the magnetic field B_x and B_y can be calculated. The y component of the magnetic field, $B_y(0, y_\infty) = 0$ at the middle of the trap for all time. y_∞ is given by Eqn. 2.25 where $a = 0.4$, $y = 4.2$, $t = 1.05$, $a1 = 0.9$, $L = 10$Mm, $L_v = 10$Mm and $b = 1$. Using these parameters gives $y_\infty = 1.01$. Substituting y_∞ into the equation for the magnetic field at the middle of the trap as $t \to \infty$ gives

$$|B_\infty| = \sqrt{B_x^2 + B_y^2} = \frac{34731.25762}{120000} \times 0.015T \approx 4.3 \times 10^{-3}T$$

Previously we mentioned that the magnetic field at the foot point remains constant for all time. Next we want to find B_{fp}, the magnetic field at the foot point for the corresponding field line in

the trap for large t. Let $A_\infty(0, y_\infty) = A_\infty(x_\infty, 0)$. Using Eqn. B.3 gives

$$\cot(\frac{A_\infty}{c_1}) = \frac{x_\infty^2 - 1/4 + (y_\infty + d/L)}{-y_\infty - d/L}.$$

Substituting $y_\infty = 1.01$ and $x_\infty = 0$ results in

$$\cot(\frac{A_\infty}{c_1}) = -1.89.$$

Using Eqn. 4.11 gives

$$x_\infty = 1.069.$$

Substituting the values $(x_\infty, y_\infty) = (1.069, 0)$ at the foot point results in,

$$|B_{fp}| = B(x_\infty, 0) = \sqrt{B_x^2 + B_y^2} = \frac{70058.00573}{120000} \times 0.015T \approx 8.75 \times 10^{-3}T.$$

Therefore, the asymptotic loss cone angle α_∞ is approximately $44.78°$ where $R = B_{fp}/B_\infty = 2.01$. Next we check to see if the analytical calculation is in agreement with the numerical results.

The highlighted boxes in Table 4.1 show the numerical values calculated in section 4.2 at the initial time $t = 1.05$ for the height $(x = 0, y = 4.2L)$ where $\alpha = 11.82°$. Looking at the highlighted row in table 4.3, the final value of y, α, t, B_{field}, B_{fp} are now calculated for a much longer time of $t_\infty = 101.05$. It can be seen that the numerical value calculated for α_∞ is in agreement with what we calculated previously as seen in Table 4.3. From Eqn. 2.26 as $t \to \infty$ we have

$$t \gg \frac{y^{1/b}}{a}.$$

The constant $a = 0.4$, $b = 1$ in the transformation is fixed. In our case $y = 4.2$, so we have

$$t \gg \frac{(4.2)^1}{0.4} \approx 10.5.$$

We have seen in our case at $t = 10.5$ and above the discrepancy between one magnetic field to the next decreases as time progresses.

All particle orbits discussed so far have been stopped at a time of 95 seconds, well before coming close to the asymptotic limit when $\alpha_\infty = 44.78°$. This raises the question whether the orbits which remain trapped for the finite time of 95 seconds are still trapped if the stopping time increases. Therefore, we have increased the stopping time for the calculation of the particle orbit with initial pitch angle $160.4°$ (orbit shown in the top left panel of Fig. 4.9) by a factor of almost 100. It turns out that this particle orbit eventually escapes from the CMT at the time of about 234

Table 4.3: Table with values of y, α, B_{field} at the middle of the trap, B_{fp} at the foot points and mirror ratio, R for $x = 0$ for $t \to \infty$

$y(L)$	$\alpha(^\circ)$	B_{field}(Tesla)	B_{fp}(Tesla)	R
0.7558643	49.6993733	0.0056250	0.0096708	1.7192404
0.8272536	48.1068712	0.0052240	0.0094276	1.8046668
0.8726224	47.2094262	0.0049906	0.0092672	1.8569289
0.8979819	46.7406265	0.0048667	0.0091762	1.8855082
0.9101053	46.5232066	0.0048090	0.0091327	1.8990738
0.9148635	46.4393253	0.0047867	0.0091156	1.9043614
0.9168643	46.4037863	0.0047773	0.0091085	1.9066107
0.9190671	46.3638938	0.0047671	0.0091010	1.9091421
0.9228039	46.2993083	0.0047497	0.0090874	1.9132551
0.9287744	46.1974456	0.0047222	0.0090656	1.9197789
0.9371356	46.0553854	0.0046841	0.0090353	1.9289535
0.9475479	45.8812712	0.0046372	0.0089976	1.9403208
0.9596741	45.6816423	0.0045835	0.0089539	1.9535226
0.9730296	45.4666333	0.0045253	0.0089056	1.9679463
0.9873153	45.2411619	0.0044644	0.0088542	1.9833044
1.0020969	45.0138998	0.0044025	0.0088008	1.9990300
1.0172812	44.7848045	0.0043403	0.0087463	2.0151370
1.0323926	44.5638347	0.0042797	0.0086917	2.0309196
1.0474088	44.3496696	0.0042206	0.0086373	2.0464520
1.0625134	44.1365904	0.0041624	0.0085836	2.0621407
1.0771875	43.9358927	0.0041070	0.0085309	2.0771360

seconds (right hand boundary of the plot) [1]. In order to find the initial angle dividing escaping particle orbits (for large t) from trapped particle orbits (the critical angle), the long term evolution of particle orbits with pitch angles starting at $\theta = 160.0^\circ$ and decreasing to 150.4° was investigated. The results are shown in the other plots in Fig. 4.9. The top right hand graph shows the evolution of the angles for a particle starting with $\theta_{init} = 160.0^\circ$. A decrease by only a factor of 0.4 in the value of the initial pitch angle to 160.0° already increases the time the particle orbit remains in the trap substantially to just over 400 seconds. Systematically deceasing the initial pitch angle we find for $\theta_{init} = 159.21^\circ$ (Fig. 4.9 middle row, left) the particle orbit escapes at roughly 9000 seconds. It is the particle orbit starting with $\theta_{init} = 159.2^\circ$ (Fig. 4.9 middle row, right) that marks the critical angle where particles with pitch angles starting at $\theta_{init} \lesssim 159.2^\circ$ will remain trapped for all time. The bottom graphs on the left and right hand side show clearly that the two test particles with $\theta_{init} = 155.4$ and 150.4 respectively are trapped for all time.

From our results so far it seems we have particle orbits escaping from the CMT model for starting subcritical angles (i.e. below $\theta_{critical} = 159.2^\circ$ for an initial position $(x, y) = (0, 4.2L)$) and

[1] The particle orbit code is set up to stop soon as the value of y becomes negative.

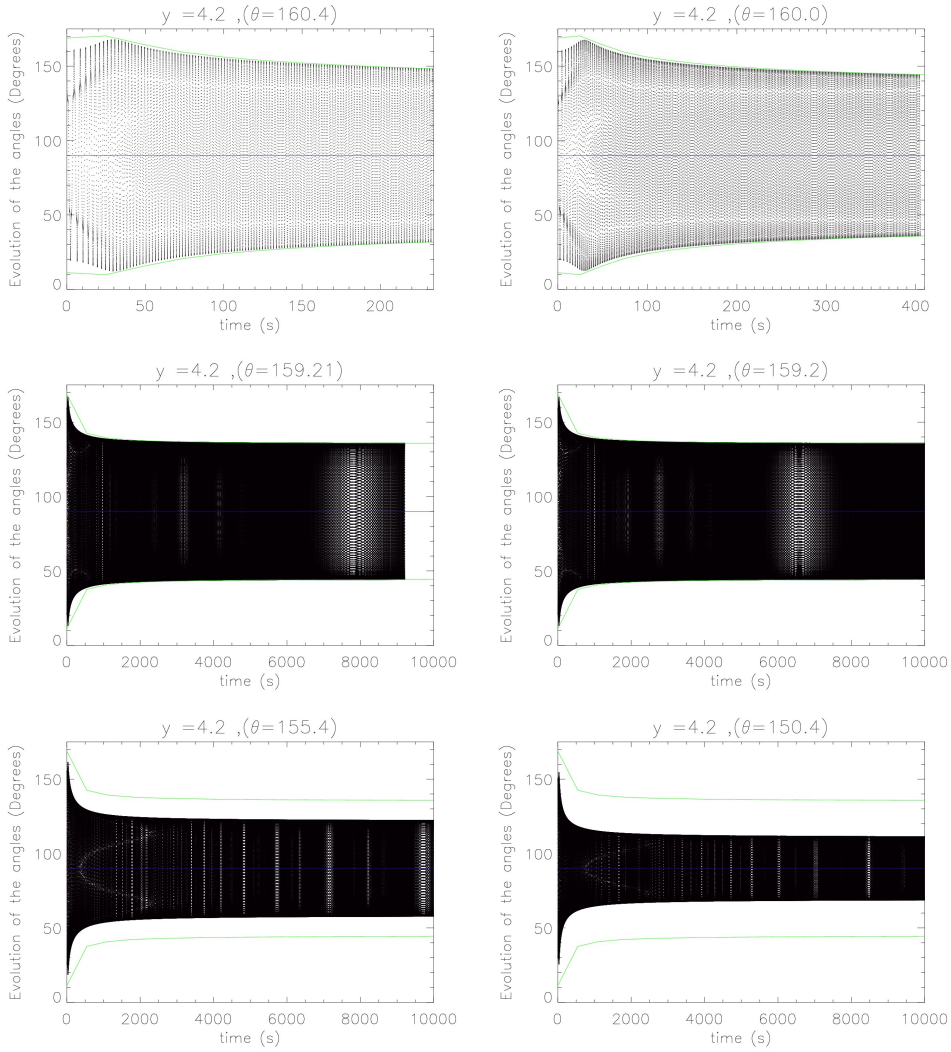

Figure 4.9: Long term time evolution of the pitch angle for particle orbits with initial pitch angles $160.4°$, $160.0°$ and $159.21°$ (subcritical), $159.0°$ (critical) and $155.4°$ and $150.4°$ (supercritical). Any particle starting with a subcritical angle escapes from the CMT and any particle starting with a supercritical angle remains trapped for all time.

particle trapping for orbits starting with supercritical angles. This leads us to ask what are the acceleration mechanisms responsible for these results? This involves looking at the perpendicular $v_{\perp}$ and parallel $v_{\parallel}$ velocities as seen in Fig. 4.10 in the right hand column of each of the particles discussed in Fig. 4.9.

In Fig. 4.10 the plots for the evolution of angles as seen in Fig. 4.9 for each initial pitch angle are reproduced, however, with one main difference that for initial pitch angle values smaller than $160.0°$ only the maxima and minima of the pitch angle curves are shown[2]. This is because

[2]The envelope of the curve created from the values of the pitch angle when the orbit is at the apex of the field line.

of the large number of bounces the particle orbits undergo over the extended time period of the calculation leading to the last four pitch angle curves seen in Fig. 4.9. As the plots for pitch angle and loss cone evolution have already been discussed, in Fig. 4.10 the evolution of the velocities for each particle orbit is shown in detail. In Fig. 4.10 the first and second plots in column two show the evolution of the parallel (black) and the perpendicular velocities (blue) for the orbits starting with $\theta = 160.4°$ and $160.0°$ respectively. The perpendicular velocity $v_\perp$ of the particle orbit initially decreases with decreasing magnetic field (one of the properties of our collapsing magnetic trap model), then begins to increase with increasing magnetic field strength. This can be explained through the invariance of magnetic moment since with decreasing magnetic field $v_\perp$ decreases. When the magnetic field in the trap begins to increase so does the $v_\perp$ of the particle orbit. Simultaneously the parallel velocity $v_\parallel$ of the particle orbit initially grows very rapidly at the start of the collapse and seems reach a plateau (or slightly decreases) with increasing magnetic field. For the particle orbit starting with $\theta = 159.2°$, $159.0°$ and $155.4°$ the initial details at the beginning of the collapse are hard to see due to the longer calculation times for these cases. However, the apparent decrease in $v_\parallel$ and the increase in $v_\perp$ is clearly seen.

The specific feature that we would like to highlight here is that the parallel velocity shows a rapid increase in the initial phase of each orbit and then seems to level off or even drop off slightly, whereas the perpendicular velocity shows a more long term evolution although it levels off in the long run. However, $v_\perp$ is often still increasing when $v_\parallel$ has already either reached its plateau or is decreasing. We hypothesise that this behaviour is due to the initial rate of change of collapse being high, hence the sharp increase in $v_\parallel$ of the particle by Fermi acceleration. As time progresses the rate of collapse decreases which corresponds to the levelling off or the slight decrease in $v_\parallel$ as seen in Fig. 4.10. The piling up of magnetic flux from above will cause the field strength to continue increasing, resulting in $v_\perp$ increasing. In general, since the growth rate for $v_\perp$ is much longer than the decay rate of $v_\parallel$, this seems to suggest that Fermi acceleration initially dominates, however, betatron acceleration is the main acceleration mechanism in the CMT model. Given the relation of the pitch angle with the components of the particle velocity, as $v_\perp$ increases with increasing magnetic field so does the pitch angle of the particle. This could be the reason why in our model we have particle trapping for angles as low as $21°$ or $159°$ for the set of initial conditions which we have discussed so far. For the specific CMT model of Giuliani et al. (2005) there seems to be a critical angle for which particle orbits starting at or above this angle will be trapped for all time and below this angle they will eventually be lost. If we were to pick different initial conditions we would see a similar behaviour in general, but a quantitatively different result.

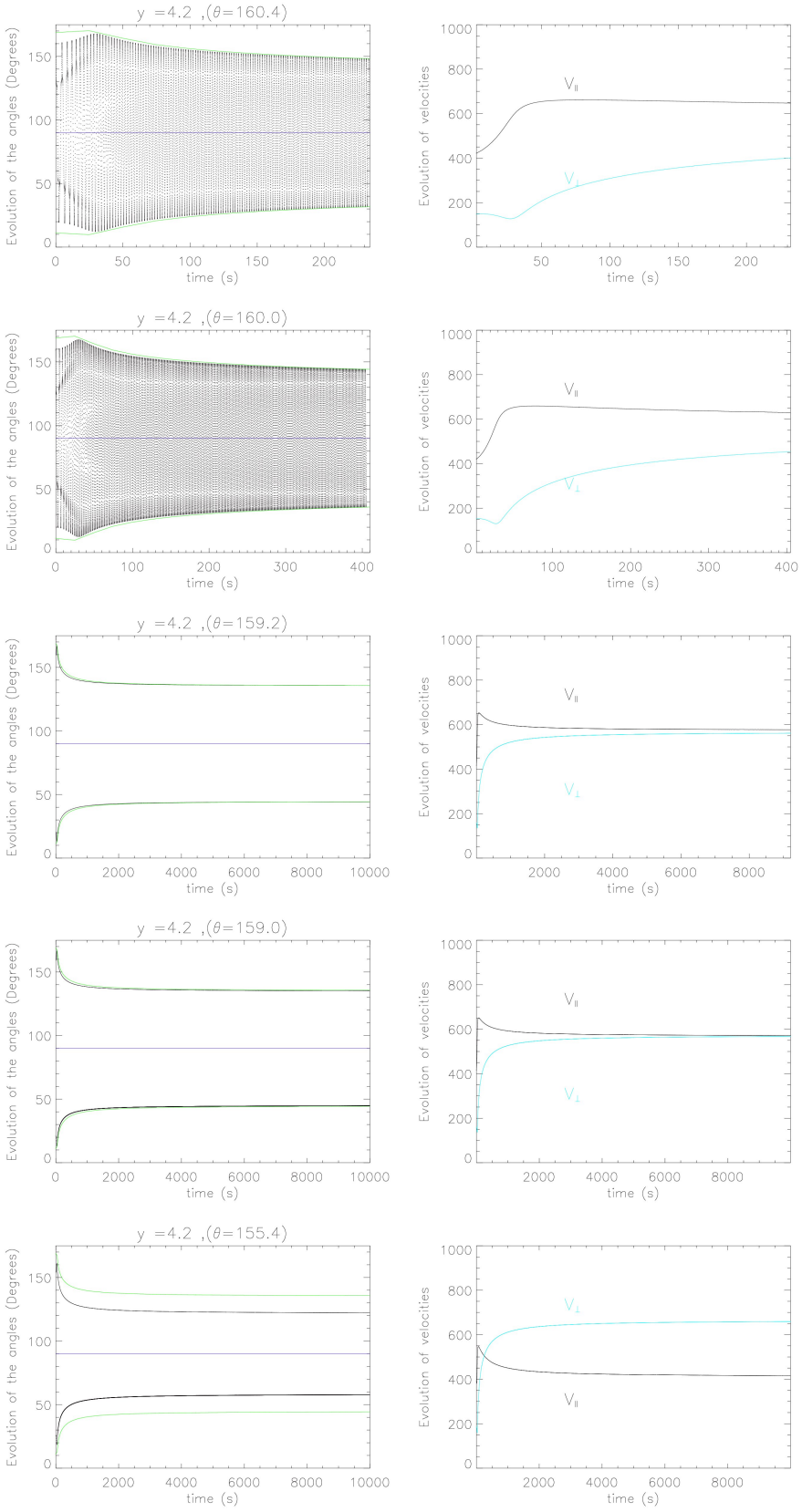

Figure 4.10: Left panel show the pitch angle evolution for the all the angles seen in Fig. 4.9 and the right panel the corresponding $v_{\parallel}$ and $v_{\perp}$. Results seem to suggest that Fermi acceleration initially dominates, however betatron acceleration is the main acceleration mechanism.

4.5 Particle Trapping and Escape in Simple Models

In order to gain a better understanding of the results in the previous calculations, we would like to be able to reproduce the main features in terms of simple models for the acceleration process. We will first look at two such models which have been published in the literature, namely the models by Aschwanden (2004a) and Somov (2004). Details of these two models will be presented in the following section. As we will see, neither of these models can explain the results we have found and this can be attributed to the basic assumptions made in these models. We will hence construct three simplified models, which are consistent with the properties of the CMT model and compare the results regarding particle trapping and escape found using these models with our orbit calculations.

4.5.1 Particle Trapping and Escape in Two Simple Models

In this section we look at the behaviour of the loss cone angle α and its variation with height in two simple CMT models published in the literature. Our particular focus will be on comparing the evolution of the loss cone angle α with the evolution of θ, the particle pitch angle in the CMT models proposed by Aschwanden (2004a) and Somov (2004). We also discuss the assumptions both these models make that allows α in the asymptotic limit to tend towards 90°, allowing for all the particles to leave the trap which is very different from the assumptions we make in our CMT model. A point to note here is that for each specific model that is discussed in this section, the original choice of notation by the authors is adopted when possible.

4.5.1.1 Aschwanden's CMT Model

The set up for this model is based on X-type reconnection occurring high up in the corona. The reconnection outflow carries the newly reconnected field lines downwards (red line in Fig. 4.11). As the field lines relax they tend towards the semi-circular green line in Fig. 4.11 and it is assumed the magnetic field strength becomes uniform. The evolution of the loss cone angle α as illustrated by the blue cone in Fig. 4.11 is assumed to be

$$\alpha(t) = \frac{\pi}{2}\left[1 - e^{-t/t_I}\right],$$

where t_I is called the"injection time", which is a free parameter of the model. From the above definition the loss cone angle at $t = 0$ is $\alpha(0) = 0$ and in the asymptotic limit for $t \to \infty$, the loss cone angle $\alpha \to \frac{\pi}{2}$. As mentioned in Section 2.1.2, the mirror ratio R is related to the loss cone

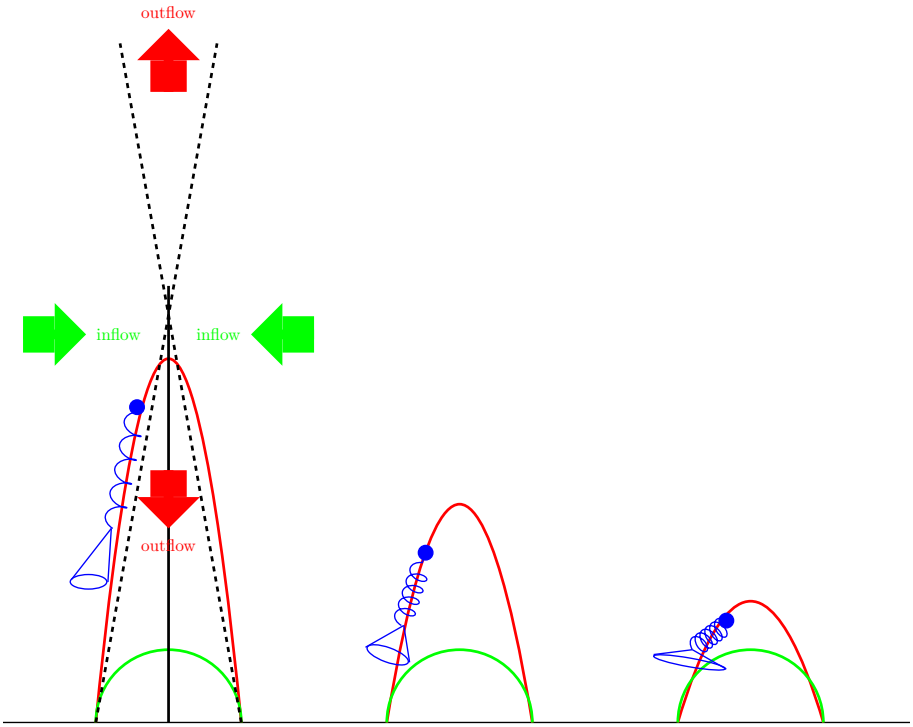

Figure 4.11: Evolution of the newly reconnected magnetic field lines (red line), which relax from the initial cusp shape to a force-free state (green line). As the field line relaxes the magnetic mirror ratio reduces and the loss cone open up to 90°.

.

angle by

$$R(t) = \frac{B_L}{B(t)} = \frac{1}{\sin^2 \alpha(t)},$$

where $B(t)$ is the magnetic field at the apex of the field line and B_L is the magnetic field at the foot point. Rearranging the above equation for $B(t)$ and substituting the expression for the loss cone angle gives an expression for the magnetic field strength at the apex of the field line as a function of time,

$$B(t) = B_L \sin^2 \left\{ \frac{\pi}{2} \left[1 - e^{-t/t_I} \right] \right\}.$$

Since the magnetic field is directly related to the evolution of the loss cone angle, when $\alpha = 0$ at $t = 0$, the magnetic field $B(0) = 0$. For $\alpha \to \frac{\pi}{2}$ in the asymptotic limit the magnetic field $B \to B_L$, where this is the strength of the magnetic field at the foot points of the trap. The evolution of the magnetic mirror ratio $R(t)$, the loss cone angle as a ratio of $\frac{\pi}{2}$ and the magnetic field as a ratio of the foot point magnetic field strength B_L is illustrated in Fig. 4.12. Both the

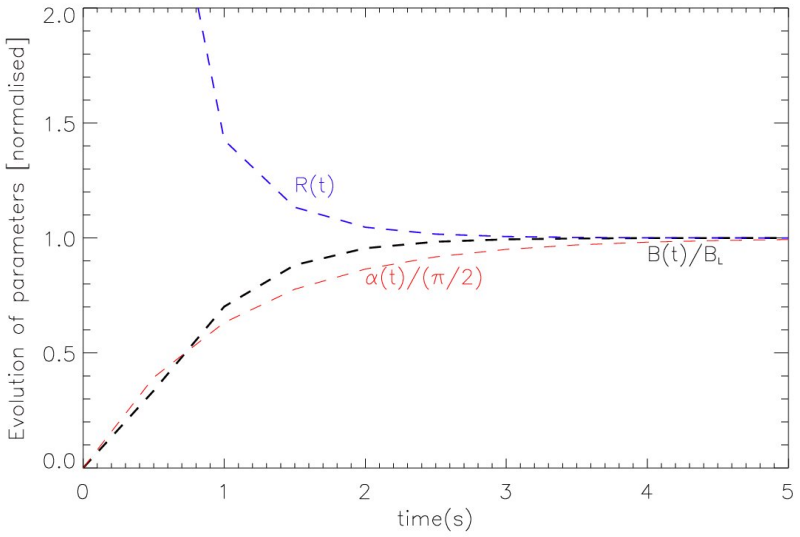

Figure 4.12: The curves show the evolution of the magnetic field at the apex of the relaxing field line $B(t)/B_L$, loss cone angle $\alpha(t)/(\pi/2)$ and mirror ratio $R(t)$. The relaxation time is $t_R = 4.84$ seconds, the injection time scale is $t_I = 1.00$ seconds (Aschwanden, 2004a).

magnetic field ratio $\frac{B(t)}{B_L}$ and the loss cone ratio $\frac{\alpha(t)}{\frac{\pi}{2}}$ start from zero and qualitatively have the same behaviour as seen by the black and red dashed lines respectively. The mirror ratio $R(t)$ illustrated by the blue dashed line is inversely related to the loss cone and the mirror ratio. There are three main assumptions made in this model which are:

- Two dimensional X-point reconnection region yielding a vanishing magnetic field at the start.
- Uniform magnetic field at $t \rightarrow \infty$ yields a fully open loss cone after field line relaxation is completed.
- Time independent pitch angle distribution of the accelerated particle distribution.

It follows from the first two assumptions that the asymptotic loss cone α_∞ fully opens up to $90°$ allowing for all the particles to eventually leave the trap. The third assumption that the particle pitch angle θ is time independent means that in this model the invariance of magnetic moment μ and longitudinal invariance J are not taken into account. Hence in this model the evolution of the particle pitch angle in relation to its loss cone angle is not considered. This model is not capable of explaining the features we found for the particle orbit in the Giuliani et al. (2005) model, although it correctly describes the general trend of increasing loss cone angle in a CMT.

4.5.1.2 Somov's CMT Model

A CMT model which does consider the invariance of magnetic moment μ as well as longitudinal invariance J was given by Somov (2004). In this model the magnetic field configuration is straightened out (see Fig. 4.13). The magnetic field $\mathbf{B_1}$ is uniform inside the trap, however it increases to $\mathbf{B_2}$ at the mirror points indicated by the region marked out by the vertical dashed lines. In this model, Fermi acceleration occurs if the mirror points are brought close together with

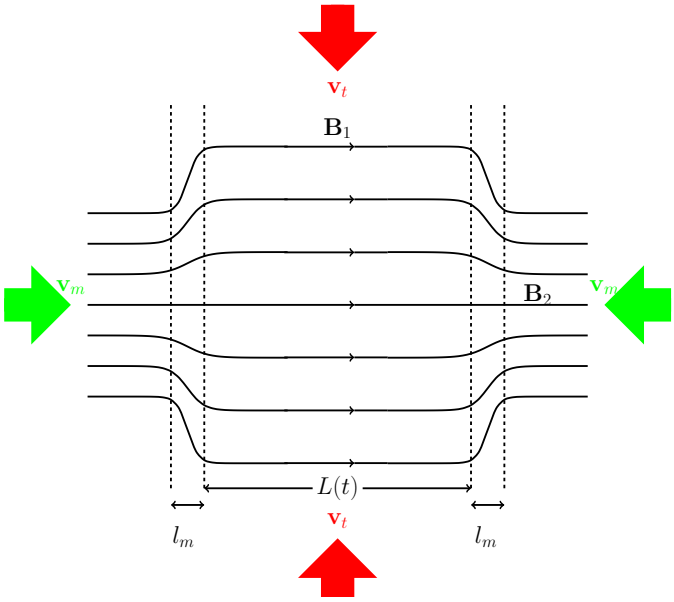

Figure 4.13: Illustrates the straighten out trap model adapted from Somov (2004). Fermi acceleration is produced by magnetic mirror points moving towards each other with velocity $\mathbf{v}_m$. Betatron acceleration is produced by the compression of the trap with velocity $\mathbf{v}_t$ causing the loss cone angle to open up fully.

the speed v_m and the trap length $L(t)$ decreases. This can be represented by the use of the dimensionless parameter $l = L(t)/L_0$. During this process the magnetic field strength $|\mathbf{B}_1|$ remains constant and hence the perpendicular momentum does not change, i.e. $p_\perp = p_{0\perp}$. The parallel momentum, however, increases due to the invariance of J, as

$$p_\parallel(l) = \frac{p_{0\parallel}}{l},$$

leading to first order Fermi acceleration. $p_{0\parallel}$ here is the initial value of the parallel momentum at $t = t_0$.

If the thickness of the trap is decreasing, this leads to an increase of the magnetic field, $B(l)$ as a function of parameter l. From the invariance of the magnetic moment the transverse momen-

tum $p_\perp$ increases leading to betatron acceleration.

Obviously both processes will usually happen simultaneously. Due to the trap contraction the loss cone angle defined by

$$\theta_{es}(l) = \arcsin\left(\frac{B(l)}{B_2}\right)^{1/2},$$

tends to 90° in the asymptotic limit, since $B(l) \to B_2$ meaning a uniform magnetic field structure at the final state. Consequently, all the particles in the model will also escape.

We saw that in the models by Aschwanden (2004a) and Somov (2004) the loss cone angle fully opens up, allowing all the particles to escape. Furthermore, whereas in investigations based on a number of simplifying assumptions (e.g Somov and Bogachev, 2003; Somov, 2004; Bogachev and Somov, 2005) some predictions can be made about, for example, the relative importance of betatron and Fermi acceleration and the resulting consequences, similar predictions are much harder to make for more detailed magnetic field models (e.g. Giuliani et al., 2005; Karlicky and Barta, 2006; Minoshima et al., 2010; Grady et al., 2012), because the relative importance of betatron vs. Fermi acceleration (i) will be different for particles with different initial conditions, (ii) may change with time during the evolution of the CMT and (iii) will depend on the details of the magnetic field model used.

Furthermore, it is well-known that in time dependent and curved magnetic fields the two mechanisms are closely linked (see e.g. Northrop, 1963). In general, one would expect the magnetic field strength within a relaxing magnetic loop to increase. Assuming that the magnetic field strength is highest at the foot points and that this field strength does not change substantially, the loss cone should generally open up during the evolution of a CMT. How much the loss cone opens depends on the magnetic field model. For our model the asymptotic value of the loss cone angle in the limit $t \to \infty$ is almost 44.8° for the particle orbit discussed in Section 4.4. The asymptotic value of the loss cone angle does not approach 90° because we have an inhomogeneous asymptotic magnetic field with a larger field strength at the foot points compared to the highest points along field lines, and thus particle orbits can remain trapped in this CMT model (contrary to e.g. the model of Aschwanden, 2004a). We emphasize again that the values of the loss cone angle at all times will be different for different initial positions, but that the qualitative behaviour will be the same.

Generally, the situation we are facing with regards to escape or trapping of particle orbits in a CMT is summarised schematically in Fig. 4.14. The red line traces out the time evolution of the loss cone angle $\alpha(t)$. It generally increases from its starting value α_{init} to an asymptotic value α_∞ as $t \to \infty$, although as seen above, this increase does not necessarily have to be monotonic as shown in the sketch. We have divided the θ-t-plane in the sketch tentatively into three regions:

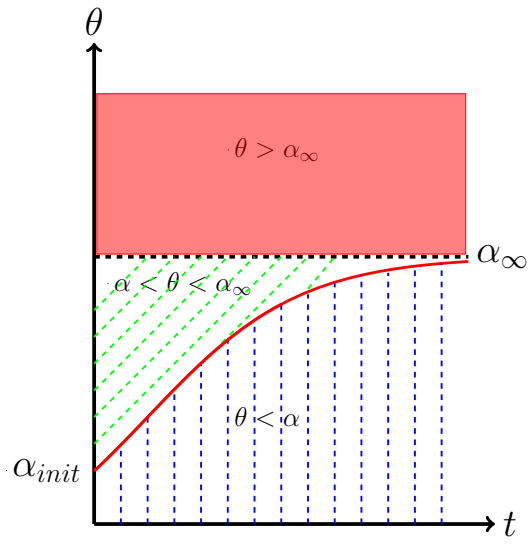

Figure 4.14: Sketch of the different regions in pitch angle vs. time evolution in a CMT. The red curve represents the time evolution of the loss cone angle $\alpha(t)$, which starts at a value α_{init} and then increases with time towards an asymptotic value α_∞. We find that orbits with initial pitch angles smaller than α_{init} escape immediately (blue hatched region), whereas orbits with initial pitch angles greater than α_∞ (pink shaded region) remain trapped (although see discussion in main text). For orbits with initial pitch between α_{init} and α_∞ (green hatched region) the outcome depends on the relative importance of Fermi vs. Betatron acceleration. We find that usually there is a critical value for the initial pitch angle below which particle orbits escape and above which particle orbits remain trapped.

a region below the red curve representing the loss cone angle α (hatched blue), a region above the asymptotic value of the loss cone angle, α_∞ (shaded pink) and the region between these two regions, where $\alpha < \theta < \alpha_\infty$ (hatched green). Clearly, particle orbits whose loss cone angle crosses into the blue hatched region will escape from the CMT. In particular, we found above that all orbits with initial pitch angle below α_{init} are lost without even bouncing once (see Fig. 4.8). On the other hand, orbits with initial pitch angles in the pink shaded region would be expected to remain trapped for all times, and that is consistent with our findings above. However, we have to mention that there could be a possibility of a CMT which increases the parallel energy of particle orbits starting with pitch angles above α_∞ in such a way that the pitch angle decreases with time and crosses into the blue hatched region. However, based on our results so far this seems to be an unlikely scenario. The most interesting region is the region hatched in green. As seen above, orbits starting with pitch angles in this region can either escape from the trap if their pitch angle does not remain above the red curve during the time evolution of the orbit, or remain trapped indefinitely if the time evolution of the pitch angle takes it into the pink shaded region. Our results indicate that there is a critical initial pitch angle and orbits which start with pitch angles smaller than this critical angle will eventually cross into the blue hatched region and escape, whereas orbits with

initial pitch angles above the critical one will remain trapped. We expect that the behaviour we found for the specific CMT model of Giuliani et al. (2005) would at least qualitatively also be found for other CMT models. To corroborate this statement, we will now look at how the results we found can be understood from a more basic theoretical point of view.

4.5.2 Trapping and Escape Using Simplified Models

In this section we attempt to develop a better understanding of the results regarding the trapping and escape of particle orbits for the CMT model we have studied by using some basic theoretical concepts. We will use a simplified scenario for the acceleration within a CMT taking into account two features of the particle orbits, namely:

1. increase in parallel velocity occurs at the apex of the field lines,
2. the position of the mirror points moves very little during the evolution of the CMT.

We note that the second assumption is an approximation to facilitate the calculations made using the particle orbit model. If it were to be exactly correct in a general CMT model it would imply no particle orbits would ever cross the lower boundary.

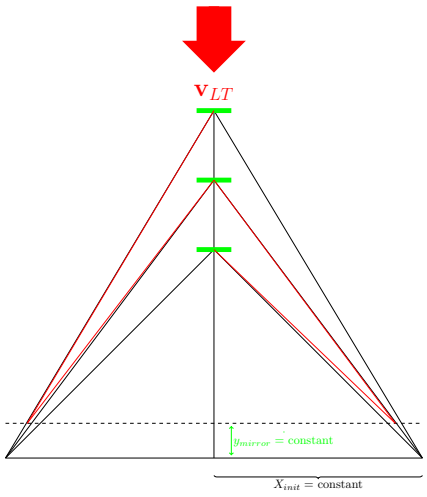

Figure 4.15: Sketch of the basic model used to explain the results found regarding escape and trapping of particle orbits in CMTs. The black lines represent the field lines and the straight red lines represent the particle orbit travelling along the field lines. The field line loop tops move downwards with speed V_{LT}. The foot point position x_{init} and the mirror height y_{mirror} are kept constant.

We will base our model for particle acceleration on the principle first proposed by Fermi in 1949 (see e.g. Longair, 1994). We represent the magnetic field lines of our simplified model by straight lines which the guiding centre follows (see Fig. 4.15). No acceleration in the parallel direction takes place except when the particle passes through the moving apex of the field line ("loop top"), where we imagine it elastically bouncing of a "wall" moving with velocity V_{LT}. This assumption

is supposed to mimic the increase in parallel velocity around the field line apex observed in our full orbit results. The two lower mirror points are kept at a fixed height y_{mirror} for all times. The foot point length x_{init} is assumed to be constant along the x-axis, since the foot points are also fixed in the full CMT model.

Due to the assumptions we made, a particle gains parallel energy every time it encounters the field line apex. The increase in parallel speed can be calculated by looking at the mechanics of the light object (particle) colliding with a very heavy object ("moving wall"). As we have two objects colliding with each other (i.e. a particle with a wall), one can think of each object as seeing the collision (event) from their point of view (frame of reference). The particle's frame of reference F is represented by the (x, y, t) coordinate system. The wall's frame of reference (F') is represented by the (x', y', t'). The basis of this calculation comes from the conservation of momentum, where the momentum of the particle is reversed, after the particle collision with the mirror (see e.g. Longair, 1994). As a result the particle gains momentum of $2mV_{LT}$ from the collision. The total velocity of the particle after the collision is

$$v = v_{\|y} + 2V_{LT}.$$

For our simple models, we also assume that magnetic field strength at the field line apex is a known function $B(t)$ and that the field line strength remains constant at the foot points. We will discuss examples for this function in detail later in this chapter. This allows us to determine the time evolution of the loss cone angle for the simplified model as well as to calculate the time development of the pitch angle at the field line apex just after each bounce.

4.5.3 The Mirror Height

Generally other assumptions have to be made to complete the simplified trap model. One of the further assumptions we have to make for our simple model is how to determine the height of the mirror points. Obviously, the mirror height is related to the initial pitch angle of the particle orbit, in the sense that particles with small initial pitch angles should mirror at a smaller height than particles with an initial pitch angle close to $90°$. We try to incorporate this feature into our simple model mathematically by assuming that the initial length between the loop apex and the mirror point (mirror length, l_{mirror}) is given by the relation

$$l_{mirror} = K_m f(\theta_{init}).$$

Here K_m is a constant and $f(\theta_{init})$ is a function describing the dependence of the mirror length upon the initial pitch angle θ_{init}. It is natural to assume that particle orbits whose initial pitch angle is equal to the initial loss cone angle α_{init}, mirror just at the lower boundary, i.e. for these

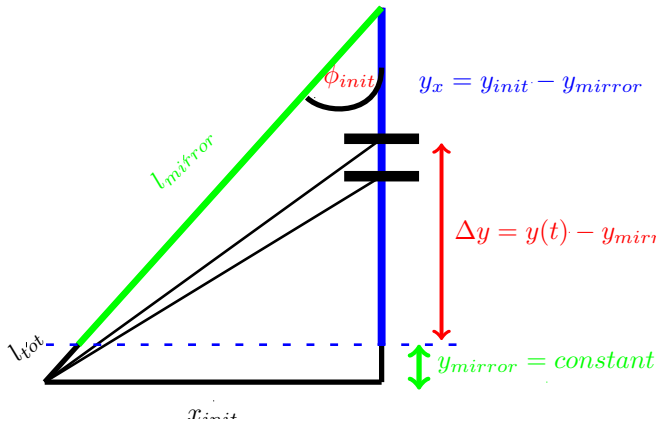

Figure 4.16: Parameters and quantities for the simplified trap model.

orbits

$$l_{tot} = K_m f(\alpha_{init}),$$

where l_{tot} is the total length of a field line from the apex to the foot point at the initial time. Rearranging this equation gives,

$$\begin{aligned} & K_m &=& \frac{l_{tot}}{f(\alpha_{init})} \\ \Rightarrow \qquad & l_{mirror} &=& \frac{l_{tot}}{f(\alpha_{init})} f(\theta_{init}). \end{aligned} \tag{4.15}$$

This still leaves the fact function $f(\theta_{init})$ to be chosen. It has to have the property that it should vanish for $\theta_{init} = 90°$ (particle orbit does not move in the parallel direction) and becomes large for θ_{init} close to $0°$ or $180°$. In order to satisfy these requirements we choose $f(\theta) = \cot^q(\theta_{init})$, where q is the power of the function. For our investigations we choose $q = 0.1$ in oder to give a small mirror height y_{mirror} (see Appendix C.3 for details). We will discuss the properties of this function for this model later. Eqn. 4.15 then becomes

$$l_{mirror} = \frac{l_{tot}}{\cot^q(\alpha_{init})} \cot^q(\theta_{init}). \tag{4.16}$$

From the geometry, (see Fig. 4.16) the total length of the trap l_{tot} is related to the initial trap height y_{init} through

$$l_{tot} = \frac{y_{init}}{\cos(\phi_{init})},$$

where the angle between the initial direction of the field line and the normal to the mirror surface is ϕ_{init}.

Substituting this into Eqn. 4.16 gives,

$$l_{mirror} = \frac{y_{init}}{\cos(\phi_{init})} \frac{\tan^q(\alpha_{init})}{\tan^q(\theta_{init})},$$

where y_{init}, $\tan^q(\theta_{init})$, $\tan^q(\alpha_{init})$ and $\cos(\phi_{init})$ are all initial parameters at the start. From Fig. 4.16

$$\cos(\phi_{init}) = \frac{y_x}{l_{mirror}}, \tag{4.17}$$

where $y_x = y_{init} - y_{mirror}$. Substituting this expression and Eqn. 4.16 into Eqn. 4.17 and rearranging for the mirror height gives,

$$\begin{aligned} y_{mirror} &= y_{init} - y_{init} \frac{\cot^q(\theta_{init})}{\cot^q(\alpha_{init})} \\ &= y_{init} \left[1.0 - \frac{f(\theta_{init})}{f(\alpha_{init})} \right] = \text{constant}. \end{aligned} \tag{4.18}$$

When $f(\theta_{init}) = f(\alpha_{init})$ then the mirror height becomes zero and the particle orbit will leave the trap.

For the purpose of our investigation we will choose initial pitch angles larger than the α_{init}. Using the geometry from Fig. 4.16, the equation for the evolution of ϕ is

$$\tan(\phi_t) = \frac{x_{init}}{y(t)}, \tag{4.19}$$

and for completeness the evolution of x_t, the x-component of the mirror position, is given by

$$x_t = \Delta y \tan(\phi_t) = (y(t) - y_{mirror}) \tan(\phi_t).$$

Generally with decreasing $y(t)$, ϕ_t will increase leading to x_t increasing. For the purpose of our calculations since we assume for simplicity the foot points remain constant, x_t remains constant.

4.5.4 Evolution of Magnetic Field $B(t)$

Our choice for the magnetic field $B(t)$ is an exponentially increasing model of the form

$$B(t) = B_\infty - B_0 e^{-t/\tau}. \tag{4.20}$$

B_∞ is the final magnetic field strength at $t \to \infty$, and τ is the free parameter which effects the rate of decay called the e-folding time. For a starting time of $t = 0$ Eqn. 4.20 gives

$$B_{start} = B(0) = B_\infty - B_0 \equiv \Delta B_0. \tag{4.21}$$

For $t \to t_f$, the final time we stop the simplified model calculation

$$B(t_f) = B_\infty - B_0 e^{-t_f/\tau} \equiv \Delta B_\infty. \tag{4.22}$$

Subtracting Eqn. 4.21 from 4.22 gives

$$\begin{aligned} -B_0 e^{-t_f/\tau} + B_0 &= \Delta B_\infty - \Delta B_0, \\ B_0 &= \frac{\Delta B_\infty - \Delta B_0}{1 - e^{-t_f/\tau}}. \end{aligned} \tag{4.23}$$

Substituting the above equation for B_0 into Eqn. 4.21 gives,

$$B_\infty = \Delta B_0 + \frac{\Delta B_\infty - \Delta B_0}{1 - e^{-t_f/\tau}}. \tag{4.24}$$

Finally substituting Eqn. 4.24 into Eqn. 4.20 gives

$$\begin{aligned} B(t) &= \Delta B_0 + \frac{\Delta B_\infty - \Delta B_0}{1 - e^{-t_f/\tau}} - \frac{\Delta B_\infty - \Delta B_0}{1 - e^{-t_f/\tau}} e^{-t/\tau}, \\ &= \Delta B_0 + \frac{\Delta B_\infty - \Delta B_0}{1 - e^{-t_f/\tau}} \left(1 - e^{-t/\tau}\right). \end{aligned} \tag{4.25}$$

Generally speaking this is the expression for the evolution of the magnetic field where $t_f \to \infty$ makes the denominator in the expression tend to one and $\Delta B_\infty = B_\infty$. In our model we choose $B_{start} = 5$G, $B_\infty = 50$G, $B_0 = 45$G and $B_{fp} = 100$G. The magnetic field for the first two simple models (model 1 and model 2) discussed in the next section are described by the above equation.

The magnetic field in the final model (model 3) is given by

$$B(t) = B_L \sin^2 \left\{ \frac{\pi}{2} \left[1 - e^{-t/t_I} \right] \right\}, \tag{4.26}$$

taken from Aschwanden (2004a) with slight modification to match our simplified model features. Since the magnetic field strength at $t = 0$ is B_{start} and as $t \to \infty$ we have $B(t) \to B_\infty$, this gives

$$B(t) = (B_\infty - B_{start}) \sin^2 \left\{ \frac{\pi}{2} \left[1 - e^{-t/\tau} \right] \right\} + B_{start}, \tag{4.27}$$

4.5.5 Loop Top Velocity V_{LT} and Pitch Angle θ

Once the apex magnetic field strength $B(t)$ at the loop top is known as a function of time, one can calculate the evolution of the loss cone, $\alpha(t)$, and the evolution of the pitch angle, $\theta(t)$. Note that we determine $\theta(t)$ only when a particle has just bounced off the field line apex. Noting that

$$\tan\theta = \frac{v_\perp(t)}{v_\parallel(t)},$$

we can use the invariance of magnetic moment μ to find $v_\perp(t)$ in terms of the initial conditions and $B(t)$,

$${v_\perp}^2 = \frac{B(t)}{B(t_{init})}{v_{\perp 0}}^2.$$

Hence,

$$\theta_t = \tan^{-1}\left\{\frac{\sqrt{\frac{B(t)}{B(t_{init})}}v_{\perp 0}}{v_\parallel(t)}\right\} \tag{4.28}$$

where $v_\parallel(t)$ is calculated using the procedure detailed in Appendix C.1, through defining a loop top velocity V_{LT}. For the three simplified models we will consider, the simplest function for V_{LT} is chosen to be a constant in time for model 1 and for the other two models an exponentially decreasing function i.e.

$$V_{LT} = v_0 e^{-t/t_v}, \tag{4.29}$$

where v_0 is the initial loop top velocity and t_v is the time scale on which V_{LT} drops off.

In summary the simplified model hence has the following ingredients:

- the loop top velocity $V_{LT}(t)$, which has to be specified as a function of time,
- the loop top magnetic field strength $B(t)$, which has to be specified as a function of time,
- the initial height of the loop top y_{init},
- the height of the mirror points y_{mirror}, which is assumed to be constant,
- the position of the foot points x_{init}, which is also assumed to be constant; this will be set indirectly by specifying the initial angle ϕ_{init} of the particle orbit with the vertical.

We also have to specify conditions for the initial velocity v_{init} and the initial pitch angle θ_{init}. The equations for these quantities discussed above can in general be solved iteratively and the

mathematical description is given in Appendix C.1. As an example the time step for the first simple model (model 1), which will be discussed in the next section is calculated analytically in Appendix C.2.

Guided by our CMT model discussed in Section 2.2 we generally want $V_{LT}(t)$ to be a function which decreases with time and has an asymptotic value of zero and $B(t)$ to be an increasing function of time with an asymptotic value of B_∞, say. We remark that our CMT model, as already mentioned before has both properties for large times, but $B(t)$ is not necessarily monotonically increasing. We will, however, try to keep our simplified approach as simple as possible and hence did not choose to include this property into our analysis. To avoid making any conclusions based on just one choice of $V_{LT}(t)$ and $B(t)$ we investigated three different combinations. We remark that while we have tried to pick initial conditions and parameter values in such a way that the results resemble the numerical values of the particle orbits calculated in the kinematic MHD CMT model shown in section 4.3, one can only expect to recover the general behaviour of quantities like the pitch angle or the parallel and perpendicular velocity components in a qualitative way and one should not expect a numerically accurate representation of the full orbit calculations.

4.6 Different Combinations of the Simplified Model

For our first combination (model 1) we make the simplest possible choice for $V_{LT}(t)$, which is to set it equal to a constant. To satisfy the condition that the asymptotic value of $V_{LT}(t)$ as $t \to \infty$ should be zero, we assume that $V_{LT}(t)$ drops to zero at a finite time t_{stop}. In practice we actually set $V_{LT}(t) = 0$ when the field line apex has decreased below a fixed height y_{min}, where $y_{min} > y_{mirror}$. For this $V_{LT}(t)$ one can actually solve the algebraic equations presented in Appendix C.1 analytically. This choice for $V_{LT}(t)$ is combined with a $B(t)$ for which we have chosen an exponentially increasing model (Eqn. 4.20). The mirror height is determined from the initial pitch angle according to Eqn. 4.18. For this combination and the other simplified models $f(\theta) = \cot^{0.1}\theta$ is used. This function is chosen in order to keep the mirror height as small as possible (see Appendix C.1, Section C.3 for more detail).

Some results for model 1 are shown in Fig. 4.17. The values and parameters picked for this case were $y_{init} = 4.2L$, $\phi_{init} = 15°$, $B_{start}/B_{fp} = 0.05$, $B_{final}/B_{fp} = 0.5$, $\tau = 0.4T$ and $V_{LT}(t) = -4L/T$. If we choose the same normalisation as used by Giuliani et al. (2005) with $L = 10^7$ m and $T = 100$ s, we get $\tau = 40$ s and $V_{LT}(t) = -400$ km/s. The magnetic field ratios imply that the initial loss cone angle has a value of $12.9°$ and that the asymptotic loss cone angle is approximately $45°$.The time evolution of the pitch angle at the field line apex compared to the loss cone angle is shown in Fig. 4.17 on the left hand column for three different initial pitch angles with values of $22°$, $23°$ and $24°$. We selected these three values, because they straddle the

critical initial pitch angle which divides trapping and escape for this particular simplified model. In all three cases we start with a pitch angle that is greater than the initial loss cone angle, but in the case of $\theta_{init} = 22°$ the curve of the pitch angle crosses into the loss cone, which means escape, whereas in the two other cases the pitch angle curves remain above the loss cone angle curve, albeit only very slightly in the case of $\theta_{init} = 23°$. One can see that the pitch angle initially increases, but then reaches a maximum and starts to decrease (this might be difficult to see in Fig. 4.17, but one can check this numerically). This is the effect of V_{LT} being non zero initially and thus Fermi acceleration becomes dominant at some point in this initial stage. After V_{LT} drops to zero, betatron acceleration takes over and the pitch angle curves start increasing again.

The column on the right in Fig. 4.17 shows the time evolution of the parallel (black) and perpendicular velocities (blue) at the field line apex. The parallel velocity shows an initial increase during the time when V_{LT} is non-zero and after that it is constant. The perpendicular velocity increases on a longer time scale as it is only affected by the increase in magnetic field strength. Despite the extreme simplification of the acceleration process in this model both sets of the figures in the left and right hand column in Fig. 4.17 show features which are qualitatively similar to the features seen in Fig. 4.10. While this is reassuring let us first see whether this will be corroborated by the other two simplified models that we investigated.

For model 2 the same magnetic field as in model 1 is used. The only change is made to the loop top velocity V_{LT} where it is described by an exponentially decreasing function i.e.

$$V_{LT} = v_0 e^{-t/\tau_v}, \tag{4.30}$$

where v_0 is the initial loop top velocity and τ_v is the time scale on which V_{LT} drops off (see Appendix C.1 for details of this model). This time scale does not need to be the same as the time scale τ on which $B(t)$ increases (see Eqn. 4.20). We have chosen $\tau_v = 0.144T$ and $\tau = 0.25T$ (corresponding to 14.4 seconds and 25 seconds in the Giuliani et al. (2005) normalisation). All initial conditions and the magnetic field ratios as well as ϕ_{init} have been chosen to remain the same as model 1. Since the loop top velocity is now exponentially decreasing, v_0, the initial velocity is chosen to be higher than the constant velocity in case one with $v_0 = -10L/T$, i.e. -1000 km/s for the initial velocity. The results for this case are shown in Fig. 4.18. As in model 1, we show the plots for cases with initial pitch angles close to the critical pitch angle and straddle the critical initial pitch angle which divides trapping and escape. The range of pitch angles for model 2 are $\theta_{init} = 26°, 27°$ and $28°$. The values for the initial pitch angle differ from the values in model 1, because the time evolution for model 2 differs from model 1. In model 2 the magnetic field evolves much slower than model 1. Qualitatively, however similar features as seen in the full orbit calculations are present, with e.g. $v_{\|}$ showing a stronger increase at the beginning when V_{LT} is large and then it levels off.

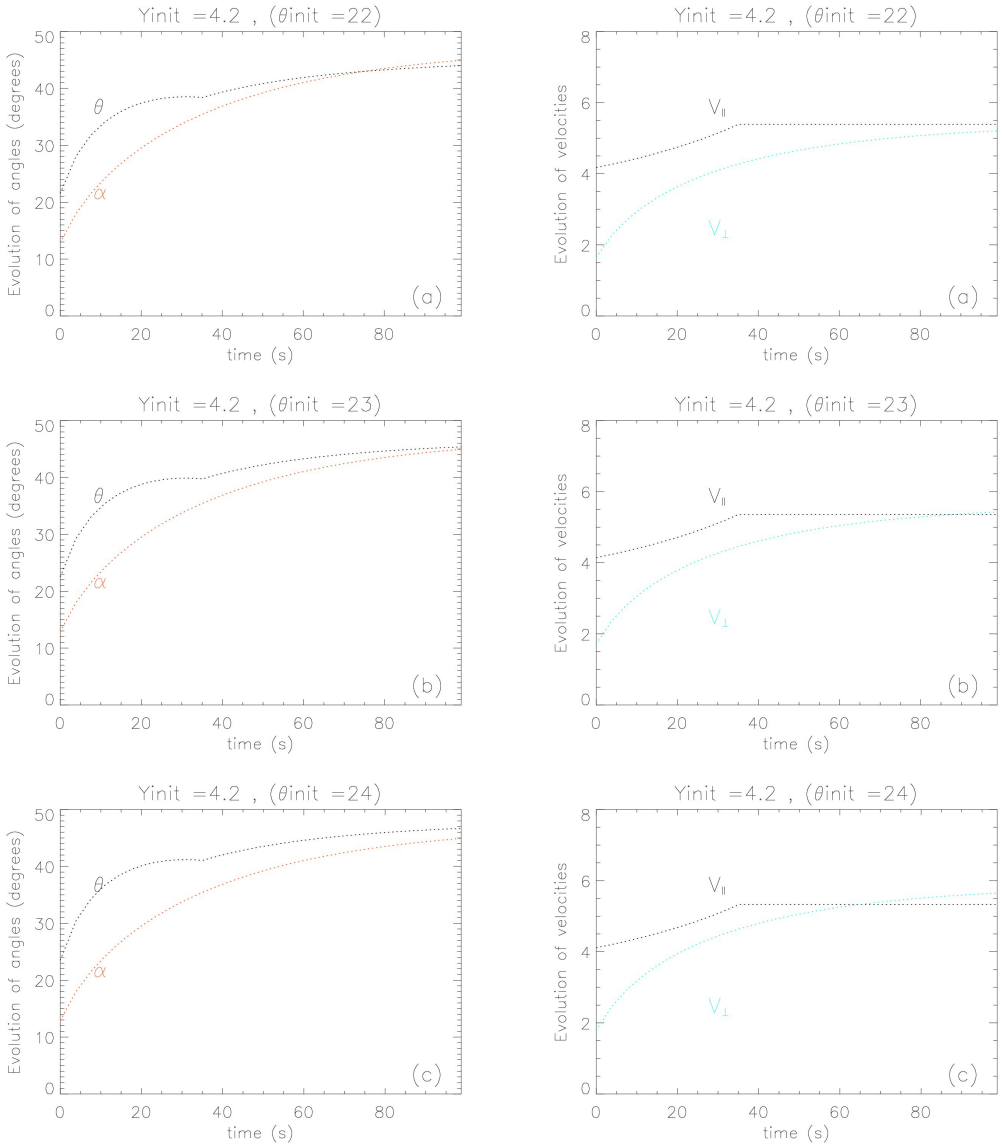

Figure 4.17: *Left*: Evolution of loss cone α (red) and pitch angle θ (black) for a simplified CMT acceleration model (model 1) with constant loop top velocity $V_{LT}(t)$. For these set of results the function $f(\theta_{init}) = \cot^{0.1}(\theta_{init})$. Shown are the results for three different starting pitch angles θ_{init} close to the critical initial pitch angle. One can see that Fermi acceleration dominates at some point in the initial phase and the pitch angle after an initial increase, begins to decrease until the loop top motion is set to zero. At this point betatron acceleration starts dominating and the pitch angle increases. *Right*: Time evolution of $v_{\perp}$ (blue) and $v_{||}$ (black) for simplified model 1. The result for three different initial pitch angles θ_{init} close to the critical initial pitch angle are shown. One can see that the parallel velocity increases in the initial phase while the loop top moves and stays constant after the loop top stops moving.

For the third and final simplified model, the function for V_{LT} and $B(t)$ are taken from Aschwanden (2004a), but with slight modifications to match our simplified model features. In particular,

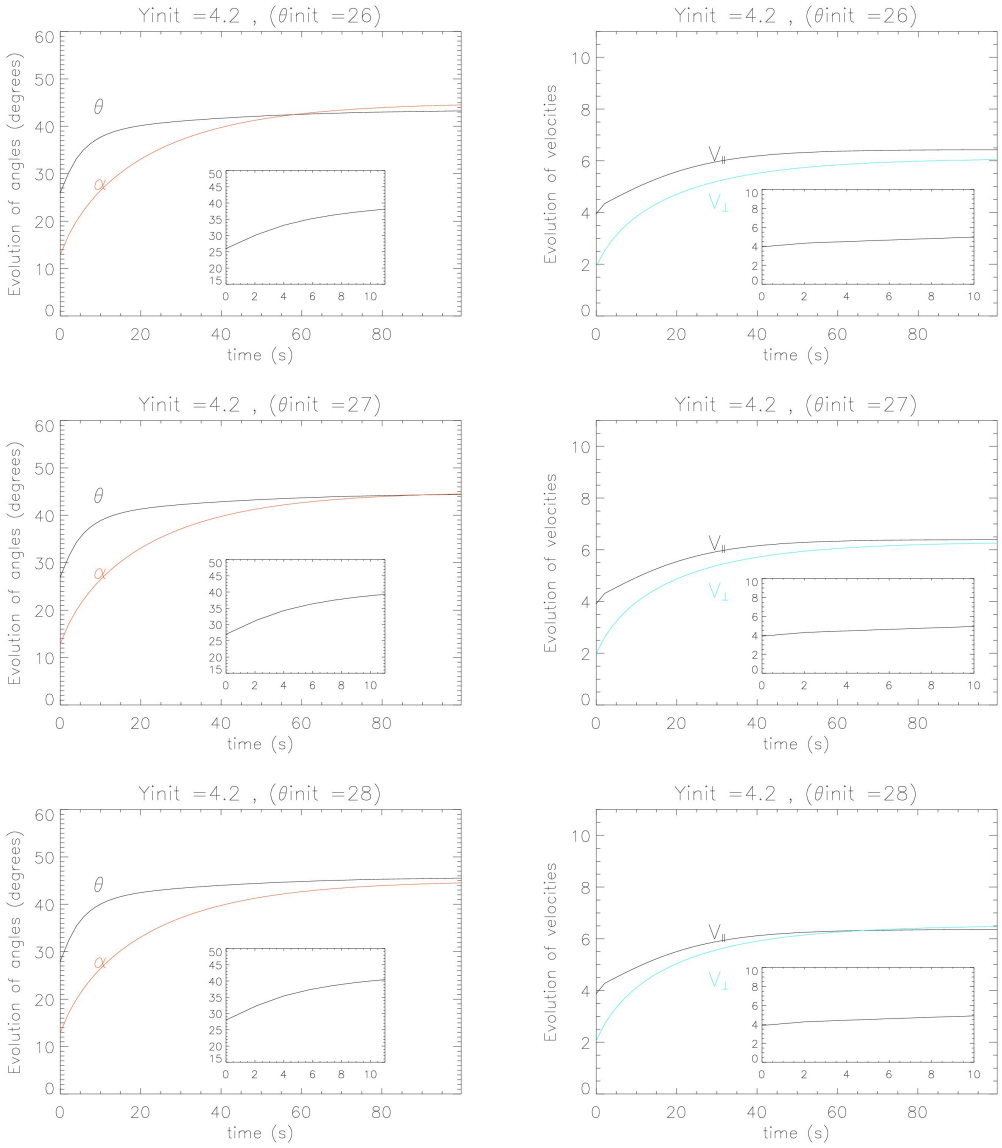

Figure 4.18: Evolution of the loss cone α and the the pitch angle θ for different starting pitch angles θ_{init} (model 2). For these set of results the function $f(\theta_{init}) = \cot^{0.1}(\theta_{init})$. The evolution of the loss cone α (red) and the pitch angle θ (blue) for an exponentially decreasing loop top velocity V_{LT} are shown in the left hand column. The insets for the plot on the left show the evolution of pitch angle. Contrary to model 1 Fermi acceleration does not dominate at any time in this case and the pitch angle curves are always increasing. Betatron acceleration is always present in this case. The column of the right shows the evolution of $v_{\perp}$ (blue) and $v_{\parallel}$ (black). The insets show magnifications of the initial phase of the time evolution of $v_{\parallel}$. One can see that while $v_{\parallel}$ increases in the initial phase of the time evolution it does not increase fast enough to cause a decrease in the pitch angle.

we assume that the asymptotic $B(t)$ as $t \rightarrow \infty$ will be smaller than the foot point field strength, whereas Aschwanden (2004a) assumes that they are the same, implying that the asymptotic loss cone angle approaches 90°. We also start with a finite magnetic field strength, whereas Aschwan-

den starts his model at a vanishing magnetic field strength at a null point in a reconnection region. In practice we can simply start the model equations at a finite time $t > 0$ to avoid the vanishing magnetic field strength. However, we make a slight modification to the magnetic field model where the loop top $B(t)$ is given by

$$B(t) = (B_\infty - B_{start}) \sin^2 \left[\frac{\pi}{2} (1 - e^{-t/\tau}) \right] + B_{start}, \tag{4.31}$$

so that the magnetic field strength at $t = 0$ is B_{start} and as $t \to \infty$ we have $B(t) \to B_\infty$. We choose the same magnetic field ratios as for the two previous cases and also keep τ_v and τ the same as in case two. The loop top velocity V_{LT} in Aschwanden's model has the same form as Eqn. 4.30. Similarly, all other parameters and initial conditions remain unchanged. The results for model 3 are shown in Fig. 4.19, where the three values $\theta_{init} = 27°$, $28°$ and $29°$ have been chosen such that they are in the region close to the critical initial pitch angle which is very close to $28°$. In this case, due to the modification made to the evolution of $B(t)$ there is an initial decrease in the pitch angle before it starts to increase in the later stages of the evolution. This is similar to what is seen in model 1. For model 2 the time evolution of the pitch angle differs because the magnetic field strength $B(t)$ increases exponentially from $t = 0$. Further investigations show that when the magnetic field time scale is increased, plots showing an initial decrease in pitch angle can be produced for this case. The third model again shows very similar qualitative features to the guiding centre orbit calculations and to the other two simplified models discussed. In particular these findings seem to corroborate that there is a critical initial pitch angle below which particle orbits escape and above which particle orbits are trapped in a CMT. This critical initial pitch angle has a value which is greater than the initial loss cone angle, but smaller than the asymptotic loss cone α_∞ and does vary from field line to field line as seen from numerical results in Table 4.3. We have also seen that Fermi acceleration may be dominating in the initial phases of the particle orbit, but it is betatron acceleration that will take over at some point in time and thus generally the pitch angle of the particle will increase with time. Hence, as a concluding remark, Fermi and betatron acceleration in realistic CMT models will generally occur simultaneously and cannot be treated separately which is a statement also corroborated by others like Karlický and Bárta (2006).

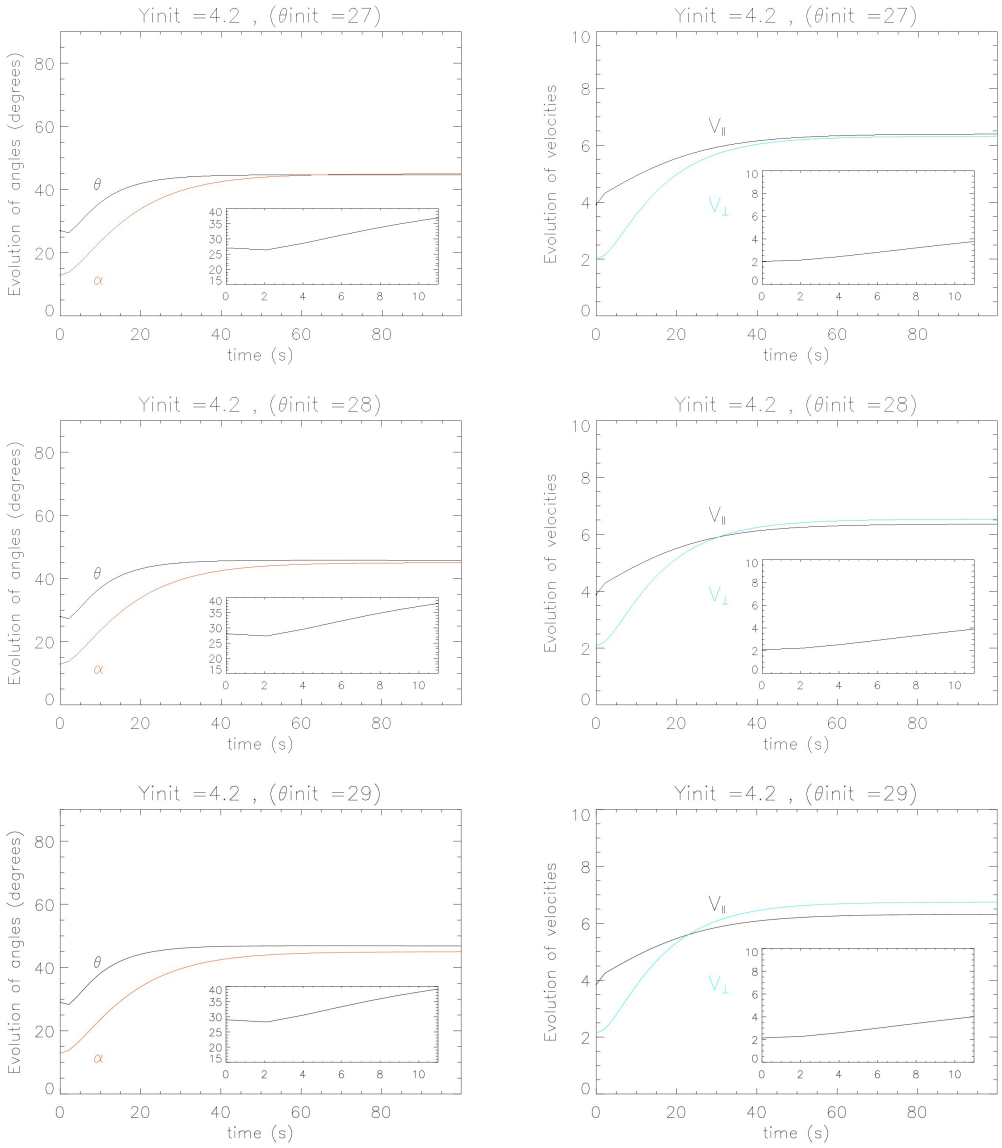

Figure 4.19: Evolution of the loss cone α and the the pitch angle θ for different starting pitch angles θ_{init} (model 3). For these set of results the function $f(\theta_{init}) = \cot^{0.1}(\theta_{init})$. The evolution of the loss cone α (red) and the pitch angle θ (blue) for an exponentially decreasing loop top velocity V_{LT} are shown in the left hand column. The insets for the plot on the left show the evolution of pitch angle for an exponentially decreasing loop top velocity V_{LT}, but a modified $B(t)$ (see main text for details). One can see that initially the pitch angle decreases which can be attributed to the slower increase of the loop top magnetic field (compared to model 2). After all, betatron acceleration starts to dominate and the pitch angle increase with time. The column on the right shows the evolution of $v_\perp$ (blue) and $v_\parallel$ (black). The insets show magnifications of the initial phase of the time evolution of $v_\perp$. In this case the $v_\parallel$ time evolution is exactly the same as in model 2, but $v_\perp$ does not increase much in the initial phase, hence leading to a decrease in the pitch angle.

4.7 Discussion and Conclusions

We have presented a detailed investigation of the conditions which affect the trapping and escape of particle orbits in models of collapsing magnetic traps, starting with the investigation of guiding centre orbit calculations in the kinematic MHD CMT model of Giuliani et al. (2005). Based on the results of our investigations and on observations made previously by Giuliani et al. (2005) and Grady et al. (2012), we designed a simplified schematic model for CMT particle acceleration and studied three different implementations of this schematic model, which all qualitatively corroborated our findings from the guiding centre orbit calculations.

In the models by Aschwanden (2004a) and Somov (2004) the final magnetic field strength was the same as the foot point magentic field strength. This resulted in an asymptotic loss cone, $\alpha_\infty = 90°$, leading to all the particles escaping which could give an explanation for foot point emissions seen in flares. However in our model and other more sophisticated models,(e.g. Giuliani et al., 2005; Karlicky and Barta, 2006; Minoshima et al., 2010; Grady et al., 2012), the final magnetic field strength is smaller than the foot point field strength, leading to a $\alpha_\infty < 90°$. This increases the probability of particles being trapped, which is what we and the other more sophisticated models listed above find, which might be able to give an explanation to emissions originating higher up in the corona (see e.g. Krucker et al., 2008). The trapping and escape mechanisms depend on how the pitch angle of the particle orbits evolves relative to the loss cone angle in the CMT, which is a feature we studied in detail in this chapter and it is a point neglected by Aschwanden (2004a). One of the other assumptions in Somov (2004) is that all particles travel the full length of the field lines per bounce period. In our case however, particles that tend to travel to the foot points are lost from the trap. Also, it was found by Giuliani et al. (2005) that the mirror force $= \mu \frac{\partial B}{\partial s}$ which causes the confinement of the particle between bounce points does not affect the particle acceleration process as such. It is the other terms in the guiding centre equation that are the dominating acceleration terms, namely, the curvature terms in the parallel equation of motion (see Chapter 3 Section 2.2 for equation). Somov (2004) neglects the curvature of the magnetic field lines and therefore, is able to look a the two main acceleration mechanism separately. However, these two mechanisms are linked together though the curvature terms in the parallel equation of motion (Northrop, 1963) as confirmed by Giuliani et al. (2005).

In our study we made sure we implemented the assumptions of (i) $\alpha_\infty < 90°$, (ii) invariance of magnetic moment and evolution of $\theta(t)$ in relation to $\alpha(t)$ and (iii) curvature of the magnetic field lines. Our findings are as follows: (a) we showed that for each magnetic field line in a collapsing magnetic trap there is a critical initial pitch angle, which divides particle orbits into trapped orbits and escaping orbits. Furthermore, we checked to see if this angle depends on the starting energy of the particle and found that it does not. This critical initial pitch angle is greater than

the initial loss cone angle for the field line, but smaller than the value of the asymptotic loss cone angle for the field line as $t \rightarrow \infty$ (see Fig. 4.14). (b) For orbits with initial pitch angle close to the critical value, Fermi acceleration can dominate in the initial phases, but betatron acceleration will take over and become the dominating acceleration mechanism. In the periods where Fermi acceleration dominates over betatron acceleration, the pitch angle will decrease and when betatron acceleration dominates the pitch angle will increase. (c) Due to the nature of more complete CMT models, both mechanisms will always operate simultaneously (as already stated by Karlický and Bárta, 2006), but the efficiency of Fermi acceleration has to decrease on a particular field line during the time evolution of a CMT because the motion of the field line must slow down. On the other hand, the magnetic field strength can still continue to increase due to the pile-up of magnetic flux from above.

In this chapter for simplicity, we have excluded the possibility of either Coulomb collisions, wave-particle interactions or turbulence on the trapping or escape of particles from CMTs. Obviously, each of these mechanisms may change the results we have found in this chapter. The effect of Coulomb collisions on particle acceleration in simple CMT models has been considered by Kovalev and Somov (2003), Karlický and Kosugi (2004) and Bogachev and Somov (2009). Minoshima et al. (2011) have investigated the effects of pitch angle scattering by Coulomb collisions on trapping and escape, but without considering the effect of dynamical friction and Karlický and Bárta (2006) included the effects of Coulomb collisions in their MHD model of a CMT. We will present the results of an initial study into the introduction of Coulomb collisions into the Giuliani et al. (2005) model in Chapter 6.

Chapter 5

Application of the CGL Double-Adiabatic Theory in a CMT Model

So far we have looked at individual particle orbits and neglected any collective phenomena in the CMT. In this chapter, we use the kinematic MHD model of Giuliani et al. (2005) to investigate how the parallel pressure $P_{\|}$, the perpendicular pressure $P_{\perp}$ and the plasma density ρ evolve under the assumptions that their time evolution is determined by the CMT model. To make this possible further assumptions are needed which will be discussed below.

It should be emphasised that the kinematic CMT model was not intended to be used for such a calculation and hence we are stretching the limits of its validity considerably. In particular, we do not include any back reaction of the pressure force onto the dynamics of the CMT, because we do not solve the momentum equation, i.e. the time evolution of the plasma quantities mentioned above remains kinematic.

The time evolution of the plasma density is determined by the continuity equation, but in order to determine the time evolution of the plasma pressure one needs further equations. Due to the nature of the CMT collapse, we have included the possibility of an anisotropic plasma pressure, with different pressures in the direction perpendicular ($P_{\perp}$) and parallel ($P_{\|}$) to the magnetic field. To describe the time evolution of $P_{\perp}$ and $P_{\|}$ we will use the double-adiabatic theory put forward by Chew, Goldberger and Low (CGL Theory, Chew et al., 1956). We emphasise that this again is a very strong assumption due to the properties of the CGL theory, e.g. that the heat flux is completely neglected. Nevertheless, using this theory can give a first indication of how the plasma could evolve in our CMT model. In a plasma with an anisotropic pressure, instabilities can arise. We will check in particular the conditions for the fire-hose and mirror instability as derived under the assumptions of the double-adiabatic theory.

As said above, in order to look at the evolution of the plasma quantities $P_{\|}$, $P_{\perp}$ and ρ using the Giuliani et al. (2005) magnetic trap model a few simplified assumptions/hypotheses are made. The main one is the use of the double-adiabatic theory. To arrive at this theory, heat flux is neglected.

The pressure tensor is assumed to be of the form

$$P = \begin{pmatrix} P_\perp & 0 & 0 \\ 0 & P_\perp & 0 \\ 0 & 0 & P_\parallel \end{pmatrix}. \tag{5.1}$$

$P_\perp$ and $P_\parallel$ are the pressure components perpendicular and parallel to the magnetic field respectively. Under the assumptions made in the CGL theory the evolution of perpendicular and parallel pressure components, $P_\perp$ and $P_\parallel$, respectively, are given by the two CGL double-adiabatic equations of state:

$$\frac{D}{Dt}\left(\frac{P_\perp}{\rho B}\right) = 0, \tag{5.2}$$

and

$$\frac{D}{Dt}\left(\frac{P_\parallel B^2}{\rho^3}\right) = 0, \tag{5.3}$$

where $\frac{D}{Dt}$ represents the convective derivative, ρ is the density of the plasma and B is the magnetic field strength. A parallel can be drawn between the double adiabatic conditions, Eqns. 5.2 and 5.3, and the adiabatic invariants, μ_B and J of the particle orbit (see e.g. Boyd and Sanderson, 2003, for discussion). Since $\mu = \frac{mv_\perp^2}{2B}$ remains constant, $B \propto \frac{<v_\perp>^2}{2}$. From Eqn. 5.2, $\frac{P_\perp}{\rho B} = C_1$, where C_1 is the constant of integration. Therefore $\frac{P_\perp}{\rho} \propto B$. Substituting for B gives

$$\frac{P_\perp}{\rho} \propto \frac{<v_\perp^2>}{2}$$

where the brackets denote an average over all the particles in the fluid element. Eqn. 5.2 can be seen as a macroscopic representation of the invariance of μ_B. For the second adiabatic invariant, J, we treat the fluid element as a flux tube and use the result from ideal MHD that the length of a flux tube, $l \propto \frac{B}{\rho}$. From Eqn. 5.3, $\frac{P_\parallel B^2}{\rho^3} = C_2$ which gives $P_\parallel B^2 \propto \rho^3$. Since $B^2 \propto l^2\rho^2$ this gives

$$\begin{aligned} P_\parallel l^2 \rho^2 &\propto \rho^3, \\ P_\parallel l^2 &\propto \rho, \\ P_\parallel &\propto \frac{\rho}{l^2}. \end{aligned}$$

Since $J = \oint p_\parallel dl$, the integral over one whole period of bouncing of the parallel momentum ($p_\parallel$) of the whole path, $< v_\parallel^2 > \propto \frac{1}{l^2}$. Replacing l in the above equation gives,

$$P_\parallel \propto < \rho v_\parallel^2 > .$$

Substituting for B using $B^2 \propto l^2\rho^2$ and for $P_\parallel$ using the above equation gives

$$\frac{P_\parallel B^2}{\rho^3} \propto <v_\parallel^2> l^2 \propto J^2. \tag{5.4}$$

From this reasoning Eqn. 5.3 can be seen as a macroscopic representation of the invariance of J.

In determining the evolution of the parallel pressure $P_\parallel$ and perpendicular pressure $P_\perp$ from Eqns. 5.2 and 5.3, the behaviour of the magnetic field strength B and the density ρ in the model need to be known. To work out the evolution of the density ρ in the trap, a parallel is drawn with the time evolution of the z-component of the magnetic field B_z from the Eqn. 2.36 in Chapter 3. This could correspond to the mass flux ρ_z through an infinitesimal area remaining constant, i.e.

$$\rho_z J_c = I. \tag{5.5}$$

From 5.5 and the initial condition $J_c = 1$ at $t = t_{init}$, $\rho = \rho_{init}$. It follows that

$$\begin{aligned} I_{init} &= I, \\ \rho_{init} &= \rho J_c. \end{aligned}$$

Rearranging for ρ gives

$$\rho(x, y, t) = J_c^{-1}\rho_{init}(x_\infty(x, y, t), y_\infty(x, y, t), t).$$

Solving of J_c^{-1} for the Giuliani et al. (2005) model gives,

$$\begin{aligned} J_c^{-1}(\mathbf{x}_\infty(\mathbf{x})) &\equiv J_c(\mathbf{x}(\mathbf{x}_\infty)) \\ &= \begin{vmatrix} \frac{\partial x_\infty}{\partial x} & \frac{\partial x_\infty}{\partial y} \\ \frac{\partial y_\infty}{\partial x} & \frac{\partial y_\infty}{\partial y} \end{vmatrix} = \begin{vmatrix} 1 & 0 \\ 0 & \frac{\partial y_\infty}{\partial y} \end{vmatrix} = \frac{\partial y_\infty}{\partial y}. \end{aligned} \tag{5.6}$$

The expression for $\frac{\partial y_\infty}{\partial y}$ is given by Eqn. 4.6 in Chapter 4. Therefore,

$$\rho = \rho_{init}\left(\frac{\partial y_\infty}{\partial y}\right) = \rho_{init} J_c^{-1}, \tag{5.7}$$

or

$$\rho_{init} = \rho\left(\frac{\partial y_\infty}{\partial y}\right)^{-1} = \rho J_c. \tag{5.8}$$

Since the evolution of the magnetic field in the model is known, and the evolution of ρ is given by Eqn. 5.8, we use Eqns. 5.2 and 5.3 to find the evolution of the parallel and perpendicular pressure in the CMT model. For the calculations presented in this chapter, we always start with an isotropic

initial condition, i.e. $P_\parallel = P_\perp$ at the beginning. As a starting point we will first look at the ratio of the parallel pressure to the initial parallel pressure, $\frac{P_\parallel}{P_{\parallel init}}$, the ratio of the perpendicular pressure to the initial perpendicular pressure , $\frac{P_\perp}{P_{\perp init}}$, the ratio of density to the initial density $\frac{\rho}{\rho_{init}}$ and the ratio of the perpendicular to parallel pressure $\frac{P_\perp}{P_\parallel}$ for an initial uniform density ρ_{init}, isotropic initial parallel pressure $P_{\parallel init}$ and isotropic initial perpendicular pressure $P_{\perp init}$. After that we investigate what happens when the initial density is stratified.

5.1 Evolution of $\frac{\rho}{\rho_{init}}$, $\frac{P_\perp}{P_{\perp init}}$, $\frac{P_\parallel}{P_{\parallel init}}$, and $\frac{P_\perp}{P_\parallel}$

Here we investigate the evolution of the ratios $\frac{\rho}{\rho_{init}}$, $\frac{P_\perp}{P_{\perp init}}$, $\frac{P_\parallel}{P_{\parallel init}}$, and $\frac{P_\perp}{P_\parallel}$ in the Giuliani et al. (2005) model. As a starting point we assume the initial density and initial pressures are uniform (i.e. space and time independent). They are all set to a constant and normalised to 1. Analytical expressions for the evolution of the magnetic field are given by Eqns. 4.4 and 4.5 in Chapter 4.

For the calculation we take the x-coordinate to run from $-2L$ to $2L$ and the y coordinate to run from $0L$ to $5L$, where all lengths here are scaled to the fundamental length scale $L = 10$Mm. The initial time is set to $t_{init} = 1.05$ and the final time $t_{final} = 2.0$ just like the particle orbit calculations. We begin by looking at the ratio of $\frac{\rho}{\rho_{init}}$ and also the magnetic field ratio $\frac{B}{B_{init}}$.

5.1.1 Evolution of $\frac{\rho}{\rho_{init}}$

Recalling Eqn. 5.8 as

$$\rho \left(\frac{\partial y_\infty}{\partial y}\right)^{-1} = \rho_{init} \left(\frac{\partial y_\infty}{\partial y}\right)^{-1}_{t=t_{init}}. \tag{5.9}$$

Rearranging Eqn. 5.9 for $\frac{\rho}{\rho_{init}}$ gives

$$\begin{aligned} \frac{\rho}{\rho_{init}} = \frac{\left(\frac{\partial y_\infty}{\partial y}\right)}{\left(\frac{\partial y_\infty}{\partial y}\right)_{t=t_{init}}} &= \frac{J_c}{J_{cinit}}, \\ \rho &= \rho_{init}\frac{J_c}{J_{cinit}}. \end{aligned} \tag{5.10}$$

Therefore, the ratio of density to the initial density is

$$\frac{\rho}{\rho_{init}} = \frac{J_c}{J_{cinit}}. \tag{5.11}$$

In Fig. 5.1 the evolution of $\frac{\rho}{\rho_{init}}$ is shown for a constant initial density ρ_{init} and constant initial

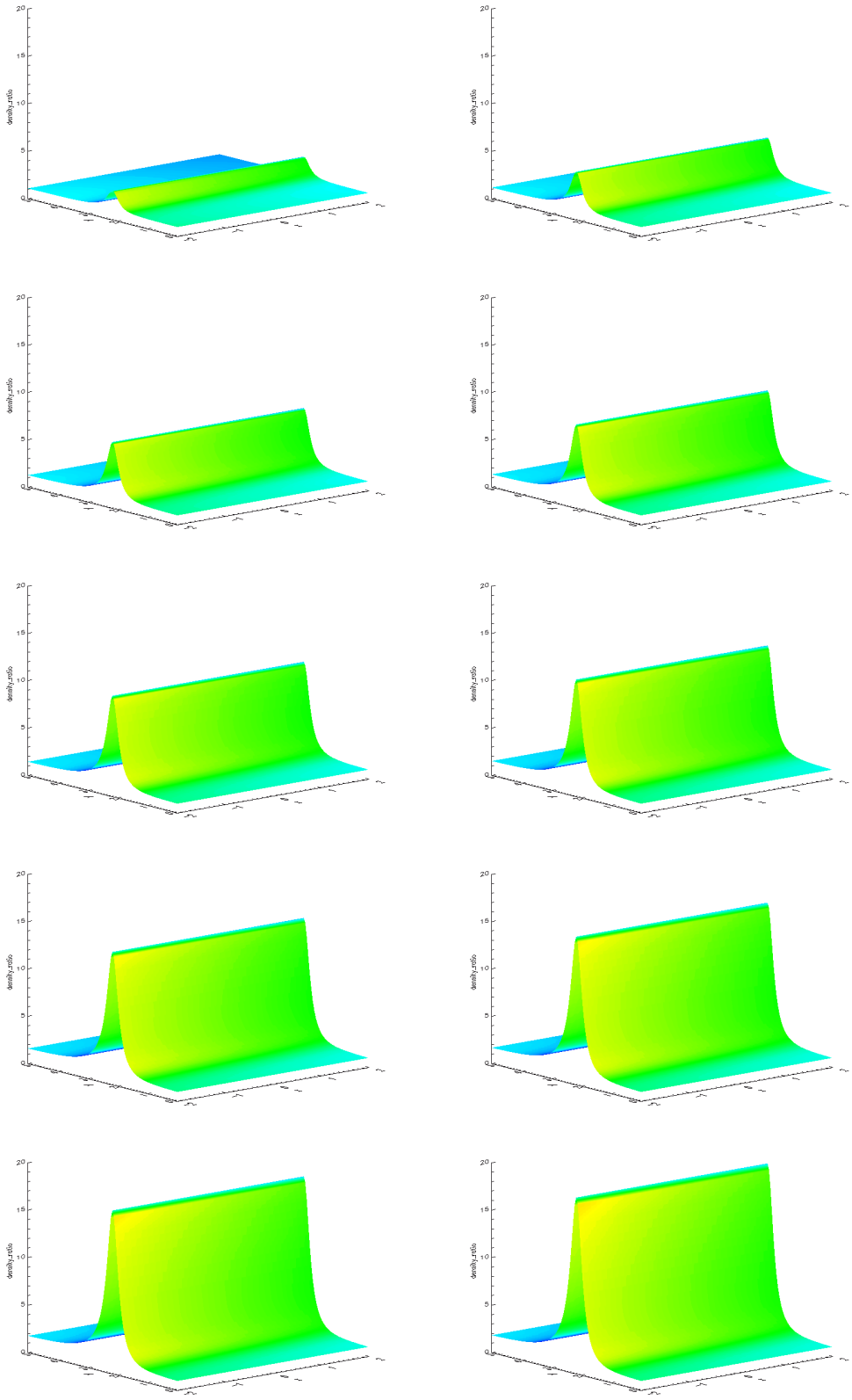

Figure 5.1: Illustrate the evolution of $\frac{\rho}{\rho_{init}}$ where this value rises from 1 to approximately 18.5 between the height $y = 2$ to $y = 3$. The first snapshot (top left) shows the density ratio at $t = 9.5$ seconds and the final figure (bottom right) for $t = 95$ seconds. The density only varies in the y direction and remains constant thought in x from the direct relation to the Jacobian J_c.

pressures, $P_{\parallel init}$ and $P_{\perp init}$. The snapshots in the figure starting from the top left hand corner and going along shows the value of the ratio plotted for every 0.095 (normalised units). Initially the ratio is equal to one and begins to increase particularly along the y direction between $y = 2$ to $y = 3$. The ratio in this region continues to increase until the maximum value of the $\frac{\rho}{\rho_{init}}$ is found to be approximately 18.58. This behaviour of ρ is directly related to the behaviour of the Jacobian $J_c = \frac{\partial y_\infty}{\partial y}$ which has a greater rate of change in the middle of the trap than at the top or bottom, hence the reason for the growth seen in the middle compared to the top and bottom of the trap. The density increases by one order of magnitude during the collapse of the CMT. It is also worth looking at the evolution of the magnetic field ratio $\frac{B}{B_{init}}$ as shown in Fig. 5.2 (the opposite, $\frac{B_{init}}{B}$ is also shown in Fig. 5.3 to aid with the discussions of later quantities). In Fig. 5.2 the snapshots starting from the top left hand corner and going along show the value of the $\frac{B}{B_{init}}$ plotted for every 0.095 (normalised units). Initially the ratio is equal to one and then begins to decrease everywhere except in the middle of the trap. A distinctive peak in the ratio is seen along the y axis just below $y = 2$ and just above $y = 3$ where the highest point is centred at approximately $(x, y) = (0, 2)$. This increase is related to the magnetic field lines piling up as the trap collapses leading to an increase in magnetic field strength. The maximum value of the $\frac{B}{B_{init}}$ is found to be approximately 5.84 with the minimum value being of the order 0.58. As expected the opposite behaviour is seen in Fig. 5.3 where the ratio $\frac{B_{init}}{B}$ decreases in the middle and increases everywhere else. The maximum value at the final time is approximately 1.72 and the minimum value is about 0.17 in the middle of the trap.

5.1.2 Evolution of $\frac{P_\perp}{P_{\perp init}}$

We now look at the behaviour of the perpendicular pressure, $\frac{P_\perp}{P_{\perp init}}$. Using the second constant of motion $C_2 = \frac{P_\perp}{\rho B}$ we have

$$C_2 = C_{2init},$$

$$\frac{P_\perp}{\rho B} = \frac{P_{\perp init}}{\rho_{init} B_{init}}.$$

Rearranging the above equation gives

$$\frac{P_\perp}{P_{\perp init}} = \left(\frac{\rho}{\rho_{init}}\right)\left(\frac{B}{B_{init}}\right). \tag{5.12}$$

It follows that

$$P_\perp = P_{\perp init}\left(\frac{\rho}{\rho_{init}}\right)\left(\frac{B}{B_{init}}\right). \tag{5.13}$$

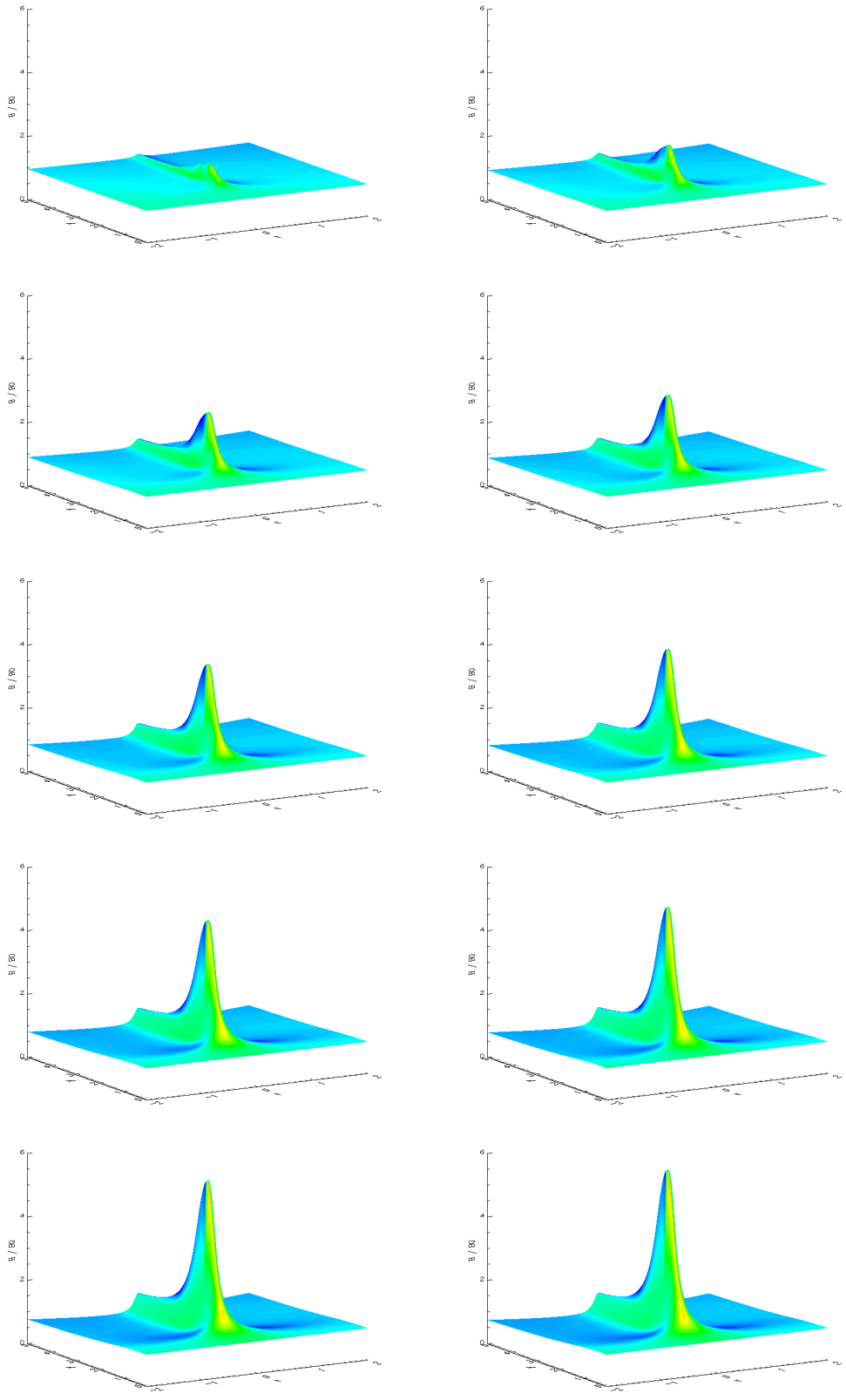

Figure 5.2: Illustrate the evolution of $\frac{B}{B_{init}}$ where it increases from an initial value of 1 to approximately 5.84 between the height $y = 2$ to $y = 3$. The first snapshot (top left) shows the magnetic field ratio at $t = 9.5$ seconds and the final figure (bottom right) for $t = 95$ seconds.

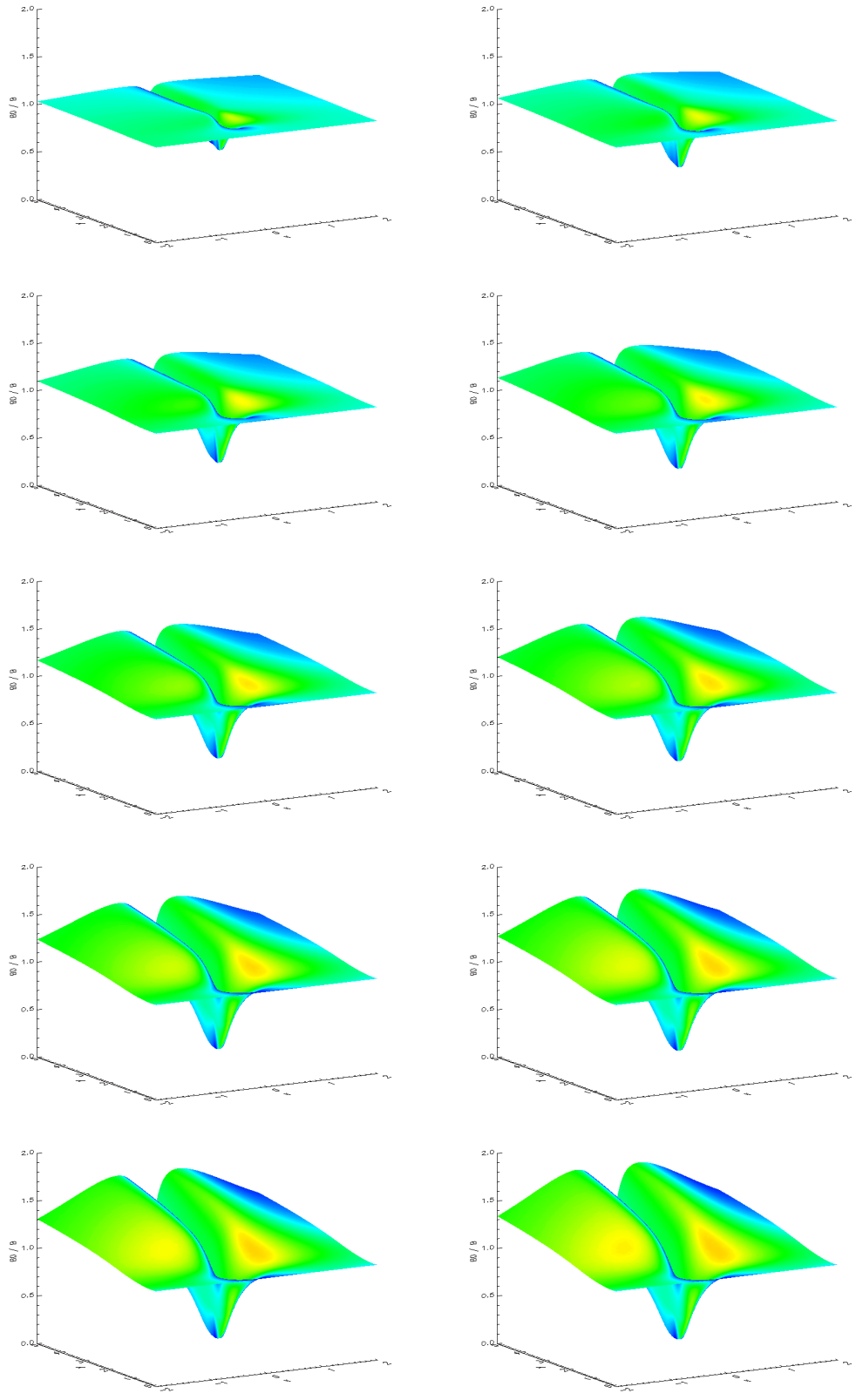

Figure 5.3: Illustrate the evolution of $\frac{B_{init}}{B}$ where it decreases from an initial value of 1 to approximately 0.17 between the height $y = 2$ to $y = 3$. The first snapshot (top left) shows the magnetic field ratio at $t = 9.5$ seconds and the final figure (bottom right) for $t = 95$ seconds where the maximum is recorded to be ≈ 1.72.

The ratio of perpendicular pressure to the initial perpendicular pressure is

$$\frac{P_\perp}{P_{\perp init}} = \left(\frac{\rho}{\rho_{init}}\right)\left(\frac{B}{B_{init}}\right). \tag{5.14}$$

In Fig. 5.4 the evolution of $\frac{P_\perp}{P_{\perp init}}$ is shown for a constant initial density and pressure. Like before the snapshots in the figure starting at the top left hand corner and going along show the value of the ratio for different values of position x and y every 0.095 (normalised units). Starting from an initial ratio of 1, the ratio everywhere seems to remain unchanged except for along the y axis between $y \approx 2$ to $y \approx 3$ and in the centre of the trap from about $x \approx 0$ and $y = 2$ to $y = 5$, with the maximum located at the centre between $y \approx 2$ to $y \approx 3$. The general structure of the figure is a superposition of $\frac{\rho}{\rho_{init}}$ as seen in Fig, 5.1 and the ratio $\frac{B}{B_{init}}$ seen in Fig. 5.2. The overall behaviour for the ratio $\frac{P_\perp}{P_{\perp init}}$ seems to follow the evolution of $\frac{B}{B_{init}}$. The maximum, seen in the centre, corresponds to the maximum seen in Fig. 5.2, which gradually increases, as seen in the figures, reaching its highest value of approximately 106. The region either side of this maximum comes from the behaviour of $\frac{\rho}{\rho_{init}}$. Therefore, the perpendicular pressure increases by up to 2 orders of magnitude during the collapse of the CMT under the assumptions made for our model.

5.1.3 Evolution of $\frac{P_\parallel}{P_{\parallel init}}$

Here we investigate the parallel pressure ratio, $\frac{P_\parallel}{P_{\parallel init}}$ in the magnetic trap model. Making use of the first constant of motion $C_1 = \frac{P_\parallel B^2}{\rho^3}$ and the constant of integration we have

$$\begin{aligned} C_1 &= C_{1init}, \\ \frac{P_\parallel B^2}{\rho^3} &= \frac{P_{\parallel init} B_{init}^2}{\rho_{init}^3}. \end{aligned} \tag{5.15}$$

Rearranging Eqn. 5.15 for the parallel pressure gives

$$\frac{P_\parallel}{P_{\parallel init}} = \left(\frac{\rho}{\rho_{init}}\right)^3 \left(\frac{B_{init}}{B}\right)^2.$$

It follows that

$$P_\parallel = P_{\parallel init}\left(\frac{\rho}{\rho_{init}}\right)^3 \left(\frac{B_{init}}{B}\right)^2. \tag{5.16}$$

The ratio of parallel pressure to the initial parallel pressure is

$$\frac{P_\parallel}{P_{\parallel init}} = \left(\frac{\rho}{\rho_{init}}\right)^3 \left(\frac{B_{init}}{B}\right)^2. \tag{5.17}$$

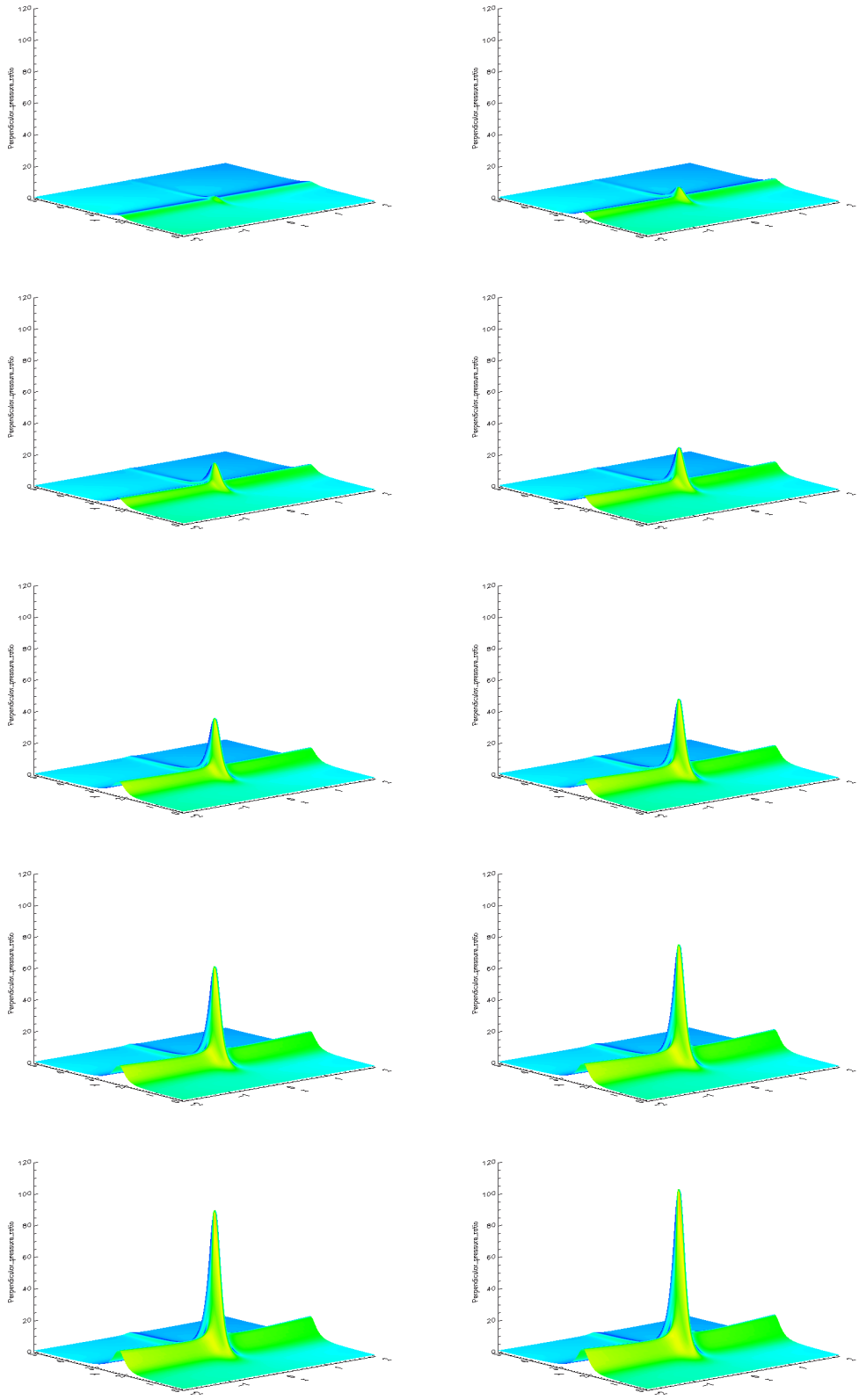

Figure 5.4: Illustrate the evolution of $\frac{P_\perp}{P_{\perp init}}$ where it rises from order of 1 to approximately 106 between the height $y = 2$ to $y = 3$. The general behaviour of the ratio is a superposition of $\frac{\rho}{\rho_{init}}$ and $\frac{B}{B_{init}}$ where the dominating behaviour comes from the magnetic field ratio.

In Fig. 5.5 the evolution of $\frac{P_\parallel}{P_{\parallel init}}$ is shown for a constant initial density and pressure. The snapshots in the figure starting at the top left hand corner and going along show the value of the ratio for different values of position x and y every 0.095 (normalised units). Starting from an initial ratio of 1 (not shown) the ratio everywhere seems to remain unchanged except for along the y axis between $y \approx 2$ to $y = 3$, with a distinctive minimum at the centre of the trap in this region. The general structure of the figure is a superposition of the snapshots for $\frac{\rho}{\rho_{init}}$ in Fig, 5.1 and the snapshots for $\frac{B_{init}}{B}$ seen in Fig. 5.3. The overall behaviour for the ratio $\frac{P_\parallel}{P_{\parallel init}}$ seems to follow the evolution of $\frac{\rho}{\rho_{init}}$. The minimum seen in the centre corresponds to the minimum seen in Fig. 5.3. The maximums either side of the minimum value reaches its highest value of $\approx 1.1 \times 10^4$ at the final time $t_{final} = 2.0$. The continually decreasing slope seen towards -2 and +2 also comes from the magnetic field ratio. Therefore, the parallel pressure increases by up to 4 orders of magnitude during the collapse of the CMT under the assumptions made.

5.1.4 Evolution of $\frac{P_\perp}{P_\parallel}$ and $\frac{P_\parallel}{P_\perp}$

Using the equations of state 5.2 and 5.3 the evolution of the perpendicular and parallel pressure components are calculated in the following way:

$$\frac{D}{Dt}\left(\frac{P_\parallel B^2}{\rho^3}\right) = 0 \quad \Rightarrow \quad \frac{D}{Dt}\left(C_1\right) = 0\,,$$

$$\frac{D}{Dt}\left(\frac{P_\perp}{\rho B}\right) = 0 \quad \Rightarrow \quad \frac{D}{Dt}\left(C_2\right) = 0\,,$$

where

$$C_1 = \frac{P_\parallel B^2}{\rho^3} \quad , \quad C_2 = \frac{P_\perp}{\rho B}.$$

C_1 and C_2 are integration constants. Using these two equations above, the pressure ratio for the perpendicular pressure to the parallel pressure is

$$\frac{P_\perp}{P_\parallel} = \frac{C_2}{C_1}\frac{B^3}{\rho^2}. \tag{5.18}$$

Making use of the fact that C_1 and C_2 will remain constant, we have,

$$C_1 = C_{1init} \quad \Rightarrow \quad C_1 = \frac{P_{\parallel init} B_{init}^2}{\rho_{init}^3},$$

$$C_2 = C_{2init} \quad \Rightarrow \quad C_2 = \frac{P_{\perp init}}{\rho_{init} B_{init}}.$$

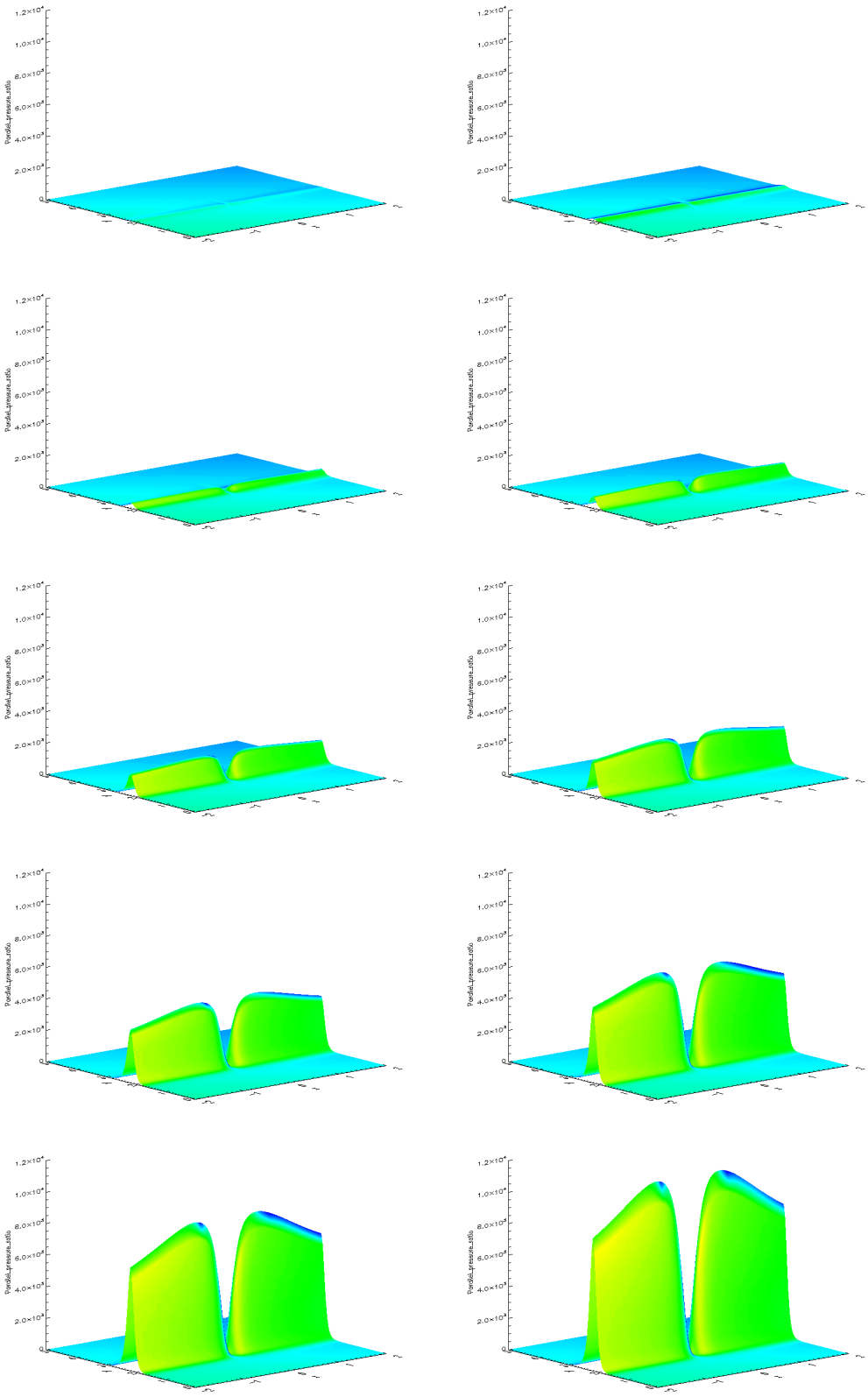

Figure 5.5: Illustrate the evolution of $\frac{P_\parallel}{P_{\parallel init}}$ where it rises from order of 1 to approximately 10^4 between the height $y = 2$ to $y = 3$. The general behaviour of the ratio is a superposition of $\frac{\rho}{\rho_{init}}$ and $\frac{B_{init}}{B}$ where the dominating behaviour comes from the density ratio.

The ratio of C_2/C_1 is given by

$$\frac{C_2}{C_1} = \frac{\frac{P_{\perp init}}{\rho_{init} B_{init}}}{\frac{P_{\parallel init} B_{init}^2}{\rho_{init}^3}} = \frac{P_{\perp init}}{P_{\parallel init}} \frac{\rho_{init}^2}{B_{init}^3}. \tag{5.19}$$

Substituting this into Eqn. 5.18 gives the final expression for the $P_\perp/P_\parallel$ as

$$\begin{aligned} \frac{P_\perp}{P_\parallel} = \frac{P_{\perp init}}{P_{\parallel init}} \frac{\rho_{init}^2}{\rho^2} \frac{B^3}{B_{init}^3} &= \frac{P_{\perp init}}{P_{\parallel init}} \left(\frac{\rho_{init}}{\rho}\right)^2 \left(\frac{B}{B_{init}}\right)^3 \\ &= \frac{P_{\perp init}}{P_{\parallel init}} \left(\frac{J_{cinit}}{J_c}\right)^2 \left(\frac{B}{B_{init}}\right)^3. \end{aligned} \tag{5.20}$$

Figure 5.6 shows the evolution of $\frac{P_\perp}{P_\parallel}$ for a constant initial density and pressure. Like before, the snapshots in the figure starting at the top left hand corner and going along show the value of the ratio for different values of position x and y every 0.095 (normalised units). Starting from an initial ratio of 1, the ratio in general seems to decrease everywhere except in the middle of the trap where two distinctive peaks appear. The highest peak reaches its maximum value of ≈ 2.15 located roughly at $(x, y) = (0, 2)$. The second peak reaches its maximum value of ≈ 1.25 and is located roughly at $(x, y) = (0, 3)$. There is a minimum located in between these two peaks. There are also lower values located either side of the minimum and the two peaks which reach values as small as zero. Figure 5.6 shows the evolution of $\frac{P_\perp}{P_\parallel}$ which seems to have the one main feature seen in Fig. 5.4, namely, the peak at $(0, y) = (0, 2)$, however it is 2 orders of magnitude smaller in value that $\frac{P_\perp}{P_{\perp init}}$ suggesting that the density ratio $\frac{\rho_{init}}{\rho}$ has a bigger influence in the behaviour of this figure. Figure 5.7 show the graph for the opposite ratio, $\frac{P_\parallel}{P_\perp}$. In general the graph seems to evolve in a similar way to the snapshots seen in Fig. 5.5 for $\frac{P_\parallel}{P_{\parallel init}}$, with the minimum value reaching ≈ 0.46 and the maximum value being of the order 807.

5.2 A Stratified Initial Density

In this section we investigate the effect of stratifying the initial density ρ_{init}. In the previous cases the initial density ρ_{init} was set to a constant. Therefore both the density evolution ρ and the ratio of density to initial density $\frac{\rho}{\rho_{init}}$ were found to be the same. Here we want to see if stratifying the density will affect the ratio $\frac{\rho}{\rho_{init}}$ in any way at later times. We make the simple assumption that at $t = t_{init}$ we have hydrostatic pressure balance. Under the assumptions of constant gravitational acceleration and isothermal temperature (see e.g. Chapter 3 of Priest, 1982) the equation for the density becomes

$$\rho = \rho_{init} e^{-y/H}, \tag{5.21}$$

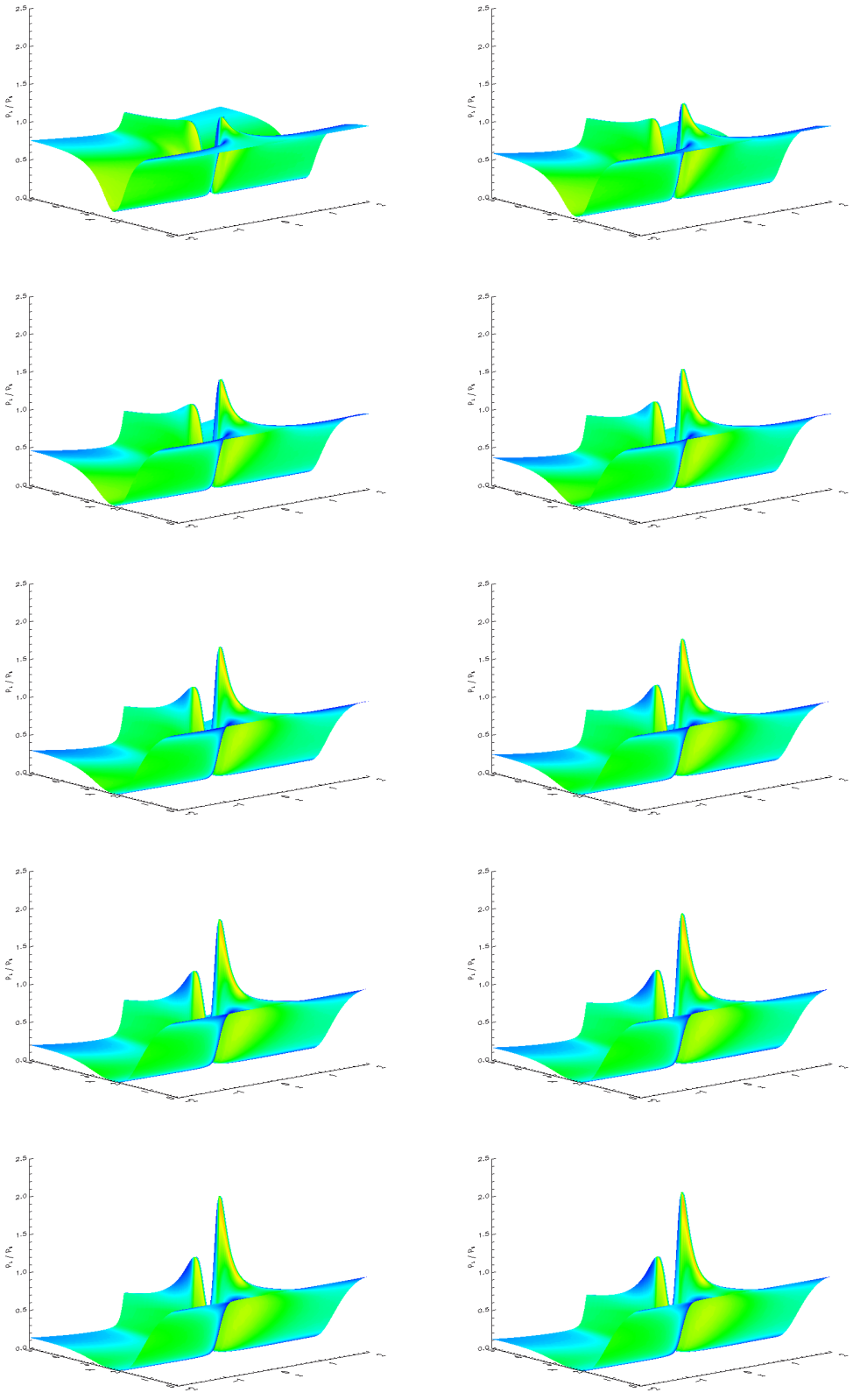

Figure 5.6: Illustrate the evolution of $\frac{P_\perp}{P_\parallel}$ where two distinct peaks with a minimum located in between. The maximum value is ≈ 2.15 and minimum is ≈ 0 at the final time of $t_{final} = 95$ seconds. The general behaviour of the ratio seems to come from the magnetic field ratio.

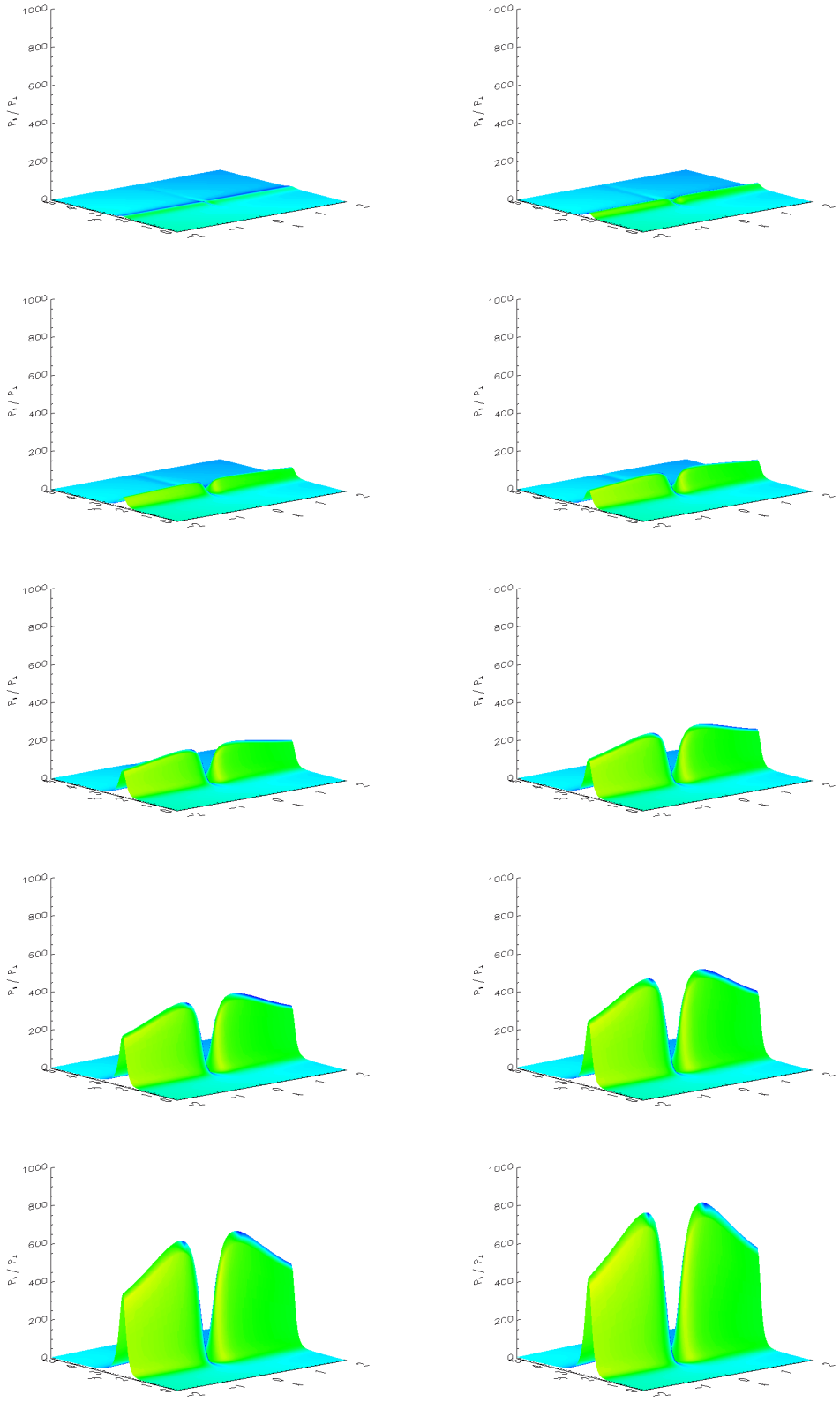

Figure 5.7: Illustrate the evolution of $\frac{P_{\|}}{P_{\perp}}$ where there is a minimum located at the centre of the trap at $x \approx 0$ and $y \approx 2$ to $y \approx 3$. For other values of x the ratio varies along $y \approx 2$ to $y = 3$ with the lowest value being ≈ 410 and the highest value ≈ 800 at $t_{final} = 95$ seconds. The general behaviour seem to come from the the density ratio $\frac{\rho}{\rho_0}$.

where $H = \frac{RT}{g}$ is the pressure scale height and $R = 8.3 \times 10^3$ m^{2}s^{-2}K^{-1} is the universal gas constant. For typical coronal values where the surface gravity on the Sun $g = \frac{GM_\odot}{R_\odot^2} \approx 273m^{-2}$ where the gravitational constant $G = 6.6726 \times 10^{-11}\ m^3s^{-2}kg^{-1}$, the mass of the Sun $M_\odot = 1.98855 \times 10^{30}$ kg, the radius of the Sun $R_\odot = 6.995 \times 10^8$ m and the temperature of the corona is approximately $T = 2 \times 10^6$K, the pressure scale height $H \approx 61$ Mm.

In Fig. 5.8 the evolution of the stratified density in the model is shown for every 0.095 (normalised unit) snapshot. At the initial time $t = t_{init}$ the density ρ is stratified for a height $y = 0$ to $y = 5$, were ρ ranges from 1 to ≈ 0.44 kg m^{-3} respectively. At $t = t_{final}$, ρ reaches its maximum value of approximately 13 kg m^{-3} where this value is less than the case for a constant density, which gave a maximum value of ≈ 18.58 kg m^{-3} at the final time $t_{final} = 2.0$. Now looking at the behaviour of $\frac{\rho}{\rho_{init}}$ for a stratified density it follows that

$$\frac{\rho(x,y,t)}{\rho_{init}(x,y,t_{init})} = \frac{\cancel{\rho_{init}e^{-y/H}}\left(\frac{J_c}{J_{cinit}}\right)}{\cancel{\rho_{init}e^{-y/H}}\left(\frac{\cancel{J_{cinit}}}{\cancel{J_{cinit}}}\right)^1} = \frac{J_c}{J_{cinit}}, \tag{5.22}$$

which is the same as Eqn. 5.10. Hence, for $\frac{P_\parallel}{P_{\parallel init}}$, $\frac{P_\perp}{P_{\perp init}}$, $\frac{P_\perp}{P_\parallel}$ and $\frac{P_\parallel}{P_\perp}$ the exact same behaviour when using a stratified initial density is also seen. For the case of $\frac{P_\parallel}{P_{\parallel init}}$ we have

$$\frac{P_\parallel}{P_{\parallel init}} = \frac{\cancel{P_{\parallel init}}\left(\frac{\rho}{\rho_{init}}\right)^3\left(\frac{B_{init}}{B}\right)^2}{\cancel{P_{\parallel init}}\left(\frac{\cancel{\rho_{init}}}{\cancel{\rho_{init}}}\right)^3\left(\frac{\cancel{B_{init}}}{\cancel{B_{init}}}\right)^2} = \left(\frac{\rho}{\rho_{init}}\right)^3\left(\frac{B_{init}}{B}\right)^2, \tag{5.23}$$

which is the same as Eqn. 5.17 for a constant initial density ρ_{init}. Similar calculations for $\frac{P_\perp}{P_{\perp init}}$, $\frac{P_\perp}{P_\parallel}$ and $\frac{P_\parallel}{P_\perp}$ can also be carried out to show that all these quantities are independent of density stratification when looking at ratios of different quantities.We conclude that while a stratified atmosphere as an initial condition has an effect on single quantities such as the density, it does not affect any ratio between quantities as the space dependent parts cancel.

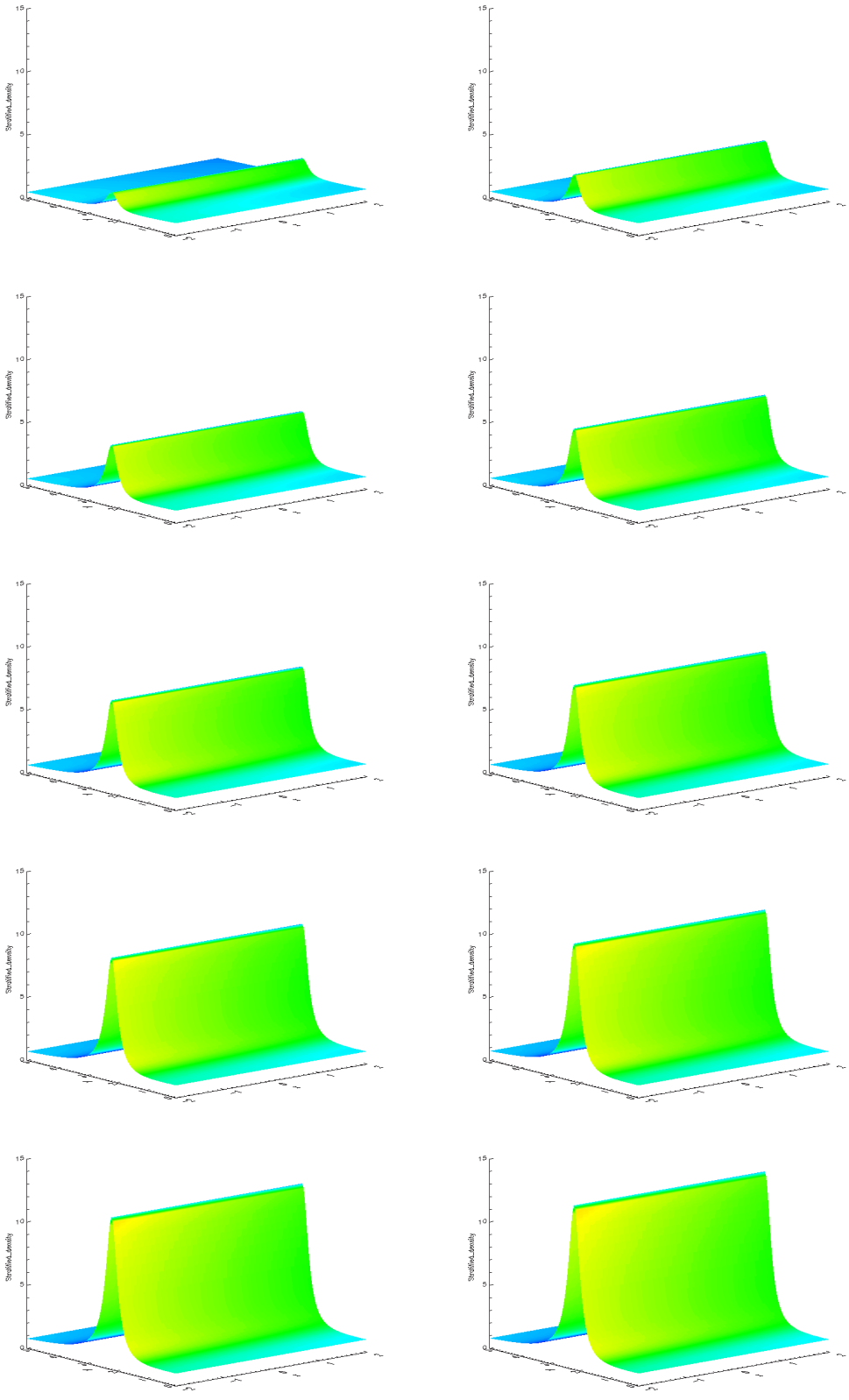

Figure 5.8: Illustrate the evolution of the stratified density $\rho = \rho_{init} e^{-y/H}$.

5.3 Fire-hose and Mirror Instability

In the previous section we investigated the time evolution of various ratios of different plasma quantities, particularly the ratios of $\frac{P_\parallel}{P_\perp}$ and $\frac{P_\perp}{P_\parallel}$ as seen in Figures 5.6 and 5.7. As we have seen, if the double-adiabatic equations hold, the plasma pressure can become anisotropic. This immediately raises the question whether the plasma could become unstable to instabilities in an anisotropic plasma, in particular the fire-hose and mirror instabilities.

In this section we check whether the two stability conditions derived from the double-adiabatic theory as mentioned above, namely, the fire-hose and mirror instability (e.g. Kulsrud, 1983), are satisfied for our CMT model. First we will check the fire-hose instability condition for a constant and then a stratified perpendicular initial pressure $P_{\perp 0}$ in our model. Finally we check the mirror instability condition for a constant and stratified density.

Before we look into these stability conditions we have to make a few remarks. The instability calculations have been carried out for situations with uniform plasma quantities and a straight magnetic field, all in static equilibrium. However, we are dealing with non-uniform and time-dependent quantities. Hence, to be able to apply the instability conditions in a meaningful way, we have to assume that a) the length scales over which the CMT model quantities change are much larger than the wavelengths of the respective instabilities (short wavelength limit) and b) that the time evolution of the CMT occurs on time scales which are much larger than the instability growth rate. If these conditions are satisfied, the instability conditions can provide useful information.

A small perturbation in a garden hose with a rapid flow of water may lead to a violent motion in the hose. Drawing an analogy from this scenario, in ideal aniotropic MHD, a magnetic flux tube can be seen as the hose and the parallel pressure $P_\parallel$ as the flow of water. If the pressure $P_\parallel$ parallel to the magnetic field becomes too high the fire-hose instability can occur. The condition for this instability in an anisotropic plasma is satisfied when (Kulsrud, 1983)

$$P_\parallel > P_\perp + \frac{B^2}{\mu_0}, \tag{5.24}$$

where $P_\parallel$ and $P_\perp$ are the parallel and perpendicular pressure, B is the magnitude of the magnetic field and the permeability of free space, $\mu_0 = 4\pi \times 10^{-7} Hm^{-1}$. Dividing Eqn. 5.24 through by $P_\perp$ gives

$$\frac{P_\parallel}{P_\perp} > 1 + \frac{B^2}{P_\perp \mu_0}. \tag{5.25}$$

Since our model is assumed to satisfy coronal conditions, the plasma beta $\beta \ll 1 \Rightarrow \nabla P \ll \mathbf{J}\times\mathbf{B}$. Therefore,

$$\beta = \frac{\text{gas pressure}}{\text{magnetic pressure}} = \frac{P_0/l_0}{B^2/2\mu_0 l_0} = \frac{2\mu_0 P_0}{B^2},$$

where

$$\frac{B^2}{P\mu_0} = \frac{2}{\beta}. \tag{5.26}$$

Using the following normalisation

$$P_\perp = \bar{P}_{\perp 0}\tilde{P}_\perp, \qquad P_\parallel = \bar{P}_{\parallel 0}\tilde{P}_\parallel, \qquad B = \bar{B}_0\tilde{B},$$

equation 5.25 can be rewritten as,

$$\frac{\tilde{P}_\parallel}{\tilde{P}_\perp} > 1 + \frac{\bar{B}_0^2}{\bar{P}_{\perp 0}\mu_0}\frac{\tilde{B}^2}{\tilde{P}_\perp}. \tag{5.27}$$

Substituting Eqn. 5.26 into the above equation gives

$$\frac{\tilde{P}_\parallel}{\tilde{P}_\perp} > 1 + \frac{2}{\beta_\perp}\frac{\tilde{B}^2}{\tilde{P}_\perp}, \tag{5.28}$$

where $\beta_\perp = \frac{2\bar{P}_{\perp 0}\mu_0}{\bar{B}_0^2}$ is the perpendicular plasma beta. For typical active region or flare parameters (see e.g. NRL Book (2007)):

$$\begin{aligned}
\bar{B}_0 &= 150G = 0.015T, \\
\mu_0 &= 4\pi \times 10^{-7} Hm^{-1}, \\
n_0 &= 10^{16} m^{-3}, \\
m_p &= 1.6726 \times 10^{-27} kg, \\
\bar{T}_0 &= 2 \times 10^6 K, \\
R &= 8.3145 \times 10^3 m^2 s^{-2} K^{-1}, \\
\bar{\rho}_0 &= n_0 m_e \approx 1.6726 \times 10^{-11} \frac{kg}{m^3}, \\
\bar{P}_0 &= \bar{\rho}_0 R \bar{T}_0 \approx 0.3 Pa,
\end{aligned}$$

we get $\beta = \frac{2\mu_0\bar{P}_0}{\bar{B}_0^2} \approx 5 \times 10^{-3} \ll 1$. Substituting $\tilde{P}_\perp = \tilde{P}_{\perp 0}(\frac{\tilde{\rho}}{\tilde{\rho}_0})(\frac{\tilde{B}}{\tilde{B}_0}) = \tilde{P}_{\perp 0}(\frac{\tilde{J}_c}{\tilde{J}_{cinit}})(\frac{\tilde{B}}{\tilde{B}_0})$ into the second term on the right hand side of Eqn. 5.28 gives,

$$\left(\frac{2}{\beta_\perp}\right)\frac{\tilde{B}^2}{\tilde{P}_\perp} = \left(\frac{2}{\beta_\perp}\right)\frac{\tilde{B}^2}{\tilde{P}_{\perp 0}(\frac{\tilde{J}_c}{\tilde{J}_{cinit}})(\frac{\tilde{B}}{\tilde{B}_0})}$$

$$= \left(\frac{2}{\beta_\perp}\right)\frac{\tilde{J}_{cinit}}{\tilde{J}_c}\tilde{B}\tilde{B}_0\frac{1}{\tilde{P}_{\perp 0}}.$$

$\tilde{P}_{\perp 0}$, as mentioned previously is assumed to be constant in space and time. The effect of a stratified initial perpendicular pressure $\tilde{P}_{\perp 0}$ on this quantity will be looked at later. Dropping the $\sim$ and substituting the above equation into 5.28 gives,

$$\frac{P_\parallel}{P_\perp} > 1 + \left(\frac{2}{\beta_\perp}\right)\frac{J_{cinit}}{J_c}BB_0\frac{1}{P_{\perp 0}}. \tag{5.29}$$

Fig. 5.9 shows the evolution of the left hand side of the inequality; the ratio of $\frac{P_\parallel}{P_\perp}$ as a contour plot. The evolution of this ratio was already seen in Fig. 5.7 and discussed in section 5.1.4. The highest value was found to be ≈ 807 and the lowest ≈ 0.46 at the final time $t = t_{final}$. The contour plot clearly shows the lowest value represented by the white colour and the coloured region between $y \approx 2$ to $y = 3$ representing the higher values with the orange/red colour. Again, like the figures discussed in section 5.1, each snapshot starting from the left hand corner is taken at 0.095 (normalised units) into the evolution of the quantity. Initially the ratio $\frac{P_\parallel}{P_\perp}$ increases between $y = 2$ to $y = 3$. As time evolves the ratio increases in both directions more so in the upwards direction from this initial region, where at the final state the initial region is the highest $\frac{P_\parallel}{P_\perp}$ ratio. Looking at the right hand side of the inequality seen in Fig. 5.10 the term $\frac{J_{cinit}}{J_c}$, which represents the ratio $\frac{\rho_{init}}{\rho}$, decreases in the middle and increases either end of the minimum. This trend is seen in Fig. 5.10 where the quantity on the right hand side decreases between 2 and 3 in the y-direction. The highest value in Fig. 5.10 is found to be ≈ 412 and the lowest ≈ 1 at the final time $t = t_{final}$. Further investigation into Fig. 5.10 reveals the general behaviour of the figure is dominated by the behaviour of the B quantity.

In Fig. 5.11 the fire-hose instability condition is checked for a constant $P_{\perp init}$. To represent this inequality, locations in the trap where this condition is satisfied are shown in white and locations where the condition is not satisfied are shown in black. One can see that there is an unstable region present in the middle of the trap between $y = 2$ to $y = 3$ and it grows upwards leaving a stable region in the middle of the trap and two stable regions in the left and right hand corner. These two stable regions at either end eventually disappear leaving the small island in the middle between $y = 1.5$ to $y = 5$ as the only stable region. Between $y = 0$ to $y = 2.0$ the trap remains stable on average for the duration of the collapse.

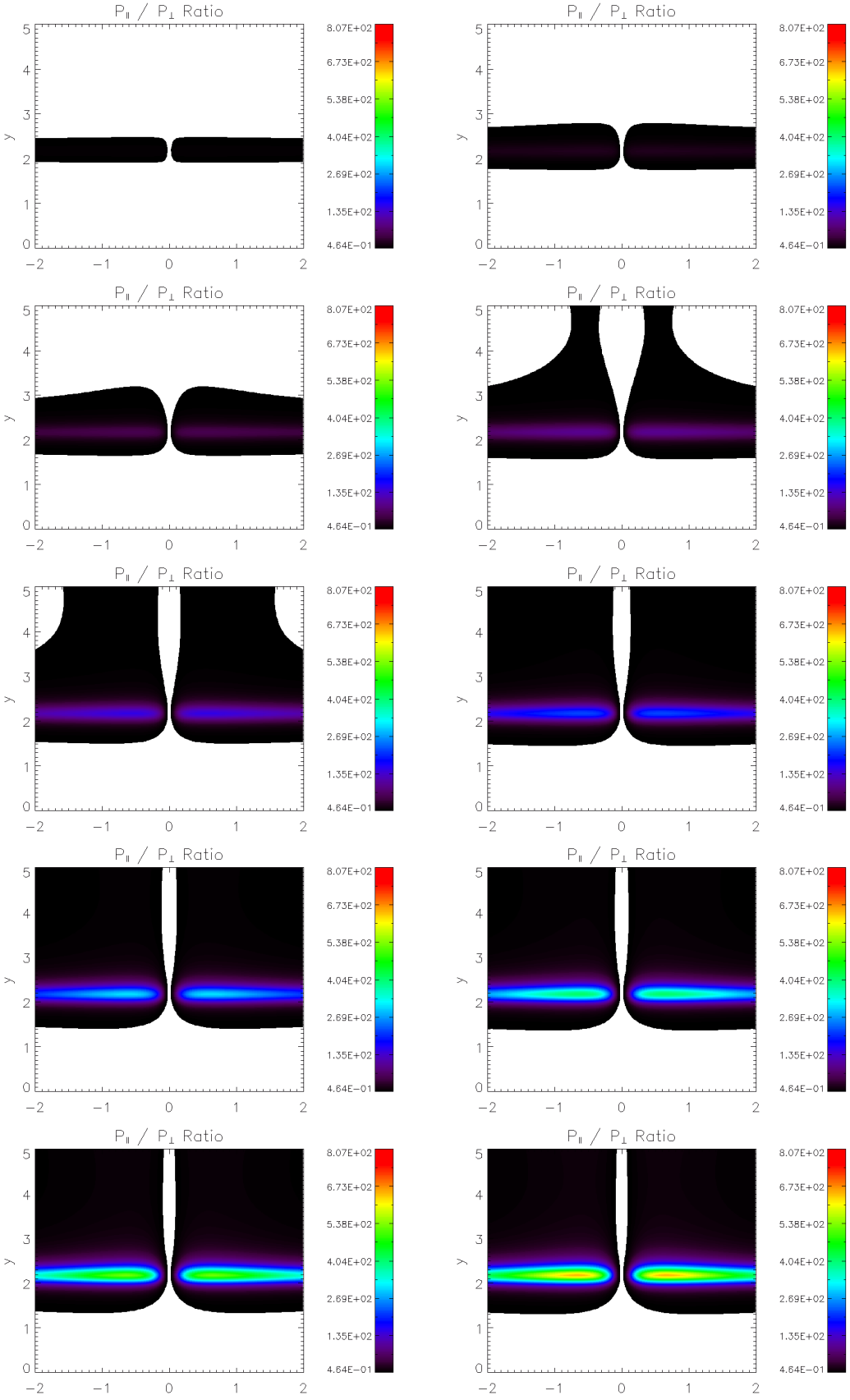

Figure 5.9: Illustrate the evolution of $\frac{P_{\|}}{P_{\perp}}$ ratio as a contour plot. The white and black regions show the lower values and the coloured regions between the heights $y = 2$ to $y = 3$ represent the highest values with the orange/red colours ≈ 800 at the final time $t = t_{final}$.

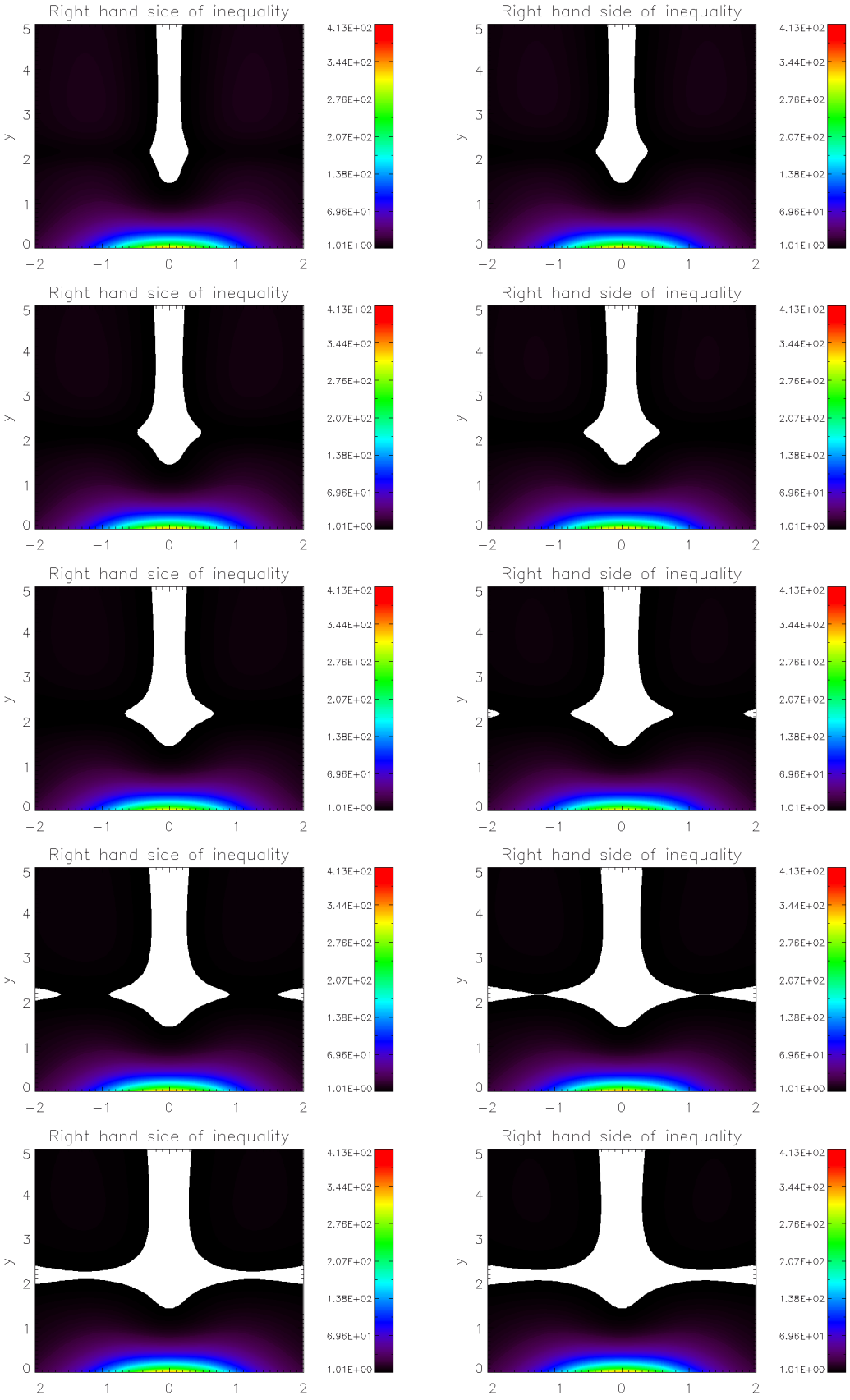

Figure 5.10: Illustrate the evolution of expression on the right hand side of equation (5.29) where $P_{\perp 0}$ is a constant.

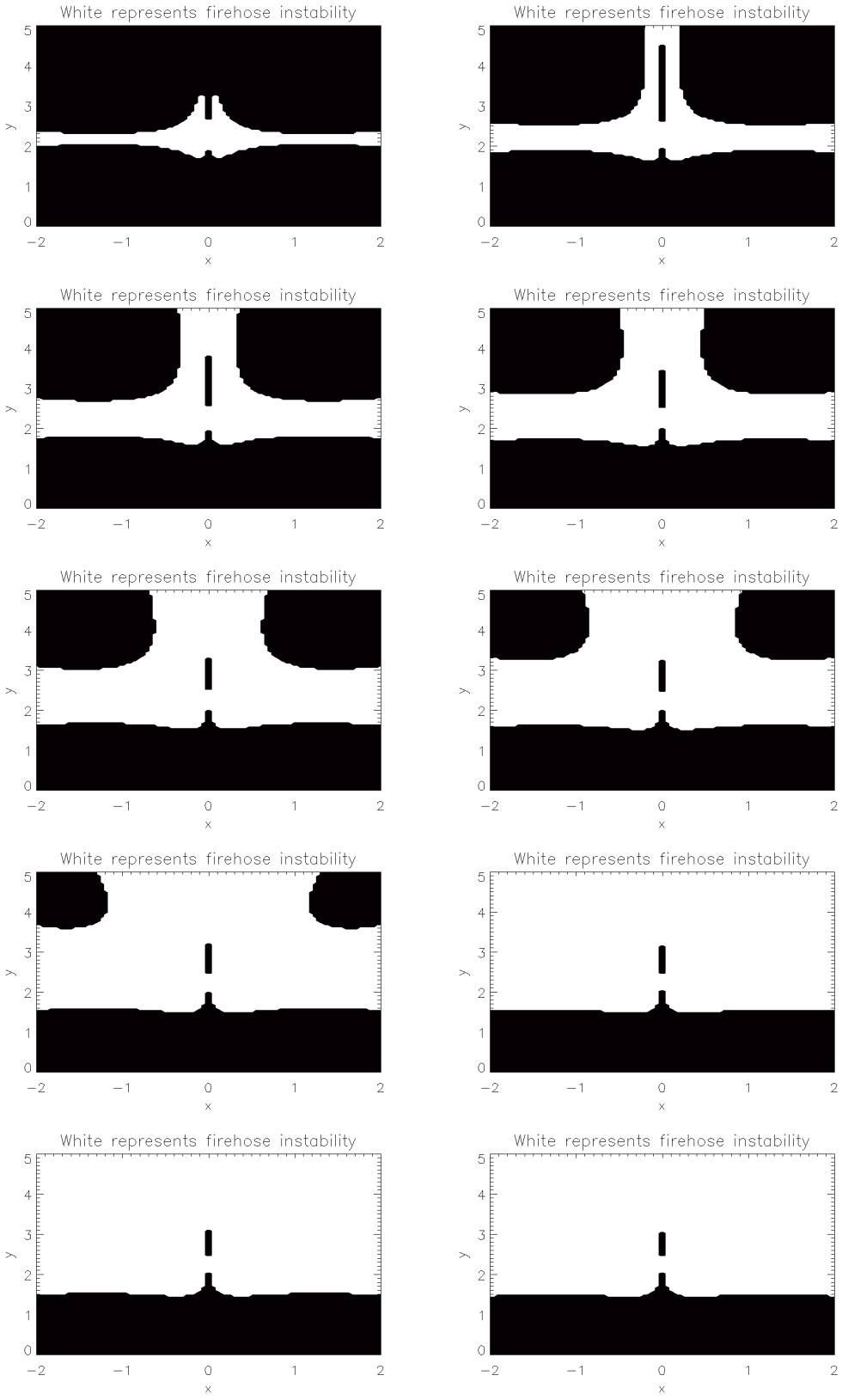

Figure 5.11: Illustrate where the magnetic trap becomes fire-hose unstable when the condition in equation (5.29) for $\beta_\perp = 0.005$ and $P_{\perp 0}$ is a constant. The white colour in the figures represents the regions in the trap that become fire-hose unstable and the black regions are regions of stability.

Next we look at the effect of a stratified initial perpendicular pressure $P_{\perp init}$ on the fire-hose instability condition in the trap. Like before, working under the assumption of hydrostatic pressure balance for a constant gravitational acceleration and isothermal temperature, the equation for the perpendicular pressure becomes

$$P_{\perp 0} = P_{\perp init} e^{-y/H}, \tag{5.30}$$

where $H = 61$ Mm is the pressure scale height for typical coronal parameters. In our model all length scales are normalised to $L = 10$ Mm, so $H = 6.1$ and $P_{\perp init}$ is normalised to 1. Substituting the stratified pressure into Eqn. 5.29 gives

$$\frac{P_{\parallel}}{P_{\perp}} > 1 + \left(\frac{2}{\beta_{\perp}}\right) \frac{J_{cinit}}{J_c} B B_{init} \frac{1}{e^{-y/H}}. \tag{5.31}$$

Looking at Fig. 5.12, which represents the evolution of the right hand side of Eqn. 5.31 for a stratified $P_{\perp init}$, the same general behaviour seen in Fig. 5.11 for a constant perpendicular pressure is seen. However, because of the stratification the right hand side of Eqn. 5.31 does not evolve to the same extent as seen in Fig. 5.11 and the values remain ever so slightly higher than the case for a constant $P_{\perp init}$ (the change is seen after the 4th significant figure). The highest and lowest values of the right hand side for a stratified perpendicular pressure are of the same order, ≈ 412 and 1, respectively. Therefore the same is true for the fire-hose instability condition as seen in Fig. 5.13. Like before the unstable regions in the model are represented by the white colour and the stable regions by black. Comparing this figure with Fig. 5.11 the same general evolution is seen, however, for a stratified pressure it seems the model is more stable than in the case for a constant perpendicular pressure.

Finally we check for the mirror instability condition in our CMT model. Complementary to the fire-hose instability, the mirror instability propagates perpendicular to the magnetic field and it occurs when the pressure $P_{\perp}$ perpendicular to the magnetic field becomes too high. The condition for mirror instability in an anisotropic plasma is given by (Kulsrud, 1983)

$$\frac{P_{\perp}^2}{6P_{\parallel}} > \frac{B^2}{2\mu} + P_{\perp}, \tag{5.32}$$

where rearranging the above equation gives

$$\frac{P_{\perp}}{P_{\parallel}} > 3\frac{B^2}{\mu P_{\perp}} + 6. \tag{5.33}$$

Normalising Eqn. 5.33 and dropping the $\sim$ gives

$$\frac{\tilde{P}_{\perp}}{\tilde{P}_{\parallel}} > 3\frac{\bar{B}_0^2}{\bar{P}_{\perp 0}\mu_0}\frac{\tilde{B}^2}{\tilde{P}_{\perp}} + 6,$$

$$\begin{aligned} \frac{\tilde{P}_\perp}{\tilde{P}_\parallel} &> \frac{6}{\beta_\perp}\frac{\tilde{B}^2}{\tilde{P}_\perp} + 6 \\ \frac{P_\perp}{P_\parallel} &> \frac{6}{\beta_\perp}\frac{J_{c0}}{J_c} B B_0 \frac{1}{P_{\perp 0}} + 6. \end{aligned} \tag{5.34}$$

Looking at Eqn. 5.34 a factor of 6 can be seen on the right hand side of the inequality. Kulsrud (1983), for example, checks to see if both the fire-hose and the mirror instability expression are identical when using kinetic theory and double-adiabatic theory. He finds the fire-hose instability condition is the same when using both the double-adiabatic theory and the kinetic theory. However, when looking into the mirror instability condition he found the right hand side of Eqn. 5.34 was missing a factor of 6 when using kinetic theory. Here we will check to see if the mirror instability condition is satisfied for the case derived using the double-adiabatic theory and the case using kinetic theory (without a factor of 6 on the right hand side of Eqn. 5.34). We investigated the mirror condition in Eqn. 5.34 for our model and find that there were no instabilities for a constant and stratified $P_{\perp 0}$ in the trap. However when the factor of 6 was eliminated from the right hand side of Eqn. 5.34, some regions in the model become mirror unstable as seen in Fig. 5.14 for a constant perpendicular pressure $P_\perp$ and for a stratified $P_\perp$ as seen in Fig. 5.15. These regions of instability are represented by the white colour and appear in a small region in the middle of the trap and grow very slowly in height in the y direction as the trap evolves.

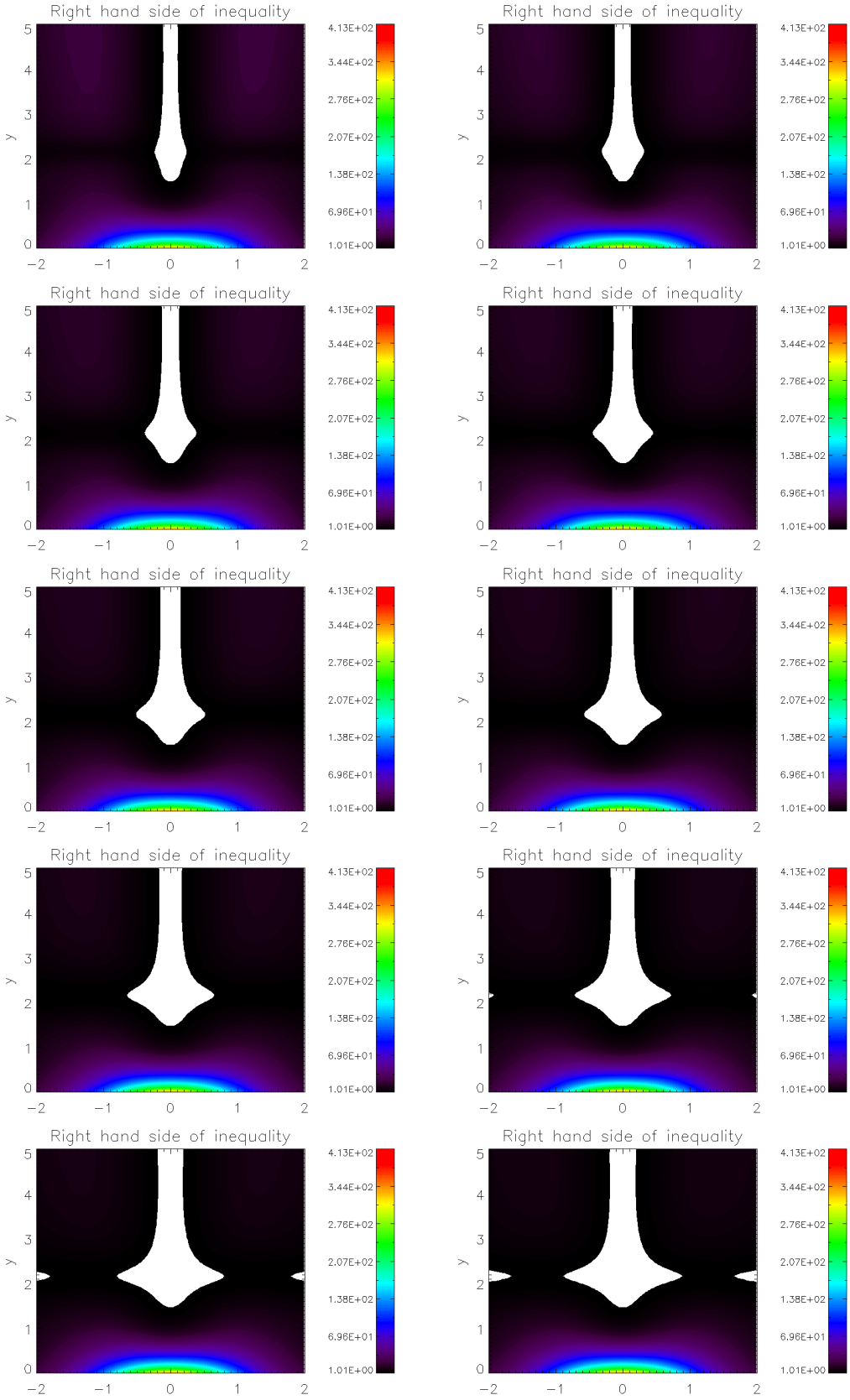

Figure 5.12: Illustrate the evolution of expression on the right hand side of equation (5.29) for a stratified initial perpendicular pressure $P_{\perp 0} = P_{\perp init} e^{-\frac{y}{H}}$.

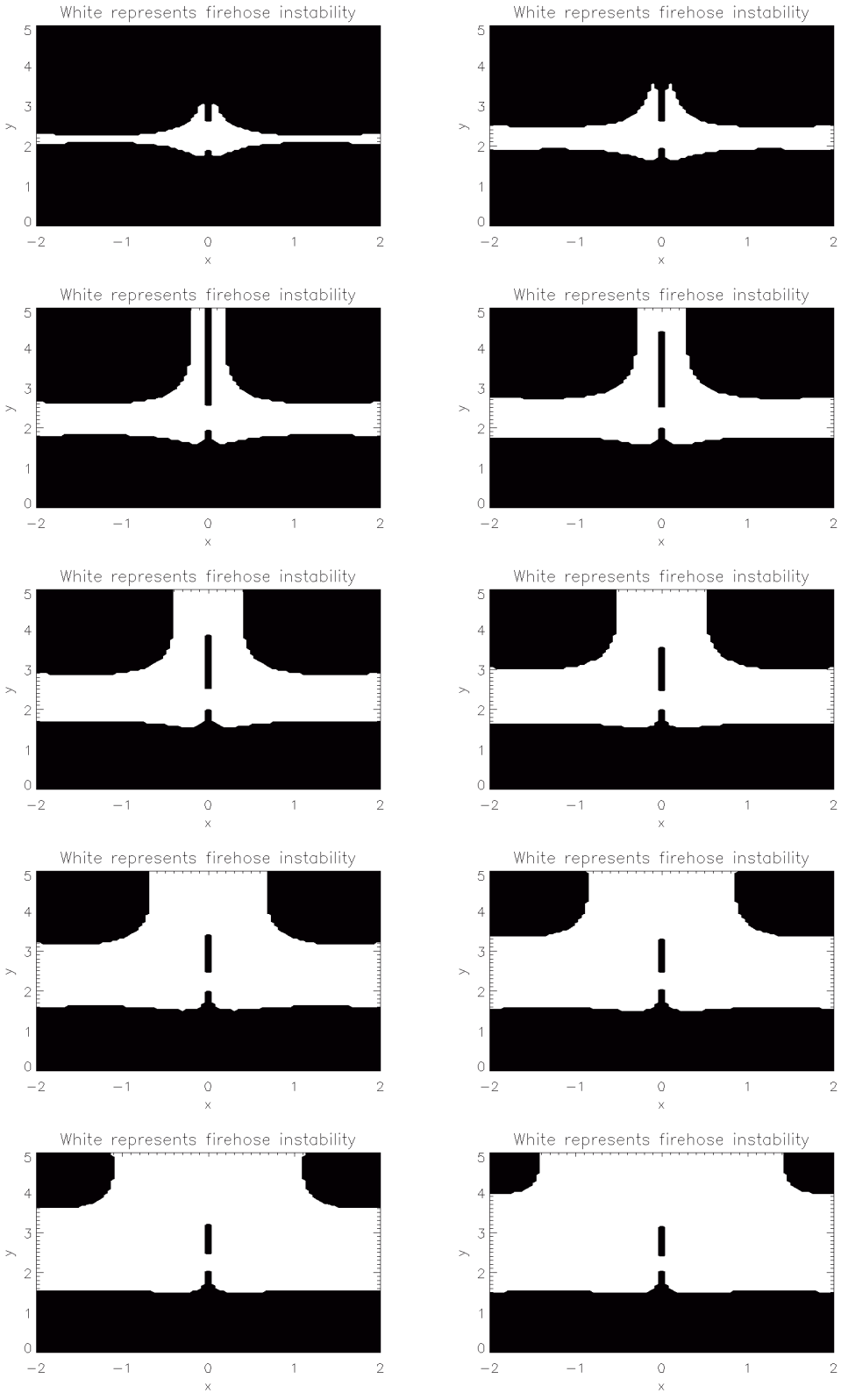

Figure 5.13: Illustrate where the magnetic trap becomes fire-hose unstable when the condition in equation (5.29) is satisfied.

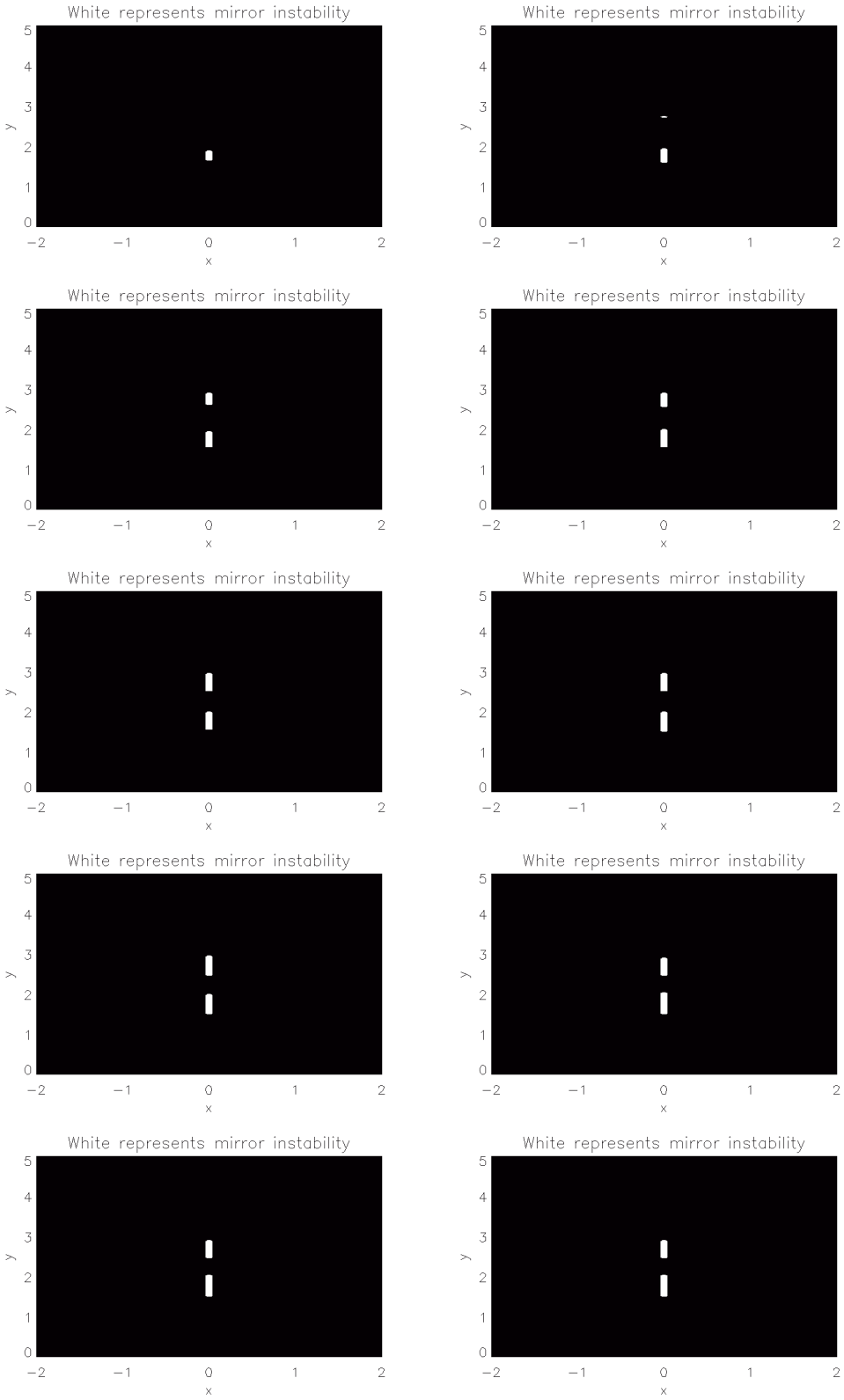

Figure 5.14: Illustrate where the magnetic trap becomes mirror unstable when the condition in equation (5.34) without a factor 6 included and the density in the trap is constant.

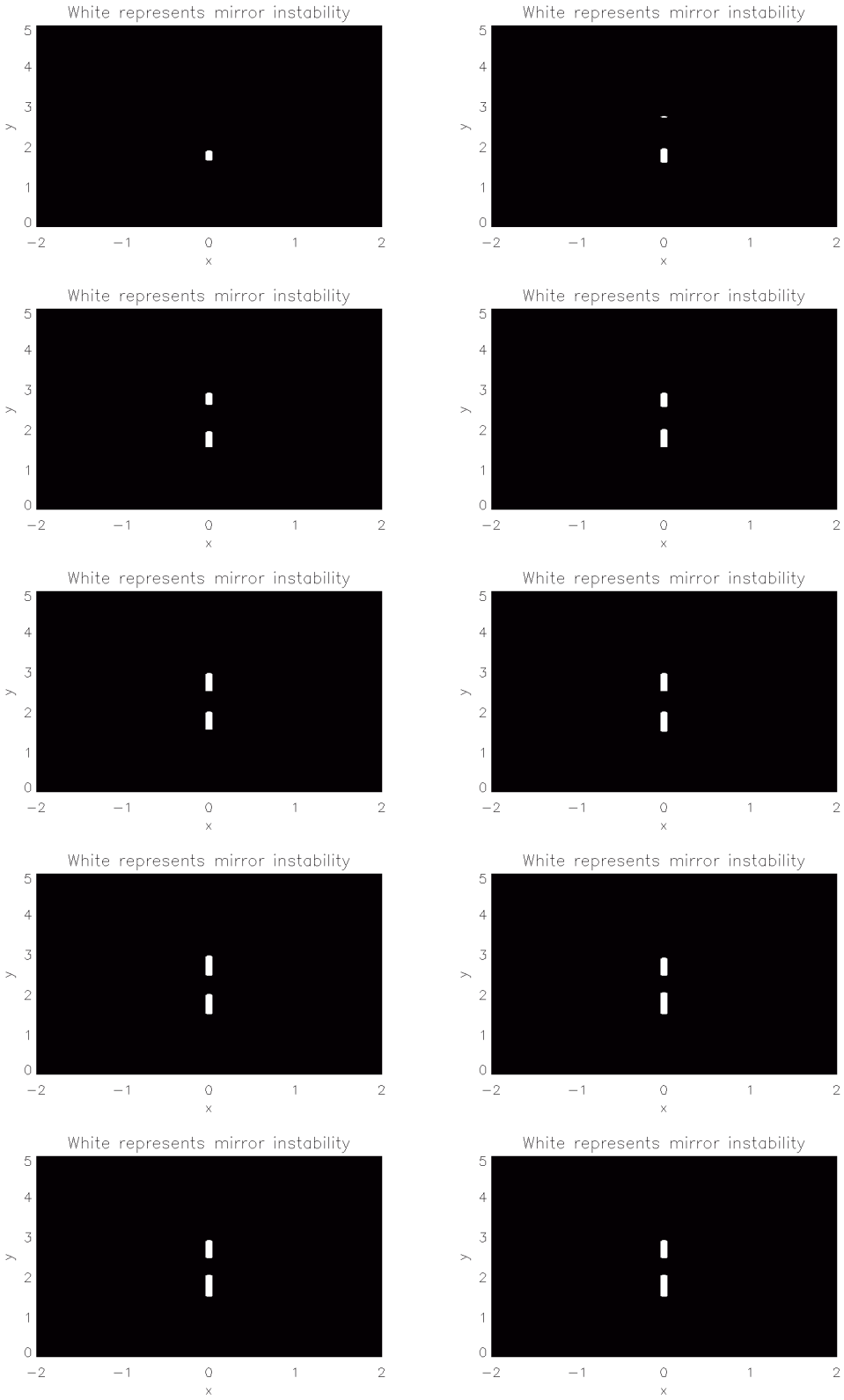

Figure 5.15: Illustrate where the magnetic trap becomes mirror unstable when the condition in equation (5.34) without a factor 6 included and the density in the trap is stratified.

5.4 Discussion and Conclusions

In this Chapter we investigated the evolution of the plasma ratios $\frac{\rho}{\rho_{init}}$, $\frac{P_\perp}{P_{\perp init}}$, $\frac{P_\parallel}{P_{\parallel init}}$, $\frac{P_\perp}{P_\parallel}$ using the Giuliani et al. (2005) CMT model. The density increased by one order, the perpendicular pressure by two orders, the parallel pressure by four orders of magnitude during the collapse of the CMT. Particularly, the ratio $\frac{P_\perp}{P_{\perp init}}$ increases by up to 2 orders of magnitude, whereas the ratio $\frac{P_\parallel}{P_{\parallel init}}$ increased by up to 4 orders of magnitude, suggesting the parallel pressure seems to be the more dominating term compared to the perpendicular pressure. All of these results where obtained under the simplified assumptions of: 1) the double-adiabatic theory i.e. no heat flux and 2) isotropic initial pressure and uniform initial density i.e. $P_\parallel = P_\perp$. On the other hand we interestingly found that for a non-uniform initial density we obtained the same results as the case with uniform density as seen in the results in section 5.2. Also based on the finding by Kulsrud (1983) we checked to see if our model under the assumptions of isotropic pressure and no heat flux does become fire-hose and mirror unstable. We found that for both constant and stratified initial pressure, the model does become fire-hose unstable represented by the white in figures 5.11 and 5.13. For the mirror instability, using the CGL approximation, the model remains stable. However, using kinetic theory the model does become mirror unstable, again represented by the white in figures 5.14 and 5.15.

The study in this chapter is very much dependent on the validity of the double-adiabatic theory where heat-flux is neglected. Assuming $P_\parallel = \rho R T_\parallel$ and $P_\perp = \rho R T_\perp$, gives

$$\frac{P_\parallel}{P_\perp} = \frac{T_\parallel}{T_\perp}.$$

As the ratio $\frac{P_\parallel}{P_\perp}$ increases with time as seen in the region between $y = 2$ to $y = 3$ in Fig. 5.7, so would the ratio $\frac{T_\parallel}{T_\perp}$ with the current assumptions in the model. But what if heat flux were to be included in the model? Then the temperature in the model could be affected by two competing mechanisms; the compression from the collapsing trap could cause the temperature in the trap to increase and at the same time heat conduction would try to decrease the temperature. With the current assumptions made in the model, the ideal kinematic MHD equations do not include the effects of pressure, P, on the evolution of the different variables like density, ρ, temperature, T, the magnetic field, $\mathbf{B}$, and the electric field, $\mathbf{E}$. If the effects from P were to be included in the model then the full momentum equations would also have to be solved in the system. Also, changing the current assumption for the flow velocity, $\mathbf{v}$, which only varies in the y-direction to also varying along the x-direction, would have an effect on the different variables in the model. These points could be seen as an outline for future work to continue with the studies initiated in this Chapter.

Chapter 6

Introducing Coulomb Collisions into the Giuliani et al. (2005) CMT Model: A First Step

In this chapter we look at how Coulomb collisions with a background plasma could influence the test particle's energy loss, travel distance, pitch angle evolution and trapping conditions for our magnetic trap model. We would like to emphasize that the work presented in this chapter should be seen as a set of numerical experiments which may in the future lead to more realistic investigations. As a starting point in trying to introduce collisional effects into this model, we make the following assumptions; the background atmosphere is static and coronal temperature is isothermal at approximately 1 to 2 MK. In a flare, the temperature can reach 10-20 MK, which in turn would lower the collisional cross section due to particles moving faster in a hot plasma. After a brief discussion of the theory and general concepts used to introduce Coulomb collisions, we begin our investigation in section 6.3 by first looking at how diffusion (pitch angle scattering) alone effects the particle behaviour in the model. In section 6.4 we introduce energy losses alongside the diffusion term and look at a simple numerical set up where the initial density in the collisional model is set to a low constant value. Cases for increasing density and its effect on the particle energy are discussed in section 6.5. Since collisions will naturally cause particles to lose energy with increasing density, we encounter a numerical effect whereby our particle orbit code stops operating. We investigate this point by checking what is the minimum energy required for the particle to complete a full orbit in a finite time in section 6.6. We look at the effects of collisions on the critical pitch angle and compare it with our findings in Chapter 4. As a final study the consequence on the particle evolution when only pitch angle scattering is included and energy losses are neglected is investigated. We end the chapter with our discussions and concluding remarks.

6.1 Coulomb Collision Theory

Coulomb collisions are the binary collisions of charged particles interacting through their own electric field Somov (2006). Aside from the effects of large scale electric and magnetic fields on charged particle motions, Coulomb collisions are always present in a plasma where the particle

velocities are not sufficient enough to overcome the two main effects, namely, pitch angle scattering and energy losses. Collisional energy losses in a non-relativistic treatment are accounted for through the decrease of the particle velocity v as (Longair, 1981):

$$\begin{aligned} \frac{dE}{dl} = \frac{d}{dl}\left(\frac{1}{2}mv^2\right) &= -\rho(\frac{q^2}{4\pi\varepsilon_0})^2\frac{4\pi}{mv^2}\ln\Lambda, \\ m\frac{dl}{dt}\frac{dv}{dl} &= -\rho(\frac{q^2}{4\pi\varepsilon_0})^2\frac{4\pi}{mv^2}\ln\Lambda, \\ \frac{dv}{dt} &= -\rho(\frac{q^2}{4\pi\varepsilon_0})^2\frac{4\pi}{m^2v^2}\ln\Lambda. \end{aligned} \tag{6.1}$$

where l is the distance a particle travels in a plasma, $v = \sqrt{{v_\parallel}^2 + \frac{2\mu B}{m}^2}$ is the particle velocity, ρ is the background density, q is the charge of an electron, ε_0 is the permeability of free space, m is the mass of the electron and $\ln\Lambda$ is the Coulomb logarithm which for coronal values is approximately 20.

The second effect, pitch angle scattering is implemented through random changes in the test particle pitch angle. The equation describing pitch angle scattering due to Coulomb collisions is introduced in the next section. Here we briefly discuss how we produce the random numbers which are needed in the equation. The random/stochastic nature of this term is modelled by using a random number generator with a normal (Gaussian) distribution. Fig. 6.1 shows a distribution

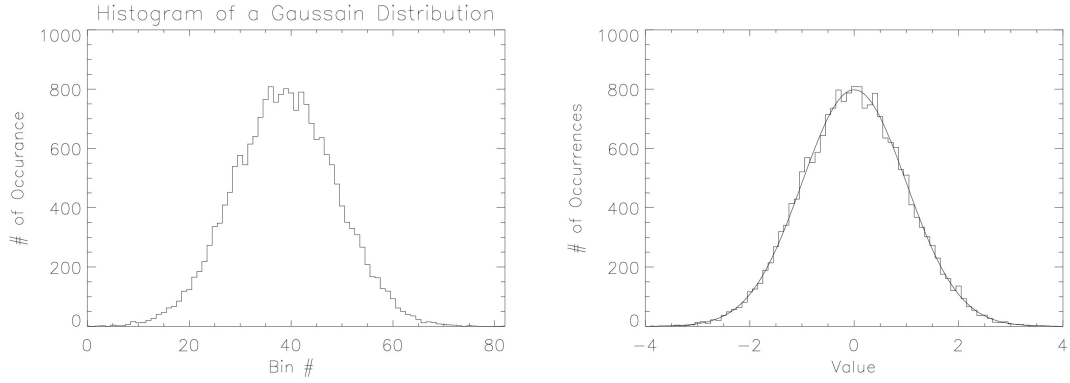

Figure 6.1: *Left*: Number of occurrence against bin number, where the highest distribution of numbers is centred around the middle bin. *Right*: normal distribution function (black solid line) overplotted on to the Gaussian distribution of particles from the random number generator.

of random numbers which have a Gaussian profile. The figure on the left shows the number of bins (binsize $= 0.1$) against the number of occurrence for a Gaussian distribution of numbers. The figure on the right shows the histogram for the values of the data plotted against the number of occurrence for the Gaussian distribution centred at zero. This is a characteristic for this type of distribution which has a mean of zero ($\mu_{mean} = 0$) and a variance, $\sigma^2 = 1$ and satisfies the

following normal distribution function

$$f(x) = \frac{1}{\sigma\sqrt{2\pi}} e^{-\frac{(x-\mu_{mean})^2}{2\sigma^2}}.$$

This distribution function is overplotted (black solid line) on top of the histogram on the right and both coincide very well. The distribution of numbers seen in the figure are produced using a seed $= 0$ as a test case. For different seed choices a different set of random numbers with a Gaussian distribution will be produced and with the current modification made to the non-relativistic particle orbit code the seed is set to the particle orbit number (i.e, particle 1 has a seed 1, particle 2 has a seed 2 and so on).

6.2 Effects of Coulomb collisions on v and μ

To introduce Coulomb energy losses and pitch angle scattering to the model we adopt a method similar to Fletcher (1995) (see also MacKinnon and Craig, 1991). We extend our guiding centre equations to a set of stochastic differential equations (SDEs) with random scattering terms. From Gardiner (1985) a set of SDEs is generally given by

$$d\mathbf{x} = \mathbf{A}(\mathbf{x}, t)dt + \mathbf{B}^{1/2}(\mathbf{x}, t)d\mathbf{W}(t), \tag{6.2}$$

which describe the evolution of a random variable **x** under the influence of advective and diffusive terms $\mathbf{A}$ and $\mathbf{B}$. $\mathbf{W}(t)$ is a stochastic term used to describe the diffusion process. In practice, it is a random number picked from an appropriate Gaussian distribution, hence the need for the random number generator discussed in section 6.1.

In our model we use the non-relativistic guiding centre approximation to calculate the particle trajectories (see Chapter 3). Supplemented by the appropriate stochastic terms, the quantities which are affected by collisions in the code are $v_{\|}$ and the magnetic moment μ. The equations for both these quantities contain energy losses and pitch angle scattering, so they will be our stochastic differential equations. It is through the variation of these two quantities that we introduce Coulomb collisions into our model.

We initially choose as our two stochastic variables v and $\varphi = \cos\theta = \frac{v_{\|}}{v}$, where θ is the particle pitch angle, satisfying the stochastic differential equations Fletcher (1995)

$$dv = A_v dt, \tag{6.3}$$

$$d\varphi = A_\varphi dt + B_\varphi dW_\varphi. \tag{6.4}$$

with

$$A_v = -K^2 4\pi\rho \frac{q^4}{m^2 v^2} \ln\Lambda, \tag{6.5}$$

$$A_\varphi = -2K^2 \frac{4\pi q^4}{m^2} \frac{\rho\varphi}{v^3} \ln\Lambda, \tag{6.6}$$

$$B_\varphi = \left[K^2 \frac{4\pi q^4}{m^2} \frac{\rho}{v^3} \ln\Lambda (1-\varphi^2) \right]^{1/2}. \tag{6.7}$$

where $K = \frac{1}{4\pi\varepsilon_0}$, A_v and A_φ are the advection terms and B_φ is the diffusion term. Our aim here is to transform from the stochastic variables (v, φ) to another pair of stochastic variables $(v_\parallel, \mu)$ using the following transformations

$$v_\parallel = v\varphi = v\cos\theta, \qquad \mu = \frac{m}{2B} v^2 (1-\varphi^2). \tag{6.8}$$

Using Ito's calculus which is seen as a Taylor series expansion in a stochastic setting, we transform the SDE's by expanding them to second order (see Gardiner, 1985, for more details). Keeping only the first order terms and only one second order term ($dW \times dW = dt$) we get,

$$\begin{aligned} dv_\parallel &= dv_\parallel(t, v, \varphi) \\ &= \frac{\partial v_\parallel}{\partial v} dv + \frac{\partial v_\parallel}{\partial \varphi} d\varphi + \frac{1}{2} \frac{\partial^2 v_\parallel}{\partial v^2} dv^2 + \frac{1}{2} \frac{\partial^2 v_\parallel}{\partial \varphi^2} d\varphi^2 \\ &\quad + \frac{\partial^2 v_\parallel}{\partial v \partial \varphi} dv d\varphi + \text{higher order terms}. \end{aligned} \tag{6.9}$$

Since $v_\parallel = v\varphi$, $\frac{\partial v_\parallel}{\partial v} = \varphi$, $\frac{\partial v_\parallel}{\partial \varphi} = v$, $\frac{\partial^2 v_\parallel}{\partial v^2} = 0$ and $\frac{\partial^2 v_\parallel}{\partial \varphi^2} = 0$, substituting equations 6.3 and 6.4 for dv and $d\varphi$ respectively gives,

$$\begin{aligned} dv_\parallel &= \varphi dv + v d\varphi \\ &\equiv \frac{v_\parallel}{v} dv + v d\varphi \\ &= (\varphi A_v + v A_\varphi) dt + v B_\varphi dW_\varphi \end{aligned} \tag{6.10}$$

Now for the magnetic moment

$$\mu = \frac{m}{2B} v^2 (1-\varphi^2),$$

the calculation is exactly the same as before except for the fact that the second derivative in μ with respect to φ is no longer zero, which gives an extra contribution. Replacing all $v_\parallel$ with μ in Eqn. 6.9 gives,

$$d\mu = d\mu(t, v, \varphi)$$

$$= \frac{\partial \mu}{\partial v} dv + \frac{\partial \mu}{\partial \varphi} d\varphi + \frac{1}{2}\frac{\partial^2 \mu}{\partial v^2} dv^2 + \frac{1}{2}\frac{\partial^2 \mu}{\partial \varphi^2} d\varphi^2 + \frac{\partial^2 \mu}{\partial v \partial \varphi} dv d\varphi + \text{higher order terms.} \tag{6.11}$$

Since $\frac{\partial \mu}{\partial v} = \frac{mv}{B}(1-\varphi^2) = 2\frac{\mu}{v}$, $\frac{\partial^2 \mu}{\partial v^2} = \frac{m}{B}(1-\varphi^2)$, $\frac{\partial \mu}{\partial \varphi} = -\frac{mv^2}{B}\varphi$ and $\frac{\partial^2 \mu}{\partial \varphi^2} = -\frac{mv^2}{B}$, substituting equations 6.3 and 6.4 for dv and $d\varphi$ respectively gives,

$$\begin{aligned} d\mu &= \left(\frac{\partial \mu}{\partial v} A_v + \frac{\partial \mu}{\partial \varphi} A_\varphi + \frac{1}{2}\frac{\partial^2 \mu}{\partial \varphi^2} {B_\varphi}^2 \right) dt + \frac{\partial \mu}{\partial \varphi} B_\varphi dW_\varphi \\ &\equiv \frac{2\mu}{v} dv - \frac{v_\parallel v}{B} d\varphi - \frac{v^2}{2B} {B_\varphi}^2 dt. \end{aligned} \tag{6.12}$$

In Eqn. 6.4 the advection term A_φ and the diffusion term B_φ are in constant competition with each other. The advective/energy loss term drives the particle pitch angle scattering term towards 0, i.e. $\varphi = \cos\theta \rightarrow 0 \Rightarrow \theta \rightarrow \frac{\pi}{2}$. On the other hand, the diffusive/scattering term drives the particle pitch angle scattering term to 1, i.e. $\varphi = \cos\theta \rightarrow 1 \Rightarrow \theta \rightarrow 0$. As in Fletcher (1995) we also use the approximation that the test particle velocities are much larger than the thermal velocity of the scattering background plasma (i.e. $v \gg v_{thermal}$). However, we would like to point out that assuming a uniform background density and an isothermal coronal temperature increases the collisional effects introduced by the advective A_v, A_ϕ and diffusive B_ϕ terms. As mentioned before this would change if the temperature were to go up which is what is seen in flares in general. Also as mentioned in Chapter 5 the compression from the field lines as the trap collapses could also increase the temperature, resulting in the ratio $\frac{v}{v_{thermal}}$ going down. This would have a direct effect of reducing the advective and diffusive terms. Hence, the assumptions we make here are not entirely realistic but provide a good starting point to introduce collisional effects into our model for the first time.

6.2.1 The Collisional Guiding Centre Equations

Since we consider collisions to happen on very small scales, we may assume that there is no displacement in the guiding centre and thus no collisional term will be added to the perpendicular guiding centre in equation 2.5. The collisional term in Eqn. 6.10 added to the parallel guiding centre equation $\frac{dv_\parallel}{dt}$ in equation 2.3 gives,

$$\frac{dv_\parallel}{dt} = -\frac{\mu}{q}\frac{\partial B}{\partial s} + \mathbf{u}_E \cdot (\frac{\partial \mathbf{b}}{\partial t} + v_\parallel \frac{\partial \mathbf{b}}{\partial s} + \mathbf{u}_E \cdot \nabla \mathbf{b}) + \left[\frac{v_\parallel}{v}\frac{dv}{dt} + v\frac{d\varphi}{dt}\right]_{coll}. \tag{6.13}$$

The equation for the evolution of μ is given by

$$\frac{d\mu}{dt} = \frac{2\mu}{v}\frac{dv}{dt} - \frac{v_\parallel v}{B}\frac{d\varphi}{dt} - \frac{v^2}{2B}{B_\varphi}^2, \tag{6.14}$$

where

$$\frac{dv}{dt} = -K^2 4\pi\rho\frac{q^4}{m^2v^2}\ln\Lambda, \tag{6.15}$$

and

$$\frac{d\varphi}{dt} = -2K^2 4\pi \ln\Lambda\frac{q^4}{m^2}\varphi\frac{\rho}{v^3} + \left[K^2\frac{4\pi\ln\Lambda q^4}{m^2}(1-\varphi^2)\frac{\rho}{v^3}\right]^{1/2}\Delta W(t). \tag{6.16}$$

All the above equations are normalised and for the normalisation of the energy loss term $\frac{dv}{dt}$, for example, see Appendix D. In the two sections which are to follow first the effects of diffusion alone (i.e. terms in the bracket in Eqn. 6.10 and 6.12 are all set to zero) will be investigated. We then look at how introducing energy losses with constant background density will effect the energy and critical pitch angle required for trapping.

6.3 Effects of Pitch Angle Scattering

As a starting point to see how Coulomb collisions affect our CMT model, we begin by only considering the effects due to pitch angle scattering. In a study done by Minoshima et al. (2011) for a different CMT model they introduce collisional effects by only including the diffusion term (pitch angle scattering due to Coulomb collisions) and neglect the advection term which introduces energy losses to the model. They investigate the height distribution of coronal electrons by focusing on energy dependent pitch angle scattering. They find when pitch angle scattering is not included, the electron heights are constant, independent of energy and are mainly distributed at the loop top. However, when they include pitch angle scattering, electron heights are energy dependent and they are distributed to a greater extent along the field lines towards lower altitudes with the

"intermediate energy "electrons at higher altitudes than the "lower and higher energy" electrons at lower altitudes. For this energy dependent distribution when diffusion is included, they find more particles enter the loss cone and are lost from the trap. Hence we would like to check if this is the same for our model; namely, will particle losses increase as a result of introducing pitch angle scattering?

We begin with two test particles both starting from a position $(x, y) = (0, 4.2L)$, a background density of $\rho = 10^{14}\ m^{-3}$ with a starting energy of $E_{init} = 5.5$keV. One particle starts with a pitch angle $\theta_{init} = 160.4°$ and the other with $\theta_{init} = 87.3°$. This is similar to the initial conditions used in Chapter 4. As mentioned in the introduction, the code is currently set up so that the chosen seed is equal to the particle orbit number. However, the seed can be changed and we will use different seeds for our next case study, but here the seed is chosen to be 1. The results are shown in Fig. 6.2 where the first row shows the results for $\theta_{init} = 160.4°$ and the second row for $\theta_{init} = 87.3°$. In the first row, the left plot shows the evolution of the magnetic moment μ, the middle plot, the

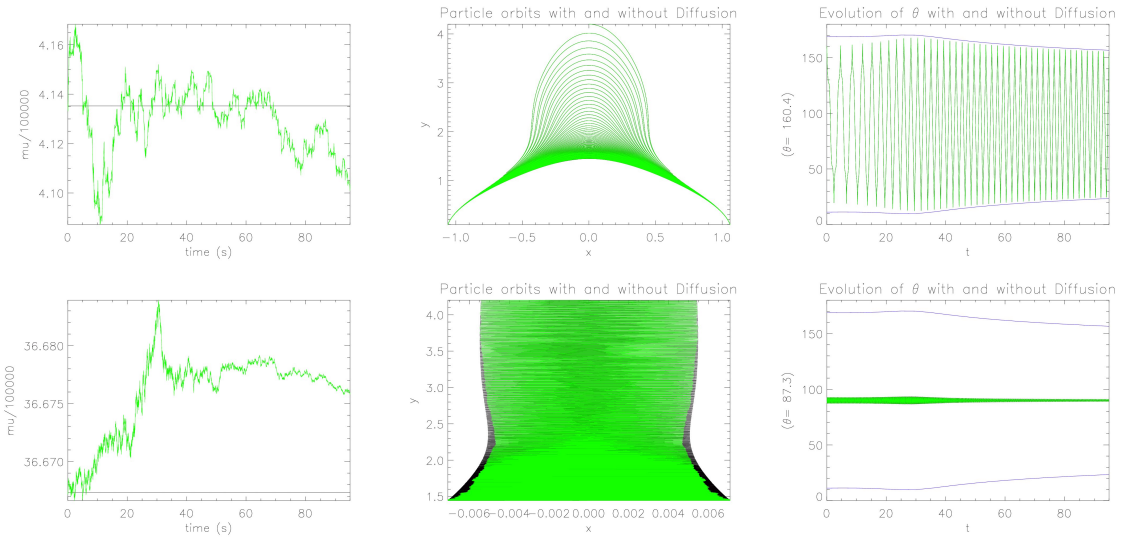

Figure 6.2: Starting from the left, rows one and two show magnetic moment, particle trajectory and pitch angle evolution for $\theta_{init} = 160.4°$ and $\theta_{init} = 87.3°$ respectively. The green represents particles which experience pitch angle scattering where $\rho = 10^{14} m^{-3}$ and black represents particles without.

particle trajectory and the right plot the evolution of the particle pitch angle. The green colour represents the case with pitch angle scattering and the black colour represents the case with no pitch angle scattering. In the first plot on the left the stochastic nature in the evolution of μ is clearly seen in the green graph when pitch angle scattering is introduced. The straight line represents the case where there is no pitch angle scattering and μ remains constant for all time. Looking at the particle trajectories in the middle plot the particle orbit with pitch angle scattering is overplotted on to the case without pitch angle scattering. The plot without pitch angle scattering cannot be

seen here since the orbits coincide spatially. The same goes for the final plot representing the evolution of the particle pitch angle and loss cone. The blue graph shows the evolution of the loss cone identical to the same set up seen in Chapter 4. It seems that the pitch angle evolution for the particle with scattering matches the case without any scattering. The second row in Fig. 6.2 looks at the same variable as discussed for the above but now the initial pitch angle is $\theta_{init} = 87.3°$. It seems that for higher pitch angles a very small difference in the orbits can be seen as shown in the middle graph. We also looked to see if increasing the density ρ to 10^{15} m^{-3} and 10^{16} m^{-3} had

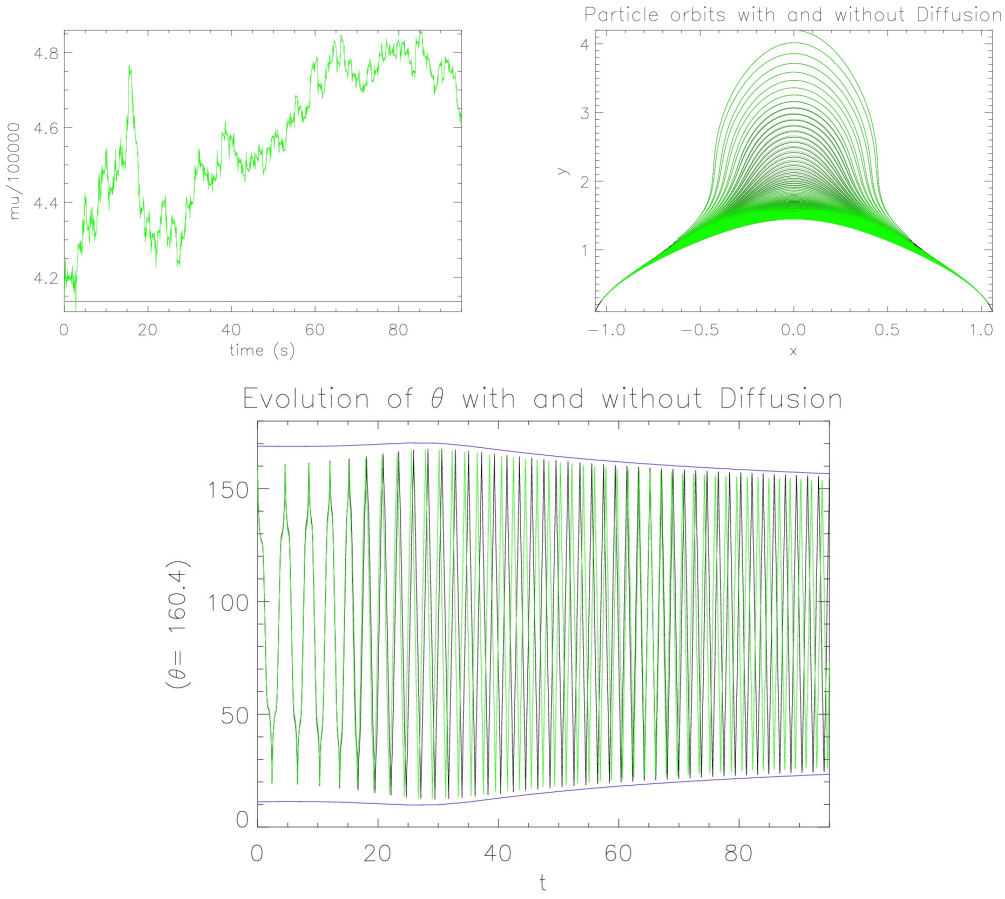

Figure 6.3: Illustrates the magnetic moment evolution, particle trajectory and pitch angle evolution for a particle with $\theta_{init} = 160.4°$. The green represents pitch angle scattering with a density of $\rho = 10^{16}$ m^{-3}. The mirror points for a particle with scattering is higher and the pitch angle seems to be moving away from the loss cone angle compared to a particle without scattering.

any effect on the particle orbit and pitch angle evolution for the two cases discussed above. We found (not shown) the same results as seen in Fig. 6.2 for $\rho = 10^{15}$ m^{-3}. However $\rho = 10^{16}$ m^{-3} which increases the pitch angle scattering effects on the particle, produces the results seen in Fig. 6.3. For this pitch angle scattering case it seems the mirror points are located higher than the case without scattering. Also in the final plot for pitch angle evolution it can be seen that the

two plots do not coincide and the scattering case (green graph) is further away from the loss cone angle than the case without scattering shown by the black graph. Generally it is very difficult to say exactly how only including pitch angle scattering in the model will effect the general trapping and escape results in relation to a case without any scattering. One would have to do a systematic study with different seeds to gain a better understanding and could compare it for example with findings from Minoshima et al. (2011) as a future point of study. However from the results obtained for $\theta_{init} = 160.4°$ and density $\rho = 10^{16}\ m^{-3}$ it would seem that more particles would be trapped since the particle pitch angle seems to move away from the loss cone angle (blue line) compared to the case without any scattering.

Going back to the case where $\rho = 10^{14}\ m^{-3}$ for $\theta_{init} = 160.4°$ in Fig. 6.2, the plot for the particle orbits (top row middle graph) shows no changes in the particle orbit between the scattering (green) and non-scattering (black) case. How would changing the seed and keeping the density the same affect the particle orbits and would there be clear differences between the orbits? We choose three different test particles given by three different seeds and kept the density in each case $10^{14}\ m^{-3}$. We checked the particle orbit plots for each test particle against the non-scattering case and found no differences in the orbits. This result can be explained by the fact that the particle remains on the same field line due to the $\mathbf{E}\times\mathbf{B}$ drift being the dominant term. However, looking at the different particles energy, μ (second row), minimum x displacement (third row) and minimum y displacement (fourth row) evolutions, clear changes in all four plots in Fig 6.4 can be seen. Here the minimum x displacement is the change in position of x from the first mirror point to the final mirror point for a finite time. The minimum y displacement is the change in position of y from the first mirror point to the final mirror point for a finite time.

The left column in Fig. 6.4 shows the energy, μ, minimum x displacement and minimum y displacement evolutions for the different particles with $\rho = 10^{14}\ m^{-3}$ respectively. The right column represents the evolution of the same quantities but for $\rho = 10^{15}\ m^{-3}$. The black line seen more clearly for $\rho = 10^{15}\ m^{-3}$ shows the case for a particle without any pitch angle scattering. The three different particle orbits (3 different seeds) are represented by three different colours which are distributed around this black curve. These changes in energy, μ, x and y can be explained by the fact that along a field line, different particles given by different seeds will acquire different velocities and magnetic moments, since the parallel velocity $v_{\parallel}$ and the magnetic moment μ both contain stochastic terms. Therefore different particles with different velocities and μ will give different energies (first row in Fig. 6.4) and different x and y positions (third and forth row in Fig. 6.4) at a given point in time. A further investigation confirmed that the choice of the seed which affects the values of the random numbers has a direct affect on the values of the final energy of the particle and this is seen from the figure where some seeds give higher energies and some give lower energies.

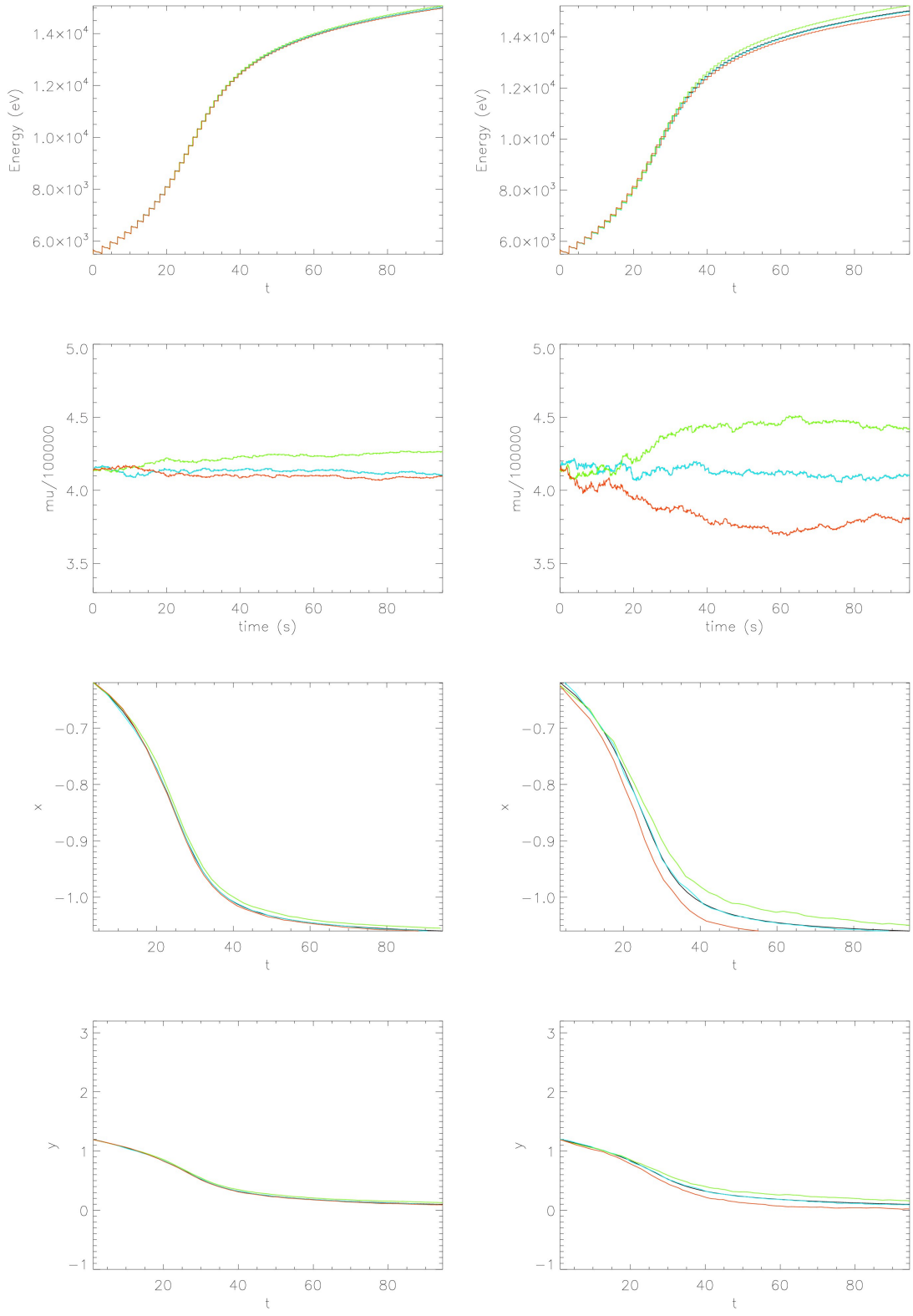

Figure 6.4: *Left column*: shows the energy, magnetic moment, x and y displacement evolution graphs for three different particles with $\rho = 10^{14}m^{-3}$, respectively. *Right column*: shows the same quantities but for $\rho = 10^{15}m^{-3}$m.

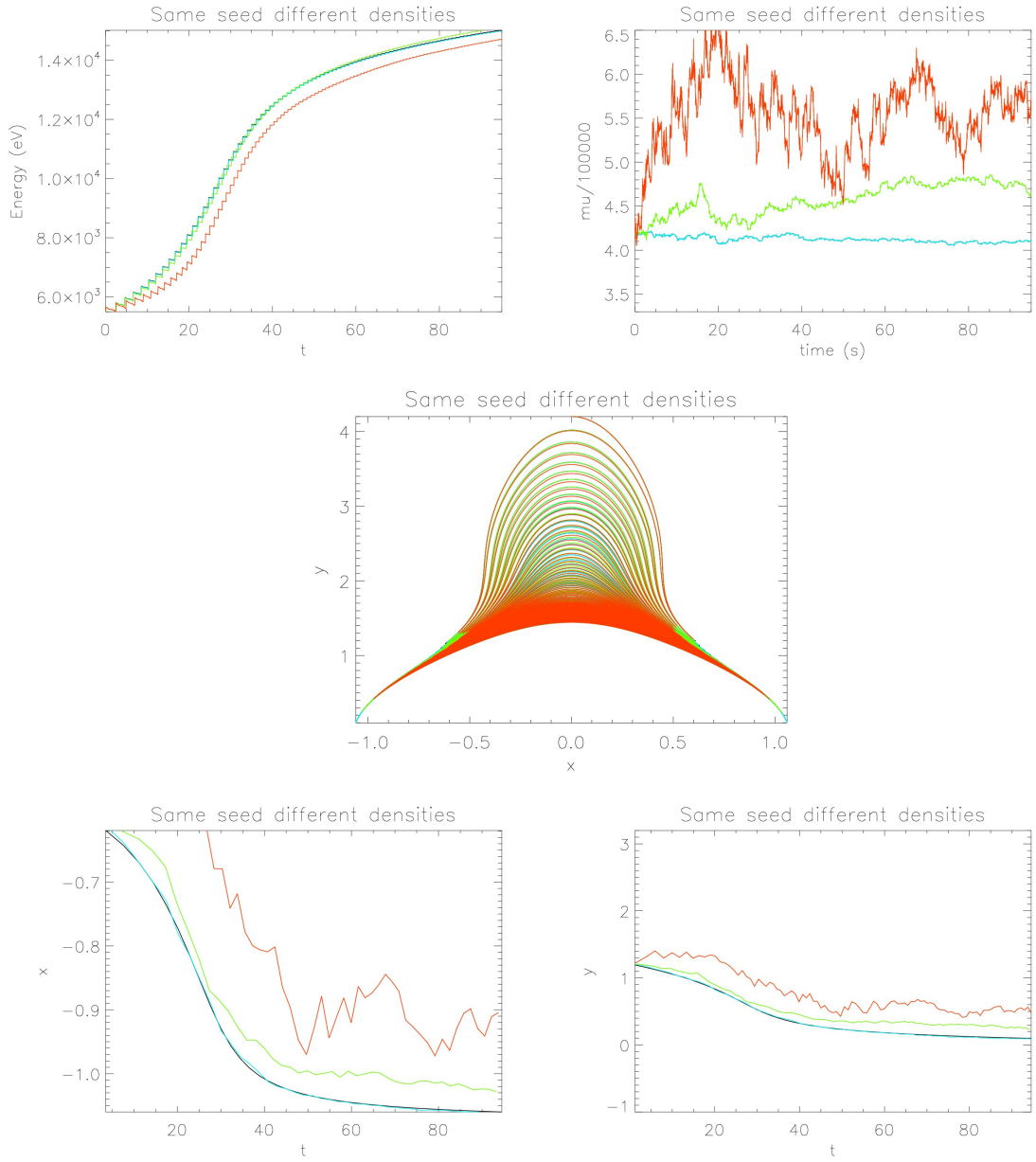

Figure 6.5: *Top left*: Energy evolution for a particle with $\rho = 10^{15}m^{-3}$ (blue), $10^{16}m^{-3}$ (green) and $10^{18}m^{-3}$ (red). *Top Right*: Magnetic moment evolution and *Middle*: particle orbit evolution with increasing mirror height as the particle density increases. *bottom left*: show the x displacement and *Bottom right*: the y displacement which increase in stochacticity as the density increases.

As a final point on the effects of pitch angle scattering on particle trapping we looked at energy, magnetic moment, particle orbit, minimum x and y displacement evolutions for a test particle with $(x, y) = (0, 4.2L)$, $\theta_{init} = 160.4°$, $E_{init} = 5.5$keV, for $\rho = 10^{15}, 10^{16}$ and 10^{18} m^{-3}. Fig. 6.5 shows the evolution of these quantities mentioned respectively. The blue line represents the case

with $\rho = 10^{15}\ m^{-3}$, green for $\rho = 10^{16}\ m^{-3}$ and red the case for $\rho = 10^{18}\ m^{-3}$. The top left plot in Fig. 6.5 shows the evolution of the energy. Initially it seems with increasing ρ the particle gains more energy (as seen for in the green plot for $\rho = 10^{16} m^{-3}$). However, for $\rho = 10^{18}\ m^{-3}$ the final energy of the particle is less than for all the other cases. This could suggest there may be some energy losses also present when only pitch angle scattering is included, but this could also be a numerical effect. The top right in Fig. 6.5 shows the evolution of μ. It is no surprise that with increasing density the stochasticity in evolution of μ (red line) also increases due to the scattering term being proportional to the $\sqrt{\rho}$. For the middle plot we see that as density increases so do the particle's mirror points, suggesting the particle (red plot) has less chance of escaping the trap as it does not travel all the way down to the foot points. For the bottom left and right plots again the stochasticity in x and y respectively is clearly seen in the red plots with increasing ρ.

To investigate the full effects of Coulomb collisions, we introduce the advection term ($\frac{dv}{dt}$ term) which introduces energy losses in the model alongside the diffusion term. In the section to follow we look at the importance of these terms on the behaviour of our CMT model.

6.4 Collisions With a Low ρ

As a starting point to study the effect of collisions in the CMT model, we choose a constant background density of $\rho = 10^9$ m^{-3}. This choice of the density relative to a typical coronal density value of the order of $10^{16}m^{-3}$ is far too low, but we choose this as a starting initial density for numerical reasons which we will discuss in section 6.5. We will compare the particle orbits, the pitch angle evolution and the energies with the results where collisional effects are neglected. We have the following initial conditions: $(x, y, z) = (0, 4.2L, 1.25 \times 10^{-6}L)$, $E_{kin} = 5.5$keV and $\theta_{init} = 160.4°$. Table 6.1 shows the minimum E_{min} and maximum E_{max} energy for the particle

Table 6.1: For density $\rho = 10^9 m^{-3}$ for $\theta = 160.4°$.

	Collisions	No-Collisions	Energy Difference (eV)
$E_{min}(eV)$	5500	5500	0
$E_{max}(eV)$	15018.096	15017.167	0.93

with and without collisions. The third column (energy difference) also shows difference in energies between E_{min} and E_{max}. The percentage change in the value of the maximum energy is $6.18 \times 10^{-3}\%$. In the non-collisional case the magnetic moment μ remains constant. However in the collisional case the value of μ changes. The difference between the maximum and minimum value of magnetic moment, $\Delta\mu = 56.30\ J/T$, giving a percentage change of $\approx 0.013\%$ which is negligible. Also, there are no significant changes in the energy, pitch angle evolution and particle orbit trajectories when compared to the non-collisional case. This can also be seen clearer in the plots in Fig. 6.6. The first plot (top left) shows the evolution of μ in the collisional model for $\rho = 10^9\ m^{-3}$. The stochastic behaviour in the evolution of μ is seen clearly from the plot. This can be explained by looking at the advection $(\frac{dv}{dt})$ and diffusion term $(\frac{d\varphi}{dt})$ in Eqns. 6.15 and 6.16. The energy loss term (advection) for the current choice of φ is smaller than the diffusion term. Hence the random process is much more dominating and this is seen in the plot. For the same reason since energy losses are small, there are no noticeable changes in the energy plots between the collisional case (green colour) which is overplotted on to the non-collisional case (see Fig. 6.6). Even though $\frac{d\varphi}{dt}$ is bigger than $\frac{dv}{dt}$ it is not large enough to have an effect on the pitch angle evolution as seen in the green plot (bottom left). Again the non-collisional case cannot be distinguished due to the two plots matching. For the final plot (bottom right) the particle orbits for the two non-collisional (black) and collisional (green) are plotted.

The second test particle orbit has exactly the same initial conditions as the first test particle orbit, however this time $\theta = 87.3°$. In Table 6.2 the energy difference in E_{min} is $\Delta E_{min} = 0.07$eV which gives a percentage change of $\approx 1.7 \times 10^{-3}\%$. For E_{max} the difference $\Delta E_{max} = 0.745$eV which gives a percentage change of $\approx 3.23 \times 10^{-3}\%$. Finally the difference between the maximum and minimum value of the magnetic moment $\Delta\mu = 129.5\ J/T$, giving a percentage change

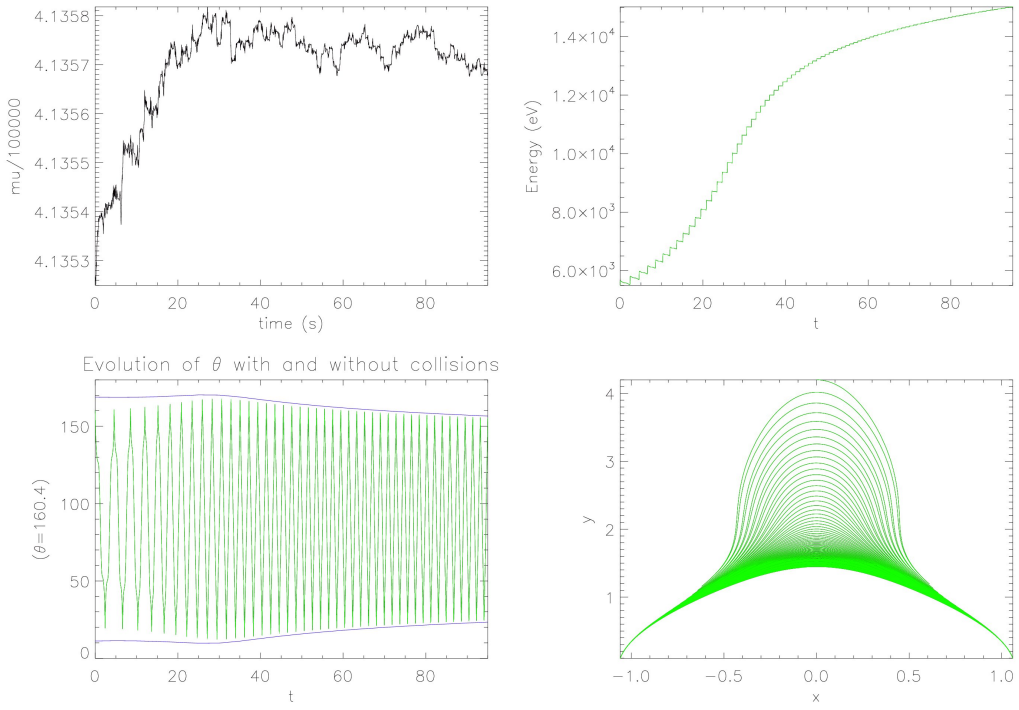

Figure 6.6: *Top left*: shows the evolution of the magnetic moment μ, *Top right*: the evolution of particle energy, *bottom left*: shows the evolution of the pitch angle θ and *Bottom right*: the particle orbits starting with $(x, y) = (0, 4.2L)$ and $\theta_{init} = 160.4°$. Green represents the particle which experiences collisional effects at a density of $\rho = 10^9\ m^{-3}$. There are no significant changes in the magnetic moment, energy, pitch angle and particle orbit graphs as particle barely feels any collisional effects due to the very low density.

of $\approx 0.035\%$. In the first plot (top left) in Fig. 6.7 the stochastic nature of μ is not as pronounced

Table 6.2: For density $\rho = 10^9 m^{-3}$

	Collisions	No-Collisions	Energy Difference (eV)
$E_{min}(eV)$	4099.14	4099.21	0.07
$E_{max}(eV)$	23008.21	23008.955	0.745

as Fig. 6.6. However the effect is still present if looked at carefully. The energy graphs (top right) again for the collisional and non-collisional coincide due to small energy losses. The initial dip seen in the graph is due to the particle going through the weak magnetic field region at the top of the trap and the particle losing energy due to the invariance of μ. The bottom two figures show no visible changes. Generally since the choice of $\rho = 10^9\ m^{-3}$ is a very small background density, the size of the changes is expected because the collisional effects are small. Hence the overall changes in the velocity of the particle in the current set up is insignificant. In the next section we look at the effects of increasing the background density on the quantities discussed in this section.

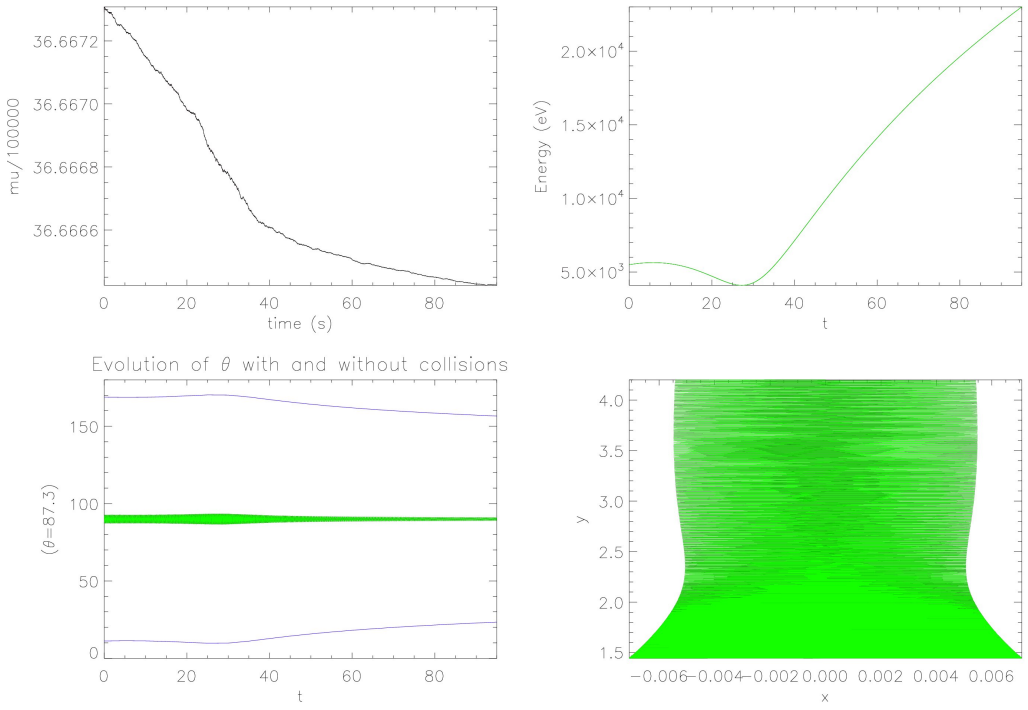

Figure 6.7: *Top left*: shows the evolution of the magnetic moment μ, *Top right*: the evolution of particle energy, *bottom left*: shows the evolution of the pitch angle θ and *bottom right*: the particle orbits starting at $(x, y) = (0, 4.2L)$ and $\theta_{init} = 87.3°$. Green represents the particle which experience collisional effects at a density of $\rho = 10^9\ m^{-3}$. There are no significant changes in the magnetic moment, energy, pitch angle and particle orbit graphs as particle barely feels any collisional effects due to the very low density.

6.5 Collisions with Increasing Density ρ

Following on from the previous section, we will investigate the effect of increasing a constant density on the evolution of μ, energy, pitch angle and particle orbit. As before we will be using the non-collisional test particle orbit as a benchmark for the collisional case. For this test particle orbit we use the same initial conditions as before and $\rho_{init} = 10^{10}, 10^{11}, 10^{13}, 10^{14} m^{-3}$. The results obtained from the model using the different densities are shown in the Tables 6.3, 6.4, 6.5 and 6.6 respectively. In Table 6.3 the energy difference $\Delta E \approx 0.015$eV giving a very small percentage change. The change in the magnetic moment for a constant density of $\rho = 10^{10}\ m^{-3}$ is $\Delta\mu \approx 196\ J/T$, giving a very small percentage change. In Table 6.4 for $\rho = 10^{11}\ m^{-3}$ the percentage change in energy is $\approx 0.08\%$ and for the magnetic moment is $\approx 0.25\%$. For a density of $\rho = 10^{13}\ m^{-3}$ as seen in Table 6.5 the percentage change in energy increase to $\approx 14.77\%$ compared to the previous two cases. The percentage change in the magnetic moment is now $\approx 14.22\%$. This is a significant change and one that shows the long-term invariance of μ is no longer valid in the case where collisions are significant. For the case where $\rho = 10^{14}\ m^{-3}$ as seen

in Table 6.6, the final energy for the collisional case is ≈ 0.19eV. Preliminary quantitative results suggest that with the initial conditions $E_{init} = 5.5$keV, $(x, y) = (0, 4.2L)$ and $\theta_{init} = 160.4^{\circ}$ the particle does not have sufficient energy to overcome the collisional effects and stops. Since the background atmosphere is not evolving, the particle trapped on the field lines experiences large dragging effects and only moves for ≈ 14 seconds in the simulation as seen in bottom left hand plots of Figs. 6.8 - 6.11.

Table 6.3: For density $\rho = 10^{10} m^{-3}$

	Collisions	No-Collisions
$E_{min}(eV)$	5500	5500
$E_{max}(eV)$	15017.182	15017.167

Table 6.4: For density $\rho = 10^{11} m^{-3}$

	Collisions	No-Collisions
$E_{min}(eV)$	5500	5500
$E_{max}(eV)$	15004	15017.167

Table 6.5: For density $\rho = 10^{12} m^{-3}$

	Collisions	No-Collisions
$E_{min}(eV)$	5450.72	5500
$E_{max}(eV)$	12798.41	15017.167

Table 6.6: For density $\rho = 10^{14} m^{-3}$

	Collisions	No-Collisions
$E_{min}(eV)$	0.19	5500
$E_{max}(eV)$	5638.68	15017.167

In Fig. 6.8 the evolution of μ (top left and going across) in the CMT for different constant density values of $\rho = 10^{10}$, 10^{11}, 10^{13}, 10^{14} m^{-3} and a stratified density of $\rho = \rho_0 e^{-\frac{y}{H}}$ where $\rho_0 = 10^{14}$ m^{-3} are shown respectively. The first plot in Fig. 6.8 shows the evolution of μ for a constant density of $\rho = 10^{10}$ m^{-3}. The graph clearly shows the random nature in the evolution of μ for a low atmospheric density. The diffusion term here is still the dominating term in relation to the advection term $\frac{dv}{dt}$. The next plot (top right) where $\rho = 10^{11}$ m^{-3} still shows the random nature present in the evolution of μ but not as prominent as the first plot. For both these cases the percentage difference between μ with and without collisions as discussed above is still very small so μ can still be considered as an approximate invariant. In the middle plot for $\rho = 10^{13}$

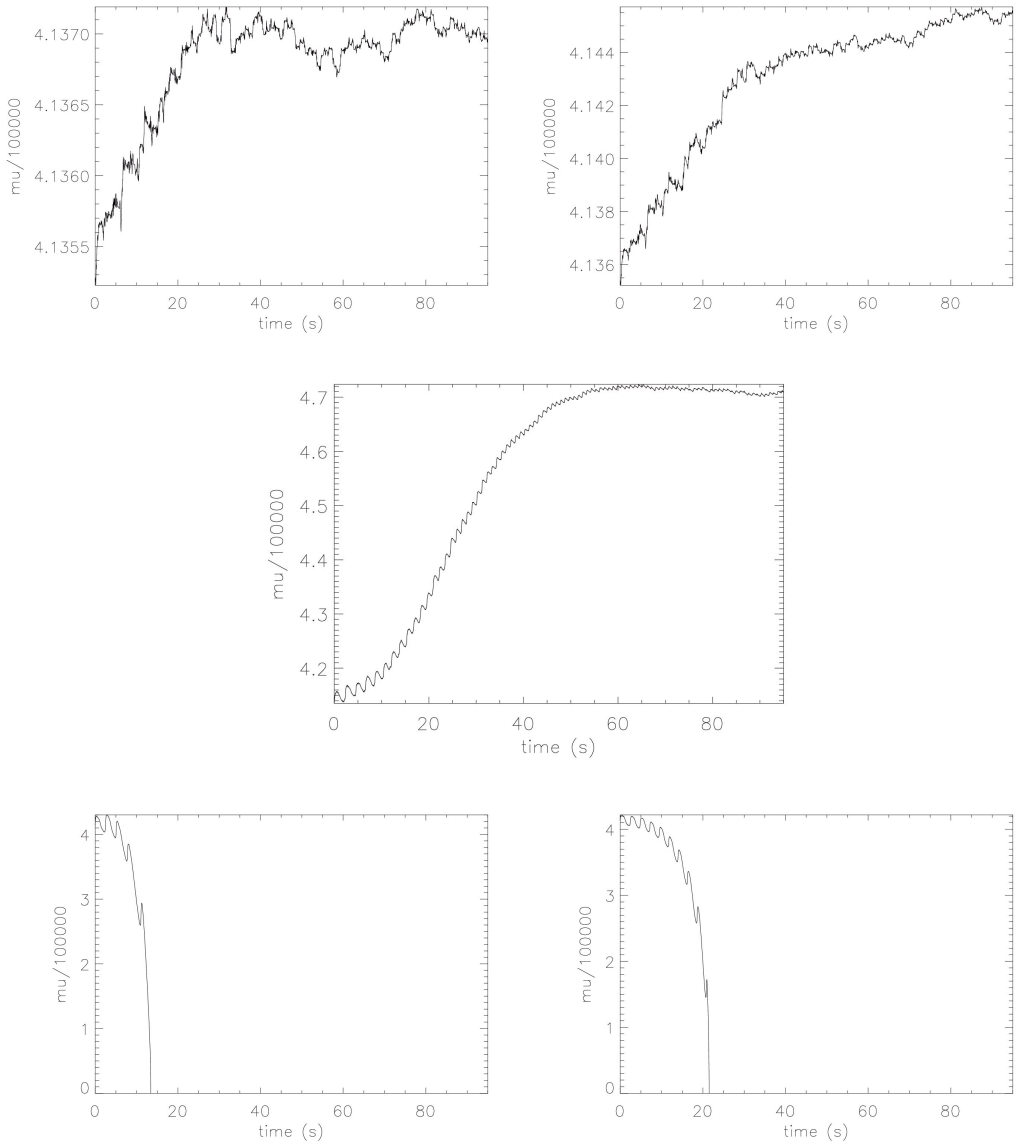

Figure 6.8: Starting from the top left hand corner and moving across, the variation of μ for densities $\rho = 10^9, 10^{11}, 10^{13}$ and $10^{14} m^{-3}$ respectively are shown. From the middle graph onwards the invariance of μ is no longer valid over long time scales.

m^{-3} we begin to see a change in the behaviour of μ. The magnetic moment begins to loose its random nature and moves towards a more predictable behaviour; gradually increasing with time and levelling off at the end of the simulations. The percentage change is now at a noticeable level (14.22%) and μ no longer can be thought of as an invariant over long times. For the bottom left hand graph where $\rho = 10^{14}\ m^{-3}$, the effects of the drag terms are so strong that the simulation stops at approximately 14 seconds. With the current assumption of a constant $\rho = 10^{14}\ m^{-3}$ the collisional effects are too strong. This causes the particle orbit to experience a large dragging

effect and stop after a few seconds. Since the evolution is cut short the particle orbit does not gain sufficient energy to overcome the collisional effect and loses energy very fast. Finally we checked to see if stratifying the density, i.e. $\rho = \rho_0 e^{-\frac{y}{H}}$ where the pressure scale height $H = 61$Mm and $\rho_0 = 10^{14}\ m^{-3}$ makes any difference to the evolution of μ. we see in Fig. 6.8 the simulation carries on for approximately another extra $8 - 10$ seconds longer than the case for constant $\rho = 10^{14}\ m^{-3}$. The stratification of the background atmosphere helps the particle evolve a bit longer with the stopping time being now approximately 22 seconds. Again this is not enough to overcome drag effects on the particle orbit.

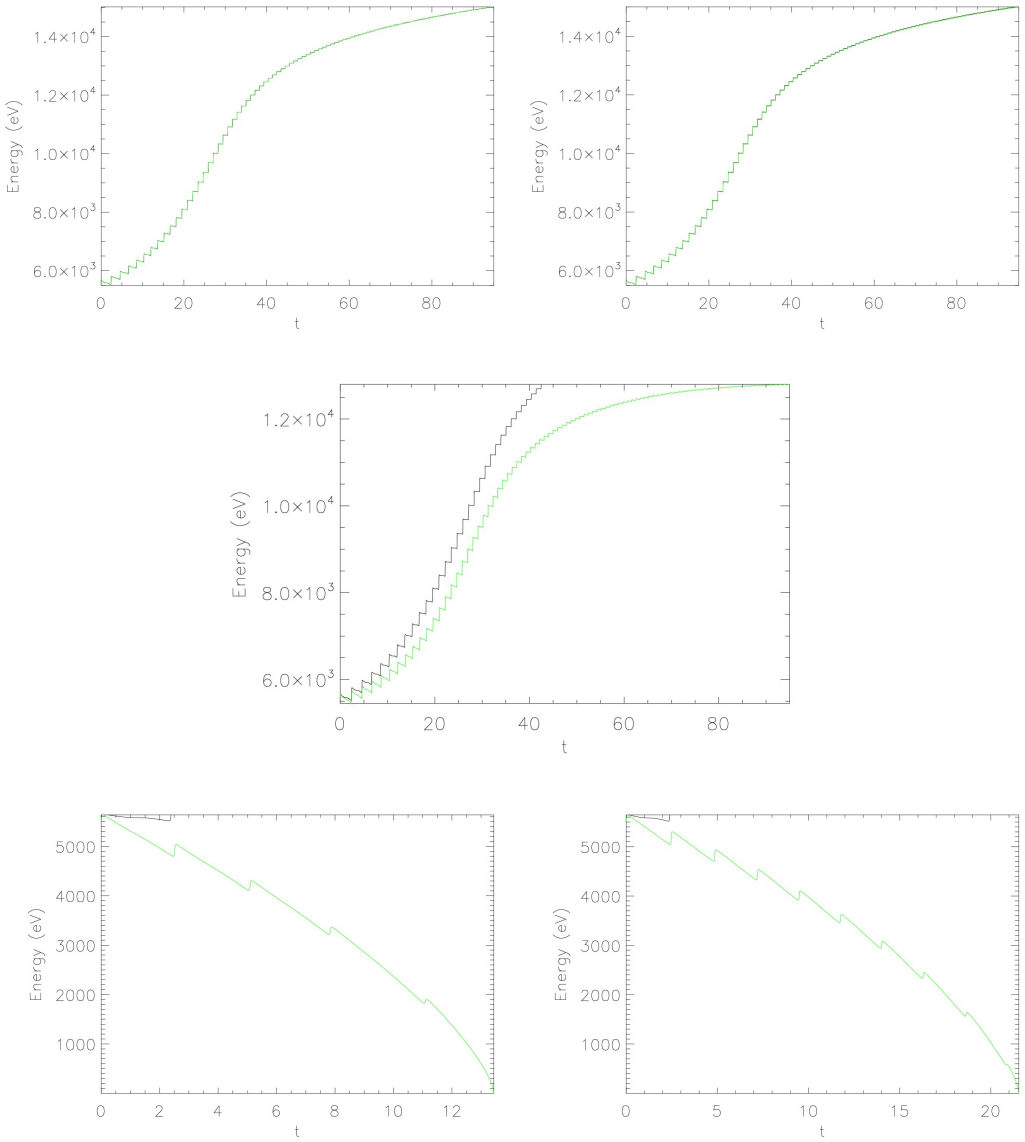

Figure 6.9: Starting from the top left hand corner and moving across, the evolution of the pitch angle with collisions (green) and non collisions in (black) for densities $\rho = 10^{10}, 10^{11}, 10^{13}$, $10^{14} m^{-3}$ and a stratified density $\rho = \rho_0 e^{-\frac{y}{H}}$ respectively are shown.

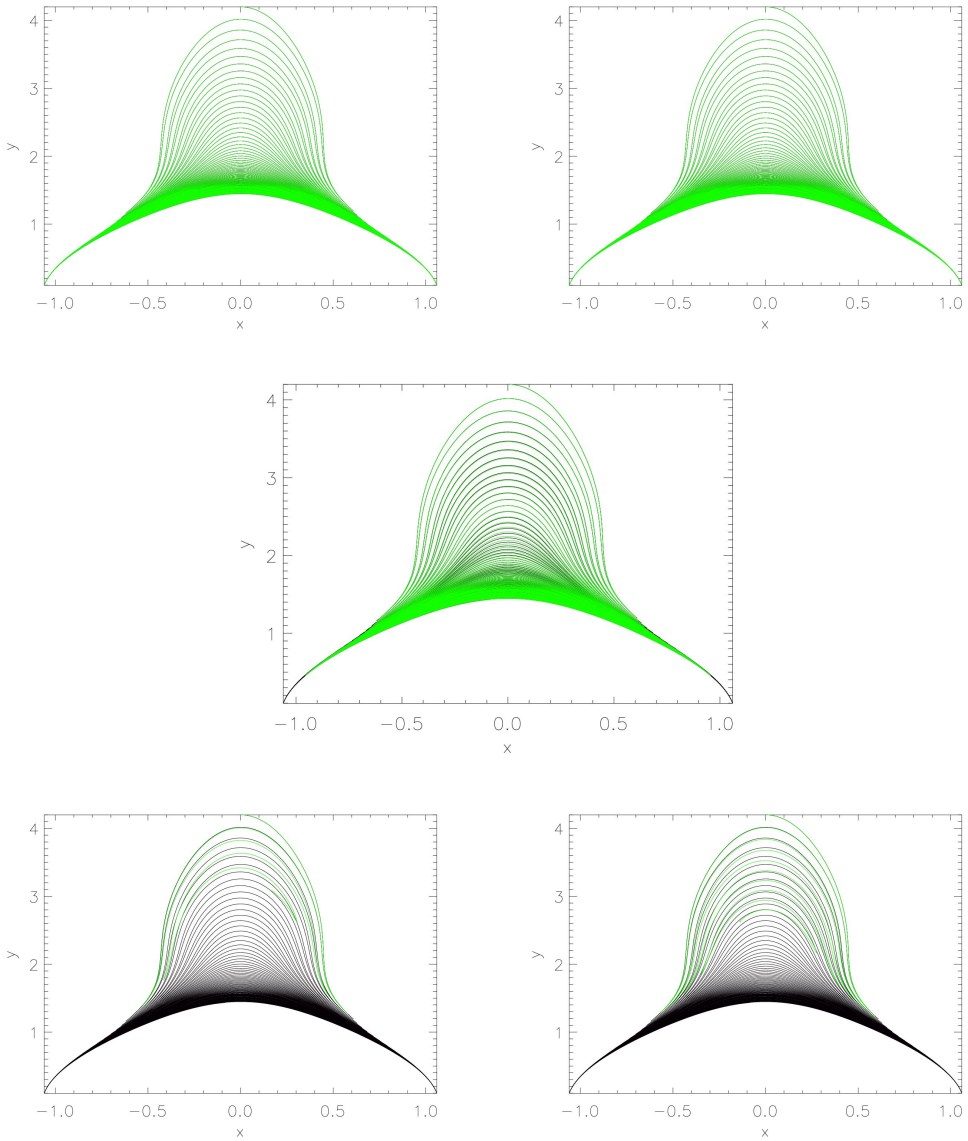

Figure 6.10: Starting from the top left hand corner and moving across, the particle orbits collisional (green) and non collisional case for densities $\rho = 10^{10}, 10^{11}, 10^{13}, 10^{14} m^{-3}$ and a stratified density $\rho = \rho_0 e^{-\frac{y}{H}}$ respectively are shown. Higher mirror points are seen with increasing density.

Figures 6.9 - 6.11 represent the energy evolution, particle orbit and pitch angle evolution for each of the plots discussed in Fig. 6.8. The green colour represents the particle orbit where collisional effects are included and the black colour represents the particle orbit where collisions are not. Since the changes in energy and μ discussed previously for the top two plots were very small, there is no evident change in the two particle orbits (top left and right) plots in Fig. 6.10. The middle graph as mentioned previously marks the point where changes in both the evolution of energy and magnetic moment become noticeable. Hence there is a clear change between the collisional

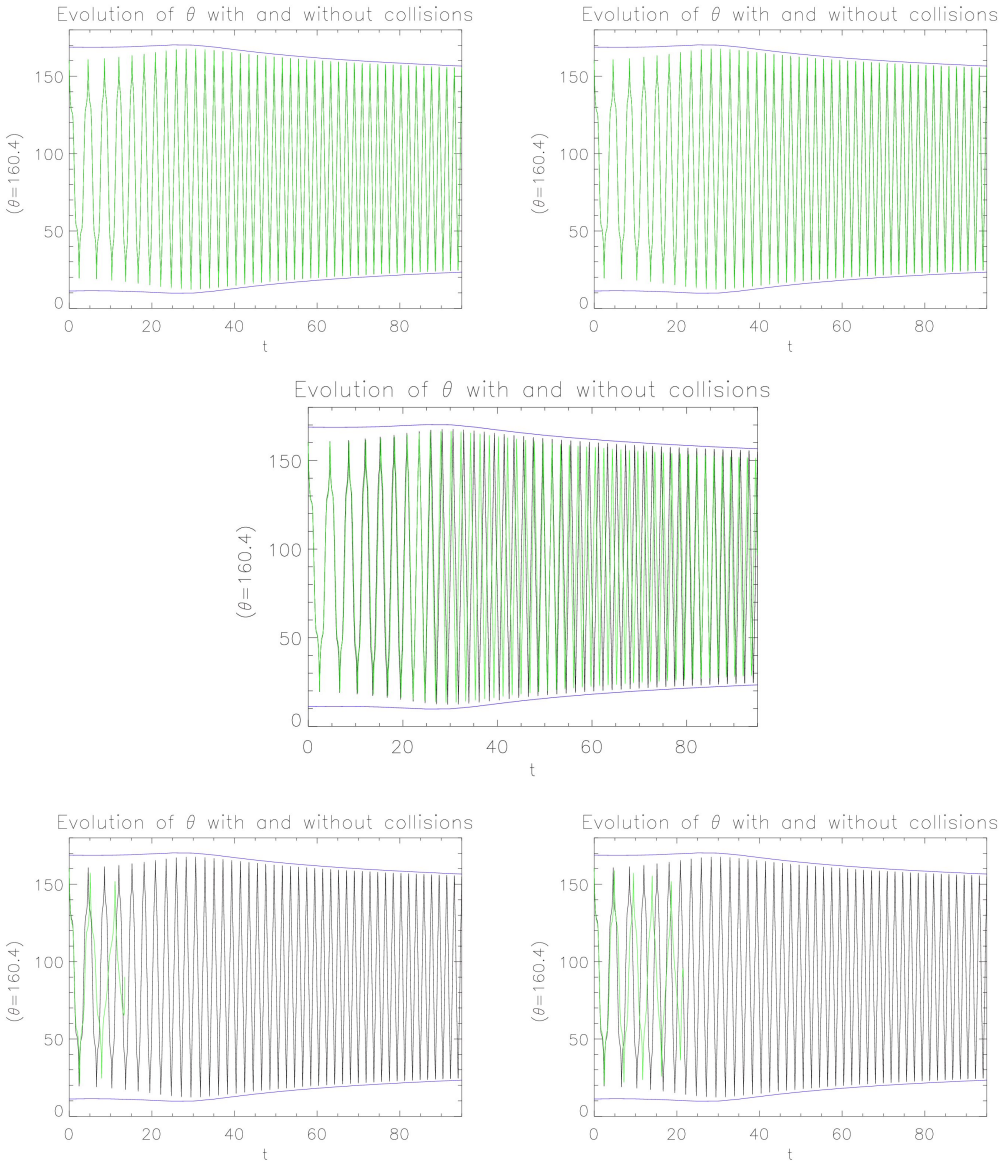

Figure 6.11: Starting from the top left hand corner and moving across, the evolution of the pitch angle with collisions (green) and non collisions in (black) for densities $\rho = 10^{10}, 10^{11}, 10^{13}$, $10^{14} cm^{-3}$ and a stratified density $\rho = \rho_0 e^{-\frac{y}{H}}$ respectively are shown.

(green) and the non-collisional (black) orbits particularly at the foot points. The collisional case seems to have higher mirror points than the non-collisional case. This suggests that a particle orbit is more likely to be trapped. Looking at the evolution of the pitch angles seen in Fig. 6.11, the blue line shows the evolution of the loss cone angle, as discussed in Chapter 4. As before, the first two plots at the top are the same. In the middle plot the difference between the two orbits is much clearer. The orbits are no longer matching and differ particularly at the latter stages of the evolution. The general behaviour of both orbits as they evolve through the region of decreasing

magnetic field in the model seems to be similar. It is when they move into a region of increasing magnetic field (≈ 30 seconds) that the green pitch angle plot seems to move away from the non-collisional plot in black. We know from our investigation in Chapter 4 that a particle orbit starting with an initial pitch angle of $\theta_{init} = 160.4^{\circ}$ will eventually escape from the trap where the pitch angle gets closer and closer to the loss cone angle (blue line). However in the case of a particle with $\theta_{init} = 160.4^{\circ}$ where collisions are introduced, the green line representing the pitch angle evolution seem to move away from the blue line. This would seem to suggest that collisional effect (seem to) cause a particle with a pitch angle starting at $\theta_{init} = 160.4^{\circ}$ or (19.6°) to be trapped for all time, since it seems θ is tending towards 90° rather than towards the loss cone angle.

6.6 The Critical Initial Energy

In this section we investigate the relationship between density and initial energy in the CMT model for a particular test particle orbit. We use the following initial conditions: $(x, y, z) = (0, 4.2L, 1.25 \times 10^{-6}L)$, $\theta_{init} = 160.4^{\circ}$, $\rho_{init} = 10^{14}m^{-3}$ and use three different values for the initial energy: $E_{init} = 7.0, 8.5, 10.6$keV. In the previous section we saw that an initial energy $E_{init} = 5.5$keV was too small to overcome the losses from the drag terms. Therefore, we look for the critical E_{init} a particle orbit with the above initial conditions requires to overcome collisional effects and gain energy over a finite time of 95 seconds.

Table 6.7: For initial energy $E_{init} = 7.0keV$

	Collisions	No-Collisions
$E_{min}(eV)$	0.945	7000
$E_{max}(eV)$	7160.65	19119.176

Table 6.8: For initial energy $E_{init} = 8.5keV$

	Collisions	No-Collisions
$E_{min}(eV)$	0.35	8500
$E_{max}(eV)$	8679.96	23203.9

Table 6.9: For initial energy $E_{init} = 10.6keV$

	Collisions	No-Collisions
$E_{min}(eV)$	1193.83	10600
$E_{max}(eV)$	11524.36	28950.64

Table 6.7 shows the maximum and minimum energies for a particle starting with a starting energy of $E_{init} = 7$keV. Also one can see the losses from the drag term are still dominating and the particle stops after some time. We increase E_{init} to 8.5keV and find the particle moves longer than for the cases where E_{init} is smaller. However this initial energy is still not sufficient enough for the particle to counteract the collisions. It is found that for $E_{init} \approx 10.6$keV the particle is able to overcome the collisional losses. The particle orbits and pitch angle evolutions for the cases discussed here are seen in Figures 6.12 and 6.13. In Fig. 6.12 the particle orbit for the non-collisional (black) and collisional (green) case for a constant $\rho = 10^{14}\ m^{-3}$ and $E_{init} = 7$, 8 and 10.6keV are shown respectively. It can be seen that the first two orbits for the collisional case stop before the finite time for the calculation, the first one earlier than the second one. The final graph shows the particle completing an orbit for $E_{init} \approx 10.6$keV for the finite time. From the plot it can be seen that the mirror points are much higher than in the non-collisional case. Looking at the particle

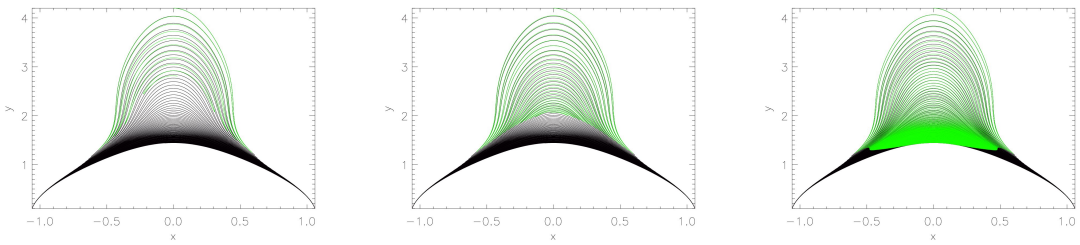

Figure 6.12: Starting from the left and moving across, the particle orbits collisional (green) and non collisional case for different initial energies $E_{init} = 7.0$, 8.5 and 10.6keV respectively are shown. Particles with collisional effects seem to mirror higher than particles with no collisional effects.

evolution plots (Fig. 6.13) for each case, a clear trend is seen in the evolution of the pitch angle for a collisional case (green) where θ is tending towards 90°. This seems to suggest, a particle starting at $\theta = 160.4°$, $E_{init} = 10.6$keV, $\rho = 10^{14}\ m^{-3}$ at a position $(x, y) = (0, 4.2L)$ will be trapped, compared to the non-collisional case which eventually escapes from the trap. We also check to

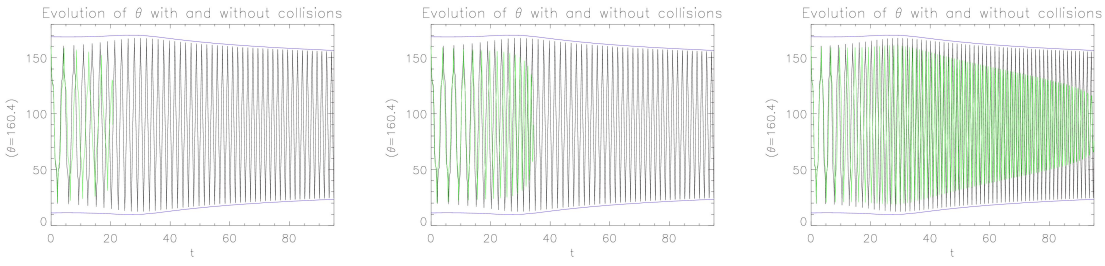

Figure 6.13: Starting from the left and moving across, the evolution of the pitch angle with collisions (green) and non collisions (black) for for different initial energies $E_{init} = 7.0$, 8.5 and 10.6keV respectively are shown. The final graph show the particle pitch angle tending towards 90°, implying the particle will be trapped for all time.

see what the minimum starting energy would be for a particle starting at $(x, y) = (0, 4.2L)$, $\theta_{init} = 87.3°$ with a background density of $\rho = 10^{14}\ m^{-3}$. Fig. 6.14 shows the particle orbit for a particle starting at $E_{init} = 9, 12.5$ and 16.2 keV. The particle orbit in black is for a particle with an initial pitch angle $\theta_{init} = 160.4°$ for a case with no collisions, to make clear the evolution of the particle with $\theta_{init} = 87.3°$ with collisional effects. It can be seen that the green orbit (with collisions) stops before the finite time as seen in the first (left) and second (middle) plot in Fig. 6.14 for starting energies, $E_{init} = 9$ and 12.5 keV respectively. Systematically the energy is increased until for a starting energy of approximately 16.2keV the particle completes an orbit for the finite time of $t = 95$ seconds. These preliminary results seem to suggest that particles with pitch angles closer to $90°$ require a higher initial energy to keep evolving than particles with smaller starting pitch angles in the collisional case.

In most of the literature the background density is chosen to be $\rho = 10^{10}\ cm^{-3}$ or $10^{16}\ m^{-3}$ for a typical active region. Karlicky and Barta (2006) choose a density $\rho = 10^{10}\ cm^{-3}$ which decreases in the vertical direction of their CMT model. Fletcher (1995) chooses a constant density of $3 \times 10^{10} - 10^{11}$ electrons cm^{-3} and Minoshima et al. (2011) choose an initial density of $\rho = 10^{10}\ cm^{-3}$ when considering pitch angle diffusion in their model. Hence, in the next section we check to see how increasing the density by a factor 10 ($\rho = 10^{15}\ m^{-3}$) and by a factor of 100 ($\rho = 10^{16}\ m^{-3}$) affects the starting energy needed for the particle to complete an orbit in the finite time.

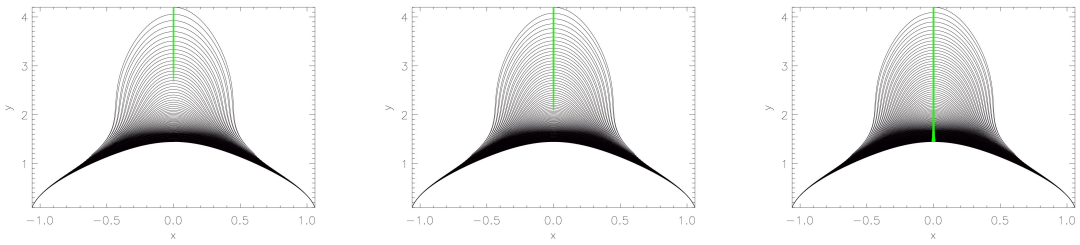

Figure 6.14: Starting from the left and moving across, the particle orbits collisional (green) and non-collisional (black) case for different initial energies $E_{init} = 9$, 12.5 and 16.2keV respectively are shown. The orbit in black represents the particle with $\theta_{init} = 160.4°$ with no collisions to illustrate how the particle with $\theta_{init} = 87.3°$ evolves for different energies for $\rho = 10^{14} m^{-3}$. Particles with pitch angles closer to $90°$ require a higher initial energy than particles with smaller starting pitch angles.

6.7 Effects of Increasing Density on Energy

In this section we look at the how increasing the density $\rho = 10^{15}\ m^{-3}$ and $10^{16}\ m^{-3}$ affects the critical starting energy for the test particle starting at $(x, y, z) = (0, 4.2L, 1.25 \times 10^{-6}L)$, $\theta_{init} = 160.4°$, $\rho_{init} = 10^{15}m^{-3}$ and $E_{init} = 20.5, 40.5, 49.1$ keV. The results obtained from the model using the different densities are shown in Tables (6.10), (6.11), (6.12) respectively. In the previous section the minimum starting energy for a constant density $\rho = 10^{14}\ m^{-3}$ and $\theta_{init} = 160.4°$ was found to be 10.6 keV. For a $\rho = 10^{15}m^{-3}$ this energy is not sufficient to overcome the drag term which increase in size due to increasing density. The particle orbit stops within the finite time of the calculation. We increase the initial starting energy for the first two simulations to be $E_{init} = 20.5$ and 40.5keV. For both cases the particle orbits still fall short of reaching the set finite time and stop. The plots for the particle orbits and pitch angle evolutions for these two test cases can be seen in the left and middle plots in Figs. 6.15 and 6.16 respectively.

Table 6.10: For initial energy $E_{init} = 20.5keV$

	Collisions	No-Collisions
$E_{min}(eV)$	0.3	20500
$E_{max}(eV)$	20760	55990

Table 6.11: For initial energy $E_{init} = 40.5keV$

	Collisions	No-Collisions
$E_{min}(eV)$	0.11	40500
$E_{max}(eV)$	40893	113212

Table 6.12: For initial energy $E_{init} = 49.1keV$

	Collisions	No-Collisions
$E_{min}(eV)$	3804	49100
$E_{max}(eV)$	53099	134063

By systematically increasing the energy, we find the required critical initial energy for the particles to complete an orbit in the finite time to be approximately 49.1keV. As with the findings in the previous section, the plot on the right in Fig. 6.15 shows the mirror points for the particle to be higher than mirror points for the non-collisional case. Also the same behaviour for the pitch angle evolution seen in the previous section is seen in Fig. 6.16, where θ is tending towards 90°. Increasing the density to $\rho = 10^{16}\ m^{-3}$ which is seen as a typical active region density, we find the critical initial energy to be $E_{init} \approx 228$keV. This is a substantial increase from the case for $\rho = 10^{15}\ m^{-3}$.

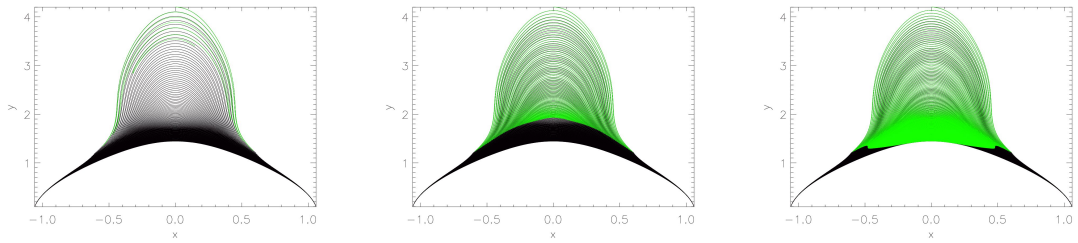

Figure 6.15: Starting from the left and moving across, the particle orbits collisional (green) and non collisional case for different initial energies $E_{init} = 20.5, 40.5$ and $49.1keV$ respectively are shown. As seen previously the mirror points with collisions are higher than without.

Before going on to our last section where we look at the critical angle for trapping in a colli-

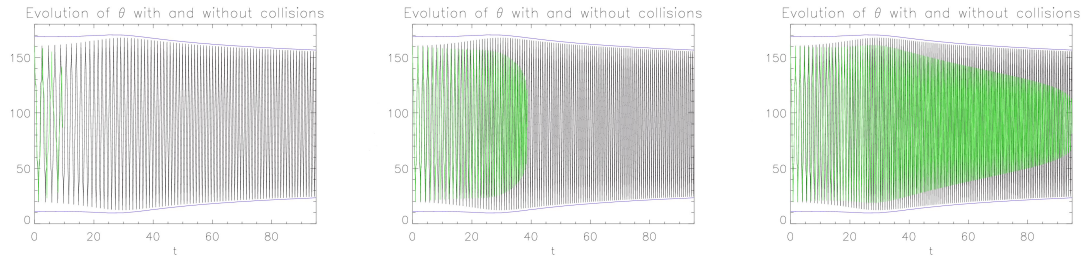

Figure 6.16: Starting from the left and moving across, the evolution of the pitch angle with collisions (green) and non-collisions in (black) for for different initial energies $E_{init} = 20.5, 40.5$ and $49.1keV$ respectively are shown. Again the pitch angle in green is tending towards $90°$.

sional case, we further analysed the effect of increasing the background density to $\rho = 10^{15}\ m^{-3}$ for a particle starting with an initial pitch angle of $\theta_{init} = 87.3°$. We find (plots not shown), the minimum energy required for the particle to overcome collisional effect was approximately 75.2keV. For an even higher density of $\rho = 10^{16}\ m^{-3}$ the initial energy needs to be approximately 349keV which is already in the relativistic regime and clearly highlights the limitation of the model with the current assumptions.

Obviously, the assumption of a uniform, static background atmosphere for a typical coronal temperature and density may be unrealistic for a flare. While beyond the remit of this thesis, one possible improvement for future work would be to include a time-dependent background density along the lines of Chapter 5. Furthermore, the possibility of a higher background temperature close to the range of a flaring plasma could be explored. This would require to change the collision terms as the high energy approximation for all rest particle energies may no longer be valid. This would decrease the effect of energy losses as well.

6.8 $\theta_{critical}$ for Particle Trapping

In Chapter 4 we found that for a particle starting with a position $(x, y, z) = (0, 4.2L, 1.25 \times 10^{-6}L)$, pitch angle $\theta_{init} = 160.4°$ and energy $E_{init} = 5.5$keV with no collisions, the critical angle, $\theta_{critical}$, where all particles with pitch angles greater than this threshold angle are trapped for all time is $\approx 21°$. In this section we want to investigate what is $\theta_{critical}$ when collisions are

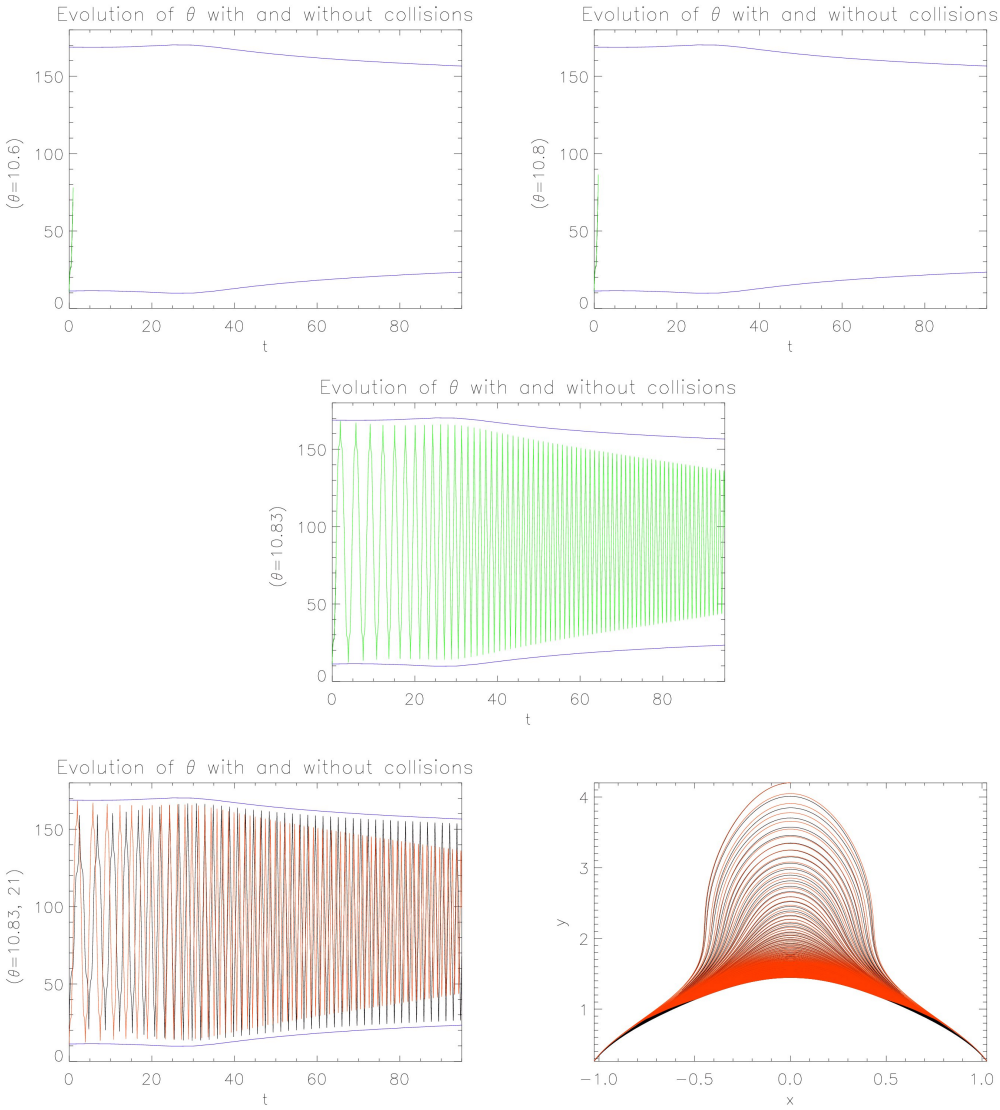

Figure 6.17: *Top left*: Pitch angle evolution for a particle starting with $\theta_{init} = 10.6°$ and *Top right*: particle starting with $\theta_{init} = 10.8°$. Both particles are lost from the trap. *Middle*: Evolution of the critical angle for an initial pitch angle of $\theta_{init} = 10.83°$. *Bottom left*: shows how the collisional pitch angle tends towards $90°$. *Bottom right*: Mirror points of the collisional particle orbit (red) are higher than the non-collisional case in black.

introduced. With the introduction of collisions into the model a stochasticity is introduced into the

particle orbits. Hence a definitive statement about what will be the critical angle for trapping when collisions are introduced into the model will be difficult to make. However, to initiate an investigation we begin with a similar approach to the non-collisional case where the particle position is the same as before. A constant background density of $\rho = 10^{14}\ m^{-3}$ with an initial energy of $E_{init} = 10.6$ keV is chosen. We naturally choose $\theta_{init} = 21^{\circ}$ as a starting pitch angle to see if we need to choose angles smaller or greater than this point to find $\theta_{critical}$ for the collisional case. It turns out for this starting angle the particle will be trapped for all time since the pitch angle tends towards 90°. Hence particles starting with $\theta \geq 21^{\circ}$ will be trapped for all time. We then check for smaller starting pitch angles to find the approximate value of $\theta_{critical}$ in the collisional case.

We start with $\theta_{init} = 10.6^{\circ}$ and find the particle is lost from the trap immediately. This can be seen in the top left hand plot in Fig. 6.17 where the green line represents the evolution of θ and the blue line the evolution of the loss cone angle. Next we check for $\theta_{init} = 10.8^{\circ}$ and the same behaviour as before is observed (top right Fig. 6.17). We systematically increase the pitch angle in small increments and find for $\theta_{init} \approx 10.83^{\circ}$ the particle is trapped for all time as seen from the middle plot. The bottom two plots in Fig. 6.17 show the evolution of the pitch angle and particle orbit respectively for two particle starting with $\theta_{init} = \theta_{critical}$. The red graphs represent the collisional case where $\theta_{init} = 10.83^{\circ}$ and the plots in black are for a particle starting with $\theta_{init} = 21^{\circ}$. From the bottom left hand graph, clearly the particle in the collisional case is tending towards 90°. The orbits are compared in the final plot and again the mirror points in the collisional case are positioned higher than the non-collisional case. Preliminary results from this study also seem to suggest that generally the critical trapping angle in the collisional case is smaller than in the case without collisions. Also the particle orbits with collisions should be seen as stochastic orbits, therefore making it difficult to make a definitive statement whether the critical trapping angle decreases when collisions are introduced. As we have stated throughout this chapter these studies need to be seen as initial numerical tests and benchmarks for future investigations where more realistic assumptions should be used.

6.9 Discussions and Conclusions

In this chapter we took the first steps to introduce Coulomb collisions into the Giuliani et al. (2005) model. We looked at the effects of a low constant density, increasing density, and found the critical initial energy necessary to overcome the collisional effects and the critical pitch angle required for trapping in the model.

We began our study with looking at how pitch angle scattering alone would have an effect on the particle evolution in the Giuliani et al. (2005) model as was done by Minoshima et al. (2011). In their results they find more particles enter the loss cone and are lost from the trap. However, we seem to find the opposite, whereby in general it seems more particles are trapped in our model. Particularly, when we looked at the pitch angle evolution (see Fig. 6.3) the pitch angle in the collisional case seems to be tending towards $90°$, away from the loss cone angle, as opposed to the non-collisional case. This would also seem to suggest that betatron acceleration is the dominating mechanism responsible for particle energisation. If we wanted to do a detailed investigation into how pitch angle scattering alone could affect particle evolution in our trap and compare it to Minoshima et al. (2011)'s model, a systematic study with many different particle (i.e, different seeds) would have to be carried out. We took the preliminary steps in doing so from the results presented in Figs. 6.4 and 6.5. With the current set up in the model where a constant background density of $\rho = 10^{14} m^{-3}$ is assumed, the initial starting energy of the order $100 - 200$ keV is still not sufficient to overcome the collisional effects if we wanted to perform a systematic study with different particles as done in Chapter 3. A collisional-relativistic model with an evolving background could be a future improvement to the model.

With the addition of the advection term, energy losses start to dominate as the density in the model was increased to values typical for the corona. With increasing density, (i) the magnetic moment μ no longer could be considered a long-term invariant, (ii) collisional particle orbits seem to have higher mirror points compared to non-collisional cases as seen in Fig. 6.10 and (iii) a critical initial energy is required for a particle to complete an orbit in a finite time. The critical initial energy increases to near relativistic values for $\rho = 10^{16} m^{-3}$, where for $\theta_{init} = 160.4°$ the minimum starting energy is about 228keV and 349keV for $\theta_{init} = 87.3°$. Also, particles with initial pitch angles close to $90°$ require a higher initial energy than particles with smaller pitch angles. For particle trapping conditions, when comparing our findings in Chapter 4 with the findings for the collisional case the critical trapping angle, $\theta_{critical}$ for the collisional case is smaller ($10.8°$) compared to the non-collisional case ($21°$). Again due to the stochastic nature of the particle orbits for the collisional case this would have to be further investigated through a systematic study with many different particles. For instance, using the same initial conditions for different particles (different seeds) and taking the average to find a general behaviour (similar to a Monte Carlo method).

As stated throughout this chapter, all of the results with the current set up of constant background density and temperature should be seen as a set of numerical test cases and benchmarks for future studies using this model. Currently, the collisional effects with a constant background are overestimated in the model. Ideally, the background plasma should also evolve as the trap evolves. This may reduce the collisional effects on the particles which reach non-thermal energies in the model.

To gain insight into the X-ray emissions at a given point in space on the Sun, one needs to know information about the local non-thermal electron distribution as well as the background density Fletcher (1995). In this thesis we do not look at particle distribution functions, however the work done in this chapter through introducing Coulomb collisions could be an initial step into constructing distribution functions for this model for the first time.

Chapter 7

Summary and Discussions

Our studies in this thesis have tried to address and answer some of the questions regarding particle energisation based on the CMT model by Giuliani et al. (2005) and the previous results of Grady (2012) and Grady et al. (2012). During the course of this investigation we have also come to understand some new concepts generally necessary for particle energisation in CMTs.

Since the energies obtained by Grady (2012) and Grady et al. (2012) in the non-relativistic model are already mildly relativistic, the incorporation of the relativistic guiding centre theory (see, Northrop, 1963) into the model is a key extension which we have presented in Chapter 3. We find two main differences between the relativistic and non-relativistic results: a) the final particle energy calculated using the relativistic approximation is always smaller than the non-relativistic case. This is due to the Lorentz factor affecting the terms in the equation of motion by reducing the size of the contributing terms, b) the mirror points for the particles using the relativistic approximation are generally higher than the non-relativistic case. Hence more particle trapping in the relativistic case could be explained by particles not travelling all the way down to the foot points. Higher mirror points could be due to terms in the parallel guiding centre equation becoming smaller as γ increases with increasing particle velocity.

In Chapter 4 we investigated the conditions which affect the trapping and escape of particle orbits in some of the CMT models in the literature (Aschwanden, 2004a; Somov, 2004; Karlicky and Barta, 2006; Minoshima et al., 2010; Grady et al., 2012). Due to a main assumption made in the simple models by Aschwanden (2004a) and Somov (2004), i.e. $\alpha_\infty = 90^\circ$, all the particles escape from the trap. Our non-relativistic CMT model can be seen as a more sophisticated model. The findings of Grady et al. (2012) formed a basis for our study in this Chapter. They found, the particle orbits that gain most energy during the trap collapse have initial pitch angles θ close to 90° and initial positions in a weak magnetic field region in the middle of the trap. Those particle orbits having the largest energy gain remained trapped during the collapse and due to their pitch angle staying close to 90° have mirror points very close to the centre of the trap. Grady et al. (2012) argue that these particle orbits are energised mainly by the betatron mechanism. Other particle orbits with initial pitch angles closer to 0° (or 180°) seem to be energised by the Fermi mechanism at the beginning, but as already pointed out by Giuliani et al. (2005) and corroborated

by Grady et al. (2012), these particle orbits gain energy when passing through the centre of the trap. At later stages these particle orbits also seem to be undergoing mainly betatron acceleration. Working under the assumptions of (i) $\alpha_\infty < 90°$, (ii) invariance of magnetic moment and evolution of $\theta(t)$ in relation to $\alpha(t)$ and (iii) curvature of the magnetic field lines, our findings are as follows: (a) for each magnetic field line in a collapsing magnetic trap there is a critical initial pitch angle, which divides particle orbits into trapped orbits and escaping orbits.This critical initial pitch angle is greater than the initial loss cone angle for the field line, but smaller than the value of the asymptotic loss cone angle for the field line as $t \to \infty$ (see Fig. 4.14). Furthermore, we find this angle is independent of the initial energy, (b) for orbits with initial pitch angle close to the critical value, Fermi acceleration seems to dominate in the initial phases, but betatron acceleration will take over and become the dominating acceleration mechanism. In the periods where Fermi acceleration dominates over betatron acceleration, the pitch angle will decrease and when betatron acceleration dominates the pitch angle will increase, and (c) due to the nature of more complete CMT models, both mechanisms will always operate simultaneously (e.g. see also Karlický and Bárta, 2006), but the efficiency of Fermi acceleration has to decrease on a particular field line during the time evolution of a CMT because the motion of the field line must slow down. On the other hand, the magnetic field strength can still continue to increase due to the pile-up of magnetic flux from above.

In Chapter 5 we investigated how an anisotropic plasma pressure ($P_{\|}$,$P_{\perp}$) and the plasma density (ρ) evolve under the assumptions that the time evolution of these quantities is determined by the Giuliani et al. (2005) CMT model. Under the simplified assumptions that i) the double-adiabatic theory is valid (i.e. no heat flux), ii) an isotropic initial pressure $P_{\|} = P_{\perp}$ and a uniform initial density ρ, we find that: a) the parallel pressure $P_{\|}$ seems to be the dominant term compared to the perpendicular pressure $P_{\perp}$, and b) that checking for instabilities, namely, fire-hose and mirror instabilities, the CMT model does become fire-hose unstable. Using the fluid theory the plasma does not become mirror unstable, however, using kinetic theory it seems to go mirror unstable.

Finally, in Chapter 6 we took preliminary steps to introduce Coulomb collisions into the non-relativistic guiding centre equations. From our numerical experiments under the assumptions of i) a static atmospheric background, ii) an isothermal coronal temperature, and iii) test particle velocities are much larger than the thermal velocity of the scattering background plasma (i.e. $v \gg v_{thermal}$), we find that, a) pitch angle scattering alone seems to have the effect of trapping more particles, a result different from Minoshima et al. (2011) where they find more particles are lost by entering the loss cone angle, b) in the fully collisional case, including both pitch angle scattering and energy losses, the pitch angle generally seems to tend towards $90°$, moving away from the loss cone. This seems to suggest that betatron acceleration is the main acceleration mechanism responsible for particle energisation, c) with increasing density, (i) the magnetic moment μ no longer could be considered a long-term invariant, (ii) a collisional particle orbits seems to

have higher mirror points compared to non-collisional cases and (iii) a critical initial energy is required for a particle to complete an orbit in a finite time. This energy for particles starting with pitch angles, θ_{init}, close to 90° requires higher initial energies than for particles starting with pitch angle close to 0° (or 180°). The critical initial energy increases to near relativistic values. For example for $\rho = 10^{16} m^{-3}$, where for $\theta_{init} = 160.4^\circ$ the minimum starting energy is about 228keV and 349keV for $\theta_{init} = 87.3^\circ$, and d) the critical trapping angle $\theta_{critical}$ for a collisional case is smaller (of the order 10.8°) compared the non-relativistic case seen in Chapter 4 which is of the order 21°.

While having made a lot of progress in our understanding of particle acceleration in CMTs in particular the Giuliani et al. (2005) CMT mode, our work in the study of particle energisation in CMTs, is far from complete.

The results from the relativistic particle orbit code seen in Chapter 3 are in line with the findings from other models (e.g. Karlický and Bárta, 2006; Minoshima et al., 2010; Grady et al., 2012), where particle trapping at the loop top is seen and this could give an explanation into X-ray emissions observed at coronal/loop-top sources. However, these results are based on the exclusion of Coulomb collisions, wave particle interaction or turbulence from the CMT model. The inclusion of these mechanisms may change the results for particle energisation and trapping for a collisional-relativistic model, and this could be one possible aim of future studies.

The trapping and escape conditions in Chapter 4 were investigated using the non-relativistic guiding centre equations. However, in the relativistic regime, splitting the particle velocity into its parallel $v_{\|}$ and perpendicular $v_{\perp}$ components to find the particle pitch angle θ needs some element of thought. The evolution of the relativistic pitch angle θ_{rel}, in relation to the loss cone angle α in a relativistic CMT could give a different relativistic critical pitch angle $\theta_{rel-crit}$, as already indicated by the systematically higher mirror points.

For the study done in Chapter 5 based on the validity of the double-adiabatic theory where heat flux is neglected, the ratio $\frac{P_{\|}}{P_{\perp}}$ increases with time in the middle of the trap as seen in Fig. 5.7. Assuming $P_{\|} = \rho R T_{\|}$ and $P_{\perp} = \rho R T_{\perp}$, the ratio $\frac{T_{\|}}{T_{\perp}}$ would also increase. However, the inclusion of heat flux could affect the temperature in the model due to the operation of two competing mechanisms; the compression from the collapsing trap could cause the temperature in the trap to increase and at the same time heat conduction would try to decrease the temperature.

With the current assumptions in Chapter 6, i.e, constant background density, isothermal temperature and $v \gg v_{thermal}$, for a case where $\rho = 10^{14}$ m^{-3} is assumed, the initial starting energy of the order $100 - 200$keV is still not sufficient to overcome the collisional effects introduced by the advective A_v, A_ϕ and diffusive B_ϕ terms. This result stopped us from performing a systematic

study with different particles as done in Chapter 3. This would change if the temperature were to go up which is what is seen in flares in general. Also as mentioned in Chapter 5 the compression from the field lines as the trap collapses could also increase the temperature, resulting in the ratio $\frac{v}{v_{thermal}}$ going down. This would require much more complicated stochastic terms, which could have the effect of reducing the advective and diffusive terms. Therefore, a future point of investigation could be to look at test particle energy loss, travel distance, pitch angle evolution and trapping conditions using a 2.5D collisional-relativistic model with an evolving background.

Finally, other, more general, avenues for future work should be mentioned. This and previous work has been carried out using one specific CMT model as proposed by Giuliani et al. (2005). However, the general theory of kinematic CMT models developed by these authors and extended by Grady et al. (2012) is far from exhausted. Extensions could include different flow fields and different magnetic field models in 2D, 2.5D or 3D. Another possibility would be to abandon the assumptions of a kinematic CMT model and move to a full MHD model (see e.g. Karlický and Bárta, 2006). This would make the case of numerical MHD simulations necessary, but would allow the inclusion of the back reaction of e.g. the pressure force onto the CMT evolution, as discussed briefly in Chapter 5.

Appendix A

Relativistic Particle Orbit Regime

A.1 Fortran Relativistic Particle Orbit Code Files

The following three files incorporate the relativistic effects in the Particle orbit code. These files replace the same files in the non-relativistic code. For the fully non-relativistic code see appendices in Grady (2012).

A.1.1 lognew.f90

The main programme which reads in the initial conditions, loops over each particle and records the data in RV files.

```
PROGRAM SINGLE

USE GLOBAL
USE M_DRIVER

IMPLICIT NONE
 INTEGER :: NOK, NBAD
 REAL(num), DIMENSION(3) :: RSTART, RSTARTKEEP,R1,R2
 REAL(num) :: T1,T2, H1,EPS, VPARSTART,mu, Erest, gamma
 INTEGER   :: pos_no_x,pos_no_y,pos_no_z,pos_no_alpha,pos_no_ekin
 INTEGER   :: EKinSteps,AlphaSteps !, FullAngle
 INTEGER,DIMENSION(3) :: RSteps, pos_no_r
 REAL(num), DIMENSION(NKEEPMAX) :: TT
 REAL(num), DIMENSION(NKEEPMAX,3) :: S, TOTAL
 INTEGER :: I,NKEEP,time_no,maxtime, counts
 REAL(num) :: EKin, Alpha, AlphaMin, AlphaMax,
 REAL(num) :: dalpha,EKinlow, Ekinhigh, T1Keep, T2Keep
 REAL, PARAMETER :: pi = 3.14159265352

!maximum time to go to
maxtime=200
```

```
!Loop for each multipar file we want to make
 DO time_no = 200,maxtime,1


 OPEN (UNIT =19, FILE = 'multipar.dat')

 !work out values of position to start on.
 !read the max/min of values for
 !initial position, energy and pitch angle
 CALL read_param2

!Adjust T2 to use loop value. (i.e. ignore value in newinput.dat)
T2 = time_no*1.0

T1Keep = T1
T2Keep = T2

!give each particle an integer to identify it. Useful for deciding
!which RV*.dat files to output and also for splitting up programs.
!to run several at once e.g. use
!'IF uniqueparticleid .le. 100 and uniqueparticleid .gt. 100 to 200
!inside the following loops to only run particles 100 to 200
uniqueparticleid=0

!The increment for the pitch angle is worked out.
dalpha = (AlphaMax-Alphamin)/(Alphasteps - 1.0d0)

!*********************************************************
!x, y and z start at 1 but can also be set to 0 depending on
!which position and energy equation is chosen. Alpha needs
!to be always set to 2 so the definition above
!does not become undefined.
!*********************************************************
do pos_no_x = 1, RSTEPS(1),1
do pos_no_y = 1, RSTEPS(2),1
do pos_no_z = 1, RSTEPS(3),1               !goes from 1 -> 1
do pos_no_alpha = 2, AlphaSteps,1
do pos_no_ekin = 1, EkinSteps,1

uniqueparticleid= uniqueparticleid + 1

!*************************************************************
!decide if we want to record the full orbit for this particle.
```

```
!At the moment records every particle. If we wanted only
!the 1009th particle then replace with
'IF (time_no .eq. maxtime .and.
mod(uniqueparticleid,1009) .eq. 0) then'
!only if the time loop is on it's final go,
!i.e, running for the full time.
!*************************************************************
if (time_no .eq. maxtime) then
   writervs=1
 else
   writervs=0
endif

!Want to keep starting values so we can record them at
!the end.
T1=T1Keep
T2=T2Keep

!*****************************************************
!redefine rstart so that it uses the value from before
!not the position of last particle
!*****************************************************
 pos_no_r=(/ pos_no_x,pos_no_y,pos_no_z /)

!*************************************************************
!pos_no_R starts from 0, if started from 1 then (stepR-1)
!added 25/5/2013
!*************************************************************
!RSTART=R1+(R2-R1)*((pos_no_r)/RSteps)
 RSTART=R1+(R2-R1)*((pos_no_r - 1.0d0)/RSteps)

 alpha = Alphamin+dalpha*(pos_no_alpha -1)
 !Degrees into radians
 alpha = alpha*(Pi/180.0d0)

!*************************************************************
!pos_no_ekin starts from 0, if started from 1 then (stepekin-1)
!added 25/5/2013
!*************************************************************
!Ekin=EKinLow+(EKinHigh-EKinLow)*pos_no_ekin/(EkinSteps*1.0d0)
 Ekin=EKinLow+(EKinHigh-EKinLow)*(pos_no_ekin-1.0d0)/(EkinSteps*1.0d0)

!normalise the values
RSTARTKEEP=RSTART
```

```
RSTART=RSTART/L
RSTARTKEEP=RSTARTKEEP/L
T1=T1/Tscl
T2=T2/Tscl

! This is not needed in the relativistic code
!convert energy from eV to joules
!Ekin = Ekin *abs(Q)
!Normalising Ekin
!Ekin = Ekin/M/Vscl**2


!call sub to calculate mu (as used in the code)
!from the values of EKin, alpha and B (via RSTART)
 CALL CALC2_MU(MU,vparstart,Ekin,Alpha,RSTART,T1)



!Call the rk sophisticated driver, which then works out the arrays for the
!time steps and positions.

 CALL RKDRIVE(RSTART,VPARSTART,MU,T1,T2,EPS,H1,NOK,NBAD,TT,S,TOTAL)

!number of data points
NKEEP = (NOK +NBAD)/NSTORE


!call the subroutine that writes out to the multipar file
 CALL WRITE_ENDTIME(RSTART,T2,MU,VPARSTART)

end do
end do
end do
end do
end do
!close the multipar file
 CLOSE(19)

!Because the multipar file outputs at different points
!with unspecified formatting we record the data in a file,
!where one particle's data is recorded per line and the
!file is given a unique name
CALL MAKEFILE(time_no)
```

```
END DO

!*****************************************************************
 Contains
!*****************************************************************

 Subroutine read_param
 Namelist/inputdata/T1,T2,H1,EPS,MU,VPARSTART,RSTART

     open(20,file='input.dat',status='unknown')
     read(20,nml=inputdata)
     close(20)

 End Subroutine read_param
!*****************************************************************

! read in the newinput.dat file.
 Subroutine read_param2
 Namelist/inputdata/T1,T2,H1,EPS,AlphaSteps,AlphaMin,AlphaMax,R1,R2,
      RSteps,EkinLow,EKinHigh,EkinSteps

     open(20,file='newinput.dat',status='unknown')
     read(20,nml=inputdata)
     close(20)
!check min and max angles match
 IF (Alphamin .LT. 160.4 .OR. AlphaMax .GT. 160.4) THEN
   PRINT*,'Check newinput.dat'
   STOP
 ENDIF
 End Subroutine read_param2

!*****************************************************************
 SUBROUTINE CALC2_MU(mu,vparstart,Ekin,alpha,RSTART,T1)
!calculate the mu and vparstart given the
!total initial energy and pitch angle.

  REAL(num), DIMENSION(3),INTENT(IN) :: RSTART
  REAL(num), INTENT(IN) :: T1, Ekin, Alpha
  REAL(num), INTENT(OUT) :: mu,vparstart
  REAL(num), DIMENSION(3) :: B,El,a2,a3,a4,a5,a6,a7,a8,a9,a10,ue
  REAL(num) :: magB,vtot,vperp,Erest,gamma

!need B to calulate mu
```

```
!calculate B at this point/time:
!don't care about the derivatives so they're called a2 .. a10

 CALL FIELDS(RSTART,T1,El,B,a2,a3,a4,a5,a6,a7,a8,a9,a10)
!CALL FIELDS(RSTART,T1,El,B,DBDX,DBDY,DBDZ,DBDT,DEDX,DEDY,DEDZ,DEDT,Vf)


!calculate magnitude of B
 magB=B(1)**2+B(2)**2+B(3)**2
 magB=sqrt(magB)

!rest mass of an electron (KeV)
 Erest = (M*c**2)*1.d0/abs(Q)

!calculate Lorenz Factor
gamma = (Ekin/Erest + 1.0)

! energy due to E X B drift
ue=cross(El,B)/dot(B,B)

!*****************************************
!added 11/7/2013
!total par velocity
!note the drift velocity must be
!subtracted to give only the particle velocity.

 vtot =  sqrt(((c**2)/(Vscl**2))*
              (1.0d0-1.0d0/gamma**2)-dot(ue,ue))

!*************************************************
!Split into parallel and perpendicular parts

 vparstart=vtot*cos(alpha)
 vperp=vtot*sin(alpha)

!calculate mu
 mu=(gamma*vperp)**2/magB/2.0_num

!Output starting data to the multipar.dat file
 WRITE (19,*) RStart,T1,Ekin,Alpha, mu*magB, 0.5*vparstart**2
 WRITE (19,*) vtot,vperp,vparstart,El,B,magB,mu
 END SUBROUTINE

!************************************************
```

```
SUBROUTINE WRITE_ENDTIME(RSTART,T2,MU,VPARSTART)
!write data to the multipar file at the end of the particle's run.

  REAL(num), DIMENSION(3),INTENT(IN) :: RSTART
  REAL(num), INTENT(IN) :: T2, MU, VPARSTART
  REAL(num), DIMENSION(3) :: B,El,a2,a3,a4,a5,a6,a7,a8,a9,a10,ue
  REAL(num) :: magB,vtot,vperp, Erest, gamma!, vpar

!write position and time
WRITE(19,*) RSTART, T2


!calculate magnetic and electric fields
 CALL FIELDS(RSTART,T2,El,B,a2,a3,a4,a5,a6,a7,a8,a9,a10)

  magB=B(1)**2+B(2)**2+B(3)**2
  magB=sqrt(magB)
  ue=cross(El,B)/dot(B,B)
  Erest = (M*c**2)*1.d0/abs(Q)    !rest mass of an electron (KeV)
  gamma = SQRT((1.0d0+((Vscl**2)/(c**2))*1.0d0*(2.0*MU*magB))/
(1.0d0-((Vscl**2)/(c**2))*1.0d0*(VPARSTART**2 + dot(UE,UE))))

!Total energy of the particle in the
!relatvistic case.

 Ekin = Erest*(gamma -1.0)
!Pitch angle of the particle
 alpha=acos(vparstart/(sqrt(((c**2)/(Vscl**2))*
              (1.0d0-1.0d0/gamma**2)-dot(ue,ue))))

!no need for Eper,Epar,cant split the energies as
!easily as in the non-rel case.
!EPar=0.5*vparstart**2
!EPerp=mu*magB

 vtot =  sqrt(((c**2)/(Vscl**2))*
          (1.0d0-1.0d0/gamma**2)-dot(ue,ue))
 vperp=vtot*sin(alpha)

WRITE(19,*) Ekin,alpha,0.0d0,0.0d0,vtot,vperp,vparstart
WRITE(19,*) El, B, magB
!WRITE(19,*) "El, B, magB"
END SUBROUTINE
```

```
SUBROUTINE MAKEFILE(time_no)
!*****************************************************
!reform the multipar.dat file into a multipar_fmt_t**.dat file
!this gives it a header so it's easier to read
!and puts one particle's data on each line.
!This code works for the version of gfortan
!*********************************************
 INTEGER :: stat,timefile
 !REAL,DIMENSION(3) :: a,b,d,e,f,h,j,k,m,n
 !REAL,DIMENSION(2) :: c,g
 !REAL ::              i,l,o
 REAL, DIMENSION(8) :: a
 REAL, DIMENSION(11) :: b
 REAL, DIMENSION(4) :: c
 REAL, DIMENSION(7) :: d,e
 CHARACTER(LEN=65) :: h1
 CHARACTER(LEN=79) :: h2
 CHARACTER(LEN=87) :: h3
 CHARACTER(LEN=47) :: h4
 CHARACTER(LEN=278) :: header_str
 !REAL, INTENT(IN) :: T2
 CHARACTER(LEN=30) :: fnameout
 INTEGER, INTENT(IN) :: time_no


!reopen the multipar.dat file so it can be read
 OPEN (UNIT = 19, FILE = 'multipar.dat', FORM="FORMATTED",
                     STATUS="OLD", ACTION="READ")

!choose a sensible filename, based on the final time being recorded.
 timefile=time_no
 WRITE(fnameout,"('multipar_fmt_t',I3.3,'.dat')"),timefile
 print*,"fnameout",fnameout

OPEN(UNIT=8,FILE=fnameout,FORM="FORMATTED",ACTION="WRITE")

!Write header for formatted file
h1='xstart ystart zstart t1 EKinStart alphaStart EperpStart EparStart'
h2=' vTotStart vPerpStart vParStart ExStart EyStart EzStart BxStart
       ByStart BzStart'
h3=' BStart mu xEnd yEnd zEnd t2 EKinEnd alphaEnd EperpEnd EparEnd
       vTotEnd vPerpEnd vParEnd'
h4=' ExEnd EyEnd EzEnd BxEnd ByEnd BzEnd BEnd'
```

```
header_str=h1 // h2 // h3 // h4

WRITE(UNIT=8,FMT='(A264)') header_str

DO

READ(UNIT=19,FMT=*,IOSTAT=stat) a
!if the input file is finished then we are done in the loop
IF (stat .lt. 0) EXIT
READ(UNIT=19,FMT=*) b
READ(UNIT=19,FMT=*) c
READ(UNIT=19,FMT=*) d
READ(UNIT=19,FMT=*) e

!if OK, write the line out to the new file.
IF (stat .eq. 0) THEN
  WRITE(UNIT=8,FMT='(37D23.15)') a,b,c,d,e
ELSE
  PRINT*, "file status was",stat
  EXIT
END IF


END DO

!clse both fiels
CLOSE(8)
CLOSE(19)]

END SUBROUTINE

END PROGRAM SINGLE
```

A.1.2 derivs_mod.f90

This uses the time, particle position, magnetic moment and parallel velocity to calculate the time derivative of vpar and the relativistic guiding centre equations from Northrop (1963).

```
Module M_derivs

  Use Global
```

```
  Use M_fields

Implicit None
 REAL, DIMENSION(8,3) :: drift
 REAL, DIMENSION(3)  :: temp
 REAL, DIMENSION(4)  :: temp2
 REAL :: sum_temp2

 Contains

   SUBROUTINE DERIVS (T, R, DRDT, VPAR, DVPARDT,MU)

 !This part of the program simply works out the right hand side of the 6
 !coupled ODEs. The values of q, m, and the electromagnetic field are to
 !be included in the code.


IMPLICIT NONE
 REAL, INTENT(IN) :: T,MU
 REAL, INTENT(IN) :: VPAR
 REAL, INTENT(OUT) :: DVPARDT
 REAL, DIMENSION(3), INTENT(IN) :: R
 REAL, DIMENSION(3),INTENT(OUT) :: DRDT
 REAL, DIMENSION(3) :: B,E,Vf
 REAL, DIMENSION(3) :: DBDX,DBDY,DBDZ,DBDT,DEDX,DEDY,DEDZ,DEDT
 REAL, DIMENSION(3) :: GRADB,DBETADT,DBETADX,DBETADY,DBETADZ
 REAL, DIMENSION(3) :: EDRIFT, DUEDX,DUEDY,DUEDZ,DUEDT
 REAL :: MODB, DMODBDS, DMODBDT,EPAR,GRADBT,gamma, Erest
 REAL, DIMENSION(3) :: GRADDRIFT,DBETADS,UEGRADB,UEGRADUE,DUEDS
 REAL, DIMENSION(3) :: ACCDRIFT, OTHERS,OTHERS1
 REAL, DIMENSION(3) :: Vothers,ACCDRIFT1,VparEparUE
 REAL, DIMENSION(3) :: SCRAE

 CALL FIELDS(R,T,E,B,DBDX,DBDY,DBDZ,DBDT,DEDX,DEDY,DEDZ,DEDT,Vf)
 MODB = SQRT(B(1)**2 + B(2)**2 + B(3)**2)

 EPAR = (DOT(E,B))/MODB

 GRADB(1) = (DOT(B,DBDX))/MODB
 GRADB(2) = (DOT(B,DBDY))/MODB
 GRADB(3) = (DOT(B,DBDZ))/MODB
 GRADBT = (DOT(B,DBDT))/MODB

!We'll call Bx/B BETAX. Got to call it something.
```

```
!So these are arrays of three (BETAX,BETAY,BETAZ)

 DBETADX = DBDX/MODB - B*GRADB(1)/MODB**2
 DBETADY = DBDY/MODB - B*GRADB(2)/MODB**2
 DBETADZ = DBDZ/MODB - B*GRADB(3)/MODB**2
 DBETADT = DBDT/MODB - B*GRADBT/MODB**2


 EDRIFT = (CROSS(E,B))/(MODB**2)


!Need to get the derivatives of components of the Edrift:

 DUEDX = (CROSS(DEDX,B) + CROSS(E,DBDX) - 2.*EDRIFT*DOT(B,DBDX))/(MODB**2)
 DUEDY = (CROSS(DEDY,B) + CROSS(E,DBDY) - 2.*EDRIFT*DOT(B,DBDY))/(MODB**2)
 DUEDZ = (CROSS(DEDZ,B) + CROSS(E,DBDZ) - 2.*EDRIFT*DOT(B,DBDZ))/(MODB**2)
 DUEDT = (CROSS(DEDT,B) + CROSS(E,DBDT) - 2.*EDRIFT*DOT(B,DBDT))/(MODB**2)

 DMODBDS=dot(B,B(1)*DBDX+B(2)*DBDY+B(3)*DBDZ)/(MODB**2)


!****************************************
!Added DMODBDT needed in the relativistic
!equations (5oct 2011)!
!****************************************

DMODBDT=dot(B,DBDT)/MODB

!print*,"DMODBDT", DMODBDT


 GRADDRIFT = CROSS(B,GRADB)/(MODB**2)

 DBETADS = (B(1)*DBETADX + B(2)*DBETADY + B(3)*DBETADZ)/(MODB)
! print*,'DBETADS=',DBETADS

 UEGRADB = (EDRIFT(1)*DBETADX + EDRIFT(2)*DBETADY + EDRIFT(3)*DBETADZ)
! print*,'UEGRADB=',UEGRADB

 DUEDS = (B(1)*DUEDX + B(2)*DUEDY + B(3)*DUEDZ)/(MODB)

 UEGRADUE = (EDRIFT(1)*DUEDX + EDRIFT(2)*DUEDY + EDRIFT(3)*DUEDZ)

!All the acceleration drift terms, to be crossed with B
```

```
!Lorentz Factor
gamma=SQRT((1.0d0+((Vscl**2)/(c**2))*1.0d0*(2.0*MU*MODB))/
       (1.0d0-((Vscl**2)/(c**2))*1.0d0*(VPAR**2 + dot(EDRIFT,EDRIFT))))


ACCDRIFT1=gamma*VPAR*DBETADT+(VPAR**2)*DBETADS+ &
         & gamma*VPAR*UEGRADB+gamma*DUEDT &
         & +VPAR*DUEDS+gamma*UEGRADUE+ &
         &((Vscl**2)/(c**2*gamma))*MU*EDRIFT*DMODBDT

VparEparUE = VPAR*EPAR*EDRIFT


!All the terms that make up the last bit of the parallel equation

!Relativistic term
OTHERS1 = DBETADT + (VPAR/gamma)*DBETADS + UEGRADB


!The Relativistic eqn of motion
DRDT=EDRIFT+((M*E0)/(Q*L*B0**2))*((MU*GRADDRIFT)/(gamma)&
 & + CROSS(B,ACCDRIFT1)/(MODB**2)) &
 & +((Vscl**2)/(c**2))*(CROSS(B,VparEparUE)/(MODB**2))+VPAR*(B/MODB)

Vothers = DRDT


!Relativistic eqn of motion
DVPARDT = ((Q*L*(B0**2))/(M*E0*gamma))*EPAR - &
  & (MU/(gamma**2))*DMODBDS + DOT(EDRIFT,OTHERS1) &
  & -((Q*L*(B0**2))*(Vscl**2))/(M*E0*gamma*(c**2))*VPAR*DOT(Vothers,E)- &
  & ((Vscl**2)/(c**2))*(MU/(gamma**2))*DMODBDT*VPAR


  temp(1)=MU*dot(B,DBDT)/MODB
  temp(2)=MU*VPAR*DMODBDS
  temp(3)=MU*dot(EDRIFT,GRADB)

  temp(1)=dot(B,DBDT)/MODB
  temp(2)=VPAR*DMODBDS
  temp(3)=dot(EDRIFT,GRADB)

  temp2(1)=-MU*DMODBDS
```

```
  temp2(2)=dot(EDRIFT,DBETADT)
  temp2(3)=dot(EDRIFT,VPAR*DBETADS)
  temp2(4)=dot(EDRIFT,UEGRADB)
  sum_temp2=temp2(1)+temp2(2)+temp2(3)+temp2(4)

 drift(1,:)=EDRIFT(:)

 drift(2,:) = ((M*E0)/(Q*L*B0**2))* MU*GRADDRIFT(:)

 SCRAE = ((M*E0)/(Q*L*B0**2))* CROSS(B,VPAR*DBETADT)/(MODB**2)
 drift(3,:)= SCRAE(:)

 SCRAE = ((M*E0)/(Q*L*B0**2))* CROSS(B,(VPAR**2)*DBETADS)/(MODB**2)
 drift(4,:)=SCRAE(:)

 SCRAE =((M*E0)/(Q*L*B0**2))* CROSS(B,VPAR*UEGRADB)/(MODB**2)
 drift(5,:)=SCRAE(:)

 SCRAE =((M*E0)/(Q*L*B0**2))* CROSS(B,DUEDT)/(MODB**2)
 drift(6,:)=SCRAE(:)

 SCRAE =((M*E0)/(Q*L*B0**2))* CROSS(B,VPAR*DUEDS)/(MODB**2)
 drift(7,:)=SCRAE(:)

 SCRAE =((M*E0)/(Q*L*B0**2))* CROSS(B,UEGRADUE)/(MODB**2)
 drift(8,:)=SCRAE(:)

 END SUBROUTINE DERIVS

End Module M_derivs
```

A.1.3 rkdrive_mod.f90

```
Module M_driver

  Use global
  Use M_derivs
  Use M_rkqs
Implicit None

 Contains

Subroutine RKDRIVE(RSTART,VPARSTART,MU,T1,T2,EPS,H1,NOK,NBAD,TT,S,TOTAL)
```

```
 !#########################################################
!Description from P.Giuliani:
!Driver routine with adaptive stepsize control.
!It goes from T1 toT2 with accuracy eps.
!Hmin is the minimum allowed stepsize. nok and
!nbad are the number of good and bad (i.e. retried)
!steps. RSTART is replaced by the end values.
!#########################################################

 IMPLICIT NONE

 INTEGER :: NOK, NBAD
 REAL, INTENT(IN) :: EPS, H1,MU
 REAL, INTENT(INOUT) :: T1,T2
 REAL, INTENT(INOUT), DIMENSION(3) :: RSTART
 REAL :: TINY
 PARAMETER ( TINY=1.0e-20)
 INTEGER :: I, J,NSTP
 REAL :: H, HDID, HNEXT, T
 REAL, DIMENSION(3) :: DRDT, R
 REAL :: VPAR, VPARSTART,DVPARDT,gamma,MODB,Erest,vtotrel
 REAL, DIMENSION(3) :: E,B,DBDX,DBDY,DBDZ,DBDT
 REAL, DIMENSION(3) :: DEDX,DEDY,DEDZ,DEDT,Vf
 REAL, DIMENSION(3) :: bb
 REAL :: efct,e1,e2,e3,e4,e41
 REAL, DIMENSION(4) :: RSCAL
 REAL, DIMENSION(NKEEPMAX) :: TT
 REAL, DIMENSION(NKEEPMAX,3) :: S, TOTAL
 REAL, DIMENSION(3) :: ENERGY
 REAL, DIMENSION(3) :: UE
 CHARACTER(LEN=14)  :: rvfilename

 T=T1
 TT(1) = T1
 H=SIGN(H1,T2-T1)
 NOK = 0
 NBAD = 0
 DO I = 1,3
   R(I) = RSTART(I)
   S(1,I) = RSTART(I)
 ENDDO
   VPAR = VPARSTART
   DO I=1,3
```

```
   TOTAL(1,I) = 0.
   END DO

 efct=1./abs(Q)
!Make the unique name for the file if it will be written

if (writervs .eq. 1) WRITE(rvfilename,"('RV',I8.8,'.dat')"),uniqueparticleid
if (writervs .eq. 1)  open(29,file=rvfilename,recl=1024,status='unknown')


 CALL DERIVS (T, R, DRDT, VPAR, DVPARDT,MU)
 CALL FIELDS(R,T,E,B,DBDX,DBDY,DBDZ,DBDT,DEDX,DEDY,DEDZ,DEDT,Vf)
 bb=B/sqrt(dot(B,B))
 UE=cross(E,B)/dot(B,B)

!Output the initial conditions to the RV**.dat file
MODB=sqrt(B(1)**2 + B(2)**2 + B(3)**2)
!Lorentz Foctor
gamma = SQRT((1.0d0+((Vscl**2)/(c**2))*(2.0*MU*MODB))/
               (1.0d0-((Vscl**2)/(c**2))*1.0d0*(VPAR**2 + dot(UE,UE))))

!electron rest mass
 Erest = (M*c**2)*1.d0/abs(Q)
!from non-relativistic case
 e1=efct*0.5_num*M*(Vscl*Vpar)**2
 e2=efct*M*(Vscl**2)*MU*sqrt(dot(B,B))
 e3=efct*0.5_num*M*dot(UE,UE)
 e4 = efct*0.5*M*(Vscl*Vpar)**2 + efct*M*(Vscl**2)*MU*sqrt(dot(B,B))

!total particle velocity (without EX B drift)
 vtotrel =  ((c**2)/(Vscl**2))*1.0d0*(1.0d0-1.0d0/gamma**2)-dot(ue,ue)


 if (writervs .eq. 1)  write(29,*)Tscl*(T-T1), & !1
     R,                                        &   !2,3,4
     VPAR,                                     &   !5
     MU*sqrt(dot(B,B)),                        &   !6
     sum((DRDT-VPAR*bb)**2),                   &   !7
     Vscl*B0*E,                                &   !8,9,10
     B0*B,                                     &   !11,12,13
     sqrt(vtotrel),                            &   !14
     e2,                                       &   !15
     e4,                                       &   !16
     Erest*(gamma -1.0),                       &   !17
```

```
     efct*Q*E0*(L/Tscl)*dot(DRDT,E),       &   !18
     efct*(M*Vscl*Vscl/Tscl)*MU*dot(B,DBDT)/sqrt(dot(B,B)), & !19
     Vscl*Vf,                              &   !20,21,22
     H                                         !23



!********************** Main Time-Loop Starts **************

 DO NSTP = 1, NSTPMAX
   CALL DERIVS (T, R, DRDT, VPAR, DVPARDT,MU)

   DO I = 1,3       !Scaling used to monitor accuracy
     RSCAL(I) = ABS(R(I))+ABS(H*DRDT(I)) + TINY
  !   PRINT *, 'scale',I,' = ',RSCAL(I)
  ENDDO
     RSCAL(4)=ABS(VPAR)+ABS(H*DVPARDT) + TINY

    RSCAL =1


    IF((T+H-T2)*(T+H-T1) > 0.) THEN
       H=T2-T   !if stepsize can overshoot, decrease
    END IF

    CALL RKQS(R,DRDT,VPAR,DVPARDT,T,H,MU,EPS,RSCAL,HDID,HNEXT)


    IF (HDID == H) THEN
      NOK = NOK+1
    ELSE
      NBAD = NBAD+1
    ENDIF

!This is for storing every NSTORE step
  IF (MOD(NSTP,NSTORE)==0) THEN
    TT((NSTP/NSTORE)+1) = T

 CALL DERIVS (T, R, DRDT, VPAR, DVPARDT,MU)
 CALL FIELDS(R,T,E,B,DBDX,DBDY,DBDZ,DBDT,DEDX,DEDY,DEDZ,DEDT,Vf)
 bb=B/sqrt(dot(B,B))

 UE=cross(E,B)/dot(B,B)
```

```
      ENERGY(1)=VPAR**2
      ENERGY(2)=MU*sqrt(dot(B,B))
      ENERGY(3)=sum((DRDT-VPAR*B/sqrt(dot(B,B)))**2)

    DO I = 1,3
      S((NSTP/NSTORE)+1,I) = R(I)
    TOTAL((NSTP/NSTORE)+1,I) = ENERGY(I)
    ENDDO


 MODB=sqrt(B(1)**2 + B(2)**2 + B(3)**2)
 gamma = SQRT((1.0d0+((Vscl**2)/(c**2))*(2.0*MU*MODB))/
            (1.0d0-((Vscl**2)/(c**2))*1.0d0*(VPAR**2 + dot(UE,UE))))


Erest = (M*c**2)*1.d0/abs(Q)
  e1=efct*0.5*M*(Vscl*Vpar)**2
  e2=efct*M*(Vscl**2)*MU*sqrt(dot(B,B))
  e3=efct*0.5*M*dot(UE,UE)

vtotrel =  ((c**2)/(Vscl**2))*1.0d0*(1.0d0-1.0d0/gamma**2)-dot(ue,ue)

e4 = efct*0.5*M*(Vscl*Vpar)**2 + efct*M*(Vscl**2)*MU*sqrt(dot(B,B))


if (writervs .eq. 1)  write(29,*)Tscl*(T-T1),&   !1
    R,                                      &   !2,3,4
    VPAR,                                   &   !5
    MU*sqrt(dot(B,B)),                      &   !6
    sum((DRDT-VPAR*bb)**2),                 &   !7
    Vscl*B0*E,                              &   !8,9,10
    B0*B,                                   &   !11,12,13
    sqrt(vtotrel),                              &   !14
    e2,                                     &   !15
    e4,                                     &   !16
    Erest*(gamma -1.0),                     &   !17
    efct*Q*E0*(L/Tscl)*dot(DRDT,E),         &   !18
    efct*(M*Vscl*Vscl/Tscl)*MU*dot(B,DBDT)/sqrt(dot(B,B)), & !19
    Vscl*Vf,                                &   !20,21,22
    H                                           !23

 ENDIF
```

```
    IF((T-T2)*(T2-T1) >= 0.) THEN          !Are we done?
      DO I = 1,3
        RSTART(I)=R(I)
      ENDDO
      VPARSTART = VPAR
      RETURN                               !normal exit
    ENDIF

!*********************************************
!Exit condition for the code when y = 0
(particle leaves the trap). Code will stop
!if particle goes below y=0
!*********************************************
IF(R(2) <0.0) THEN
 !PRINT *, 'Particle has gone too far in x direction at t = ', T
   DO I = 1,3
      RSTART(I)=R(I)
      ENDDO
   T2 = T
    VPARSTART = VPAR
      RETURN
 ENDIF
   H=HNEXT


 ENDDO             !if we get to nstpmax...
 PRINT *, 'too many steps in odeint'
 STOP

!Note: This point was never reached for any
!particle discussed in this thesis
!(nstpmax was always sufficient for the
!particle to escape the trap or the rap to collapse)

 RETURN

 End Subroutine RKDRIVE

End Module M_driver
```

A.2 Normalisation of the Relativistic Equations of Motion

Here the normalisation of the relativistic guiding centre equation describing the perpendicular motion of the particle is presented. We start with the equations for the guiding centre position:

$$\begin{aligned}\dot{\mathbf{R}}_\perp &= \frac{\mathbf{b}}{B(1-E_\perp{}^2/c^2B^2)} \times \left\{ -\left(1-\frac{E_\perp{}^2}{c^2B^2}\right)\mathbf{E} \right. \\ &+ \frac{\mu_r}{\gamma q}\nabla\left[B\left(1-\frac{E_\perp{}^2}{c^2B^2}\right)^{1/2}\right] + \frac{m\gamma}{q}\left(v_\parallel\frac{d\mathbf{b}}{dt}+\frac{d\mathbf{u}_E}{dt}\right) \\ &+ \left.\frac{v_\parallel E_\parallel}{c^2}\mathbf{u_E} + \frac{\mu_r}{\gamma q}\frac{\mathbf{u}_E}{c^2}\frac{\partial}{\partial t}\left[B\left(1-\frac{E_\perp{}^2}{c^2B^2}\right)^{1/2}\right]\right\} + O(\epsilon) \end{aligned} \tag{A.1}$$

where $E_\perp \ll cB$, $\frac{E_\perp}{B} \ll c$ and the term in the red, the $\mathbf{E}\times\mathbf{B}$ drift, gives the largest contribution to the perpendicular velocity component. Hence we have the following equation

$$\dot{\mathbf{R}}_\perp = \frac{\mathbf{b}}{B}\times\left\{-\mathbf{E}+\frac{\mu_r}{\gamma q}\nabla B+\frac{m\gamma}{q}\left(v_\parallel\frac{d\mathbf{b}}{dt}+\frac{d\mathbf{u}_E}{dt}\right)+\frac{v_\parallel E_\parallel}{c^2}\mathbf{u_E}+\frac{\mu_r}{\gamma q}\frac{\mathbf{u}_E}{c^2}\frac{\partial B}{\partial t}\right\} \tag{A.2}$$

Using the fact that $V_0 = \frac{L_0}{t_0} = \frac{E_0}{B_0}$ and the gyro-frequency $\Omega_0 = \frac{qB_0}{m}$ gives

$$\begin{aligned}\dot{\mathbf{R}}_\perp = \mathbf{u}_E &+ \frac{m_0E_0}{qL_0{B_0}^2}\left\{\frac{\mathbf{b}}{B}\times\left[\frac{\mu_r\nabla B}{\gamma}+\gamma(v_\parallel\frac{d\mathbf{b}}{dt}+\frac{d\mathbf{u}_E}{dt})+\frac{{v_0}^2}{c^2\gamma}\mu_r\mathbf{u}_E\frac{\partial B}{\partial t}\right]\right\} \\ &+ \frac{{v_0}^2}{c^2}v_\parallel E_\parallel\frac{\mathbf{b}}{B}\times\mathbf{u}_E. \end{aligned} \tag{A.3}$$

Hence,

$$\begin{aligned}\dot{\mathbf{R}}_\perp = \mathbf{u}_E &+ \frac{1}{\Omega_0 t_0}\left\{\frac{\mathbf{b}}{B}\times\left[\frac{\mu_r\nabla B}{\gamma}+\gamma(v_\parallel\frac{d\mathbf{b}}{dt}+\frac{d\mathbf{u}_E}{dt})+\frac{{v_0}^2}{c^2\gamma}\mu_r\mathbf{u}_E\frac{\partial B}{\partial t}\right]\right\} \\ &+ \frac{{v_0}^2}{c^2}v_\parallel E_\parallel\frac{\mathbf{b}}{B}\times\mathbf{u}_E \end{aligned} \tag{A.4}$$

This is the calculation for normalised equation of motion in the parallel direction

$$\begin{aligned}m\frac{d(\gamma v_\parallel)}{dt} = \frac{dp_\parallel}{dt} &= qE_\parallel - \frac{\mu_r}{\gamma}\frac{\partial}{\partial s}\left[B\left(1-\frac{E_\perp{}^2}{c^2B^2}\right)^{1/2}\right] \\ &+ m\gamma\mathbf{u}_E\cdot(\frac{d\mathbf{b}}{dt}), \end{aligned} \tag{A.5}$$

where $E_\perp \ll cB$. Therefore, we have,

$$\underbrace{m\frac{d(\gamma v_\parallel)}{dt}}_{m(\gamma\frac{dv_\parallel}{dt}+v_\parallel\frac{d\gamma}{dt})} = qE_\parallel - \frac{\mu_r}{\gamma}\frac{\partial B}{\partial s} + m\gamma\mathbf{u}_E\cdot(\frac{d\mathbf{b}}{dt}), \tag{A.6}$$

where

$$\frac{d\gamma}{dt} = \frac{q}{mc^2}(\dot{\mathbf{R}}_\perp + \mathbf{b}v_\parallel)\cdot\mathbf{E} + \frac{\mu_r}{mc^2\gamma}\frac{\partial B}{\partial t}. \tag{A.7}$$

Combining A.6 and A.7 gives

$$\frac{dv_\parallel}{dt} = \mathbf{u}_E\cdot\frac{d\mathbf{b}}{dt} + \frac{qE_\parallel}{m\gamma} - \frac{\mu_r}{m\gamma^2}\frac{\partial B}{\partial s} - v_\parallel\left\{\frac{q}{\gamma mc^2}(\dot{\mathbf{R}}_\perp + \mathbf{b}v_\parallel)\cdot\mathbf{E} + \frac{\mu_r}{mc^2\gamma^2}\frac{\partial B}{\partial t}\right\}. \tag{A.8}$$

Using the fact that $V_0 = \frac{L_0}{t_0} = \frac{E_0}{B_0}$ and the gyro-frequency $\Omega_0 = \frac{qB}{m}$ gives

$$\begin{aligned}\frac{dv_\parallel}{dt} = \mathbf{u}_E\cdot\frac{d\mathbf{b}}{dt} &+ (\frac{qE_0t_0}{\gamma m_0v_0})E_\parallel - \frac{1}{\gamma^2}\mu_r\frac{\partial B}{\partial s}\\ &- (\frac{qE_0t_0v_0}{m_0c^2\gamma})v_\parallel(\dot{\mathbf{R}}_\perp + \mathbf{b}v_\parallel)\cdot\mathbf{E} - \frac{{v_0}^2}{\gamma^2c^2}\mu_r\frac{\partial B}{\partial t}v_\parallel,\end{aligned} \tag{A.9}$$

which gives Eq.3.2

$$\begin{aligned}\frac{dv_\parallel}{dt} = \mathbf{u}_E\cdot\frac{d\mathbf{b}}{dt} &+ \Omega_0t_0\frac{E_\parallel}{\gamma} - \frac{\mu_r}{\gamma^2}\frac{\partial B}{\partial s}\\ &- \Omega_0t_0\frac{{v_0}^2}{c^2}\frac{v_\parallel}{\gamma}\left(\dot{\mathbf{R}}_\perp + \mathbf{b}v_\parallel\right)\cdot\mathbf{E}\\ &- \frac{{v_0}^2}{c^2}\frac{\mu_r}{\gamma^2}\frac{\partial B}{\partial t}v_\parallel.\end{aligned} \tag{A.10}$$

In our case $E_\parallel = 0$, hence

$$\begin{aligned}\frac{dv_\parallel}{dt} = \mathbf{u}_E\cdot\frac{d\mathbf{b}}{dt} &- \frac{\mu_r}{\gamma^2}\frac{\partial B}{\partial s}\\ &- \Omega_0t_0\frac{{v_0}^2}{c^2}\frac{v_\parallel}{\gamma}\left(\dot{\mathbf{R}}_\perp + \mathbf{b}v_\parallel\right)\cdot\mathbf{E}\\ &- \frac{{v_0}^2}{c^2}\frac{\mu_r}{\gamma^2}\frac{\partial B}{\partial t}v_\parallel\end{aligned} \tag{A.11}$$

Appendix B

Coordinates Along Magnetic Field Lines

B.1 Equations for x_0 and y_0

The flux function A_0 is solved for x_0 and y_0 by initially using the trigonometric identity

$$\arctan\alpha \pm \arctan\beta = \arctan\left(\frac{\alpha \pm \beta}{1 \mp \alpha\beta}\right). \tag{B.1}$$

Setting $\alpha = \left(\frac{y_0+d/L}{x_0+1/2}\right)$ and $\beta = \left(\frac{y_0+d/L}{x_0-1/2}\right)$ the right hand side of Eqn. 2.23 in terms of α and β gives

$$c_1\left\{\arctan\alpha - \arctan\beta\right\} = c_1 \arctan\left\{\frac{\alpha-\beta}{1+\alpha\beta}\right\}.$$

This gives

$$A_0 = c_1 \arctan\left\{\frac{\alpha-\beta}{1+\alpha\beta}\right\}. \tag{B.2}$$

Taking $\tan$ of both sides Eq. B.2 becomes

$$\begin{aligned}\tan\left(\frac{A_0}{c_1}\right) = \frac{\alpha-\beta}{1+\alpha\beta} &= \frac{\frac{(y_0+d/L)(x_0-1/2)-(y_0+d/L)(x_0+1/2)}{({x_0}^2-1/4)}}{\frac{({x_0}^2-1/4)+(y_0+d/L)^2}{({x_0}^2-1/4)}} \\ &= \frac{-y_0-\frac{d}{L}}{{x_0}^2-\frac{1}{4}+{y_0}^2+2y_0\frac{d}{L}+\frac{d^2}{L^2}}\end{aligned} \tag{B.3}$$

Rearranging Eqn. B.3 as a quadratic in x_0 and y_0 respectively, we have

$${x_0}^2+{y_0}^2+\frac{2d}{L}y_0+\frac{d^2}{L^2}-\frac{1}{4}+\cot\left(\frac{A_0}{c_1}\right)(y_0+\frac{d}{L})=0 \tag{B.4}$$

or

$${y_0}^2+\left\{\frac{2d}{L}+\cot\left(\frac{A_0}{c_1}\right)\right\}y_0+\left\{{x_0}^2+\frac{d^2}{L^2}-\frac{1}{4}+\frac{d}{L}\cot\left(\frac{A_0}{c_1}\right)\right\}=0. \tag{B.5}$$

Appendix C

Extra Details for the Simplified Model

C.1 Simplified Model: Mathematical Description

The simplified model for a non-linear loop top velocity V_{LT} as shown in the illustration can be completely expressed in terms of the motion in the y-direction and all other quantities can be derived from that. We start by imagining the state of the system just after the particle has bounced off the field line apex for the n^{th} time. Let the time of the bounce be t^n and the position $y_n = y(t_n)$. The velocity of the particle orbit in the y-direction then has the value $v_{y,n}$. The particle will then move down the mirror point with this velocity, bounce off the mirror point without changing the absolute value of its velocity (it is at this point that the assumption of the mirror points being static simplifies matters considerably) and move back up to the field line apex for the next bounce off the loop top at time t_{n+1}. During the bounce off the field line apex the parallel component of v_y, notated as $v_{\|y}$ will change to

$$v_{\|y,n+1} = v_{\|y,n} + 2V_{LT}(t_{n+1}) \tag{C.1}$$

The particle will have travelled a total distance of $y_{n+1} + y_n - 2y_{mirror}$ (distance down and distance up) in the time $t_{n+1} - t_n$ leading to the following equation

$$v_{\|y,n}\,[t_{n+1} - t_n] = y_{n+1} + y_n - 2y_{mirror}$$

Rearranging for y_{n+1} gives

$$y_{n+1} = -y_n + 2y_{mirror} + v_{\|y,n}(t_{n+1} - t_n) \tag{C.2}$$

On the other hand, since the field line apex is moving with velocity $V_{LT}(t)$, we also have

$$y_{n+1} = y_n + \int_{t_n}^{t_{n+1}} V_{LT}(t)\,dt = y_n + F_y(t_{n+1}) - F_y(t_n) \tag{C.3}$$

with $F_y(t) = \int V_{LT}(t)dt$. A point to note here is that t_{n+1} of the next bounce is unknown and has to be calculated.

This can be done by substituting Eqn. C.2 into to C.3 to eliminate the unknown y_{n+1} to get the transcendental equation

$$F_y(t_{n+1}) - v_{\|y,n} t_{n+1} = F_y(t_n) - v_{\|y,n} t_n - 2(y_n - y_{mirror}). \tag{C.4}$$

Usually Eq. C.4 will have to be solved numerically for t_{n+1} using an iterative scheme such as e.g. the Newton-Raphson method. However, for the case of a constant $v_{LT}(t)$ the equation becomes linear and can be solved analytically (see next section). For the Newton Raphson method the function that needs to be set to zero is

$$f = [F_y(t_{n+1}) - F_y(t_n)] + 2(y_n - y_{mirror}) - v_{\|y} [t_{n+1} - t_n] = 0 \tag{C.5}$$

and the derivative of the function with respect to t_{n+1} is

$$\frac{df}{dt_{n+1}} = V_{LT}(t_{n+1}) - v_{\|y} \tag{C.6}$$

Once t_{n+1} is known, all other relevant quantities can be determined and the process can be repeated until the end of the calculation.

C.2 Time Step in Model 1

We begin with a simplified assumption that our loop top V_{LT} remains constant. This will give us a linearly decreasing loop top height of

$$y(t) = V_{LT}(t - t_0) + y_{init}, \tag{C.7}$$

where y_{init} and t_0 are the initial height and time at the loop top respectively. From these two assumptions we can find an analytical expression for the bounce times in the simplified trap. The locations of each bounce time are shown in Fig. C.1, where the numbers $(1) - (4)$ indicate the time calculated for the particle at a specific location in the trap. Location (1) representing $t^{n+1/4}$, the time immediately after a bounce off the bottom foot point, (2) representing $t^{n+1/2}$, the time immediately after bouncing off the moving mirror at the loop top, (3) representing $t^{n+3/4}$, the time immediately after bouncing off the second foot point and (4) representing t^{n+1}, the time completed for one full particle orbit. So the following equations give the time at each point:

$$(1) \qquad t^{n+1/4}: \qquad \frac{y(t^n) - y_{mirror}}{{v_{\|y}}^n} = t^{n+1/4} - t^n$$

$$(2) \qquad t^{n+1/2}: \qquad \frac{y(t^{n+1/2}) - y_{mirror}}{{v_{\|y}}^n} = t^{n+1/2} - t^{n+1/4} = t^{n+1/2} - \left\{ \frac{y(t^n) - y_{mirror}}{{v_{\|y}}^n} + t^n \right\}$$

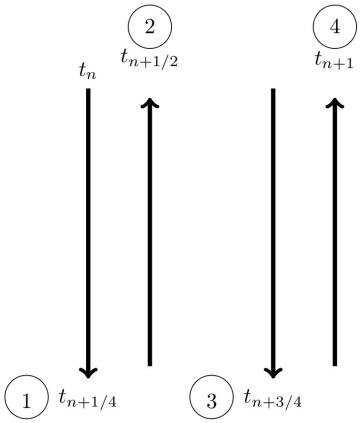

Figure C.1: The numbers in the circles mark the times for each bounce point in the simplified trap seen in Fig. 4.15. For one full particle orbit the particle performs four bounces to reach t^{n+1}.

$$(3) \qquad t^{n+3/4}: \qquad \frac{y(t^{n+1/2}) - y_{mirror}}{{v_{\|y}}^{n+1/2}} = t^{n+3/4} - t^{n+1/2}$$

$$(4) \qquad t^{n+1}: \qquad \frac{y(t^{n+1}) - y_{mirror}}{{v_{\|y}}^{n+1/2}} = t^{n+1} - t^{n+3/4}$$

v_y the velocity component along the direction normal to the surface of the mirror $\mathbf{e}_y$. $v_{\|y}$ is the parallel component of the particle velocity v_y. $y(t^n)$ is the height of the trap at the starting time t^n. $t^{n+1/4}$, $t^{n+1/2}$ and t^{n+1} are the bounce times at (2), (3) and (4) respectively with their corresponding trap heights $y(t^{n+1/4})$, $y(t^{n+1/2})$ and $y(t^{n+1})$. $v_{\|}^{n+1/2}$ is the new parallel velocity of the particle after bouncing off the moving mirror point at the loop top. From (2) we have

$$\begin{aligned} y(t^{n+1/2}) - y_{mirror} &= {v_{\|y}}^n t^{n+1/2} - \left\{ y(t^n) - y_{mirror} + {v_{\|y}}^n t^n \right\} \\ y(t^{n+1/2}) &= {v_{\|y}}^n (t^{n+1/2} - t^n) - y(t^n) + 2y_{mirror}. \end{aligned} \tag{C.8}$$

Rearranging for $t^{n+1/2}$ gives

$$t^{n+1/2} = \frac{y(t^{n+1/2}) + y(t^n) - 2y_{mirror}}{{v_{\|y}}^n} + t^n. \tag{C.9}$$

Substituting (3) into (4) gives

$$t^{n+1} = \frac{y(t^{n+1}) - y_{mirror}}{{v_{\|y}}^{n+1/2}} + \left\{ \frac{y(t^{n+1/2}) - y_{mirror}}{{v_{\|y}}^{n+1/2}} + t^{n+1/2} \right\} \tag{C.10}$$

substituting Eqn.(C.8) for $y(t^{n+1/2})$ and rearranging for t^{n+1} gives,

$$\begin{aligned} t^{n+1} &= \frac{y(t^{n+1}) - y_{mirror}}{{v_{\|y}}^{n+1/2}} + \left\{ \frac{{v_{\|y}}^{n}(t^{n+1/2} - t^{n}) - y(t^{n}) + 2y_{mirror} - y_{mirror}}{{v_{\|y}}^{n+1/2}} + t^{n+1/2} \right\} \\ &= \frac{y(t^{n+1}) - \cancel{y_{mirror}}}{{v_{\|y}}^{n+1/2}} + \left\{ \frac{{v_{\|y}}^{n}(t^{n+1/2} - t^{n}) - y(t^{n}) + \cancel{y_{mirror}}}{{v_{\|y}}^{n+1/2}} + t^{n+1/2} \right\} \end{aligned}$$

$$t^{n+1} = t^{n+1/2}\left\{1 + \frac{{v_{\|y}}^{n}}{{v_{\|y}}^{n+1/2}}\right\} - \frac{{v_{\|y}}^{n}t^{n} - y(t^{n+1}) + y(t^{n})}{{v_{\|y}}^{n+1/2}} \tag{C.11}$$

As this point we need a further two steps before we find t^{n+1}, namely:

- Solve Eqn. C.9 for $t^{n+1/2}$.
- Solve Eqn. C.11 for t^{n+1}.

For the first point the height of the loop top varies linearly as

$$y(t^{n+1/2}) = V_{LT}(t^{n+1/2} - t^{n}) + y(t^{n}).$$

Substituting $y(t^{n+1/2})$ into Eqn. C.9 gives,

$$t^{n+1/2} = \frac{1}{({v_{\|y}}^{n} - v_{LT})}\left\{{v_{\|y}}^{n}t^{n} + 2y(t^{n}) - v_{LT}t^{n} - 2y_{mirrror}\right\}. \tag{C.12}$$

For the second point substituting $y(t^{n+1}) = V_{LT}(t^{n+1} - t^{n+1/2}) + y(t^{n+1/2})$ into Eqn. C.11 gives,

$$\begin{aligned} t^{n+1} &= t^{n+1/2}\left\{1 + \frac{{v_{\|y}}^{n}}{{v_{\|y}}^{n+1/2}}\right\} + \frac{\{V_{LT}(t^{n+1} - t^{n+1/2}) + y(t^{n+1/2})\} - y(t^{n}) - {v_{\|y}}^{n}t^{n}}{{v_{\|y}}^{n+1/2}} \\ t^{n+1} &= \frac{1}{(1 - \frac{V_{LT}}{{v_{\|y}}^{n+1/2}})}\left\{t^{n+1/2}\{1 + \frac{{v_{\|y}}^{n}}{{v_{\|y}}^{n+1/2}}\} + \frac{y(t^{n}) - y(t^{n}) - {v_{\|y}}^{n}t^{n} - V_{LT}t^{n}}{{v_{\|y}}^{n+1/2}}.\right\} \end{aligned}$$

Multiplying the top and bottom by ${v_{\|y}}^{n+1/2}$ gives,

$$t^{n+1} = \frac{1}{{v_{\|y}}^{n+1/2} - V_{LT}}\left\{({v_{\|y}}^{n+1/2} + {v_{\|y}}^{n})t^{n+1/2} - {v_{\|y}}^{n}t^{n} - v_{LT}t^{n}\right\}.$$

Substituting Eqn. C.12 into t^{n+1} gives,

$$t^{n+1} = \frac{1}{{v_{\|y}}^{n+1/2} - V_{LT}}\left\{\frac{({v_{\|y}}^{n+1/2} + {v_{\|y}}^{n})}{({v_{\|y}}^{n} - V_{LT})}\left({v_{\|y}}^{n}t^{n} + 2y(t^{n}) - V_{LT}t^{n} - 2y_{mirror}\right)\right.$$

$$-{v_{\|y}}^n t^n - V_{LT} t^n \Big\}.$$

The loop top velocity is v_{LT} is negative relative to the y-axis. Replacing all $-v_{LT}$ with $|v_{LT}|$ in the above equation gives,

$$t^{n+1} = \frac{1}{{v_{\|y}}^{n+1/2} + |V_{LT}|} \left\{ \frac{({v_{\|y}}^{n+1/2} + {v_{\|y}}^n)}{({v_{\|y}}^n + |V_{LT}|)} \left({v_{\|y}}^n t^n + 2y(t^n) + |V_{LT}| t^n - 2y_{mirror} \right) \right.$$
$$\left. -{v_{\|y}}^n t^n + |V_{LT}| t^n \right\}.$$

Since ${v_{\|y}}^{n+1/2} = {v_{\|y}}^n + 2|V_{LT}|$ this gives,

$$\begin{aligned} t^{n+1} &= \frac{1}{{v_{\|y}}^n + 3|V_{LT}|} \left\{ \frac{2\cancel{({v_{\|y}}^n + |v_{LT}|)}}{\cancel{({v_{\|y}}^n + |v_{LT}|)}} [{v_{\|y}}^n t^n + 2y(t^n) + |V_{LT}| t^n - 2y_{mirror}] \right. \\ &- \left. {v_{\|y}}^n t^n + |V_{LT}| t^n. \right\} \end{aligned}$$

The above equation becomes,

$$t^{n+1} = \frac{1}{{v_{\|y}}^n + 3|V_{LT}|} \left\{ {v_{\|y}}^n t^n + 3|V_{LT}| t^n + 4y(t^n) - 4y_{mirror} \right\}. \tag{C.13}$$

C.3 Variation of y_{mirror} with $f(\theta)$

From initial studies using the simple CMT model it was found that with increasing pitch angle θ_{init} the mirror height y_{mirror} keeps increasing. This posed the question whether the model is still valid for the current choice of the starting pitch angle. A plot of the function $f(\theta) = \cot(\theta)$ against θ in radians is given in the top left hand corner of Fig. C.2. For the case of model 1 the initial conditions are $\phi_{init} = 15^\circ$ and $\alpha_{init} = 12.92^\circ$. The top right hand corner plot in Fig.(C.2), shows y_{mirror} against pitch angle θ. It is clearly seen that y_{mirror} has negative values which do not fit the requirements of our model, since for negative values of y_{mirror} the particle will escape immediately. Hence, cutting out the negative range of y_{mirror}, we only consider the positive range (i.e; $y_{mirror} \geq 0$). A magnification of the same region is shown in the plot at the bottom left hand corner. The horizontal blue line marks the point where $y_{mirror} = 0$ and the vertical red line indicates the point where $\theta_{init} = \alpha_{init} = 12.92^\circ$. This is the point where $l_{mirror} = l_{tot}$. Since we have the problem of y_{mirror} increasing with increasing initial pitch angle, we wanted to investigate how deceasing the slope of the function, $f(\theta_{init}) = \cot(\theta_{init})$, would affect the behaviour of the y_{mirror}. Fig. C.2 show the function $f = \cot^q(\theta)$ for power indices of 0.1, 0.25, 0.5, 0.75 and 1. The table of results below shows the values of $y(t)$, y_{mirror} and $y(t) - y_{mirror}$ for the different powers of q, when the trap has completely stopped. Firstly in all tables the dependence of y_{mirror} on θ can be seen. In table C.1 for a power index of 1, the lowest and highest values of y_{mirror} are 1.40 and 2.13 respectively. Considering the fact that $y_{init} = 4.2$ these values for y_{mirror} are

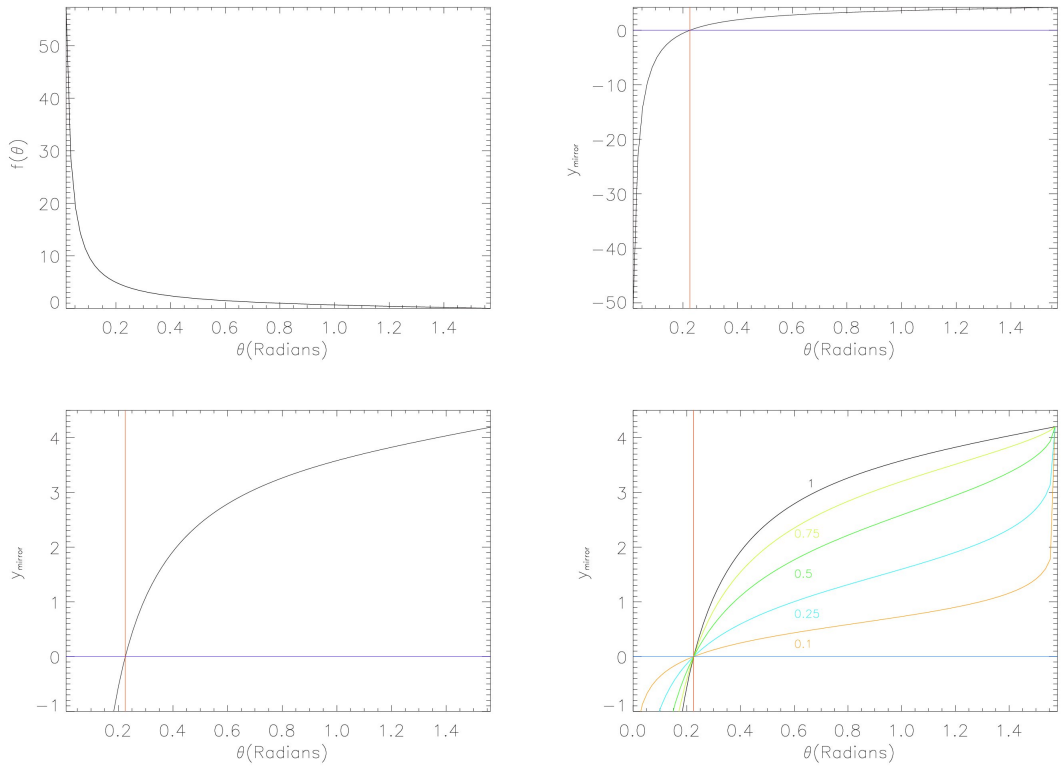

Figure C.2: *Top left*:plot of the function $f(\theta_{init}) = \cot(\theta_{init})$. *Top Right*: gives the total y_{mirror} range plotted against θ_{init}. *Bottom left*: gives the total y_{mirror} range plotted against θ_{init} in the positive range. For this graph the vertical red line indicates the point where $\theta_i = 12.92°$. The horizontal blue line marks the point where $y_{mirror} = 0$. The point where these to lines meet is where $\theta_i = \alpha_i$ and $l_{mirror} = l_{tot}$ which is one of the assumptions we make in our model. *bottom right*: Graph of y_{mirror} against θ for different power indices of q.

Table C.1: Table with values of initial pitch angle θ_{init}, y(t), y_{mirror} and $y(t) - y_{mirror}$. This results are based on $f = \cot(\theta_{init})$, $\alpha = 12.92°$, $y_{init} = 4.2$, $\phi_{init} = 15°$ and $y_{stop} = 2.73$ which are all fixed quantities.

θ°_{init}	$y(t)$	y_{mirror}	$y(t) - y_{mirror}$
19	2.38	1.40	0.98
20	2.46	1.55	0.91
21	2.55	1.69	0.86
22	2.62	1.81	0.80
25	2.48	2.13	0.34

already at a noticeable height. For a power index of 0.75 in table C.2 sees these values drop to 1.10 and 1.73 for the minimum and maximum values for y_{mirror} respectively. It is the same story in table C.3 and C.4 where the values of y_{mirror} are decreasing with decreasing power indices.

Table C.2: Same quantities as discussed in Table C.1. Results based on $f = \cot^{0.75}(\theta_{init})$.

θ°_{init}	$y(t)$	y_{mirror}	$y(t) - y_{mirror}$
19	2.612132	1.102667	1.509465
20	2.668173	1.228899	1.439274
21	2.719261	1.345147	1.374114
22	2.382331	1.452678	0.9296534
25	2.533715	1.732754	0.8009605

Table C.3: Same quantities as discussed in Table C.1. Results based on $f = \cot^{0.5}(\theta_{init})$.

θ°_{init}	$y(t)$	y_{mirror}	$y(t) - y_{mirror}$
19	2.442475	0.7717299	1.670745
20	2.480824	0.8655205	1.615303
21	2.515904	0.9530752	1.562829
22	2.548073	1.035128	1.512945
25	2.629913	1.254055	1.375859

Table C.4: Same quantities as discussed in Table C.1. Results are based on $f = \cot^{0.25}(\theta_{init})$.

θ°_{init}	$y(t)$	y_{mirror}	$y(t) - y_{mirror}$
19	2.721513	0.4054337	2.316078
20	2.270561	0.4576995	1.812862
21	2.284618	0.5071578	1.777460
22	2.297007	0.5541170	1.742890
25	2.325282	0.6824768	1.642805

Table C.5: Same quantities as discussed in Table C.1. Results based on $f = \cot^{0.1}(\theta_{init})$.

θ°_{init}	$y(t)$	y_{mirror}	$y(t) - y_{mirror}$
19	2.628659	0.1671281	2.461531
20	2.628334	0.1894398	2.438894
21	2.627151	0.2107258	2.416425
22	2.625141	0.2310953	2.394046
25	2.614351	0.2875900	2.326761

In table C.5 the results for $f = \cot^{0.1}(\theta_{init})$ are shown. All values of y_{mirror} are substantially smaller than their corresponding $y(t)$ value. We naturally choose $f = \cot^{0.1}(\theta)$ as our function and use it all through the cases discussed in the next section.

Appendix D

Normalisation for the Energy Loss Term

D.1 Normalisation of the Coefficient $\frac{dv}{dt}$

Th normalisation of the collisional coefficient for $\frac{dv}{dt} = -K^2 4\pi\rho\frac{q^4}{m^2v^2}\ln\Lambda$ is given in the following way:

$$\begin{aligned}\frac{v_0}{t_0}\frac{d\tilde{v}}{d\tilde{t}} &= -K^2 4\pi\rho\frac{q^4}{m^2 v_0\tilde{v}^2}\ln\Lambda \\ &= -K^2 4\pi\rho\frac{q^4}{m^2}\frac{1}{\tilde{v}^2}\left(\frac{{T_0}^4}{{L_0}^3}\right)\ln\Lambda. \end{aligned} \tag{D.1}$$

Using the gyro-frequency of an electron $\omega_e = \frac{\rho q^2}{m\varepsilon_0}$ gives

$$\frac{d\tilde{v}}{d\tilde{t}} = -\frac{\ln\Lambda}{4\pi}\frac{{\omega_e}^4}{\rho}\left(\frac{{T_0}^4}{{L_0}^3}\right)\frac{1}{\tilde{v}^2}, \tag{D.2}$$

where coefficient $\frac{\ln\Lambda}{4\pi}\frac{{\omega_e}^4}{\rho}\left(\frac{{T_0}^4}{{L_0}^3}\right)$ is dimensionless. Since $\rho\frac{q^4\ln\Lambda}{4\pi{\varepsilon_0}^2m^2}\left(\frac{{T_0}^4}{{L_0}^3}\right)$ gives us a dimensionless quantity we scale the density, time and length in the code in the following way:

$$\begin{aligned}\rho &= \rho_0\tilde{\rho}, \\ T &= T_0\tilde{T}, \\ L &= L_0\tilde{T}, \end{aligned}$$

where we choose $L_0 = 10^7$m and $T_0 = 100$s as the normalisation for length and time in the code. If for example, we choose to normalise the density by $\rho_0 = 10^{15}\ m^{-3}$ then we would get,

$$\rho_0\tilde{\rho}\frac{q^4\ln\Lambda}{4\pi{\varepsilon_0}^2m^2}\left(\frac{{T_0}^4}{{L_0}^3}\right) = \frac{\ln\Lambda}{4\pi}\left[1.013\times10^9\right]\tilde{\rho}, \tag{D.3}$$

where the charge of an electron $q = 1.0622\times10^{-19}$C, permittivity of free space $\varepsilon_0 = 8.8542\times10^{-12}Fm^{-1}$, mass of an electron $m = 9.1094\times10^{-31}$kg and we choose a coulomb logarithm $\ln\Lambda \approx 20$ for a coronal temperature of 10^6K (Priest, 1982). For a typical velocity normalisation

in our code

$$v \approx 400\frac{L_0}{T_0} = 4 \times 10^7 \frac{m}{s}.$$

Therefore $\tilde{v}^2 = 1.6 \times 10^5$ and the order of $\frac{d\tilde{v}}{d\tilde{t}} \approx \tilde{\rho}\frac{10^9}{10^4} \approx 10^4$.

Bibliography

M. J. Aschwanden. Pulsed Particle Injection in a Reconnection-Driven Dynamic Trap Model in Solar Flares. ApJ, 608:554–561, June 2004a. doi: 10.1086/392494.

M. J. Aschwanden. *Physics of the Solar Corona. An Introduction*. Praxis Publishing Ltd, August 2004b.

M. J. Aschwanden. Particle acceleration and kinematics in solar flares - A Synthesis of Recent Observations and Theoretical Concepts (Invited Review). *Space Science Reviews*, 101:1–227, January 2002. doi: 10.1023/A:1019712124366.

S. A. Bogachev and B. V. Somov. Acceleration of Charged Particles in Collapsing Magnetic Traps During Solar Flares. *Astronomy Reports*, 45:157–161, February 2001. doi: 10.1134/1.1346724.

S. A. Bogachev and B. V. Somov. Comparison of the Fermi and Betatron Acceleration Efficiencies in Collapsing Magnetic Traps. *Astronomy Letters*, 31:537–545, August 2005. doi: 10.1134/1.2007030.

S. A. Bogachev and B. V. Somov. Formation of power-law electron spectra in collapsing magnetic traps. *Astronomy Letters*, 33:54–62, January 2007. doi: 10.1134/S1063773707010070.

S. A. Bogachev and B. V. Somov. Effect of Coulomb collisions on the particle acceleration in collapsing magnetic traps. *Astronomy Letters*, 35:57–69, January 2009. doi: 10.1134/S1063773709010071.

T. J. M. Boyd and J. J. Sanderson. *The Physics of Plasmas*. Cambridge University Press, February 2003.

P. J. Cargill, L. Vlahos, G. Baumann, J. F. Drake, and Å. Nordlund. Current Fragmentation and Particle Acceleration in Solar Flares. Space Sci. Rev., page 36, May 2012. doi: 10.1007/s11214-012-9888-y.

G. F. Chew, M. L. Goldberger, and F. E. Low. The Boltzmann Equation and the One-Fluid Hydromagnetic Equations in the Absence of Particle Collisions. *Royal Society of London Proceedings Series A*, 236:112–118, July 1956. doi: 10.1098/rspa.1956.0116.

B. N. Dwivedi. *Dynamic Sun*. Cambridge University Press, 2003.

A. G. Emslie, H. Kucharek, B. R. Dennis, N. Gopalswamy, G. D. Holman, G. H. Share, A. Vourlidas, T. G. Forbes, P. T. Gallagher, G. M. Mason, T. R. Metcalf, R. A. Mewaldt, R. J. Murphy, R. A. Schwartz, and T. H. Zurbuchen. Energy partition in two solar flare/CME events. *Journal of Geophysical Research (Space Physics)*, 109:A10104, October 2004. doi: 10.1029/2004JA010571.

A. G. Emslie, B. R. Dennis, G. D. Holman, and H. S. Hudson. Refinements to flare energy estimates: A followup to "Energy partition in two solar flare/CME events" by A. G. Emslie et al. *Journal of Geophysical Research (Space Physics)*, 110:A11103, November 2005. doi: 10.1029/2005JA011305.

S. Eradat Oskoui, T. Neukirch, and K. J. Grady. Loss cone evolution and particle escape in collapsing magnetic trap models in solar flares. *ArXiv e-prints*, February 2014.

E. Fermi. On the Origin of the Cosmic Radiation. *Physical Review*, 75:1169–1174, April 1949. doi: 10.1103/PhysRev.75.1169.

L. Fletcher. On the generation of loop-top impulsive hard X-ray sources. A&A, 303:L9, November 1995.

L. Fletcher, B. R. Dennis, H. S. Hudson, S. Krucker, K. Phillips, A. Veronig, M. Battaglia, L. Bone, A. Caspi, Q. Chen, P. Gallagher, P. T. Grigis, H. Ji, W. Liu, R. O. Milligan, and M. Temmer. An Observational Overview of Solar Flares. Space Sci. Rev., 159:19–106, September 2011. doi: 10.1007/s11214-010-9701-8.

T. G. Forbes and L. W. Acton. Reconnection and Field Line Shrinkage in Solar Flares. ApJ, 459: 330–+, March 1996. doi: 10.1086/176896.

C.W. Gardiner. *Handbook of stochastic methods for physics, chemistry, and the natural sciences*. Springer, 1985.

E. Gibson. *The quiet sun.* 1977.

P. Giuliani, T. Neukirch, and P. Wood. Particle Motion in Collapsing Magnetic Traps in Solar Flares. I. Kinematic Theory of Collapsing Magnetic Traps. ApJ, 635:636–646, December 2005. doi: 10.1086/497366.

L. Golub and J. M. Pasachoff. *The Solar Corona*. September 1997.

K. J. Grady. *Solar flare particle acceleration in collapsing magnetic traps.* 2012. URL https://library.st-andrews.ac.uk/search/Y?search=keith+grady.

K. J. Grady and T. Neukirch. An extension of the theory of kinematic MHD models of collapsing magnetic traps to 2.5D with shear flow and to 3D. A&A, 508:1461–1468, December 2009. doi: 10.1051/0004-6361/200913230.

K. J. Grady, T. Neukirch, and P. Giuliani. A systematic examination of particle motion in a collapsing magnetic trap model for solar flares. A&A, 546:A85, October 2012. doi: 10.1051/0004-6361/201218914.

M. Karlický. X-Ray Emission of the April 6, 2001 Flare Modelled by Processes in a Collapsing Magnetic Trap. *Hvar Observatory Bulletin*, 29:137–147, 2005.

M. Karlický. X-Ray Emission from Flare Collapsing Trap. Space Sci. Rev., 122:161–168, February 2006. doi: 10.1007/s11214-006-5885-3.

M. Karlicky and M. Barta. Collapsing magnetic trap as accelerator of electrons in solar flares. In *IAU Joint Discussion*, volume 1 of *IAU Joint Discussion*, August 2006.

M. Karlický and M. Bárta. X-Ray Loop-Top Source Generated by Processes in a Flare Collapsing Trap. ApJ, 647:1472–1479, August 2006. doi: 10.1086/505460.

M. Karlický and T. Kosugi. Acceleration and heating processes in a collapsing magnetic trap. A&A, 419:1159–1168, June 2004. doi: 10.1051/0004-6361:20034323.

V. A. Kovalev and B. V. Somov. The Role of Collisions in the Particle Acceleration in Solar-Flare Magnetic Traps. *Astronomy Letters*, 29:409–415, June 2003. doi: 10.1134/1.1579790.

S. Krucker, M. Battaglia, P. J. Cargill, L. Fletcher, H. S. Hudson, A. L. MacKinnon, S. Masuda, L. Sui, M. Tomczak, A. L. Veronig, L. Vlahos, and S. M. White. Hard X-ray emission from the solar corona. A&A Rev., 16:155–208, October 2008. doi: 10.1007/s00159-008-0014-9.

R. M. Kulsrud. *MHD description of plasma: Handbook of plasma physics*. October 1983.

R. Liu, H. Wang, and D. Alexander. Implosion in a Coronal Eruption. ApJ, 696:121–135, May 2009. doi: 10.1088/0004-637X/696/1/121.

R. Liu, C. Liu, T. Török, Y. Wang, and H. Wang. Contracting and Erupting Components of Sigmoidal Active Regions. ApJ, 757:150, October 2012. doi: 10.1088/0004-637X/757/2/150.

M. S. Longair. *High energy astrophysics*. 1981.

M. S. Longair. *High energy astrophysics. Vol.2: Stars, the galaxy and the interstellar medium*. 1994.

A. L. MacKinnon and I. J. D. Craig. Stochastic simulation of fast particle diffusive transport. A&A, 251:693–699, November 1991.

G. Mann, A. Warmuth, and H. Aurass. Generation of highly energetic electrons at reconnection outflow shocks during solar flares. A&A, 494:669–675, February 2009. doi: 10.1051/0004-6361:200810099.

J. A. Miller, P. J. Cargill, A. G. Emslie, G. D. Holman, B. R. Dennis, T. N. LaRosa, R. M. Winglee, S. G. Benka, and S. Tsuneta. Critical issues for understanding particle acceleration in impulsive solar flares. J. Geophys. Res., 102:14631–14660, July 1997. doi: 10.1029/97JA00976.

T. Minoshima, S. Masuda, and Y. Miyoshi. Drift-kinetic Modeling of Particle Acceleration and Transport in Solar Flares. ApJ, 714:332–342, May 2010. doi: 10.1088/0004-637X/714/1/332.

T. Minoshima, S. Masuda, Y. Miyoshi, and K. Kusano. Coronal Electron Distribution in Solar Flares: Drift-kinetic Model. ApJ, 732:111, May 2011. doi: 10.1088/0004-637X/732/2/111.

T. Neukirch. Theory of Energy Storage and Release in the Solar Corona. In *The Dynamic Sun: Challenges for Theory and Observations*, volume 600 of *ESA Special Publication*, December 2005.

T. Neukirch, P. Giuliani, and Wood P.D. *Particle Acceleration in Flares: Theory*. Cambridge University Press, 2007.

Theodore G. Northrop. *The Adiabatic Motion of Charged Particels*. Wiley, New York, 1963.

D. L. NRL Book. NRL (Naval Research Laboratory) plasma formulary, revised, 2007.

E. R. Priest. *Solar magneto-hydrodynamics*. 1982.

K. K. Reeves, D. B. Seaton, and T. G. Forbes. Field Line Shrinkage in Flares Observed by the X-Ray Telescope on Hinode. ApJ, 675:868–874, March 2008. doi: 10.1086/526336.

K. K. Reeves, H. D. Winter, and N. L. Larson. The Effects of Including Non-Thermal Particles in Flare Loop Models. In L. Bellot Rubio, F. Reale, and M. Carlsson, editors, *4th Hinode Science*

Meeting: Unsolved Problems and Recent Insights, volume 455 of *Astronomical Society of the Pacific Conference Series*, page 199, May 2012.

K. Schindler. *Physics of Space Plasma Activity*. November 2006.

P. J. A. Simões and E. P. Kontar. Implications for electron acceleration and transport from non-thermal electron rates at looptop and footpoint sources in solar flares. A&A, 551:A135, March 2013. doi: 10.1051/0004-6361/201220304.

P. J. A. Simões, L. Fletcher, H. S. Hudson, and A. J. B. Russell. Implosion of Coronal Loops during the Impulsive Phase of a Solar Flare. ApJ, 777:152, November 2013. doi: 10.1088/0004-637X/777/2/152.

B. V. Somov. Solar flare physics. In A. V. Stepanov, E. E. Benevolenskaya, & A. G. Kosovichev, editor, *Multi-Wavelength Investigations of Solar Activity*, volume 223 of *IAU Symposium*, pages 417–424, 2004. doi: 10.1017/S1743921304006349.

B. V. Somov and S. A. Bogachev. The Betatron Effect in Collapsing Magnetic Traps. *Astronomy Letters*, 29:621–628, September 2003. doi: 10.1134/1.1607500.

B. V. Somov and T. Kosugi. Collisionless Reconnection and High-Energy Particle Acceleration in Solar Flares. ApJ, 485:859–+, August 1997. doi: 10.1086/304449.

Boris V Somov. *Plasma Astrophysics, Part I: Fundamentals and Practice*. Astrophysics and Space Science Library. Springer, New York, NY, 2006.

P. A. Sturrock, T. E. Holzer, D. M. Mihalas, and R. K. Ulrich, editors. *Physics of the sun. Volume 3: Astrophysics and solar-terrestrial relations*, volume 3, 1986.

L. Sui, G. D. Holman, and B. R. Dennis. Determination of Low-Energy Cutoffs and Total Energy of Nonthermal Electrons in a Solar Flare on 2002 April 15. ApJ, 626:1102–1109, June 2005. doi: 10.1086/430086.

A. Warmuth, G. Mann, and H. Aurass. Modelling shock drift acceleration of electrons at the reconnection outflow termination shock in solar flares. Observational constraints and parametric study. A&A, 494:677–691, February 2009. doi: 10.1051/0004-6361:200810101.

H. D. Winter, P. Martens, and K. K. Reeves. Simulating the Effects of Initial Pitch-angle Distributions on Solar Flares. ApJ, 735:103, July 2011. doi: 10.1088/0004-637X/735/2/103.

P. Wood and T. Neukirch. Electron Acceleration in Reconnecting Current Sheets. Sol. Phys., 226: 73–95, January 2005. doi: 10.1007/s11207-005-5686-y.

V. V. Zharkova, K. Arzner, A. O. Benz, P. Browning, C. Dauphin, A. G. Emslie, L. Fletcher, E. P. Kontar, G. Mann, M. Onofri, V. Petrosian, R. Turkmani, N. Vilmer, and L. Vlahos. Recent Advances in Understanding Particle Acceleration Processes in Solar Flares. Space Sci. Rev., 159:357–420, September 2011. doi: 10.1007/s11214-011-9803-y.